VARIATIONAL MULTISCALE METHOD FOR COUPLED SYSTEMS: FREE-SURFACE FLOWS AND STRATIFIED TURBULENCE

BY

LIXING ZHU

DISSERTATION

Submitted in partial fulfillment of the requirements
for the degree of Doctor of Philosophy in Civil Engineering
in the Graduate College of the
University of Illinois at Urbana-Champaign, 2019

Urbana, Illinois

Doctoral Committee:

Professor Arif Masud, Chair
Professor C. Armando Duarte
Associate Professor Oscar Lopez-Pamies
Assistant Professor Jinhui Yan

ABSTRACT

This dissertation presents a robust numerical method for the class of coupled systems comprised of multiple interacting partial differential equations (PDE). Particular emphasis is placed on incompressible Navier-Stokes equations that are coupled with a hyperbolic scalar PDE. The method is derived based on the variational multiscale (VMS) framework. Specifically, two classes of coupled systems are considered: free-surface flows with a sharp interface marker and stratified turbulence with a smooth temperature field.

The additional nonlinearity introduced by the active scalar field to the nonlinear Navier-Stokes equation system is effectively accounted for by variationally derived stabilization term. In the context of the free-surface flows that are modeled by immiscible two-phase fluids, the dependency of fluid mechanical properties (i.e., density and viscosity) on the implicit interface marker (e.g., signed distance field) results in an interface that traverses through the elements. Applying VMS method to the coupled system results in an interface stabilization term. It is shown that the structure of the stabilization term leads to the so-called Ghost-Penalty method. In the context of internal dissipation in thermodynamics for incompressible flow with Boussinesq approximation, an energy conservation equation is appended that gives rise to a thermomechanically coupled system. The coupled fine-scale sub-problem is locally resolved to yield the closure model. The fine-scale turbulence features are accounted for by the VMS strategy wherein the hierarchical application of VMS results in further enhancement of the mass conservation.

The new method for coupled systems is implemented using hexahedral and tetrahedral elements, and the code is parallelized for the distributed memory system. A range of problems is presented to show the mathematical and computational features of the method.

ACKNOWLEDGEMENTS

First and foremost, the author would like to express his deepest gratitude to his advisor, Dr. Arif Masud. Not only most of the subjects covered in this dissertation were suggested by Dr. Masud, but his constant mentoring and help were also essential for accomplishing these studies. His persistence of high-quality research and his inspirational personality have won the author's highest respect and admiration.

The author also wants to thank other members of his dissertation committee, Dr. C. Armando Duarte, Dr. Oscar Lopez-Pamies, and Dr. Jinhui Yan, for their penetrative comments and encouraging discussions in preliminary and final exams. The author started the journey on mechanics and numerical methods by taking the courses from Dr. Duarte and Dr. Lopez-Pamies. Dr. Yan selflessly offered many insights and experience with computer methods in fluid dynamics. Their thoroughness in research and sharpness in vision illustrates the definition of excellence.

The numerical results presented in this dissertation relied on the computational resources provided by several facilities, including Illinois Campus Cluster Program, Blue Waters in National Center for Supercomputing Applications (NCSA), Comet in San Diego Supercomputer Center (SDSC), Stampede2 and Frontera in Texas Advanced Computing Center (TACC). The author wishes to express his gratitude for these programs.

The author also wants to thank his former and current colleagues: Dr. JaeHyuk Kwack, Dr. Timothy J Truster, Dr. Harishanker Gajendran, Dr. Pinlei Chen, Soonpil Kang, Marcelino Anguiano-Chavez, Shoaib A. Goraya, and Ignasius Pradipta Anugraha Wijaya, for their support, insights, and friendship. The author was also a lot benefited from the discussions with Xiaoyi Lu and Qiming Zhu.

Last but not least, the author would like to thank his wife Qiuchen, his parents, and his parents-in-law for their enduring support.

To my family

TABLE OF CONTENTS

CHAPTER 1: INTRODUCTION

1.1. BACKGROUNDS AND MOTIVATION

Incompressible flows coupled with passive/active scalar fields are encountered in various natural phenomena and engineering practices, ranging from the atmospheric science [117], where a temperature field is transported through the turbulent flows, to the hydraulic engineering [139], where the fluid dynamics convect an implicit interface marker. Other regimes of applications with this class of coupled systems embrace combustion [15] or, more generally, the chemical reaction in a scalar mixing layer and the evolution of magnetic fields in stellar astrophysics [171]. Here the scalar fields are the concentration of chemical constituents or the components of electromagnetic fields. Most of these physical problems amongst the listed applications are nearly impossible to attain experimental data. The complexity of this class of coupled mathematical problems, partially due to the additional nonlinearity brought in to the system by the active scalar field, engendered fundamental difficulties in resolving these problems analytically, even in a very much simplified setting. Therefore, computational fluid dynamics (CFD) is the only reliable tool to address the new physics due to the coupling effects and obtain high-fidelity data to guide industrial designs.

One essential ingredient in any CFD framework is a fluid dynamics solver. For the simplicity of discussion, this dissertation is not going to cover other low Mach number approximation but put the foci on the incompressible hydrodynamics. The governing partial differential equations (PDE) are the incompressible Navier-Stokes equations that represent two conservation laws: momentum and mass. There are two major challenges for a robust numerical method for this set of PDEs: advection-dominant flow (i.e., high Reynolds number) and the inf-sup or Ladyzhenskaya-Babuška-Brezzi conditions [16]. In continuum mechanics, conservation laws can be derived through the Leibniz-Reynolds transport theorem [39] and thus has the nature of hyperbolic PDE due to the material derivative. The characteristics of hyperbolic PDEs are directional, particularly in the advection-dominant flow, which indicates that the numerical discretization needs to be aware of the flow direction. In the context of finite differences and

finite volumes, this issue is addressed through upwind-biased schemes [99]. The inf-sup condition arises in the saddle-point problems like the momentum balance equation with a constraint of incompressibility, which prevents using equal order interpolation of unknown mixed fields (i.e., collocated grids in finite volume/difference method and same shape functions in finite element method). As conventional practices, a staggered grid [88] and its counterparts in finite-element regime—Taylor-hood elements [12] are widely used.

In the context of the finite-element method, the numerical instability resulting from the advection-dominant flow and inf-sup condition is addressed in the unified framework of stabilized methods. The original works on this subject are achieved by Hughes and his coworkers, including streamline upwind/Petrov-Galerkin (SUPG) [20] and Galerkin/least-square (GLS) [70] methods for advection-diffusion equations, where a residual-based stabilized form is proposed to prevent the spurious solutions field when the Peclet number becomes large. These stabilized weak forms are then extended to the incompressible Stokes/Navier-Stokes problems [68], where the inf-sup condition is also overcome. pressure-stabilizing/Petrov–Galerkin [155] that helps with the inf-sup condition also falls into this regime. A more generalized framework—Variational Multiscale [66,67], is hereafter proposed by Hughes, which provides the rigorous mathematical foundation of the stabilized or the multiscale methods. The general philosophy of the VMS-type method is to variationally project the fine-scale solution that is filtered out by the discretization to the coarse-scale sub-problems. Two major branches of seeking solutions of fine scales are the Green's function and the residual-free bubble, which had been proved to be equivalent [17]. The resulting stabilized form includes the components from SUPG, GLS, and PSPG and inherently contains an error estimator [93]. Masud and his coworkers have employed this framework to develop stabilized method for various PDEs in many different physics, including advection-diffusion equation for heat transfer and drug delivery [113,115], incompressible Navier-Stokes equations for fluid mechanical problems [84,105], Darcy flow for geophysics [111], and Schrödinger wave equation for electronic properties of materials [103,112]. Specifically, in this series of works on stabilized method, the fine-scale problems are discretized with bubble function, an idea can be traced back to the works of residual-free

bubbles [18,19,48,49] by Brezzi and Franca and their coworkers. However, it is not practical to derive the residual-free bubble for nonlinear PDE; thus, the standard bubble functions are adopted.

Another fundamental but notorious difficulty in fluid dynamics solver is the turbulence—the indeterminacy of flow field in all dimensions of space and time. Although Navier-Stokes equations are generally valid across all scales, even for the limits of continuum mechanics, the computational cost of fully resolved simulation (i.e., direct numerical simulation (DNS)) is in the cubic order of Reynolds number [134]. Within the current architecture of computers, DNS is only practical for flows with relatively low Reynolds numbers. Therefore, a model must be utilized for industrial-strength simulations to reduce the resolution of the simulation. According to the resolution of the resolved scales and preservation of indeterminacy, turbulence modeling techniques can be classified as two primary classes: large-eddy simulation (LES) [143] and Reynolds-Averaged Navier-Stokes (RANS) [138]. LES-type methods usually require that the grid is sufficiently refined to resolve 80% of the energy of the entire domain and preserve the fluctuation of the flow fields while the RANS-type method often targets space and time averaged results. There are some hybrid methods that not exactly fall into these two regimes, including detached eddy simulation (DES) [146] and very-large-eddy simulation (VLES) , which utilize different strategies of modeling in different regions of the computational domain. Essentially, the purpose of the LES and RANS technique is to model the Reynolds stress, the gap between the unfiltered and filtered nonlinear convection term. For this reason, turbulence modeling is frequently referred to as a "closure problem".

VMS philosophy is inherently consistent with turbulence modeling since a fine-scale solution has already built for flow fields, and the projection from the fine scale to coarse scale is also well defined. The rest of the work for a feasible VMS-type LES model is as simple as identifying the sub-grid Reynolds stress in the weak form. The pioneering work has been achieved by Hughes and his colleagues in incompressible flows [13] and compressible flows [46], where the fine-scale/subgrid-scale fields are modeled with approximated Green's function and driven by the coarse-scale residual. This feature ensures the proposed turbulence model automatically vanished at the place where the flow field is fully resolved

(i.e., DNS). Under the VMS framework, Masud and Calderer [30,107] further refine the method and evolve into a multilevel VMS method, which eventually removes all *ad hoc* devices in the turbulence modeling.

The active scalar field in the governing system is introduced to represent other physics, which is two-way coupled with fluid dynamics. One class of this type of coupled system is free-surface problems. Two fundamental frames of reference in continuum mechanics are Lagrangian and Eulerian. Following this way of thinking, the representation of the free surface falls into two regimes: interface tracking and interface capturing. The interface-tracking techniques explicitly track the free surfaces as moving boundary, including particle finite-element methods [76,125,132], smooth particle hydrodynamics [38,120], constrained interpolation profile (CIP) method [151], etc. Masud and his colleagues [29,84] develops mesh moving strategies based on a pseudo elasticity problem with underlying arbitrary Lagrangian-Eulerian (ALE) frame of references. However, the capacity of the interface-tracking technique relies on the extent of mesh moving. In the problems with rotation and over-turning free surfaces, the mesh is often distorted to the extent that the Jacobian is nearly zero or even negative, and the simulation can not be pushed forward without remeshing of the computational domain.

Due to such constraints of interface-tracking methods, the other type of method—interface-capturing technique is widely used for the free surfaces in the two-phase flows. The idea of the interface-capturing type method is to implicitly capture the evolution of the interface through a scalar field. By the choice of the scalar field, this type of method can be further classified as volume-of-fluid (VOF) method [87,148] that uses a marker scalar field (zero or one) which is governed by the mass conservation equation, and level-set method [54,148,149] that uses signed distance field which is governed by an advection equation. The signed distance field is smooth near the interface; thus, it has better accuracy of interface representing when compared to the VOF method with the same resolution. However, the governing hyperbolic PDE of the level-set method is not conservative, which brings in technical difficulties in a long-time run. Therefore, some auxiliary processes need to be amended, including the re-initialization process [11,44,147] and mass conservation algorithm [81,144]. In the interface-capturing

method, due to the Eulerian frame of references, some elements are going to be transverse by the interface. The stiff matrices of those elements are ill-conditioned when the partition of one phase is too small, or the gap of density and viscosity of two phases is very large. To address this issue, several techniques [21,22,26,59] have been proposed in the literature to control the jump of velocity gradients across the interface.

Another type of coupled system of fluid dynamics and an active scalar field is the density-stratified flows. Unlike the free-surface problems, the introduced temperature field is not bringing any discontinuity into the system. However, the density stratification is involved with the flow physics; namely, it may enhance the production of turbulence, and it may also affect the damping mechanism of turbulence. Therefore, the foci of numerical methods for this type of problem are the evolved closure problems. Comparing to the isothermal case, a new subgrid-scale Reynolds flux term arises in the stratified flow due to the nonlinear advection in the conservation law of energy. The conventional subgrid-scale model for LES for isothermal flow has been extended to density-stratified turbulence [85,137,160]. The effective viscosity and thermal diffusivity are selected either by expanding the unknown fields to finer scales or by phenomenological assumptions (e.g., turbulent Prandtl number). The VMS type LES models are also reported in the literature, including the stable stratification [168] and natural convections [165].

1.2. OUTLINES OF THE DISSERTATION

The dissertation presents the derivation of a new stabilized form of advection-diffusion equation that takes the fine-scale time-dependency into account, an interface stabilization which shows the mathematical foundation of ghost-penalty type method, an enhanced multilevel VMS turbulence model for isothermal flows and a new VMS residual-based turbulence model for incompressible flows with density stratification. Some auxiliary algorithms to serve for the robustness of long-time are also covered. The remaining chapters are organized as follows:

- Chapter 2 presents an interface-capturing method for two-phase flows with large-amplitude free-surface motion. The method is developed by embedding the level-set equation in the momentum balance equations via dependency of the material properties on the signed distance field. For plunging free-surface motions, the method is augmented with a reinitialization process that is based on a stabilized form of the Eikonal equation and reconstructs the signed distance field. Conservation of mass in extreme free-surface motions is maintained via a mass-conservation term that is based on the notion of minimizing the error in the computed signed distance field. Benchmark test cases of two-dimensional (2D) and three-dimensional (3D) dam-break problems are presented to validate the method and show its range of applicability.
- Chapter 3 presents our interface stabilized method for moving and deforming interface problem in immiscible, discrete, multi-phase flows. The jump in viscosity and density of the fluids across the arbitrarily deforming phase boundaries can trigger instability in the solution. The main contribution in this chapter is the variationally consistent derivation of interface stabilization terms that appear naturally when the Variational Multiscale (VMS) method is applied to the coupled system of partial differential. Benchmark problems in 2D and 3D are presented to highlight the salient features of the proposed interface stabilization method and to show its range of applications.
- Chapter 4 presents a residual-based turbulence model for problems with free surfaces. To accommodate the moving boundaries, we cast the formulation in an Arbitrary Lagrangian-Eulerian frame of reference. The free surface boundary condition is imposed weakly which results in a formulation that conserves the volume of the fluid. A variety of benchmark problems show the accuracy and range of applicability of the proposed formulation, and results are compared with published data. A wavy bed problem is investigated to show the interaction of turbulence generated at the bottom surface with the free surface, thereby leading to irregular free surface elevations.

- Chapter 5 presents a residual-based isothermal turbulence model. The method is derived based on Variational Multiscale ideas that assume a decomposition of the solution fields into overlapping scales that are termed as coarse and fine scales. The fine scales are further split hierarchically into fine-scales level-I and fine-scales level-II. The hierarchical variational problems that govern the two fine-scale components are modeled employing bubble functions approach. The model for level-II scales is variationally embedded in the mixed field level-I problem to yield a stable level-I formulation. Subsequently, the model for level-I scales that in fact constitutes the fine-scale turbulence model is then variationally injected in the coarse-scale variational form. A significant feature of the method is that it does not contain any embedded tunable parameters. Three classes of numerical tests are carried out to validate the LES model, including homogeneous turbulence, turbulence with 1D homogeneity, and transition from laminar to turbulent flow.
- Chapter 6 extends the multilevel VMS LES model to the incompressible flow with density stratification. The hierarchical application of VMS and three-level scale separation results in a new residual-based VMS turbulence model without any embedded or tunable parameters for implicit LES. The coupling between the mechanical and thermal phases is preserved in the fine-scale model. A thorough study on the structure of the fully coupled anisotropic turbulence model is carried out to illustrate the necessity and superiority of the coupling in the fine scales. The variational consistency is also validated through a convergence rate study in both spatial and temporal refinement on a Beltrami-type problem with an exact solution. The statistical results of LES of Rayleigh-Benard convection with proposed model show good alignment with DNS and other LES model with finer mesh.
- Chapter 7 finishes with some concluding remarks on the contributions of this dissertation. Also, the potential future research plans are outlined.

CHAPTER 2: INTERFACE-CAPTURING METHOD FOR FREE-SURFACE PLUNGING AND BREAKING WAVES*

2.1. INTRODUCTION

Breaking of high amplitude waves is a process that involves conversion of wave energy into turbulent energy, leading to violent transformation of free surfaces that exert massive hydrodynamic loads on off-shore installations and coastal infrastructure. Such waves are typically triggered in hurricanes and tropical storms, as well as in off-coast seismic activity that gives rise to high amplitude Tsunami waves. Catastrophic structural failure of large water reservoirs and dams also produces high amplitude waves that impart massive hydrodynamic loads on the downstream structures. Impulsive loads from waves breaking against substructures are generally much larger than the quasi-static forces and cause severe damage to structural elements. Therefore, modeling of breaking waves interacting with structures has been important in ocean and marine engineering. Furthermore, most of the offshore wind farms lie in shallow waters of depths between 5 to 30m [33] and therefore understanding hydrodynamic loads from high-amplitude waves has important design-related implications.

The two dominant characteristic features of breaking waves are high Reynolds numbers and strong free surface kinematics. Wave impact force greatly depends on the evolution of free surface profiles, instantaneous wave height, local changes in velocities, and geometric properties associated with the breaking process [75,79]. From the design perspective the free-surface waves that are most relevant to offshore structures are the spilling and plunging breakers [159]. The energy from the plunging breakers gets dissipated over a relatively small area, thereby giving rise to high impulsive loads that onto the structures.

Various approaches that are used for the modeling of free surfaces and two-phase flows involving moving interfaces include: (i) the interface-tracking methods, and (ii) the interface-capturing methods.

* This chapter has been adapted from "Zhu, L., Goraya, S.A. and Masud, A., 2019. Interface-Capturing Method for Free-Surface Plunging and Breaking Waves. *Journal of Engineering Mechanics*, 145(11), p.04019088.". The copyright owner has provided written permission to reprint the work.

Interface tracking techniques employ formulations that are written in an Arbitrary Lagrangian-Eulerian (ALE) [29,32,65,71,84,102] frame together with time evolving spatial meshes that explicitly track the kinematics of the free surface. ALE based methods are however limited by the extent to which they can accommodate the distortion of the mesh [102], and excessive distortion can eventually lead to mesh breakdown. Another class of interface tracking techniques is based on a Lagrangian description of fluids, namely the Particle Finite Element Method (PFEM) [132], where the continuum parts associated with rapidly moving interfaces are discretized with particles, while the domain away from the interfaces employs a Lagrangian description. This method has shown success in overcoming the mesh distortion issues because a contiguous mesh is no longer needed. Yet another method, termed as Constrained Interpolation Profile (CIP) [150] has been proposed that employs Soroban grids and has time-evolution and mesh adaptivity features for the free surfaces.

The interface-capturing techniques are based on Eulerian frame of reference and employ fixed grids wherein the representation of complicated topology of the free surfaces is implicitly tracked via a scalar transport equation. These techniques have been employed in the context of finite element and finite volume methods. In the volume-of-fluid (VOF) scheme [43,87,97] for Cartesian grids, a step function is used to indicate the fraction of fluid within the cell. The discontinuity induced due to the step function representation of the two-phase subdomains requires edge-based stabilized methods for the VOF approach to be successful [43]. On the other hand, the level set method [8,81,128,147] uses a continuous scalar field to mark the interface and therefore overcomes the numerical drawback associated with VOF scheme. Herein, instead of searching the partially filled elements, the interface is represented by the iso-contour of zero level set.

In this paper free-surface flow is described as a two-phase flow with well-defined interfaces, wherein fluids are modeled via residual-based stabilized form of the incompressible Navier-Stokes equations. The background mesh does not move, while the highly nonlinear motion of the air-water interface is tracked via a hyperbolic equation that is driven by the velocity field furnished by the Navier-Stokes equations. A significant contribution in this work is an interface-capturing method that is derived

by embedding the level-set field in the material coefficients, thus providing pointwise spatiotemporal information on the evolving material interface, at a fixed, but otherwise arbitrary grid point.

The nonlinear terms in the incompressible Navier-Stokes equations require stabilization to address instabilities associated with high convection, in addition to addressing the inf-sup condition on the combination of interpolation functions for the velocity and pressure fields. Amongst the celebrated stabilized methods are the Streamline Upwind/Petrov-Galerkin (SUPG) method [20], and the Galerkin/Least-squares (GLS) method [67]. In this work we blend ideas from VMS method [66,67] that were used in developing stabilized form of the incompressible Navier-Stokes equations [84], with the VMS stabilized form of the advection-diffusion equation [113], to derive the new method. Variational embedding of the fine-scale model in the coarse-scale weak form results in interface capturing terms with embedded discontinuity that helps in maintaining sharp definition of the interface, We emphasize the structural similarity of interface capturing term with the Ghost penalty term [8,23] and with the stabilization proposed for the cut finite element methods [28]. For complex 3D plunging waves, the method is augmented with a re-initialization process [147] that is based on a stabilized form of Eikonal equation. A mass correction term [144] is employed to minimize mass loss via applying a correction to the computed signed distance field.

An outline of the paper is as follows. We first present the derivation of the method for rapidly fluctuating free-surface motions. The techniques for mass conservation and re-initialization are discussed next. A set of numerical test cases with increasing degree of complexity is presented to show the mathematical attributes of the proposed method. Conclusions are drawn at the end.

2.2. STABILIZED INTERFACE FORMULATION OF THE INCOMPRESSIBLE NAVIER-STOKES EQUATIONS

We write the Navier-Stokes equations where material coefficients are written as a function of the level-set field ϕ.

$$\rho(\phi)\boldsymbol{v}_{,t} + \rho(\phi)\boldsymbol{v}\cdot\nabla\boldsymbol{v} - 2\eta(\phi)\nabla\cdot\boldsymbol{\varepsilon}(\boldsymbol{v}) + \nabla p = \rho(\phi)\boldsymbol{f} \quad \text{in} \quad \Omega\times]0,T[, \tag{2.1}$$

$$\nabla \cdot \boldsymbol{v} = 0 \quad \text{in} \quad \Omega \times]0,T[, \tag{2.2}$$

$$\boldsymbol{v} = \boldsymbol{g} \quad \text{on} \quad \Gamma_g \times]0,T[, \tag{2.3}$$

$$\boldsymbol{\sigma} \cdot \boldsymbol{n} = \left(2\eta(\phi)\boldsymbol{\varepsilon}(\boldsymbol{v}) - p\boldsymbol{I}\right) \cdot \boldsymbol{n} = \boldsymbol{h} \quad \text{on} \quad \Gamma_h \times]0,T[, \tag{2.4}$$

$$\boldsymbol{v}(\boldsymbol{x},0) = \boldsymbol{v}_0 \quad \text{on} \quad \Omega \times \{0\}, \tag{2.5}$$

where (2.1) is the momentum balance equation and (2.2) is the incompressibility condition. $\boldsymbol{v}$ and p are velocity and pressure, respectively. $\boldsymbol{g}$ is the Dirichlet boundary condition, $\boldsymbol{v}$ is the Neumann boundary condition, and $\boldsymbol{v}_0$ is the initial condition. $\boldsymbol{\sigma}$ is the stress tensor and $\varepsilon(\boldsymbol{v})$ is the strain rate tensor, which is defined as $\boldsymbol{\varepsilon}(\boldsymbol{v}) = \nabla^s \boldsymbol{v} = (\nabla \boldsymbol{v} + (\nabla \boldsymbol{v})^T)/2$. ρ is the density and η is the dynamics viscosity and these parameters possess distinctly different values for air and water phases. As we show in the numerical section, since both material parameters are a function of the signed distance field, they are evaluated via volume-proportional averaging in the elements that are traversed by the iso-contour of the zero level-set.

We append a time dependent advection equation for the level set ϕ to the transient Navier-Stokes equations.

$$\dot{\phi} + \boldsymbol{v} \cdot \nabla \phi = 0 \quad \text{in} \quad \Omega \times]0,T[\tag{2.6}$$

$$\phi(\boldsymbol{x},0) = \phi_0(\boldsymbol{x}) \quad \text{in} \quad \Omega \times]0,T[\tag{2.7}$$

where (2.6) is the level-set advection equation, ϕ is the signed distance field, ϕ_0 is the initial condition, and $\boldsymbol{v}$ is the velocity field that is furnished by the Navier-Stokes equations.

The appropriate spaces of trial solution and weighting functions for the velocity and the signed distance fields are the standard $(H^1(\Omega))^{n_{sd}}$ spaces, and that for the pressure field is the standard $L_2(\Omega)$ space. The standard weak form of the incompressible and immiscible two-phase Navier-Stokes equations and the level-set advection equation are:

$$\left(\boldsymbol{w}, \rho(\phi)\dot{\boldsymbol{v}}\right) + \left(\boldsymbol{w}, \rho(\phi)\boldsymbol{v} \cdot \nabla \boldsymbol{v}\right) + \left(\nabla \boldsymbol{w}, 2\eta(\phi)\nabla^s \boldsymbol{v}\right) - \left(\nabla \cdot \boldsymbol{w}, p\right) = \left(\boldsymbol{w}, \rho(\phi)\,\boldsymbol{f}\right) + \left(\boldsymbol{w}, \boldsymbol{h}\right)_{\Gamma_h} \tag{2.8}$$

$$\left(q, \nabla \cdot \boldsymbol{v}\right) = 0 \tag{2.9}$$

$$\left(\psi, \dot{\phi} + \boldsymbol{v} \cdot \nabla \phi\right) = 0 \tag{2.10}$$

where $(\bullet,\bullet) = \int_{\Omega} (\bullet)\, d\Omega$ is the $L_2(\Omega)$ inner product.

The following section highlights the significant steps of the derivation while referring the interested to our earlier works [30,84,105] on the stabilized form of Navier-Stokes equations.

2.2.1. Variational Multiscale Split

The bounded domain Ω is discretized into non-overlapping element sub-domains Ω^e with boundaries Γ^e, where $\Omega = \bigcup_{e=1}^{n_{umel}} \Omega^e$ and n_{umel} is the total number of elements in the mesh. We denote the union of element interiors and element boundaries as $\Omega' = \bigcup_{e=1}^{n_{umel}} (\text{int})\Omega^e$ and $\Gamma' = \bigcup_{e=1}^{n_{umel}} \Gamma^e$, respectively. We assume an overlapping additive decomposition of velocity field $\boldsymbol{v}(\boldsymbol{x},t)$ and its weighting function $\boldsymbol{w}(\boldsymbol{x})$ into coarse or resolvable and fine or unresolved scales.

$$\boldsymbol{w}(\boldsymbol{x}) = \bar{\boldsymbol{w}}(\boldsymbol{x}) + \boldsymbol{w}'(\boldsymbol{x}) \quad \text{and} \quad \boldsymbol{v}(\boldsymbol{x},t) = \bar{\boldsymbol{v}}(\boldsymbol{x},t) + \boldsymbol{v}'(\boldsymbol{x}) \tag{2.11}$$

The fine-scale velocity field $\boldsymbol{v}'$ represents part of physics that is not adequately resolved by the given spatial discretization. Likewise, we assume an overlapping sum decomposition of the signed distance field into coarse- or resolvable- scales and fine- or sub-grid scales.

$$\psi(\boldsymbol{x}) = \bar{\psi}(\boldsymbol{x}) + \psi'(\boldsymbol{x}) \quad \text{and} \quad \phi(\boldsymbol{x},t) = \bar{\phi}(\boldsymbol{x},t) + \phi'(\boldsymbol{x},t) \tag{2.12}$$

We would like to state that in the level-set advection equation, the fine-scale signed distance field ϕ' should be viewed as a measure of error facilitated by the error estimator inherent in the fine-scale sub-problem in the VMS method. Substituting the additively decomposed form of (2.11) and (2.12) into (2.8), (2.9) and (2.10), and employing the linearity of the weighting function slot, we segregate the coupled system into the coarse-scale and fine-scale sub-problems that are written in the residual form.

Coarse-scale sub-problems:

$$R_1\left(\bar{\boldsymbol{w}};\bar{\boldsymbol{v}},\boldsymbol{v}',p,\bar{\phi},\phi'\right)=\left(\bar{\boldsymbol{w}},\rho\left(\bar{\phi}+\phi'\right)\dot{\bar{\boldsymbol{v}}}\right)+\left(\boldsymbol{w},\rho\left(\bar{\phi}+\phi'\right)\left(\bar{\boldsymbol{v}}+\boldsymbol{v}'\right)\cdot\nabla\left(\bar{\boldsymbol{v}}+\boldsymbol{v}'\right)\right)$$
$$+\left(\nabla\bar{\boldsymbol{w}},2\eta\left(\bar{\phi}+\phi'\right)\nabla^s\left(\bar{\boldsymbol{v}}+\boldsymbol{v}'\right)\right)-\left(\nabla\cdot\bar{\boldsymbol{w}},p\right) \tag{2.13}$$
$$-\left(\bar{\boldsymbol{w}},\rho\left(\bar{\phi}+\phi'\right)\boldsymbol{f}\right)-\left(\bar{\boldsymbol{w}},\boldsymbol{h}\right)_{\Gamma_h}=0$$

$$R_2\left(q;\bar{\boldsymbol{v}},\boldsymbol{v}'\right)=\left(q,\nabla\cdot\left(\bar{\boldsymbol{v}}+\boldsymbol{v}'\right)\right)=0 \tag{2.14}$$

$$R_3\left(\bar{\psi};\bar{\boldsymbol{v}},\boldsymbol{v}',\bar{\phi},\phi'\right)=\left(\bar{\psi},\left(\bar{\boldsymbol{v}}+\boldsymbol{v}'\right)\cdot\nabla\left(\bar{\phi}+\phi'\right)\right)=0 \tag{2.15}$$

Fine-scale sub-problems:

$$R_4\left(\boldsymbol{w}';\bar{\boldsymbol{v}},\boldsymbol{v}',p,\bar{\phi},\phi'\right)=\left(\boldsymbol{w}',\rho\left(\bar{\phi}+\phi'\right)\dot{\bar{\boldsymbol{v}}}\right)+\left(\boldsymbol{w}',\rho\left(\bar{\phi}+\phi'\right)\left(\bar{\boldsymbol{v}}+\boldsymbol{v}'\right)\cdot\nabla\left(\bar{\boldsymbol{v}}+\boldsymbol{v}'\right)\right)$$
$$+\left(\nabla\boldsymbol{w}',2\eta\left(\bar{\phi}+\phi'\right)\nabla^s\left(\bar{\boldsymbol{v}}+\boldsymbol{v}'\right)\right)-\left(\nabla\cdot\boldsymbol{w}',p\right) \tag{2.16}$$
$$-\left(\boldsymbol{w}',\rho\left(\bar{\phi}+\phi'\right)\boldsymbol{f}\right)-\left(\boldsymbol{w}',\boldsymbol{h}\right)_{\Gamma_h}=0$$

$$R_5\left(\psi';\bar{\boldsymbol{v}},\boldsymbol{v}',\bar{\phi},\phi'\right)=\left(\psi',\left(\bar{\boldsymbol{v}}+\boldsymbol{v}'\right)\cdot\nabla\left(\bar{\phi}+\phi'\right)\right)=0 \tag{2.17}$$

Remark. Equations (2.15) and (2.17) are the coarse-scale and fine-scale variational problems for the level-set field. Fine-scale sub-problem (2.17) is to be viewed as an error estimator that facilitates a model to be embedded in (2.15) for an enhanced solution of the level set field ϕ.

2.2.2. Derivation of the Fine-Scale Model

The coarse-scale and fine-scale sub-problems are nonlinear with respect to both the fine-scale velocity and the signed distance field. To derive the fine-scale model, we linearize $R_4\left(\boldsymbol{w}';\boldsymbol{v},p,\phi\right)$ with respect to the fine-scale velocity field $\boldsymbol{v}'$. The linearized fine-scale sub-problem is:

$$\mathcal{L}\left(R_4\left(\boldsymbol{w}';\bar{\boldsymbol{v}},\boldsymbol{v}',p,\bar{\phi},\phi'\right)\right)=\frac{d}{d\varepsilon}R_4\left(\boldsymbol{w}';\bar{\boldsymbol{v}},\boldsymbol{v}'+\varepsilon\delta\boldsymbol{v}',p,\bar{\phi},\phi'\right)\Big|_{\varepsilon=0}$$
$$=\left(\boldsymbol{w}',\rho\delta\boldsymbol{v}'\cdot\nabla\left(\bar{\boldsymbol{v}}+\boldsymbol{v}'\right)\right)+\left(\boldsymbol{w}',\rho\left(\bar{\boldsymbol{v}}+\boldsymbol{v}'\right)\cdot\nabla\delta\boldsymbol{v}'\right)+\left(\nabla\boldsymbol{w}',2\eta\nabla^s\delta\boldsymbol{v}'\right) \tag{2.18}$$

The right-hand side in (2.18) represents the residual of coarse-scale momentum balance equation. To keep the derivation simple, we drop the higher order fine-scale terms, and this also helps decouple the two fine-scale sub-problems. Consequently, dependence of fine-scale momentum balance on ϕ' and

dependence of fine-scale advection equation on $\boldsymbol{v}'$ is suppressed. We rewrite (2.18) in terms of the residual of the Euler-Lagrange equation of the coarse scales.

$$\left(\boldsymbol{w}', \rho\delta\boldsymbol{v}' \cdot \nabla\boldsymbol{v}\right) + \left(\boldsymbol{w}', \rho\boldsymbol{v} \cdot \nabla\delta\boldsymbol{v}'\right) + \left(\nabla\boldsymbol{w}', 2\eta\nabla^s\delta\boldsymbol{v}'\right) = \left(\boldsymbol{w}', \boldsymbol{r}_{\text{NSE}}\right) \tag{2.19}$$

where $-\boldsymbol{r}_{\text{NSE}} = \rho\dot{\tilde{\boldsymbol{v}}} + \rho\boldsymbol{v} \cdot \nabla\boldsymbol{v} - \nabla \cdot 2\eta\nabla^s\boldsymbol{v} + \nabla p - \rho\boldsymbol{f}$ is the residual of the Euler-Lagrange equations for the coarse scales in the Navier-Stokes flow model. Following along the lines of our previous work [84,105], we expand the fine-scale weighting function and trial solution in (2.19) via element-wise bubble functions as:

$$\boldsymbol{w}' = b^e\boldsymbol{\gamma} \quad \text{and} \quad \boldsymbol{v}' = b^e\boldsymbol{\beta} \tag{2.20}$$

Substituting (2.20) into (2.19), we solve for the coefficient β, and reconstruct the fine-scale field $\delta\boldsymbol{v}'$ as follows:

$$\delta\boldsymbol{v}' = \boldsymbol{\tau}_{\text{NSE}}\boldsymbol{r}_{\text{NSE}} \tag{2.21}$$

where the stabilization tensor $\boldsymbol{\tau}_{\text{NSE}}$ is defined as:

$$\boldsymbol{\tau}_{\text{NSE}} = b^e \left[\begin{array}{l} \int_{\Omega^e} \rho\left(b^e\right)^2 \left(\nabla\boldsymbol{v}\right)^T d\Omega + \int_{\Omega^e} \rho b^e\boldsymbol{v} \cdot \nabla b^e d\Omega\boldsymbol{I} \\ + \int_{\Omega^e} \eta^e \left(\nabla b^e \otimes \nabla b^e\right) d\Omega + \int_{\Omega^e} \eta \left\|\nabla b^e\right\|^2 d\Omega\boldsymbol{I} \end{array} \right]^{-1} \int_{\Omega^e} b^e d\Omega \tag{2.22}$$

The denominator in (2.22) is comprised of four integral terms: the first two terms arise from the linearized convection operator in (2.19), while the last two terms emanate from the diffusion operator in (2.19).

Remark: For the discussion on bubble functions and resulting stabilization tensor, interested readers is referred to [29,84] on the stabilized form for the incompressible Navier-Stokes equations.

Likewise, the fine-scale signed distance field can be expressed in an analogous form that is driven by the residual of the coarse scale level-set equation, namely,

$$\phi' = \tau_{\text{LSA}} r_{\text{LSA}} \tag{2.23}$$

The derivation of the fine scale model ϕ' is further elaborated upon in the section on the stabilized advection equation for the level-set field.

2.2.3. Interfacial Stabilization via Fine-scale Modeling

We embedded the signed distance field in the momentum balance equations via the dependency of density ρ and dynamic viscosity η on ϕ. Accordingly, this gives rise to coarse and fine scale density and viscosity fields as follows:

$$\begin{aligned}\rho\left(\bar{\phi}+\phi'\right)&=\bar{\rho}+\left(\rho_{+}-\rho_{-}\right)H_{,\phi}\left(\bar{\phi}\right)\phi'\\ \eta\left(\bar{\phi}+\phi'\right)&=\bar{\eta}+\left(\eta_{+}-\eta_{-}\right)H_{,\phi}\left(\bar{\phi}\right)\phi'\end{aligned} \tag{2.24}$$

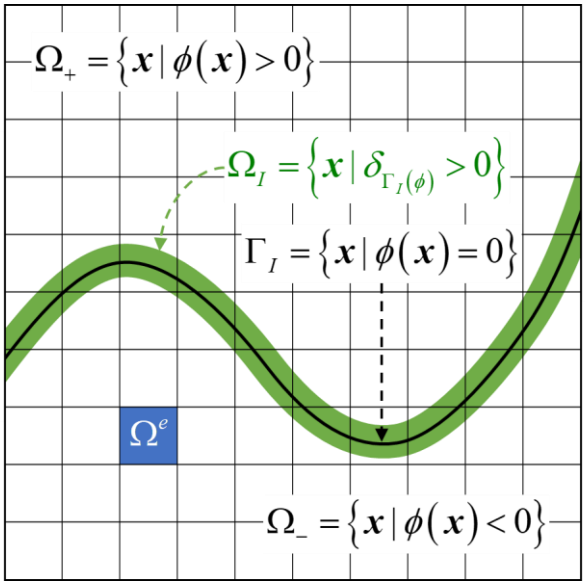

Figure 2.1 Two-phase flow on an Eulerian mesh. Phases are defined by the sign of ϕ, the interface is defined by the zero level-set, ghost-penalty-type stabilization is operational in a narrow band along the interface, and standard stabilization is operational over element interiors.

It is important to note that $H_{,\phi}\left(\bar{\phi}\right)$ yields the Dirac delta function $\delta_{\Gamma_I(\bar{\phi})}$, which is defined along the embedded interface that is given by the zero contour of the signed distance field as shown in Figure 2.1. Along this interface lies a narrow band and the width of this band is defined via regularization of the Dirac delta function $\delta_{\Gamma_I(\bar{\phi})}$. This band is the sub-region in which the fine-scale signed distance field affects the mechanical material parameters.

We now linearize the coarse-scale variational formulation for the momentum balance equation. The dependency of the mechanical properties on the signed distance field introduces the Heaviside function $H(\phi)$ that further adds to the nonlinearity in the system. Since we need to linearize the coarse-scale formulation with respect to fine-scale fields, i.e., $\boldsymbol{v}'$ and ϕ', to simplify the derivation we drop the higher-order cross-coupling terms. The linearization operator for coarse-scale momentum balance equation is defined as:

$$\mathcal{L}\left(R_1\left(\bar{\boldsymbol{w}};\bar{\boldsymbol{v}},\boldsymbol{v}',p,\bar{\phi},\phi'\right)\right)=\frac{d}{d\varepsilon}R_1\left(\bar{\boldsymbol{w}};\bar{\boldsymbol{v}},\boldsymbol{v}'+\varepsilon\delta\boldsymbol{v}',\phi,p\right)\Big|_{\varepsilon=0}+\frac{d}{d\varepsilon}R_1\left(\bar{\boldsymbol{w}};\boldsymbol{v},\phi+\varepsilon\delta\phi',p\right)\Big|_{\varepsilon=0} \tag{2.25}$$

Applying (2.25) onto (2.13), and rearranging the terms we get,

$$\begin{aligned}&\left(\bar{\boldsymbol{w}},\rho\dot{\bar{\boldsymbol{v}}}\right)+\left(\bar{\boldsymbol{w}},\rho\boldsymbol{v}\cdot\nabla\boldsymbol{v}\right)+\left(\nabla\bar{\boldsymbol{w}},2\eta\nabla^s\boldsymbol{v}\right)-\left(\nabla\cdot\bar{\boldsymbol{w}},p\right)\\&\left(\bar{\boldsymbol{w}},\rho\delta\boldsymbol{v}'\cdot\nabla\left(\bar{\boldsymbol{v}}+\boldsymbol{v}'\right)\right)+\left(\bar{\boldsymbol{w}},\rho\left(\bar{\boldsymbol{v}}+\boldsymbol{v}'\right)\cdot\nabla\delta\boldsymbol{v}'\right)+\left(\nabla\bar{\boldsymbol{w}},2\eta\nabla^s\delta\boldsymbol{v}'\right)\\&+\left(\bar{\boldsymbol{w}},\left(\rho_+-\rho_-\right)\delta_{\Gamma_I}\phi'\left(\dot{\bar{\boldsymbol{v}}}+\boldsymbol{v}\cdot\nabla\boldsymbol{v}-\boldsymbol{f}\right)\right)+\left(\nabla\bar{\boldsymbol{w}},2\left(\eta_+-\eta_-\right)\delta_{\Gamma_I}\phi'\nabla^s\boldsymbol{v}\right)\\&=\left(\bar{\boldsymbol{w}},\rho\boldsymbol{f}\right)+\left(\bar{\boldsymbol{w}},\boldsymbol{h}\right)_{\Gamma_h}\end{aligned} \tag{2.26}$$

Terms in the first row in (2.26) are the standard Galerkin terms, while the terms in the second row depend on the fine-scale velocity field. Terms in the third row are the interfacial terms that are driven by the jump in the material properties on either side of the interface. Furthermore, the Dirac delta function facilitated by the fine-scale signed distance field localizes the terms appearing in the third row to a narrow band along the interface (see Figure 1). In the limit, this narrow band represents the interface. The interfacial terms in the third row of (2.26) can be simplified to the following form:

$$\left(\bar{\boldsymbol{w}},\left(\rho_+-\rho_-\right)\delta_{\Gamma_I}\phi'\left(\dot{\bar{\boldsymbol{v}}}-\boldsymbol{f}\right)\right)+\left(\nabla\bar{\boldsymbol{w}},2\left(\eta_+-\eta_-\right)\delta_{\Gamma_I}\phi'\nabla^s\bar{\boldsymbol{v}}\right)=\left(\nabla\bar{\boldsymbol{w}},2\hat{\eta}\phi'\nabla^s\bar{\boldsymbol{v}}\right)_{\Omega_I} \tag{2.27}$$

where $\hat{\eta}$ is defined as the interfacial viscosity given as

$$\hat{\eta}=\eta_+-\eta_--\frac{\eta}{\rho}\left(\rho_+-\rho_-\right) \tag{2.28}$$

Substituting the fine-scale velocity field from (2.21) and fine-scale signed distance field from (2.23) into (2.26), we obtain the domain interior and interfacial stabilized formulation for the fully coupled system.

$$\begin{aligned}\left(\bar{\boldsymbol{w}},\rho\dot{\bar{\boldsymbol{v}}}\right)+\left(\bar{\boldsymbol{w}},\rho\boldsymbol{v}\cdot\nabla\boldsymbol{v}\right)+\left(\nabla\bar{\boldsymbol{w}},2\eta\nabla^{s}\boldsymbol{v}\right)-\left(\nabla\cdot\bar{\boldsymbol{w}},p\right)-\left(\bar{\boldsymbol{w}},\rho\boldsymbol{f}\right)-\left(\bar{\boldsymbol{w}},\boldsymbol{h}\right)_{\Gamma_h}\\ -\left(\boldsymbol{\chi},\boldsymbol{\tau}_{\mathrm{NSE}}\boldsymbol{r}_{\mathrm{NSE}}\right)+\left(\nabla\bar{\boldsymbol{w}},\hat{\eta}\delta_{\Gamma_I}\tau_{\mathrm{LSA}}r_{\mathrm{LSA}}\nabla^{s}\bar{\boldsymbol{v}}\right)=0\end{aligned}\tag{2.29}$$

where $\boldsymbol{\chi}=\rho\left(-\nabla\boldsymbol{v}\cdot\bar{\boldsymbol{w}}+\left(\nabla\cdot\boldsymbol{v}\right)\bar{\boldsymbol{w}}+\boldsymbol{v}\cdot\nabla\bar{\boldsymbol{w}}\right)+\eta\left(\nabla\left(\nabla\cdot\bar{\boldsymbol{w}}\right)+\Delta\bar{\boldsymbol{w}}\right)+\nabla q$. It is important to note that the nonlinear stabilized form (2.29) is entirely expressed in terms of the coarse scales. Henceforth, the superposed bars are dropped.

2.2.4. Stabilized Advection Equation for the Level-Set Field

In Eulerian methods for moving boundary problems, the kinematics of the evolving interfaces is tracked by a scalar field that is governing by the level-set advection equation. Numerical instability in advection dominated cases is a well-documented issue and therefore various techniques have been proposed to develop stable formulations, namely, Galerkin/Least-Square (GLS) [70], Streamline-upwind/Petrov-Galerkin (SUPG) [20] and VMS [113] methods.

Since the problem under consideration is that of pure advection, it requires stabilization. As the flow physics evolves, the complex kinematics of the evolving interface gives rise to finer feature that may not get adequately resolved on the otherwise fixed grid. This causes the residual of the Euler-Lagrange equation for the signed distance field starts growing, which can adversely affect the location of the interface, thereby deteriorating the computed flow physics. In this context, we view the fine scale sub-problem facilitated by the VMS framework as serving the role of an error estimator that yields a correction term which is then embedded in the coarse-scale sub-problem to improve the accuracy of the signed distance field.

The variational multi-scale split of the level-set advection equation was well addressed in the previous section and the coarse-scale and fine-sale subproblems are defined in (2.15) and (2.17), respectively. In the following sub-sections, we will first solve the fine-scale sub-problem to derive a model for fine-scale signed distance field ϕ' and then substitute this fine-scale model in the coarse-scale variational form.

2.2.4.1. Derivation of the fine-scale model

We employ the linearity of the trial solution slot in (17) and re-arrange it as follows

$$\left(\psi', \dot{\phi}' + \boldsymbol{v}\cdot\nabla\phi'\right)_{\Omega'} = -\left(\psi', \dot{\bar{\phi}} + \boldsymbol{v}\cdot\nabla\bar{\phi}\right)_{\Omega'} = \left(\psi', r_{\mathrm{LSA}}\right)_{\Omega'} \tag{2.30}$$

where $r_{\mathrm{LSA}} = -\dot{\bar{\phi}} - \boldsymbol{v}\cdot\nabla\bar{\phi}$ represents the residual of the coarse-scale level set advection equation defined over the sum of element interiors. Without loss of generality, we assume that the fine-scale weighting function and trial solution are represented via bubble functions within element subdomains, i.e. $\psi' = b^e\gamma$ and $\phi' = b^e\beta$. Here β and γ are the coefficients of the fine-scale trial solution and weighting function, respectively. Expanding fine-scale fields via bubble function in (2.30), we get

$$\left(b^e\gamma, \dot{\beta}b^e + \boldsymbol{v}\cdot\nabla b^e\beta\right)_{\Omega'} = \left(b^e\gamma, r_{\mathrm{LSA}}\right)_{\Omega'} \tag{2.31}$$

Since the fine-scale field is time-dependent, we employ backward Euler method as the time integrator, though we want to point out that any appropriate time integrator, for example, generalized α method, can also be used. The spatially discretized form (2.31) can be written as

$$\left(b^e\gamma, (\Delta t)^{-1} b^e\beta + \boldsymbol{v}\cdot\nabla b^e\beta\right)_{\Omega'} = \left(b^e\gamma, r_{\mathrm{LSA}}\right)_{\Omega'} \tag{2.32}$$

where Δt denotes the time-step. Taking the element-wise constant coefficients β and γ out of the integral expressions, we get an analytical expression for the coefficient of the trial solution β as follows.

$$\beta = \left(b^e, (\Delta t)^{-1} b^e + \boldsymbol{v}\cdot\nabla b^e\right)^{-1}_{\Omega^e} \left(b^e, r_{\mathrm{LSA}}\right)_{\Omega^e} \tag{2.33}$$

We can now construct the fine-scale signed distance field through interpolation via bubble function. Employing the mean value theorem and assuming coarse-scale residual to be constant over element interior, a simplified expression of the fine-scale signed distance field is obtained:

$$\phi' = b^e\beta = \underbrace{b^e \int_{\Omega^e} \frac{b^e}{(\Delta t)^{-1}\left(b^e\right)^2 + b^e\boldsymbol{u}\cdot\nabla b^e} d\Omega}_{\tau_{\mathrm{LSA}}} r_{\mathrm{LSA}} = \tau_{\mathrm{LSA}} r_{\mathrm{LSA}} \tag{2.34}$$

where τ_{LSA} is the stabilization tensor for the time-dependent level set advection equation.

2.2.4.2. The resulting coarse-scale sub-problem

We re-arrange the coarse-scale sub-problem (2.15), apply divergence theorem and substitute the fine-scale model for the signed distance field.

$$\left(\bar{\psi},\frac{\partial}{\partial t}\bar{\phi}+\boldsymbol{v}\cdot\nabla\bar{\phi}\right)-\left(\bar{\psi},\tau\frac{\partial}{\partial t}\left(\frac{\partial}{\partial t}\bar{\phi}+\boldsymbol{v}\cdot\nabla\bar{\phi}\right)\right)+\left(\tau\boldsymbol{v}\cdot\nabla\bar{\psi},\frac{\partial}{\partial t}\bar{\phi}+\boldsymbol{v}\cdot\nabla\bar{\phi}\right)=0 \tag{2.35}$$

The level set advection equation is temporally a first-order system. We drop the second-order time derivative of signed distance field, thereby yielding a stabilized first-order system.

$$\left(\psi,\frac{\partial\phi}{\partial t}+\boldsymbol{v}\cdot\nabla\phi\right)+\left(\tau\boldsymbol{v}\cdot\nabla\psi,\frac{\partial\phi}{\partial t}+\boldsymbol{v}\cdot\nabla\phi\right)-\left(\psi,\tau\boldsymbol{v}\cdot\nabla\frac{\partial\phi}{\partial t}\right)=0 \tag{2.36}$$

Remark. The first term in the stabilized form is the standard Galerkin term. The second term has the same structural form as the stabilization term derived in the constant-in-time fine-scale VMS method for advection equation [113]. The last term is derived based on time-dependency of the fine-scale VMS formulation.

Remark. The time-dependent fine-scale models can also be integrated via higher order time marching schemes. For details, interested reader is referred to the derivation of the time-dependent fine-scale model [30]. As an example, we present the final stabilized formulation of level-set advection equation in the context of generalized α-method as

$$\begin{aligned}&\left(\bar{\psi},\dot{\bar{\phi}}_{n+\alpha_m}+\boldsymbol{v}\cdot\nabla\bar{\phi}_{n+\alpha_f}\right)+\left(\bar{\psi},\frac{\alpha_m}{\gamma\Delta t}\tau_{\mathrm{LSA}}r_{\mathrm{LSA}}\left(\dot{\bar{\phi}}_{n+\alpha_m},\bar{\phi}_{n+\alpha_f}\right)\right)\\&+\left(-\alpha_f\boldsymbol{v}\cdot\nabla\bar{\psi},\tau_{\mathrm{LSA}}r_{\mathrm{LSA}}\left(\dot{\bar{\phi}}_{n+\alpha_m},\bar{\phi}_{n+\alpha_f}\right)\right)=0\end{aligned} \tag{2.37}$$

2.2.5. Stabilized Form of the Incompressible Navier-Stokes Equations with Free Surface

The stabilized weak form of the incompressible and immiscible two-phase Navier-Stokes equations can be written as

$$\mathcal{B}_{\mathrm{Gal}}^{\mathrm{NSE}}\left(\boldsymbol{w},q;\boldsymbol{v},p,\phi\right)+\mathcal{B}_{\mathrm{VMS}}^{\Omega^e}\left(\boldsymbol{w},q;\boldsymbol{v},p,\phi\right)+\mathcal{B}_{\mathrm{VMS}}^{\Omega_I}\left(\boldsymbol{w};\boldsymbol{v},\phi\right)=\mathcal{L}_{\mathrm{Gal}}^{\mathrm{NSE}}\left(\boldsymbol{w};\phi\right) \tag{2.38}$$

$$\mathcal{B}_{\text{Gal}}^{\text{LSA}}\left(\psi;\boldsymbol{v},\phi\right)+\mathcal{B}_{\text{VMS}}^{\text{LSA}}\left(\psi;\boldsymbol{v},\phi\right)=0 \tag{2.39}$$

The bilinear terms in (38) are defined as

$$\begin{aligned}
\mathcal{B}_{\text{Gal}}^{\text{NSE}}\left(\bar{\boldsymbol{w}},q;\bar{\boldsymbol{v}},p\right)&=\left(\boldsymbol{w},\rho\left(\phi\right)\dot{\boldsymbol{v}}\right)+\left(\boldsymbol{w},\rho\left(\phi\right)\boldsymbol{v}\cdot\nabla\boldsymbol{v}\right)+\left(\nabla\boldsymbol{w},2\eta\left(\phi\right)\nabla^{s}\boldsymbol{v}\right)\\
&\quad-\left(\nabla\cdot\boldsymbol{w},p\right)+\left(q,\nabla\cdot\boldsymbol{v}\right)\\
\mathcal{B}_{\text{VMS}}^{\Omega^{e}}\left(\boldsymbol{w},q;\boldsymbol{v},p,\phi\right)&=-\left(\boldsymbol{\chi},\boldsymbol{\tau}_{\text{NSE}}\boldsymbol{r}_{\text{NSE}}\right)\\
\mathcal{B}_{\text{VMS}}^{\Omega_{I}}\left(\boldsymbol{w};\boldsymbol{v},\phi\right)&=\left(\nabla\boldsymbol{w},2\hat{\eta}\delta_{\Gamma_{I}\left(\phi\right)}\tau_{\text{LSA}}r_{\text{LSA}}\nabla^{s}\bar{\boldsymbol{v}}\right)\\
\mathcal{B}_{\text{Gal}}^{\text{LSA}}\left(\psi;\boldsymbol{v},\phi\right)&=\left(\psi,\dot{\phi}+\boldsymbol{v}\cdot\nabla\phi\right)\\
\mathcal{B}_{\text{VMS}}^{\text{LSA}}\left(\psi;\boldsymbol{v},\phi\right)&=\left(\tau_{\text{LSA}}\boldsymbol{v}\cdot\nabla\psi,\dot{\phi}+\boldsymbol{v}\cdot\nabla\phi\right)\\
\mathcal{L}_{\text{Gal}}^{\text{NSE}}\left(\boldsymbol{w};\phi\right)&=\left(\boldsymbol{w},\rho\left(\phi\right)\boldsymbol{f}\right)+\left(\boldsymbol{w},\boldsymbol{h}\right)_{\Gamma_{h}}
\end{aligned} \tag{2.40}$$

where $\mathcal{B}_{\text{Gal}}^{\text{NSE}}$ and $\mathcal{B}_{\text{Gal}}^{\text{LSA}}$ are the standard Galerkin terms, $\mathcal{B}_{\text{VMS}}^{\Omega^{e}}$ are the interior stabilization term and $\mathcal{B}_{\text{VMS}}^{\Omega_{I}}$ is the interfacial stabilization term to help with the instability arising due to the free-surface sloshing motion. It is important to note that the structure of the so-called ghost penalty term (Baiges et al. 2017) arises naturally in the proposed method.

2.3. REINITIALIZATION AND MASS CONSERVATION

2.3.1. The Re-Initialization Process

Although the evolution of signed distance field ϕ is governed by the level set advection equation (2.6), this equation may warp the signed distance field that can in turn affect the location of the interface and thus introduce numerical errors in the finite element calculations. This effect is usually accumulative that grows with time and can make the computed field deviate from the strict definition of a signed distance field. To correct this error, a re-initialization process is carried out that helps recover the signed distance field. One specific property of signed distance field which is usually employed is that the norm of its gradient is equation to one (i.e., $\left\|\nabla\phi\right\|=1$). This equation is also known as the Eikonal equation. In this work, the pseudo-time form [147] of Eikonal equation is employed in the context of finite elements,

and it is stabilized via the SUPG method. In addition, a weakly imposed boundary condition is applied to fix the location of the interface during the reinitialization process. The stabilized weak form is:

$$\left(\psi, \frac{\partial \phi_r}{\partial t} + \text{sign}\left(\phi_0\right)\left(\left\|\nabla \phi_r\right\| - 1\right)\right) + \left(\tau_{\text{SUPG}}\, \text{sign}\left(\phi_0\right) \frac{\nabla \phi_r}{\left\|\nabla \phi_r\right\|} \cdot \nabla \psi, \frac{\partial \phi_r}{\partial t} + \text{sign}\left(\phi_0\right)\left(\left\|\nabla \phi_r\right\| - 1\right)\right) + \left(\nabla \psi, \kappa_{\text{DC}} \nabla \phi_r\right) + \left(\psi, K\left(\phi_r - \phi_0\right)\right)_{\Gamma_I} = 0 \tag{2.41}$$

where ϕ_r is the signed distance field after re-initialization, ϕ_0 is the signed distance field after solving the free-surface fluid flow problem, K is the spring coefficient to enforce the interfacial boundary condition, and $\tau_{\text{SUPG}} = h^e/2$ is the SUPG stabilization parameter. In Eqn. (2.41), the first term is the standard Galerkin term, the second term is the SUPG based stabilization, the third term is the discontinuity-capturing term and the last term is weakly imposed boundary condition at the moving interface.

2.3.2. Global Mass Conservation

In a closed domain Ω (i.e., no inflow or outflow fluxes at the domain boundaries), the mass of the system that is comprised of two immiscible fluids is represented as

$$M = \int_\Omega \left(\rho_+ H\left(\phi\right) + \rho_-\left(1 - H\left(\phi\right)\right)\right) d\Omega = \int_\Omega \left(\left(\rho_+ - \rho_-\right) H\left(\phi\right) + \rho_-\right) d\Omega \tag{2.42}$$

where $H\left(\phi\right)$ is the discontinuous Heaviside function, and ρ_+ and ρ_- are densities of the fluid in the two sub-regions. Mass conservation means that the current mass M_t is equal to the initial mass M_0, which in fact is known from the initial conditions. We add a global constant perturbation $\tilde{\phi}$ to the re-initialized signed distance field ϕ_r to enforce mass conservation [144].

$$M_t = \int_\Omega \left(\left(\rho_+ - \rho_-\right) H\left(\phi_r + \tilde{\phi}\right) + \rho_-\right) d\Omega = M_0 \tag{2.43}$$

We approximate the Heaviside function with the regularized version, expand it through Taylor series, and drop second order terms to solve for $\tilde{\phi}$

$$\tilde{\phi} = \frac{M_0 - \int_\Omega \rho_-\, d\Omega - \int_\Omega \left(\rho_+ - \rho_-\right) H_\varepsilon\left(\phi_r\right) d\Omega}{\int_\Omega \left(\rho_+ - \rho_-\right) H'_\varepsilon\left(\phi_r\right) d\Omega} \tag{2.44}$$

In applications to free-surface problems, where the difference in density between the two phases is very large (e.g., $\rho_{\text{water}} \gg \rho_{\text{air}}$), the expression for the global constant mass correction can be simplified as

$$\tilde{\phi} = \frac{V_0 - \int_\Omega H_\varepsilon(\phi_r)\, d\Omega}{\int_\Omega H'_\varepsilon(\phi_r)\, d\Omega} \tag{2.45}$$

where V_0 is the initial volume of water and $H_\varepsilon(\phi)$ is the regularized Heaviside function defined as:

$$H_\varepsilon(\phi) = \begin{cases} 0 & \text{if} \quad \phi \le -\varepsilon \\ \frac{1}{2}\left(1 + \frac{\phi}{\varepsilon} + \frac{1}{\pi}\sin\left(\frac{\phi\pi}{\varepsilon}\right)\right) & \text{if} \quad |\phi| < \varepsilon \\ 1 & \text{if} \quad \phi \ge \varepsilon \end{cases} \tag{2.46}$$

Remark. The mass conservation term appears as a correction to the computed signed distance function and it accounts for the dissipation of mass due to numerical diffusion.

2.4. NUMERICAL TESTS

We first present the convergence rate study to illustrate the consistency and stability of the proposed stabilized method for advection equation that models the level-set field. We then couple the interface-capturing algorithm within the Navier-Stokes equation and carry out a series of numerical tests on two-phase flows. Finally, we present two-dimensional and three-dimensional dam-break flows to show the versatility of the proposed method for solving harder free-surface flow problems.

2.4.1. Pseudo-1D Advection

The first test case [123] is a smooth initial scalar field ϕ_0 that is advected with a given velocity field $\boldsymbol{v}(x, y)$ which represents one-dimensional flow over a two-dimensional domain [0,1]×[0,1]. The initial condition and spatial distribution of the velocity field are given as:

$$\phi_0(x, y) = \exp\left(-(x-0.5)^2 - (y-0.5)^2\right) - \exp\left(-0.15^2\right) \tag{2.47}$$

$$\boldsymbol{v}(x,y)=\frac{1}{\sqrt{2+\pi}}\exp\left(\frac{\sqrt{2}x+\sqrt{\pi}y}{\sqrt{2+\pi}}\right)\begin{Bmatrix}\sqrt{2}\\ \sqrt{\pi}\end{Bmatrix} \tag{2.48}$$

The computational domain and initial condition are shown in Figure 2.2. Since zero flux is applied at the inflow, only the portion of the domain which is influenced by initial condition is considered in the convergence rate test that employs the L_∞ norm, which is defined as:

$$\|e\|_\infty=\max_{x\in\Omega}\left|\phi^h(\boldsymbol{x})-\phi^e(\boldsymbol{x})\right| \tag{2.49}$$

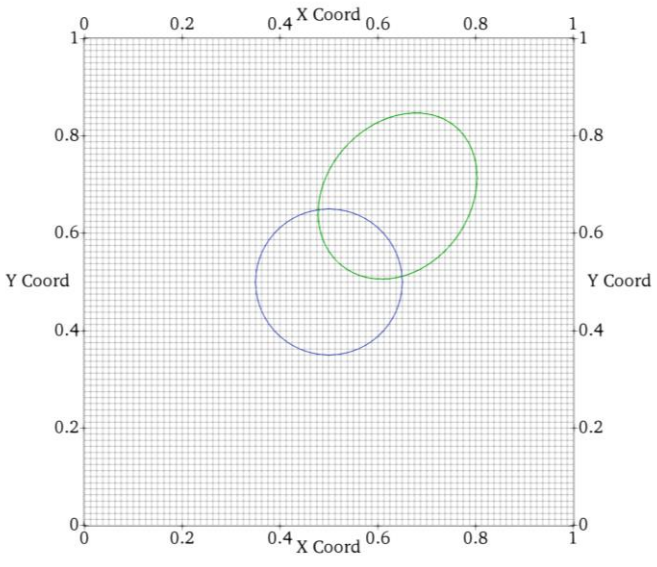

Figure 2.2 Initial and final interface location for the pseudo 1D advection test

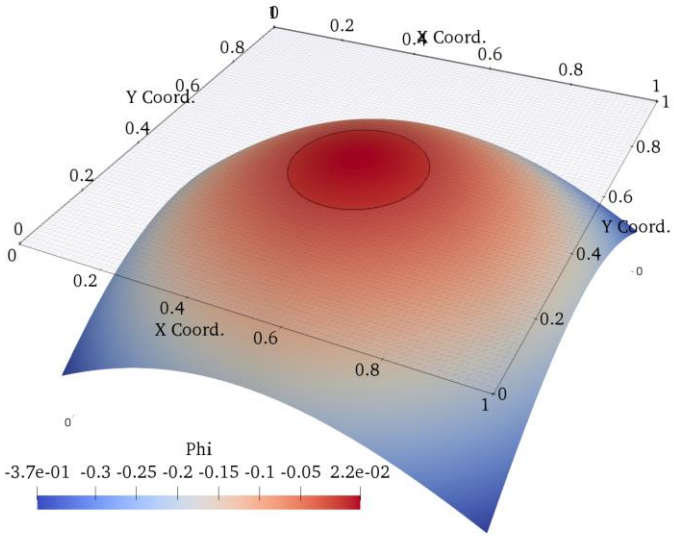

a) Initial state

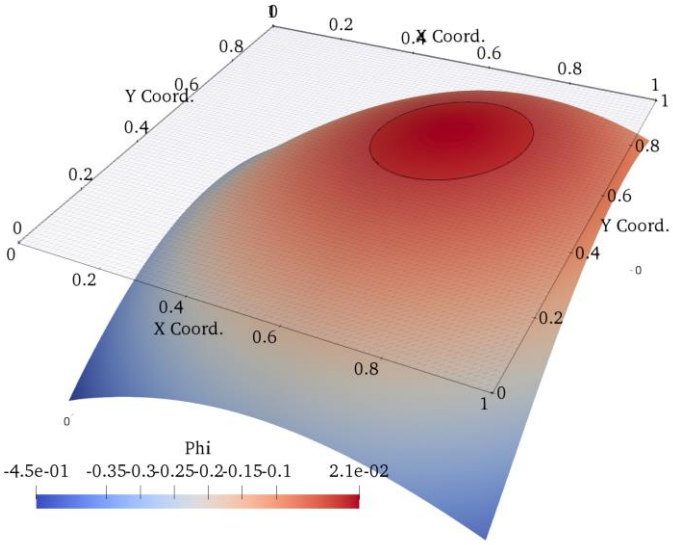

b) End state

Figure 2.3. Warped scalar field at initial and final stage for the pseudo 1D advection

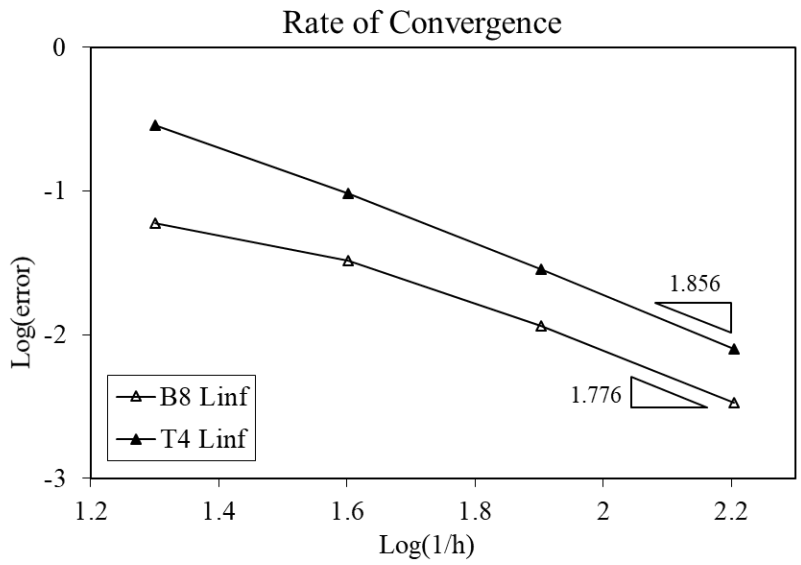

Figure 2.4. Convergence rates on uniform meshes for linear 3D elements

Four hierarchical meshes are used and the problem is run to a fixed number of time-steps (N = 16). The $\Delta t/\Delta x$ ratio in CFL number is set equal to 1.0 by systematically reducing Δx and Δt. Figure 2.3a shows the spatial distribution of the scalar level-set field and the iso-surface with zero value is the circular geometrical object that is convected with the flow. Figure 2.3b shows the spatial distribution of the zero contour and the warped level-set field at the end of the sixteenth time-step. The convergence rates attained for both linear hexahedral and linear tetrahedral elements are shown in Figure 4, and the computed rates from last two finest meshes attain an asymptotic optimal convergence.

2.4.2. Dam-break Flow (2D)

The collapse of a water column under gravity is a widely-used benchmark problem to study the features of a numerical method for free-surface kinematics. A water column of height 2a is instantly released in a tank (see Figure 2.5), which collapses under the effect of gravity and flows towards the opposite wall of the tank. The density of water is 1000 kg/m^3 and that of air is 1 kg/m^3. The dynamic viscosity of water is 1.0×10^{-3} Pa·s and for air is 1.0×10^{-5} Pa·s. The experiment data reported in [89] is based on a water tank apparatus that is open at the top. Sloshing water that crosses the top edge of the

tank falls back in the tank due to gravitational forces. In order to replicate the experimental setup, the top boundary of the mesh is kept high enough so that the computed free surface does not hit the mesh boundary at the top and this helps avoid artificial reflection of the water column, that would affect the flow physics. Consequently, two different domain sizes and mesh resolutions are considered: $4a \times 4.8a$, 80×80 and $4a \times 6a$, 120×160. The finer mesh being less dissipative necessitates a larger domain height to prevent contact with the top boundary.

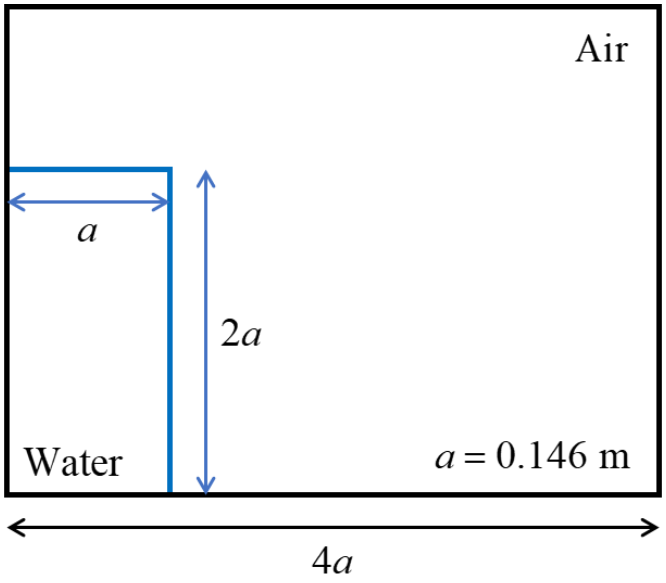

Figure 2.5 Two-dimensional dam-break problem: spatial dimensions

Because of the rapid change in the surface profile and large motion of the water column, all aspects of the algorithm are invoked, i.e., (i) stabilized method for the two fluids, (ii) time-dependent level-set method, (iii) SUPG stabilized Eikonal system, and (iv) the mass conservation algorithm. Consequently, this problem serves as a good test case for checking the robustness of the framework.

The initial and final states of the dam-break flow are both stationary and thus the exact initial energy as well as the asymptotic final energy of the system are known. Viscous effects result in the dissipation of the system energy and therefore its rate of decay is an important measure of the energy dissipation features of the method. Because of extreme free surface kinematics, a mass correction algorithm is embedded in the method that compensates for the mass loss due to complex interfacial

kinematics in the long-time simulations. Since the density of air is negligibly small as compared to that of water, the system mechanical energy head E_m (potential and kinematic head) and relative mass M are calculated via integration over the water domain only.

$$E_m = \int_{\Omega} \left(gh + \frac{1}{2} \boldsymbol{v} \cdot \boldsymbol{v} \right) H(\phi) \, d\Omega \tag{2.50}$$

$$M = \int_{\Omega} H(\phi) \, d\Omega \tag{2.51}$$

where $H(\phi)$ is the regularized Heaviside function. The history of mechanical energy head and mass variation are shown in Figure 2.6. The finer mesh being less dissipative results in better approximation of the kinetic energy. However, the coarser mesh still yields the same asymptotic behavior of energy decay as that for the fine mesh. In addition, the initial rate of decay of energy, which is given by the slope of the curves is approximately the same for both the meshes, which shows that coarse mesh is also able to accurately model the flow physics. The mass history of the finer mesh shows better overall conservation property with maximum mass variation of 2%. Since the mass correction term is not a variationally derived term, it only provides first-order correction to mass conservation.

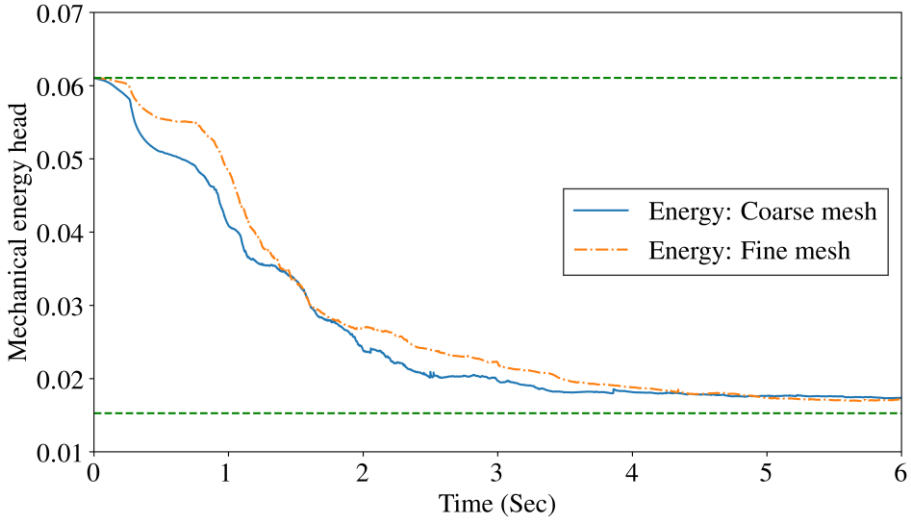

a) Energy history for long-time run of the dam-break flow.

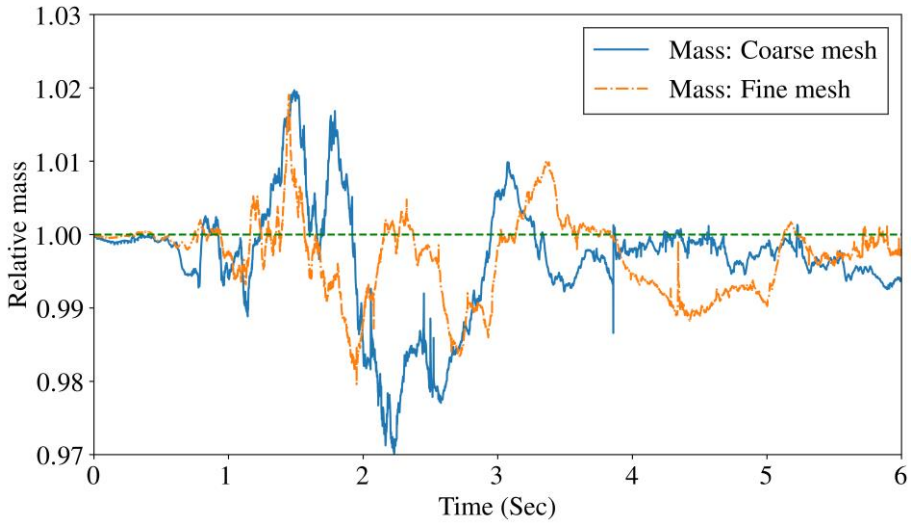

b) Mass history for long-time run of the dam-break flow.

Figure 2.6 Energy and mass history for long-time run of the dam-break flow: coarse and fine meshes

2.4.3. Dam-Break Flow with an Obstacle (2D)

The next test case is dam-break flow with an obstacle, where the air-water interface results in complex evolving topology. It serves as a good benchmark problem because of the availability of the

experimental data [87] on the history of pressure at several locations on the obstacle, and the depth of water column at various locations upstream and downstream of the obstacle. The dimensions of the computational domain and the initial location of the water column are shown in Figure 7. The obstacle is located 2.3955m away from the left wall. The mesh is comprised of 128×64 linear quadrilateral elements that cover the entire computational domain, while the obstacle is represented by 7×10 grid of quads. Figure 8 shows a series of snapshots of the free-surface evolution and pressure distribution at different time points during the simulation. In Figure 9, we provide time history of the pressure field at spatial point P1, P3, P5 and P7 which are the spatial locations of the data points in the experimental set up [87]. Points P1 and P3 are at the upstream face of the obstacle, while points P5 and P7 are at the top of the right vertical wall, as shown in Figure 7. We also compare our results with the reported numerical data [43,87]. The time history of pressure at P1 and P3 shows good agreement with the published experiment and numerical data. The peak pressure at P1 that occurs at approximately 0.4s is much higher as compared to the experimental value, and this can be attributed to infinite stiffness of the obstacle because it is modeled via Dirichlet boundary condition. In Figure 10, the time history of water height at two different locations (H3: 0.582 m from the left wall, and H4: 1.732 m from the left wall) are compared with the published experimental and numerical data and again a good correlation is attained. Figure 11a presents time history of mass variation which shows that initially there is negligible mass loss up until the wave first impacts the obstacle. Also plotted is the case where mass correction term is deactivated, and it shows 14% loss in mass during the course of the simulation. Fig 11b presents the zoomed view for the case where the mass conservation algorithm is activated which shows that the maximum mass variation is less than 2% even for this rapidly oscillating large amplitude free surface flow problem.

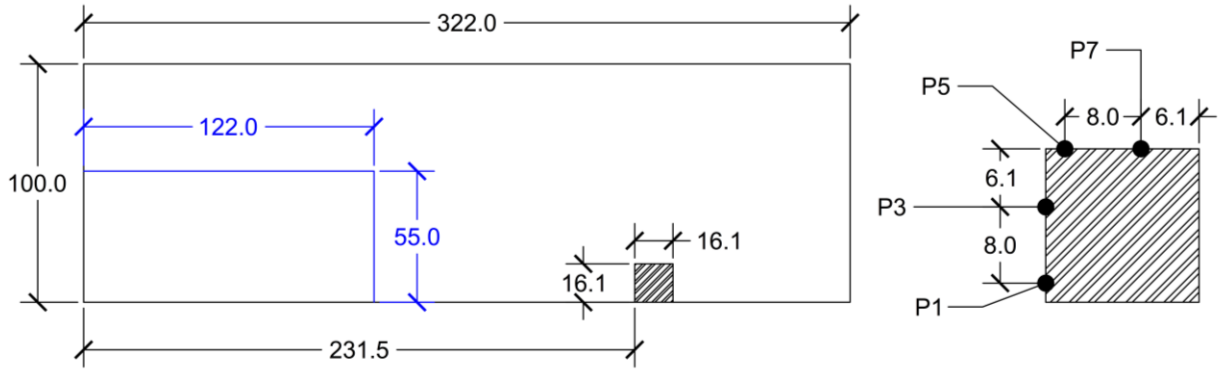

Figure 2.7 Schematics of the two-dimensional dam-break flow with obstacle (units: cm)

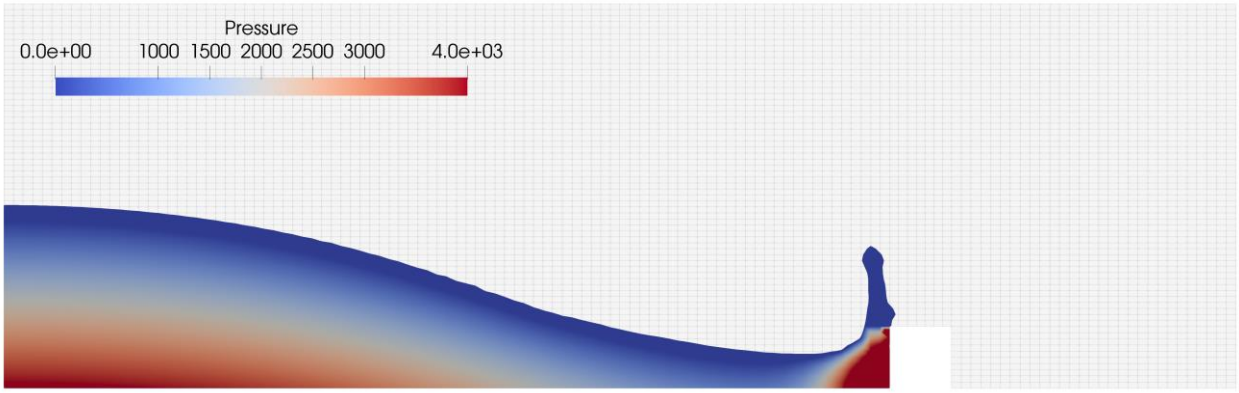

(a) t = 0.5s

Figure 2.8 2D dam-break flow with obstacle: pressure field and air-water interfaces

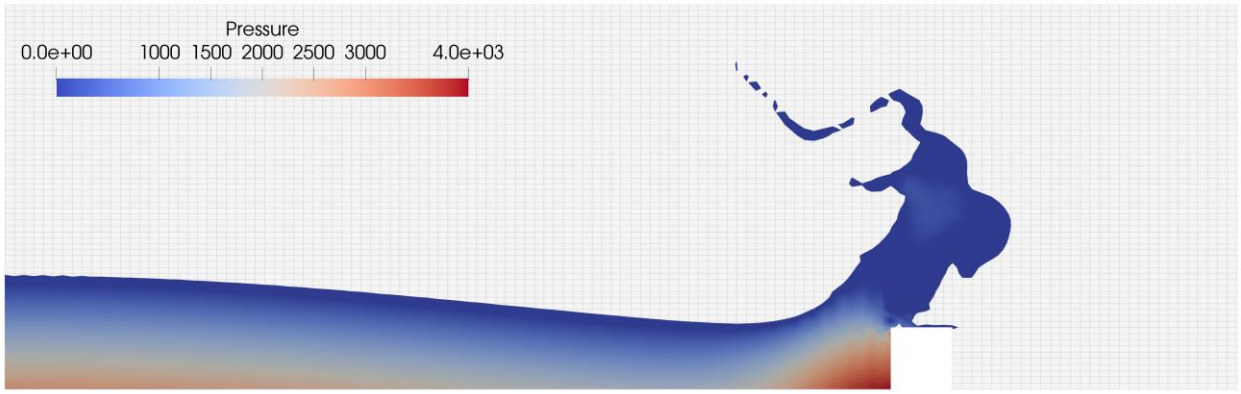

(b) t = 1.0s

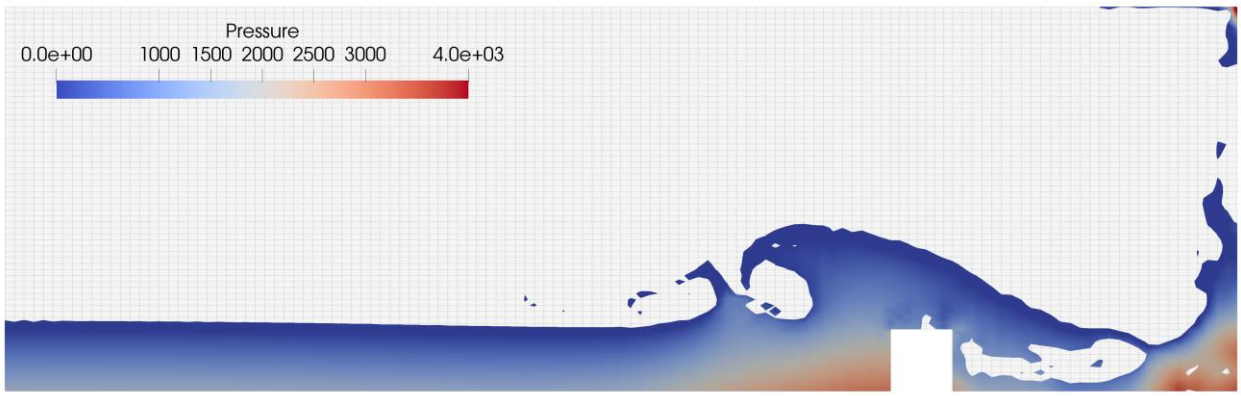

(c)t = 1.5s

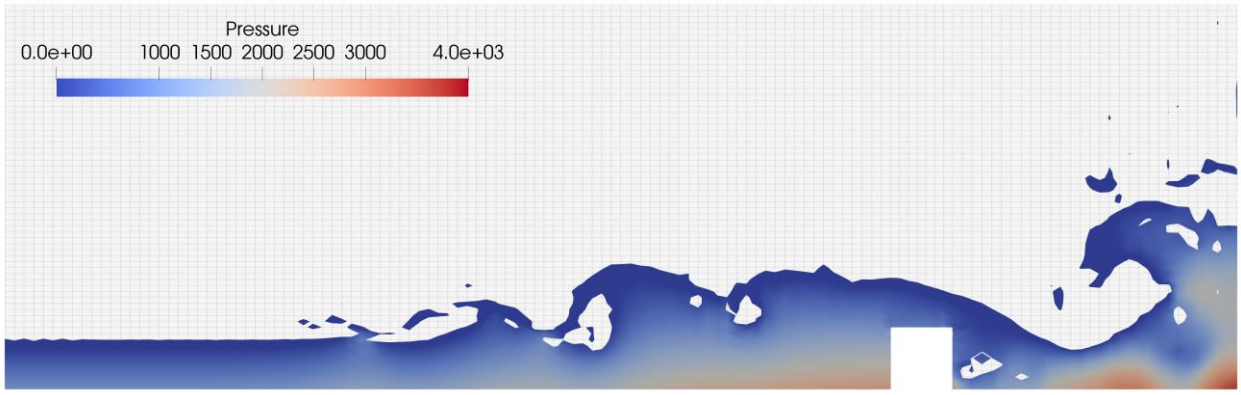

(d) t = 2.0s

Figure 2.8 (cont.)

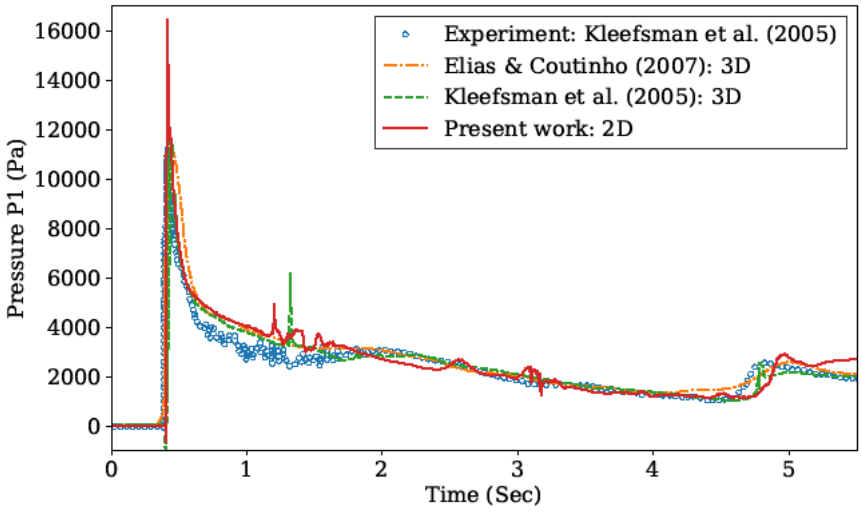

(a)

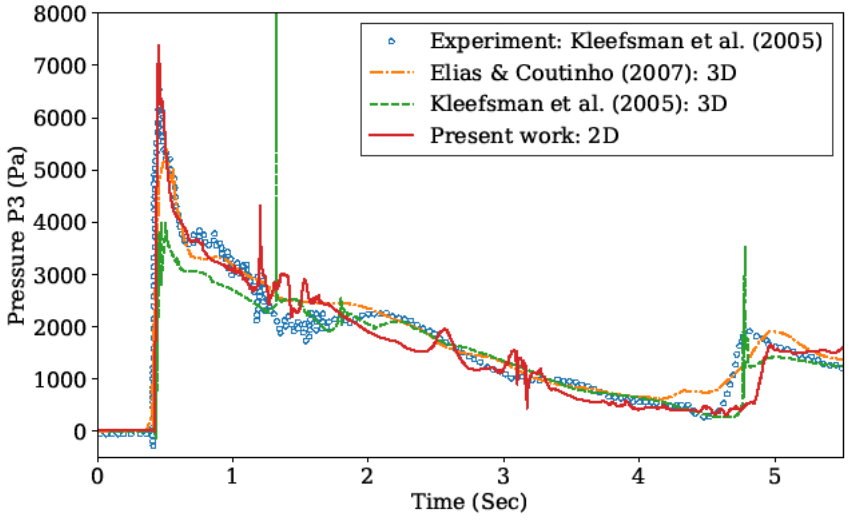

(b)

Figure 2.9 Time history of pressure at various locations on the obstacle: (a) P1, (b) P3, (c) P5 and (d) P7

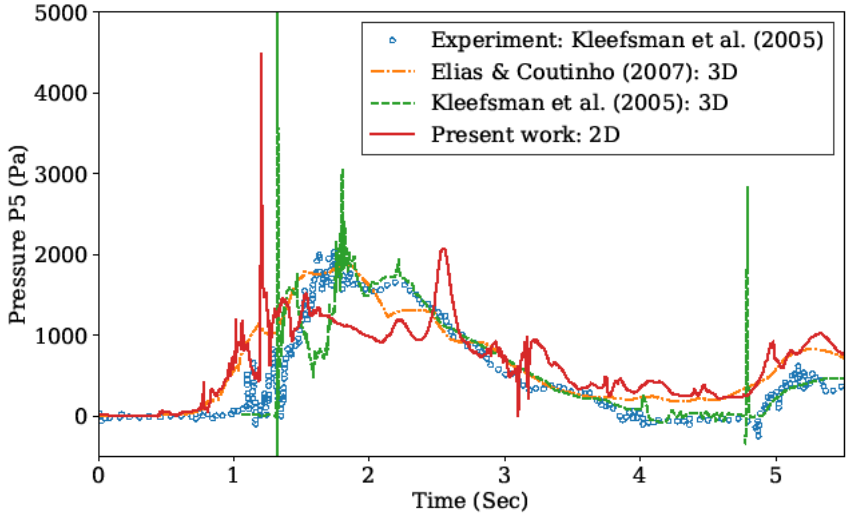

(c)

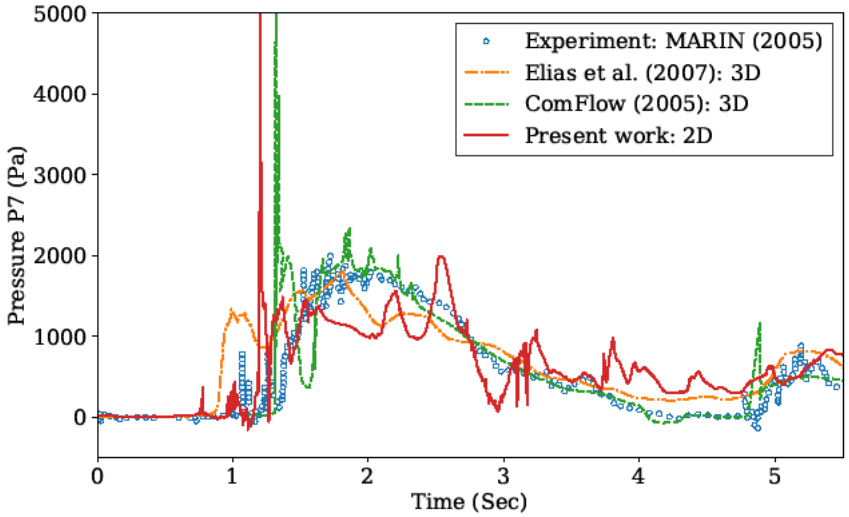

(d)

Figure 2.9 (cont.)

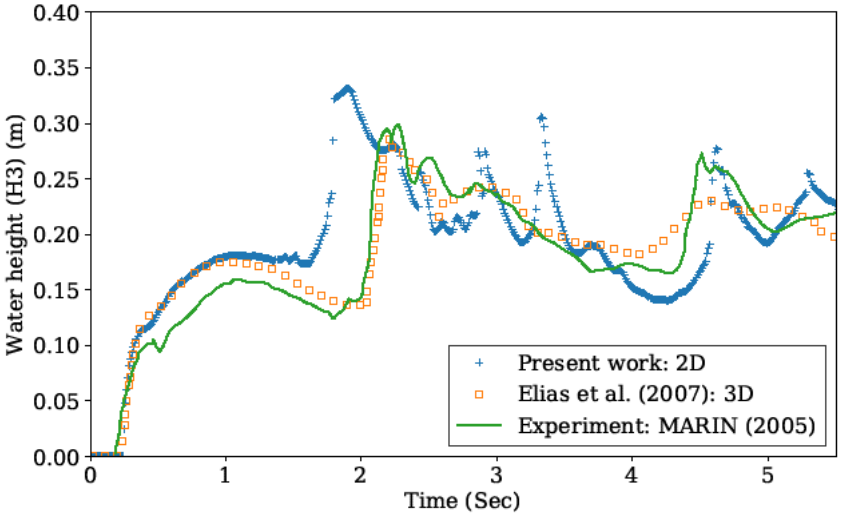

(a)

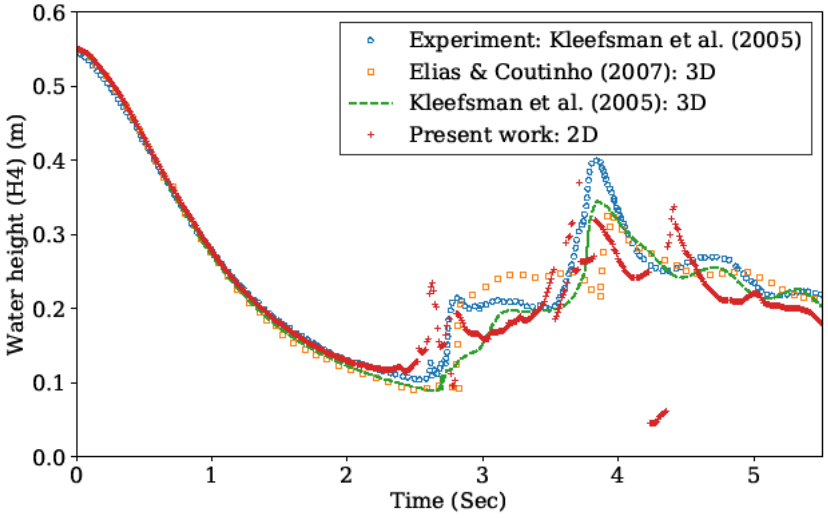

(b)

Figure 2.10 Time history of water height at two locations: (a) H3 and (b) H4

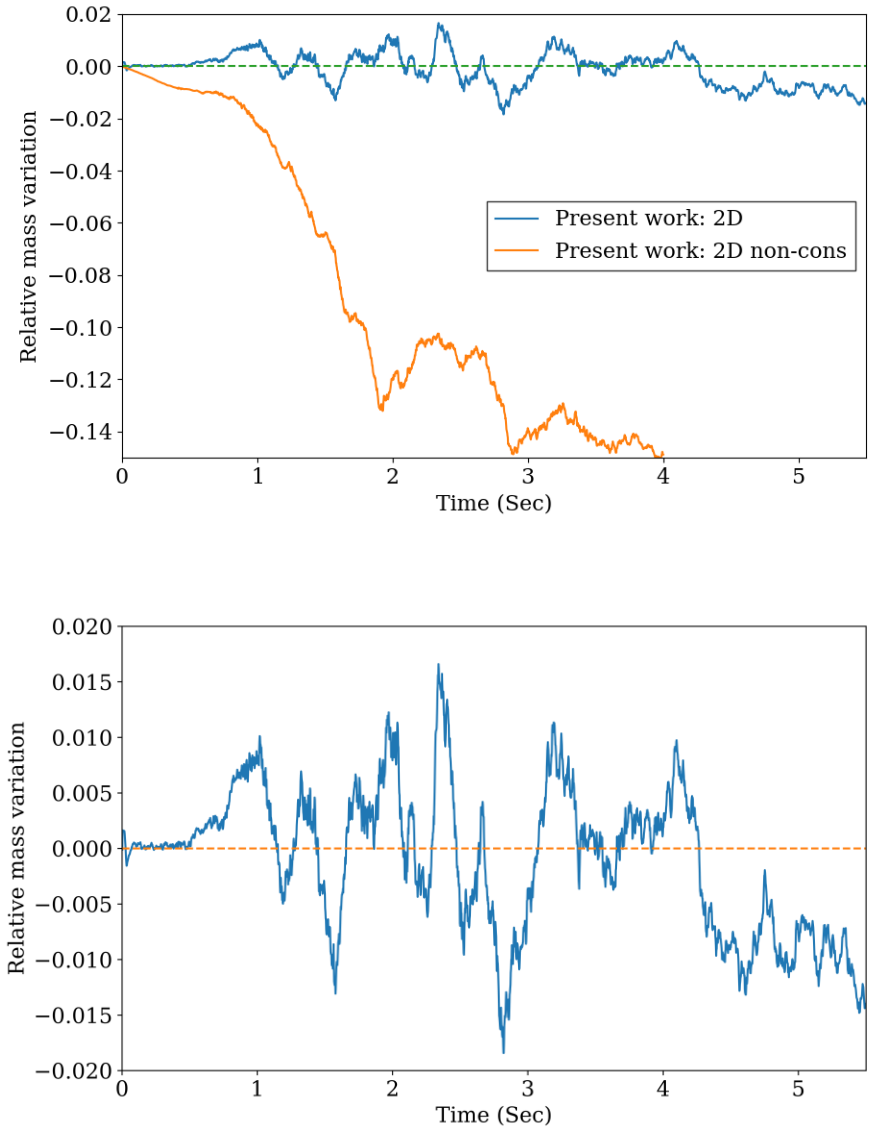

Figure 2.11 Mass time history of the water body in the 2D dam-break flow with an obstacle

2.4.4. Free-Surface Wave Interacting with a Rectangular Column (3D case)

Waves breaking against structures and wave structure interaction are important problems in ocean and marine engineering. Since large impulsive forces can cause severe damage to structural elements, therefore, in the designing of coastal structures in the nearshore region, wave forces and ambient fluid conditions need to be considered. This test case has published experimental data as well as numerically

computed time history of velocity and impulsive force and therefore serves as a good test bed for studying the attributes of the proposed method.

The computational domain is a rectangular box with dimensions 1.6m×0.6m×0.6m. The width of the square column is 0.12m and its height is the same as that of the computational domain. The location of the structural column is shown in Figure 12. The initial water body is of dimension 0.4m×0.6m×0.3m. The domain is discretized with a structured mesh of linear hexahedral elements, and taking advantage of geometric symmetry of the problem, only half of the domain is discretized. Zero normal velocity condition is imposed at the plane of symmetry along with slip condition in the other two directions along this plane. Furthermore, slip conditions are applied at all the other boundaries of the computational domain. The mesh resolution is 128×48×24 with slight refinement around the structural column where element width is 1 cm.

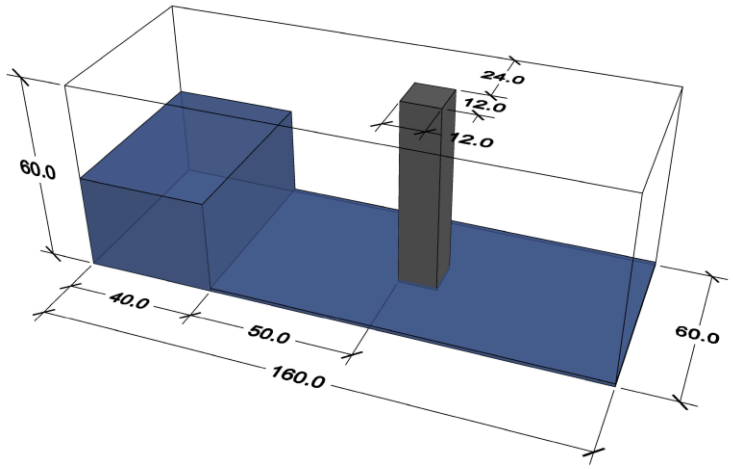

Figure 2.12 Schematic diagram for dam-break wave interacting with a square column (unit: centimeters)

Since in the experiment setup there is some residual water at the bottom of the tank, we have also added a thin layer of water with depth equal to 1 cm at the floor of the computational domain. The density and dynamic viscosity of water and air are 1000 kg/m^3 (water) and 1 kg/m^3 (air), and 1.0×10^{-3} Pa·s (water) and 1.0×10^{-5} Pa·s (air), respectively.

Free surface flow is initialized as a dam-break flow and subsequent free surface motions including wave splitting and water splashing are induced because of interaction with the square column. Generalized α-method is used for time integration. The step size for first 100 steps is 0.005s which is then reduced to 0.001s for subsequent calculations. The coupled system of Navier-Stokes equations and level-set equation are monolithically solved via a parallel sparse direct solver. In each time-step, the converged signed distance field is re-initialized to conform it to its strict definition. We present the time history of the computed horizontal velocity at 0.146 m upstream of the center of the column and 0.026 m off the floor and compare it with reported experimental data [57] and numerical data [38,95,135]. Petroff and Yeh had obtained experimental data for this problem which is reported in [135]. We see in Figure 13 that the proposed method accurately predicts the time of impact, the maximum velocity at the instant of impact and subsequent decay in velocity as a function of time. Figure 14 shows the computed impact force that is obtained via integrating the normal pressure on the front and back surfaces of the column and integrating the shear stress along the side wall of the column. Once again, a good comparison with the reported data can be seen. Figure 15 shows the snapshots of the free surface kinematics and the complex free surface patterns around the column. The runup height along the distal wall and the plunging wave generated due to reflection gives rise to intricate 3D free surface patterns. Figure 16 presents streamlines that are colored by the vorticity magnitude in the water subdomain to highlight the complex nature of internal flow structures around the column.

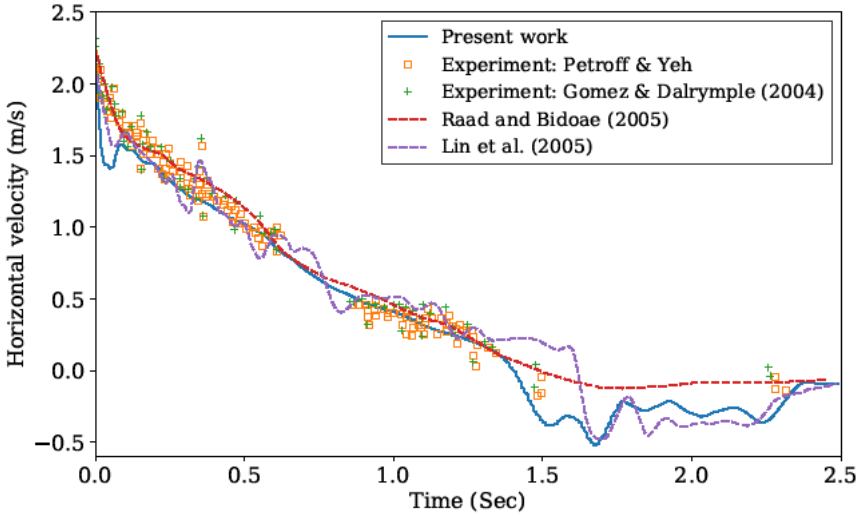

Figure 2.13 Time history of the horizontal velocity

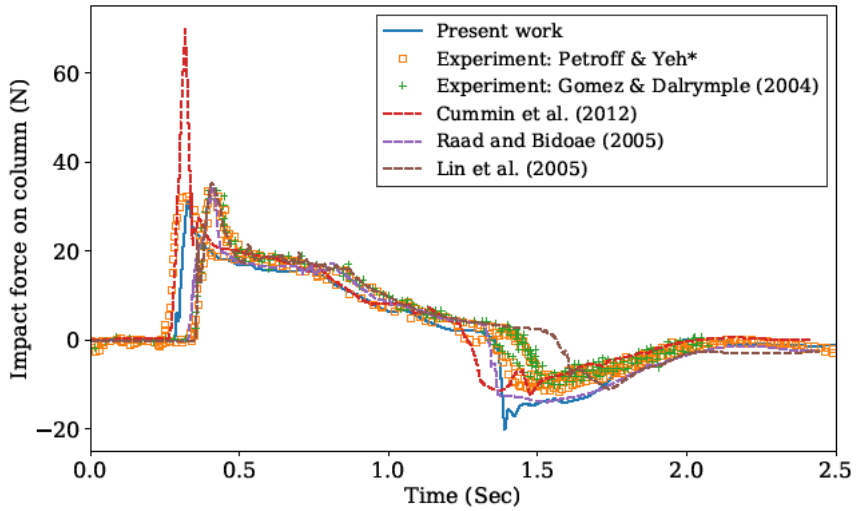

Figure 2.14 Time history of water impact on the column

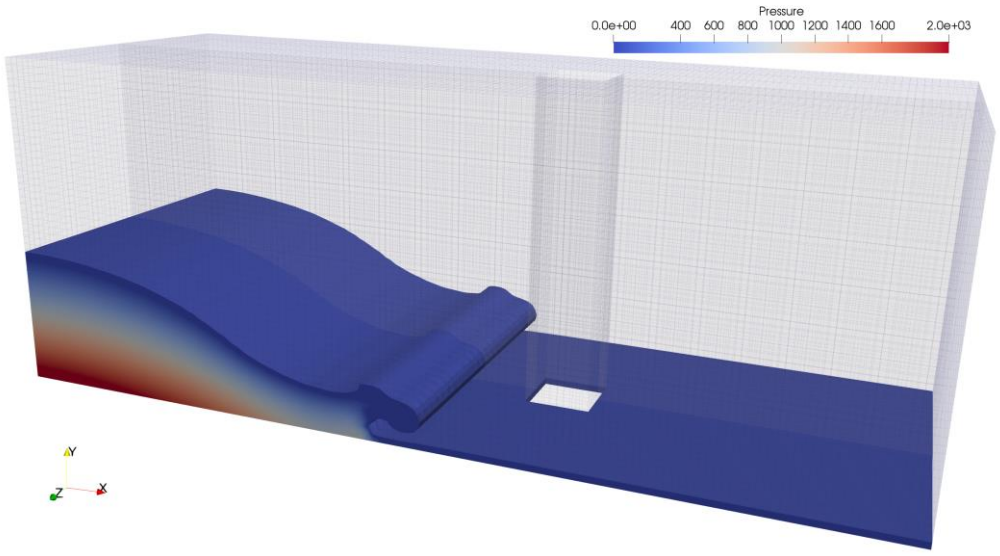

(a) t = 0.25s

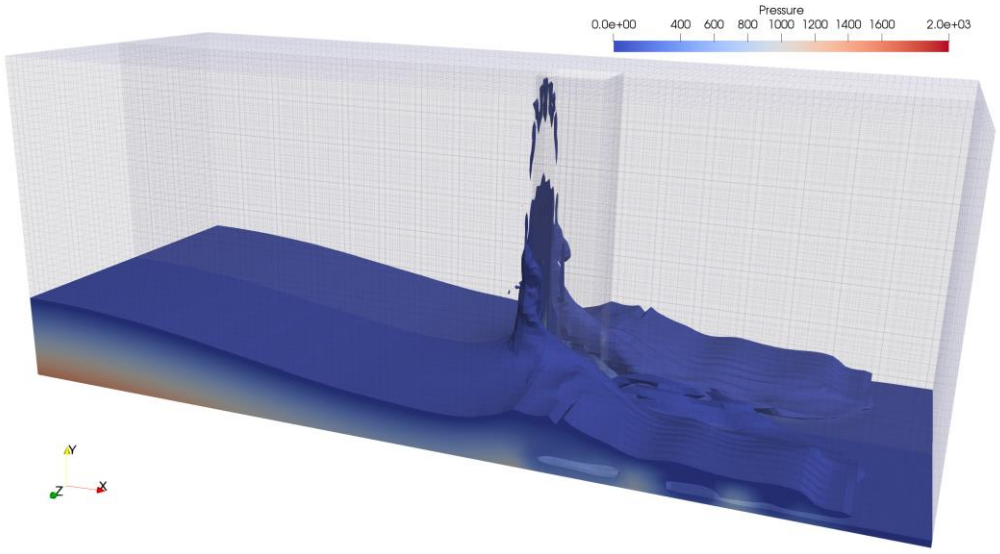

(b) t = 0.5s

Figure 2.15 Snapshots of interaction between dam-break wave and square column in various time

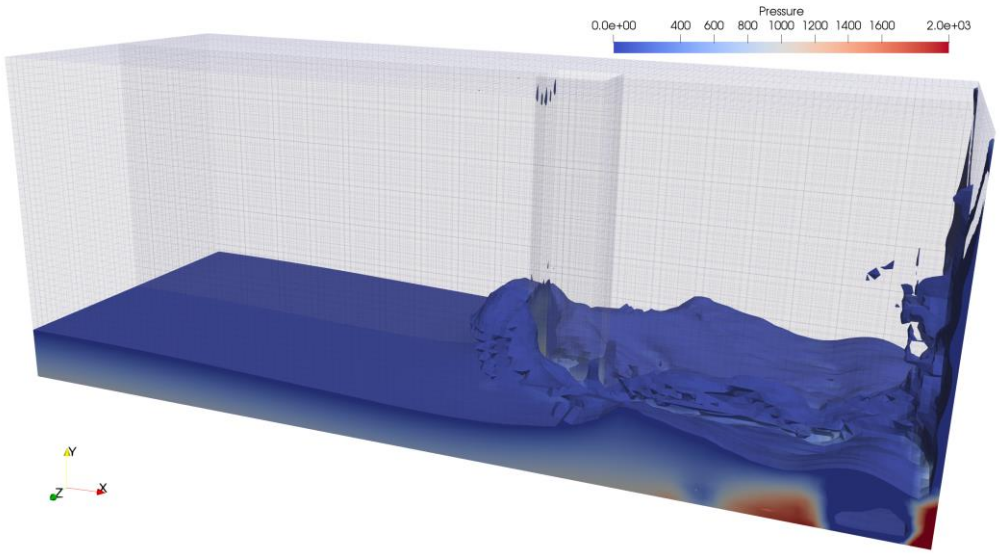

(c) t = 0.75s

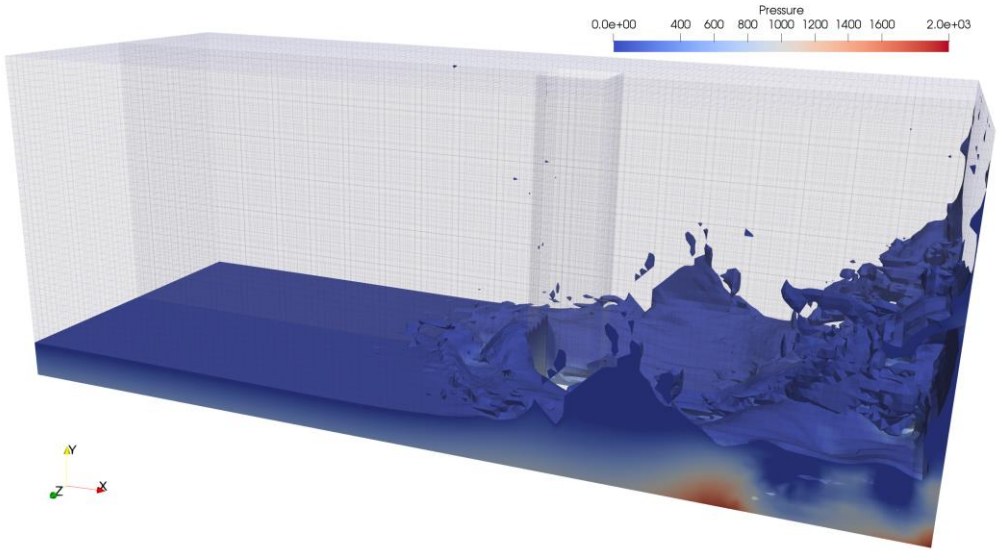

(d) t = 1.0s

Figure 2.15 (cont.)

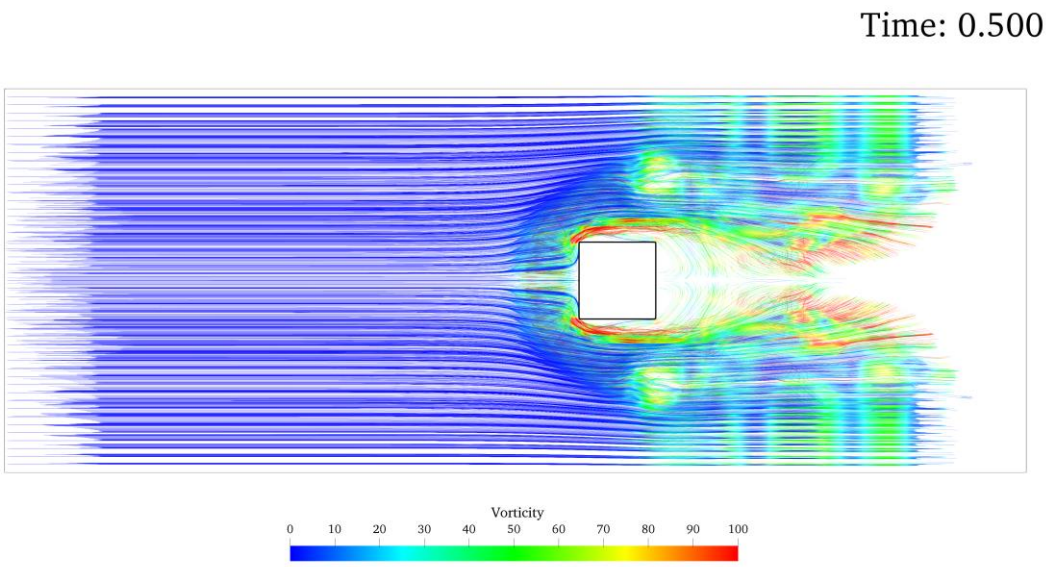

(a) t = 0.5s: two wave fronts that split by the column starting to merge

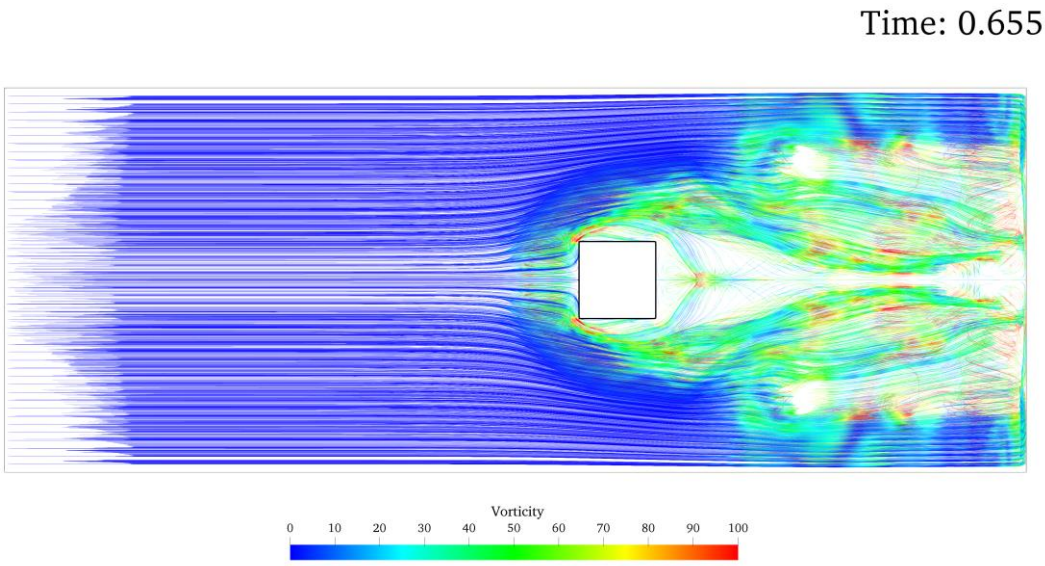

(b) t = 0.6s: water fronts reach the other side of the domain and the two main waves are interacting

Figure 2.16 Snapshots of streamlines colored by vorticity in various time

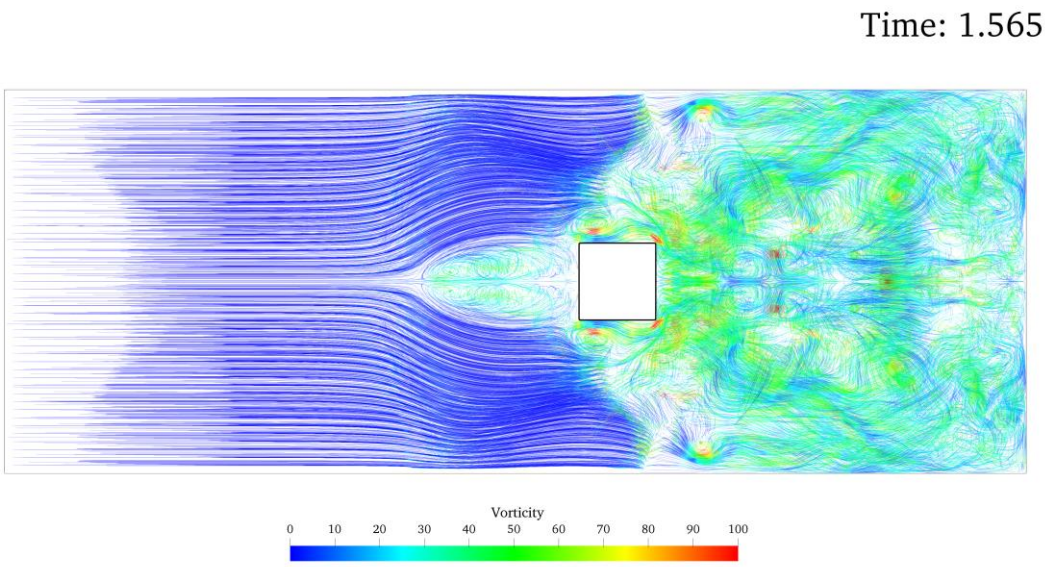

(c) t = 1.565s: back waves go beyond the column again and impact force on column reaches the peak in negative

Figure 2.16 (cont.)

2.5. CONCLUSIONS

We have presented an interface-capturing finite element method that is comprised of a variationally derived ghost-penalty type term which appears naturally via VMS stabilization of the system furnished by the Navier-Stokes equations and the level-set equation. The evolution of the interface is consistently represented in the governing system through the dependence of the material properties on the signed distance field. We employ time-dependent fine-scales in the level-set advection equation where fine-scales are viewed as correction terms to the signed distance field and they help improve the accuracy of the signed distance field when computed over cruder discretization. It is important to note that for the class of problems involving breaking waves, the free-surface kinematics can get complex and therefore spatial discretization that are initially considered adequate for mild free-surface motions can become crude discretization as the free-surface nonlinearity evolves. In this context, the fine-scale signed distance field becomes important for consistently correcting the computed coarse scale signed distance field. For numerical stability in the long time calculations with plunging and breaking waves we also need to ensure conservation of mass in order to conserve momentum and energy in the closed system. This is done via a

mass-correction term that is added to the stabilized form. Furthermore, the complexity of the free-surfaces necessitate that the level-set field complies with the strict definition of the signed distance field. This requires a reinitialization process that invokes solving a stabilized pseudo-time form of the Eikonal equation. A benchmark problem in 2D is presented to highlight the salient features of the proposed level-set method. The full algorithm is tested on 2D dam break flow using linear elements and good comparison with the experimental data as well as with the published computed data is attained. The fully coupled method is implemented in 3D using equal-order 8-node brick elements for all the fields, i.e., velocity, pressure, and the signed distance fields. The complexity of the 3D free-surface flow around the rectangular column shows the robustness of the method to handle large amplitude free-surface oscillations as well as plunging and breaking acting of the waves without giving rise to numerical instability issues that are typical in this class of problems.

CHAPTER 3: VARIATIONALLY DERIVED INTERFACE STABILIZATION FOR DISCRETE MULTIPHASE FLOWS AND RELATION WITH THE GHOST-PENALTY TERM

3.1. INTRODUCTION

Modeling of two-phase flows and free surface flows with moving fluid boundaries is fundamental to many problems in fluid mechanics. Examples include free surface wave action on marine structures, sloshing and mixing in storage tanks, and surface instabilities that arise in free falling water columns. Another class of problems where two-fluid interfacial dynamics plays an important role is the mixing of immiscible fluids where jumps in the density and/or viscosity across the interface boundary can trigger various types of physical instabilities. In all these problem classes, spatiotemporal stability of the deforming interfaces is a key ingredient for accurate modeling of multiphase flow.

In computational modeling of interfacial phenomena in fluids, both interface-tracking methods [29,65,71,80,84,102,132,150] and interface-capturing methods [8,43,82,87,96,131,147,149] have been employed. Interface tracking techniques are invariably used in conjunction with the Arbitrary Lagrangian-Eulerian (ALE) framework [29,65,71,84,102] that enables the motion of the domain boundaries. However, for large free-surface motion, excessive distortion leads to mesh breakdown [80]. Employing Lagrangian description of fluids, Particle Finite Element Method (PFEM) [132] that overcomes the mesh distortion issues because it does not require a contiguous mesh, and Constrained Interpolation Profile (CIP) [150] method that employs Soroban grids to facilitate mesh adaptivity have been proposed for moving interface problems.

An alternate family of methods employed for moving interfaces is based on the so-called interface-capturing techniques. These techniques are invariably written in an Eulerian frame of reference and an auxiliary scalar field termed as the signed distance field is employed to implicitly trace the location of the interface. Compared to the interface-tracking algorithms, an important feature of the interface-capturing methods is the representation of complicated topology of the evolving interface via the solution of the scalar transport equation, termed as the level set equation. In the level set method

[149,131,147,82,8], the iso-contour of the zero level set of the scalar field marks the spatial location of the interface and therefore intrinsically tracks the interface. The interface-capturing techniques are in turn classified by the continuity of the scalar field and have been employed in the context of the finite element [43,96] and the finite volume methods [87].

Interface capturing methods that employ level set techniques for moving interfaces create elements that are traversed by zero contour of the level set. From the perspective of interfacial flow physics, local flow fields across these interfaces can give rise to Rayleigh-Taylor instability [152] (when lighter fluid is accelerated into heavier fluid) or Kelvin-Helmholtz instability [158] that arises due to local shear in the velocity field. However, from a computational perspective these arbitrarily moving interfaces give rise to numerical instabilities that are non-physical and therefore can render the method non-convergent. In order to control these non-physical instabilities, various numerical techniques have been presented in the literature, namely (i) the unfitted finite element method [59], (ii) the fictitious domain method [25,55], (iii) the ghost penalty method [21], (iv) the cut finite element method [22,24,26–28,60], and (v) the X-FEM method [5]. These methods are based on adding a term to the formulation that provides control over the jump in the normal gradient across the deforming interphase boundaries. In this context (a) face stabilization technique that is operational over the discrete $\mathbb{R}^{n_{sd}-1}$ space, and (b) full gradient stabilization technique that is operational in a narrow band across the interface and provides control of the full $\mathbb{R}^{n_{sd}}$ gradient [28] have been proposed. In either case, a positive parameter is needed, which is largely left unspecified by the theory. Some guidelines have been provided to select the value of this parameter [8,23] to suppress potential ill-posedness of the interfacial contribution to the stiffness matrix. A good review of the various aspects of the cut finite element methods is presented in [22].

We propose an interface stabilized method for free-surfaces and for discrete multiphase flows. Our premise is that in the ALE based techniques the motion of the interface boundary and therefore of the computational mesh appears in the governing system of momentum balance equations [29,65,71,84,102]. Likewise, for an Eulerian method where mesh stays fixed, the evolution of the interface between the

phases should also be uniformly and consistently represented in the continuum form of the governing momentum balance equations. This is accomplished by making the material properties a continuous function of the level-set field wherein the location of the zero contour defines the interface across which the material properties may change sharply. By embedding the level set field in the continuum equations via the dependence of local mechanical properties of the fluids on the spatial location of the interface we get a coupled system of equations. The discrete system that emanates from this coupled system of PDEs needs to address three important technical issues: (i) The restriction imposed by the *inf-sup* condition for the incompressible viscous fluids, (ii) Instability that can arise due to the skew advection term when time dependent form of level set equation is employed, and (iii) Interfacial instability that may arise due to discontinuity in the material properties across the deforming internal interfaces. The first two issues are related to the Navier-Stokes equations and the level-set advection equation and a successful approach to address them is to employ stabilization techniques. Among these techniques the Galerkin/Least-Square (GLS) [70] and the Streamline Upwind Petrov Galerkin (SUPG) [69] methods are of prime significance and have been used with considerable success in the literature.

The significant and unique contribution in the present paper is a systematic application of the VMS-based ideas to the coupled system, which results in a method with three essential ingredients: (i) a stabilized method for incompressible flows that satisfy discrete *inf-sup* condition, (ii) a stabilized level-set method to capture the moving boundary on an otherwise fixed background mesh, and (iii) interface stabilization terms to control nonphysical oscillation around moving internal interphase boundaries. Variationally consistent derivation presented here shows that interface stabilization terms have a structure which is similar to that of the Ghost penalty terms [8,23]. This derivation is based on the earlier works of the senior author on Navier-Stokes equations [84,105] and the advection-diffusion equation [113]. It is important to realize that VMS framework [67] has been used in the literature in two contexts: (i) as a method for developing fine-scale models to account for the missing physics in the coarse scales, and (ii) as an error estimator for the numerically computed fields. In the present developments, application of VMS to Navier-Stokes equations is to be viewed in the former context, while for the time dependent

level-set equation, application of VMS is to be viewed in the context of improving spatial accuracy in the location of zero contour of the level-set field in addition to stabilizing the hyperbolic form of the equation.

An outline of the paper is as follows. Section 3.2 presents a systematic procedure for the application of the VMS method to a coupled system of PDEs, rather than applying stabilization individually to each PDE, and subsequently coupling the stabilized discrete forms. A significant contribution of the proposed method is the delineation that applying VMS to the coupled system results in cross-coupling terms that naturally lead to "interfacial stabilization". An outline of the underlying residual-based stabilized form of the incompressible Navier-Stokes equations is presented, which is extended to incorporate the level-set based evolving interfacial boundary. In the process the structure of the variationally derived ghost-penalty type terms is illustrated. Section 3.3 presents a VMS-stabilized level-set method where the variationally derived fine-scale model is shown to play a significant role in the structure of the interface stabilization terms, that is analyzed in Section 3.4. A set of numerical test cases with increasing degree of complexity is presented in Section 3.6, and conclusions are drawn in Section 3.7.

3.2. MULTIPHASE INCOMPRESSIBLE NAVIER-STOKES EQUATIONS WITH EMBEDDED LEVEL-SET FIELD

We employ Navier-Stokes equations and the level-set equation as a model system of coupled PDEs for the derivation of interface stabilized form for immiscible viscous fluids. In the ALE-based methods mesh velocity that describes the evolution of the discrete interface between the two fluids appears in the governing equations. Along these lines, in an Eulerian method it is appropriate to embed the inter-domain interface location in the continuum equations for momentum balance via the dependency of the material parameters on the level set field. Consequently, right from the beginning we assume the value of density and viscosity to be given by the location of the zero contour of the level set function ϕ, i.e., $\rho(\phi)$ and $\eta(\phi)$, and these parameters of density and viscosity are assumed to vary sharply across the interface. We then apply the VMS method to the coupled system to derive the stabilized form. A unique

feature of the derivation is that interfacial terms that have a structure which is similar to the ghost penalty type term arise as a part of the stabilized form, thereby justifying the variational basis of the ghost-penalty type methods [21].

Let $\Omega \subset \mathbb{R}^{n_{sd}}$ be a connected, open and bounded region with piecewise smooth boundary Γ. The number of space dimensions n_{sd} is equal to 2 or 3. In addition, we have an embedded boundary Γ_I (possibly with smooth curved faces) that traverses through the domain and represents the interface between the two phases. We assume the material coefficients to be constant (but otherwise arbitrary) in each of the two phases of the fluid. Consequently, pointwise value of the material parameters (i.e., $\rho(\phi)$ and $\eta(\phi)$) is specified by the location of the evolving interface boundary Γ_I which is given by the zero contour of the level-set field ϕ. The governing equations and appropriate boundary conditions for the two-phase incompressible Navier-Stokes equations are

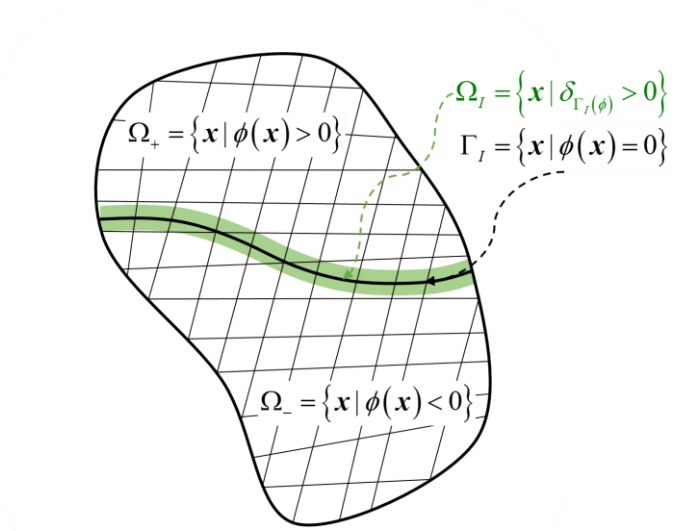

Figure 3.1 Schematics of domain interior and interfacial subregions: Interfacial stabilization terms are restricted to the localized subregion along Γ_I.

$$\rho(\phi)\boldsymbol{v}_{,t} + \rho(\phi)\boldsymbol{v}\cdot\nabla\boldsymbol{v} - 2\eta(\phi)\nabla\cdot\boldsymbol{\varepsilon}(\boldsymbol{v}) + \nabla p = \rho(\phi)\boldsymbol{f} \quad \text{in} \quad \Omega\times]0,T[, \tag{3.1}$$

$$\nabla\cdot\boldsymbol{v} = 0 \quad \text{in} \quad \Omega\times]0,T[, \tag{3.2}$$

$$\boldsymbol{v} = \boldsymbol{g} \quad \text{on} \quad \Gamma_g \times]0,T[, \tag{3.3}$$

$$\boldsymbol{\sigma} \cdot \boldsymbol{n} = \left(2\eta(\phi)\boldsymbol{\varepsilon}(\boldsymbol{v}) - p\boldsymbol{I}\right) \cdot \boldsymbol{n} = \boldsymbol{h} \quad \text{on} \quad \Gamma_h \times]0,T[, \tag{3.4}$$

$$\boldsymbol{v}(\boldsymbol{x},0) = \boldsymbol{v}_0 \quad \text{on} \quad \Omega \times \{0\}, \tag{3.5}$$

where $\boldsymbol{v}$ is velocity, p is dynamic pressure and $\boldsymbol{f}$ is the body force vector. Eqn. (3.1) is the momentum balance equation, and (3.2) is the continuity equation, where ρ is the density and η is the dynamic viscosity. Both parameters are considered as functions of the signed distance field. Vectors $\boldsymbol{g}$ and $\boldsymbol{h}$ are the Dirichlet and Neumann boundary conditions given in (3.3) and (3.4), respectively, and $\boldsymbol{v}_0$ is the initial condition. $\boldsymbol{\sigma}$ is the total stress and $\boldsymbol{\varepsilon}(\boldsymbol{v})$ is the rate-of-deformation tensor which is defined as $\boldsymbol{\varepsilon}(\boldsymbol{v}) = \nabla^s \boldsymbol{v}$, where $\nabla^s \boldsymbol{v} = (\nabla \boldsymbol{v} + (\nabla \boldsymbol{v})^T)/2$ is the symmetric gradient operator.

The level set field ϕ is governed by the time dependent advection equation.

$$\dot{\phi} + \boldsymbol{v} \cdot \nabla \phi = 0 \quad \text{in} \quad \Omega \times]0,T[\tag{3.6}$$

$$\phi(\boldsymbol{x},0) = \phi_0(\boldsymbol{x}) \quad \text{in} \quad \Omega \tag{3.7}$$

where (3.6) is the level-set advection equation, ϕ is the signed distance field, $\boldsymbol{v}$ is the velocity field furnished by the Navier-Stokes equations, and ϕ_0 is the initial condition for the level-set field. The location of interface is given by zero value of the signed distance field, $\Gamma_0 = \{\boldsymbol{x} \mid \phi_0(\boldsymbol{x}) = 0\}$.

The appropriate spaces of weighting functions for the velocity, pressure, and signed distance fields are:

$$\begin{array}{ll} \text{Velocity} & \mathcal{V} = \left\{ \boldsymbol{w} \mid \boldsymbol{w} \in \left(H^1(\Omega)\right)^{n_{sd}}, \boldsymbol{w} = 0 \quad \text{on} \quad \Gamma_g \right\} \\ \text{Pressure} & \mathcal{P} = \left\{ q \mid q \in L_2(\Omega) \right\} \\ \text{Level-set Field} & \Psi = \left\{ \psi \mid \psi \in \left(H^1(\Omega)\right)^{n_{sd}} \right\} \end{array} \tag{3.8}$$

where $L_2(\Omega)$ are the square integrable functions, and $H^1(\Omega)$ consists of functions that possess square-integrable generalized derivatives through order one. The appropriate spaces of trial solutions $\mathcal{V}_t$ for the

velocity field, $\mathcal{P}_t$ for the pressure field, and Ψ_t for the signed distance field are time-dependent spaces corresponding to $\mathcal{V}$, $\mathcal{P}$ and Ψ, respectively.

The standard weak form of the incompressible and immiscible two-phase Navier-Stokes equations is: Find $\boldsymbol{V} = \{\boldsymbol{v}, p, \phi\} \in \mathcal{V}_t \times \mathcal{P}_t \times \Psi_t$, such that $\forall \boldsymbol{W} = \{\boldsymbol{w}, q, \psi\} \in \mathcal{V} \times \mathcal{P} \times \Psi$,

$$\text{Navier-Stokes:} \quad \begin{cases} \left(\boldsymbol{w}, \rho(\phi)\dot{\boldsymbol{v}}\right) + \left(\boldsymbol{w}, \rho(\phi)\boldsymbol{v}\cdot\nabla\boldsymbol{v}\right) + \left(\nabla\boldsymbol{w}, 2\eta(\phi)\nabla^s\boldsymbol{v}\right) - \left(\nabla\cdot\boldsymbol{w}, p\right) \\ \qquad = \left(\boldsymbol{w}, \rho(\phi)\,\boldsymbol{f}\right) + \left(\boldsymbol{w}, \boldsymbol{h}\right)_{\Gamma_h} \\ \left(q, \nabla\cdot\boldsymbol{v}\right) = 0 \end{cases} \tag{3.9}$$

$$\text{Level-set Advection:} \qquad \left(\psi, \dot{\phi} + \boldsymbol{v}\cdot\nabla\phi\right) = 0 \tag{3.10}$$

Remark. At this point in the derivation of the method it suffices to know that the signed distance field evolves together with the physics of the problem and is given by a stabilized form of level set equations that is delineated in Section 3.3.

3.2.1. VMS-based Stabilized Interface Method

This section presents VMS based stabilization of the coupled system of PDEs that is comprised of the Navier-Stokes equations, and the hyperbolic level set equation. The main contribution in this paper is the variational derivation of interface stabilized form that is similar in its structure to the ghost-penalty method for interfacial velocity field [21]. A traditional application of the ghost penalty method requires specification of a positive weighting parameter that is left unspecified by the theory and is largely defined based on stability estimates [21] and scaling arguments [23]. The proposed method presents a systematic procedure to derive an analytical expression for this parameter.

We start by applying VMS idea to a system of PDEs rather than applying the method individually and separately to each PDE. We assume overlapping decomposition of the unknown field into coarse (or resolved) scales and fine (or sub-grid) scales. For nonlinear field equations, this decomposition is to be viewed in the context of projection of fine scales on the coarse scale space. Accordingly, additive decomposition of the velocity field $\boldsymbol{v}(\boldsymbol{x},t)$ and its weighting function $\boldsymbol{w}(\boldsymbol{x})$ is represented as follows,

$$\boldsymbol{w}(\boldsymbol{x}) = \bar{\boldsymbol{w}}(\boldsymbol{x}) + \boldsymbol{w}'(\boldsymbol{x}) \quad \text{and} \quad \boldsymbol{v}(\boldsymbol{x},t) = \bar{\boldsymbol{v}}(\boldsymbol{x},t) + \boldsymbol{v}'(\boldsymbol{x}) \tag{3.11}$$

Likewise, we assume an overlapping sum decomposition of the signed distance field

$$\psi(\boldsymbol{x}) = \bar{\psi}(\boldsymbol{x}) + \psi'(\boldsymbol{x}) \quad \text{and} \quad \phi(\boldsymbol{x},t) = \bar{\phi}(\boldsymbol{x},t) + \phi'(\boldsymbol{x},t) \tag{3.12}$$

Substituting (3.11) and (3.12) in (3.9) and (3.10) leads to two systems of coupled equation: one at the coarse-scale level and the other at the fine-scale level.

System of Coarse-scale sub-problems:

It is important to note that both coarse- and fine-scales from the velocity field of the fluid and signed distance field that defines moving boundaries of the fluid are uniformly present in the weak form of the two PDEs.

$$\text{Navier-Stokes:} \begin{cases} R_1(\bar{\boldsymbol{w}};\bar{\boldsymbol{v}},\boldsymbol{v}',p,\bar{\phi},\phi') = \left(\bar{\boldsymbol{w}},\rho(\bar{\phi}+\phi')\dot{\bar{\boldsymbol{v}}}\right) + \left(\boldsymbol{w},\rho(\bar{\phi}+\phi')(\bar{\boldsymbol{v}}+\boldsymbol{v}')\cdot\nabla(\bar{\boldsymbol{v}}+\boldsymbol{v}')\right) \\ \qquad\qquad + \left(\nabla\bar{\boldsymbol{w}}, 2\eta(\bar{\phi}+\phi')\nabla^s(\bar{\boldsymbol{v}}+\boldsymbol{v}')\right) - \left(\nabla\cdot\bar{\boldsymbol{w}}, p\right) \\ \qquad\qquad - \left(\bar{\boldsymbol{w}},\rho(\bar{\phi}+\phi')\boldsymbol{f}\right) - \left(\bar{\boldsymbol{w}},\boldsymbol{h}\right)_{\Gamma_h} = 0 \\ R_2(q;\bar{\boldsymbol{v}},\boldsymbol{v}') = \left(q,\nabla\cdot(\bar{\boldsymbol{v}}+\boldsymbol{v}')\right) = 0 \end{cases} \tag{3.13}$$

$$\text{Leve-set Advection:} \qquad R_3(\bar{\psi};\bar{\boldsymbol{v}},\boldsymbol{v}',\bar{\phi},\phi') = \left(\bar{\psi},\dot{\bar{\phi}}+\dot{\phi}'+(\bar{\boldsymbol{v}}+\boldsymbol{v}')\cdot\nabla(\bar{\phi}+\phi')\right) = 0 \tag{3.14}$$

Remark. In the present work we employ the time dependent form of the level set equation discussed in Section 3.3.

System of Fine-scale sub-problems:

Likewise, the coupled system at the fine scale level has coarse-scale and fine-scale fields for $\boldsymbol{v}$ and ϕ fully embedded.

$$\text{Navier-Stokes:} \begin{cases} R_4(\boldsymbol{w}';\bar{\boldsymbol{v}},\boldsymbol{v}',p,\bar{\phi},\phi') = \left(\boldsymbol{w}',\rho(\bar{\phi}+\phi')\dot{\bar{\boldsymbol{v}}}\right) + \left(\boldsymbol{w}',\rho(\bar{\phi}+\phi')(\bar{\boldsymbol{v}}+\boldsymbol{v}')\cdot\nabla(\bar{\boldsymbol{v}}+\boldsymbol{v}')\right) \\ \qquad\qquad + \left(\nabla\boldsymbol{w}', 2\eta(\bar{\phi}+\phi')\nabla^s(\bar{\boldsymbol{v}}+\boldsymbol{v}')\right) - \left(\nabla\cdot\boldsymbol{w}', p\right) \\ \qquad\qquad - \left(\boldsymbol{w}',\rho(\bar{\phi}+\phi')\boldsymbol{f}\right) - \left(\boldsymbol{w}',\boldsymbol{h}\right)_{\Gamma_h} = 0 \end{cases} \tag{3.15}$$

Leve-set Advection: $$R_5\left(\psi';\bar{\boldsymbol{v}},\boldsymbol{v}',\bar{\phi},\phi'\right)=\left(\psi',\dot{\bar{\phi}}+\dot{\phi}'+\left(\bar{\boldsymbol{v}}+\boldsymbol{v}'\right)\cdot\nabla\left(\bar{\phi}+\phi'\right)\right)=0 \tag{3.16}$$

Fine-scale sub-problem provides an avenue to develop a model for the fine-scale fields in terms of the residuals of the Euler-Lagrange equations of the coarse scales. This feature of analytical modeling of the fine scales is the uniquely distinct feature of the VMS method that is in stark contrast with other numerical methods that are employed for enhancing stability and accuracy of the methods. The coarse-scale and fine-scale sub-problems are nonlinear with respect to both the fine-sale velocity and the signed distance field, consequently we need to linearize these equations. Specifically, we linearize the momentum balance equation only with respect to fine-scale velocity field, where the linearization operator is defined as follows

$$\mathcal{L}\left(R_4\left(\boldsymbol{w}';\bar{\boldsymbol{v}},\boldsymbol{v}',\phi,p\right)\right)=\frac{d}{d\varepsilon}R_4\left(\boldsymbol{w}';\bar{\boldsymbol{v}},\boldsymbol{v}'+\varepsilon\delta\boldsymbol{v}',\phi,p\right)\Big|_{\varepsilon=0} \tag{3.17}$$

Applying (3.17) to (3.15) results in the linearized fine-scale sub-problem.

$$\begin{aligned}\left(\boldsymbol{w}',\rho\left(\bar{\phi}+\phi'\right)\delta\boldsymbol{v}'\cdot\nabla\left(\bar{\boldsymbol{v}}+\boldsymbol{v}'\right)\right)+\left(\boldsymbol{w}',\rho\left(\bar{\phi}+\phi'\right)\left(\bar{\boldsymbol{v}}+\boldsymbol{v}'\right)\cdot\nabla\delta\boldsymbol{v}'\right)+\left(\nabla\boldsymbol{w}',2\eta\left(\bar{\phi}+\phi'\right)\nabla^s\delta\boldsymbol{v}'\right)\\=-R_4\left(\boldsymbol{w}';\bar{\boldsymbol{v}},\boldsymbol{v}',p,\bar{\phi},\phi'\right)\end{aligned} \tag{3.18}$$

We rearrange (3.18) by keeping the terms that depend on $\delta\boldsymbol{v}'$ on the left hand side and substitute the expression of the residual from (3.15).

$$\left(\boldsymbol{w}',\rho\left(\phi\right)\delta\boldsymbol{v}'\cdot\nabla\boldsymbol{v}\right)+\left(\boldsymbol{w}',\rho\left(\phi\right)\boldsymbol{v}\cdot\nabla\delta\boldsymbol{v}'\right)+\left(\nabla\boldsymbol{w}',2\eta\left(\phi\right)\nabla^s\delta\boldsymbol{v}'\right)=-\left(\boldsymbol{w}',\boldsymbol{r}_{\mathrm{NSE}}\right) \tag{3.19}$$

Following along the lines of our earlier works [84,105], we expand the fine-scale weighting function and trial solution in (3.19) via bubble functions that are nonzero within the element interior, i.e., $\boldsymbol{w}'=b^e\boldsymbol{\gamma}$ and $\boldsymbol{v}'=b^e\boldsymbol{\beta}$. The fine-scale model is as follows,

$$\delta\boldsymbol{v}'=\boldsymbol{\tau}_{\mathrm{NSE}}\boldsymbol{r}_{\mathrm{NSE}} \tag{3.20}$$

where the stabilization tensor $\boldsymbol{\tau}_{\mathrm{NSE}}$ and coarse-scale residual $\boldsymbol{r}_{\mathrm{NSE}}$ of the momentum balance equation are defined as

$$\boldsymbol{\tau}_{\mathrm{NSE}} = b^e \left[\begin{array}{l} \rho \int_{\Omega^e} \left(b^e\right)^2 \left(\nabla \boldsymbol{v}\right)^T d\Omega + \int_{\Omega^e} b^e \boldsymbol{v} \cdot \nabla b^e d\Omega \boldsymbol{I} \\ + \int_{\Omega^e} \eta^e \left(\nabla b^e \otimes \nabla b^e\right) d\Omega + \int_{\Omega^e} \eta \nabla b^e \cdot \nabla b^e d\Omega \boldsymbol{I} \end{array} \right]^{-1} \int_{\Omega^e} b^e d\Omega \qquad (3.21)$$

$$\boldsymbol{r}_{\mathrm{NSE}} = -\rho \dot{\bar{\boldsymbol{v}}} - \rho \boldsymbol{v} \cdot \nabla \boldsymbol{v} + \nabla \cdot 2\eta \nabla^s \boldsymbol{v} - \nabla p + \rho \boldsymbol{f}$$

Remark. For the discussion on bubble functions and the stabilization tensor, interested reader is referred to VMS stabilization form [84,105] for incompressible Navier-Stokes equations.

Remark. We can derive the residual-based fine-scale signed distance field with a generic form $\phi' = \tau_{\mathrm{LSA}} r_{\mathrm{LSA}}$. To keep the presentation concise, discussion on this derivation is deferred to Section 3.

3.2.2. The Coarse-scale Sub-problem

The important point to note is that the composition of density and viscosity with the level-set field introduces the Heaviside function $H(\phi)$ in the formulation. Though this brings in further nonlinearity in the system, appearance of ϕ in the governing system provides an avenue to variationally develop interface stabilization method. The coarse-scale sub-problems is linearized about the fine-scale solution $\{\boldsymbol{v}', \phi'\}$ to be able to substitute the fine-scale velocity and signed distance fields. Accordingly, the linearized operator for the coarse-scale momentum balance equation and the advection equation is defined as

$$\mathcal{L}\left(R_1\left(\bar{\boldsymbol{w}}; \bar{\boldsymbol{v}}, \boldsymbol{v}', p, \bar{\phi}, \phi'\right)\right) = \frac{d}{d\varepsilon} R_1\left(\bar{\boldsymbol{w}}; \bar{\boldsymbol{v}}, \boldsymbol{v}' + \varepsilon\delta\boldsymbol{v}', \phi, p\right)\Big|_{\varepsilon=0} + \frac{d}{d\varepsilon} R_1\left(\bar{\boldsymbol{w}}; \boldsymbol{v}, \bar{\phi}, \phi' + \varepsilon\delta\phi', p\right)\Big|_{\varepsilon=0} \qquad (3.22)$$

As compared to (3.17), the linearized operator in (3.22) also includes the contribution emanating from linearization about the fine-scale signed distance field.

The jump in the density ρ and dynamic viscosity η across the interface between phases can be defined via Heaviside function $H(\phi)$ as

$$\rho = \rho_+ H(\phi) + \rho_- \left(1 - H(\phi)\right) \quad \text{and} \quad \eta = \eta_+ H(\phi) + \eta_- \left(1 - H(\phi)\right) \qquad (3.23)$$

where the subscript $(\bullet)_+ = (\bullet)\big|_{\phi>0}$ and $(\bullet)_- = (\bullet)\big|_{\phi<0}$ denotes the material parameters of discrete phases that represented by different signs of signed distance field. We substitute the additively decomposed form of ϕ in (3.23), which can be further simplified as

$$\begin{aligned}\rho\left(\bar{\phi}+\phi'\right) &= \left(\rho_+ - \rho_-\right)H\left(\bar{\phi}+\phi'\right) + \rho_- \\ &= \underbrace{\left(\rho_+ - \rho_-\right)H\left(\bar{\phi}\right) + \rho_-}_{\rho(\bar{\phi})} + \left(\rho_+ - \rho_-\right)H_{,\phi}\left(\bar{\phi}\right)\phi' + O\left(\phi'^2\right)\end{aligned} \tag{3.24}$$

The higher order terms that depend on ϕ' in (3.24) are dropped. It is important to note that $H_{,\phi}\left(\bar{\phi}\right)$ yields the Dirac delta function $\delta_{\Gamma_I(\bar{\phi})}$, which is defined along the embedded interface given by zero value of the signed distance field. Likewise, we can derive an analogous expression for viscosity across Γ_I.

$$\eta\left(\bar{\phi}+\phi'\right) = \eta\left(\bar{\phi}\right) + \left(\eta_+ - \eta_-\right)H_{,\phi}\left(\bar{\phi}\right)\phi' \tag{3.25}$$

Applying the linearization operator defined in (3.22) to the coarse-scale momentum balance equation in (3.13) and substituting linear expansion of the density in (3.24) and viscosity in (3.25), we get the linearized coarse-scale formulation:

$$\begin{aligned}&\left(\bar{\boldsymbol{w}}, \rho\delta\boldsymbol{v}'\cdot\nabla\left(\bar{\boldsymbol{v}}+\boldsymbol{v}'\right)\right) + \left(\bar{\boldsymbol{w}}, \rho\left(\bar{\boldsymbol{v}}+\boldsymbol{v}'\right)\cdot\nabla\delta\boldsymbol{v}'\right) + \left(\nabla\bar{\boldsymbol{w}}, 2\eta\nabla^s\delta\boldsymbol{v}'\right) \\ &+\left(\bar{\boldsymbol{w}}, \left(\rho_+ - \rho_-\right)\delta_{\Gamma_I}\phi'\left(\dot{\bar{\boldsymbol{v}}} + \boldsymbol{v}\cdot\nabla\boldsymbol{v} - \boldsymbol{f}\right)\right)_{\Omega_I} + \left(\nabla\bar{\boldsymbol{w}}, 2\left(\eta_+ - \eta_-\right)\delta_{\Gamma_I}\phi'\nabla^s\boldsymbol{v}\right)_{\Omega_I} = -R_1\left(\boldsymbol{w}';\bar{\boldsymbol{v}},\boldsymbol{v}',p,\bar{\phi},\phi'\right)\end{aligned} \tag{3.26}$$

Remark. We denote the $\delta\phi'$ in (3.26) with ϕ' for the sake of brevity.

In addition, we have the continuity equation

$$\left(q, \nabla\cdot\boldsymbol{v}'\right) = -\left(q, \nabla\cdot\bar{\boldsymbol{v}}\right) \tag{3.27}$$

The residual form of coarse-scale momentum balance equations (3.26) and continuity equation (3.27) can be re-arranged as

$$\begin{aligned}
&\left(\bar{\boldsymbol{w}},\rho\dot{\bar{\boldsymbol{v}}}\right)+\left(\bar{\boldsymbol{w}},\rho\boldsymbol{v}\cdot\nabla\boldsymbol{v}\right)+\left(\nabla\bar{\boldsymbol{w}},2\eta\nabla^{s}\boldsymbol{v}\right)-\left(\nabla\cdot\bar{\boldsymbol{w}},p\right)-\left(\bar{\boldsymbol{w}},\rho\boldsymbol{f}\right)-\left(\bar{\boldsymbol{w}},\boldsymbol{h}\right)_{\Gamma_h}+\left(q,\nabla\cdot\bar{\boldsymbol{v}}\right)\\
&\quad+\left(\bar{\boldsymbol{w}},\rho\delta\boldsymbol{v}'\cdot\nabla\boldsymbol{v}\right)+\left(\bar{\boldsymbol{w}},\rho\boldsymbol{v}\cdot\nabla\delta\boldsymbol{v}'\right)+\left(\nabla\bar{\boldsymbol{w}},2\eta\nabla^{s}\delta\boldsymbol{v}'\right)+\left(q,\nabla\cdot\boldsymbol{v}'\right)\\
&\underbrace{+\left(\bar{\boldsymbol{w}},\left(\rho_{+}-\rho_{-}\right)\delta_{\Gamma_I}\phi'\left(\dot{\bar{\boldsymbol{v}}}+\boldsymbol{v}\cdot\nabla\boldsymbol{v}-\boldsymbol{f}\right)\right)_{\Omega_I}}_{\text{Interface Stabilization 1}}\underbrace{+\left(\nabla\bar{\boldsymbol{w}},2\left(\eta_{+}-\eta_{-}\right)\delta_{\Gamma_I}\phi'\nabla^{s}\boldsymbol{v}\right)_{\Omega_I}}_{\text{Interface Stabilization 2}}=0
\end{aligned}\tag{3.28}$$

Terms in the first row in (3.28) are the standard Galerkin terms, while the terms in the second row depend on the fine-scale velocity field. The Dirac delta function facilitated by the fine-scale signed distance field localizes the interface terms to a narrow band Ω_I along the interface, as shown in Fig. 1. Consequently, the terms in the third row are the interfacial terms defined over Ω_I that account for the jump in the mechanical properties from either side of the interface. In the limit, this narrow band represents the interface Γ_I.

3.2.3. Stabilized Form of the Multiphase Navier-Stokes Equations with Embedded Interfaces

After substituting fine-scale solution derived in Section 2.1 in equation (28) the nonlinear stabilized form (3.28) is completely expressed in terms of the coarse scale fields. Henceforth, the superposed bars are dropped. For ease of presentation we write the derived formulation in an abstract form:

$$\boxed{\mathcal{B}_{\text{Stab}}\left(\boldsymbol{w},q;\boldsymbol{v},p,\phi\right)=\mathcal{L}_{\text{Stab}}\left(\boldsymbol{w};\phi\right)}\tag{3.29}$$

where $\mathcal{B}_{\text{Stab}}$ and $\mathcal{L}_{\text{Stab}}$ are defined as follows:

$$\begin{aligned}
\mathcal{B}_{\text{Stab}}\left(\boldsymbol{w},q;\boldsymbol{v},p,\phi\right)&=\mathcal{B}_{\text{Gal}}\left(\bar{\boldsymbol{w}},q;\bar{\boldsymbol{v}},p\right)+\mathcal{B}_{\text{VMS}}^{\Omega^e}\left(\boldsymbol{w},q;\boldsymbol{v},p,\phi\right)+\mathcal{B}_{\text{VMS}}^{\Omega_I}\left(\boldsymbol{w};\boldsymbol{v},\phi\right)\\
\mathcal{B}_{\text{Gal}}\left(\bar{\boldsymbol{w}},q;\bar{\boldsymbol{v}},p\right)&=\left(\boldsymbol{w},\rho\left(\phi\right)\dot{\boldsymbol{v}}\right)+\left(\boldsymbol{w},\rho\left(\phi\right)\boldsymbol{v}\cdot\nabla\boldsymbol{v}\right)+\left(\nabla\boldsymbol{w},2\eta\left(\phi\right)\nabla^{s}\boldsymbol{v}\right)\\
&\quad-\left(\nabla\cdot\boldsymbol{w},p\right)+\left(q,\nabla\cdot\boldsymbol{v}\right)\\
\mathcal{B}_{\text{VMS}}^{\Omega^e}\left(\boldsymbol{w},q;\boldsymbol{v},p,\phi\right)&=-\left(\boldsymbol{\chi},\boldsymbol{\tau}_{\text{NSE}}\boldsymbol{r}_{\text{NSE}}\right)\\
\mathcal{B}_{\text{VMS}}^{\Omega_I}\left(\boldsymbol{w};\boldsymbol{v},\phi\right)&=\left(\nabla\boldsymbol{w},2\hat{\eta}\delta_{\Gamma_I(\phi)}\tau_{\text{LSA}}r_{\text{LSA}}\nabla^{s}\boldsymbol{v}\right)_{\Omega_I}\\
\mathcal{L}_{\text{Stab}}\left(\boldsymbol{w};\phi\right)&=\left(\boldsymbol{w},\rho\left(\phi\right)\boldsymbol{f}\right)+\left(\boldsymbol{w},\boldsymbol{h}\right)_{\Gamma_h}
\end{aligned}\tag{3.30}$$

where $\mathcal{B}_{\text{Gal}}$ are the standard Galerkin terms, $\mathcal{B}_{\text{VMS}}^{\Omega^e}$ is the interior stabilization term and $\mathcal{B}_{\text{VMS}}^{\Omega_I}$ is the interfacial stabilization term that helps with the instability arising due to the arbitrary motion of the interface boundary.

Remark. The structure of the domain interior stabilization terms that emanate from (3.28) and are represented by $\mathcal{B}_{\text{VMS}}^{\Omega_I}$ is same as that in [84,105].

Remark. The structure of the interface stabilization terms is delineated in Section 3.4.

3.3. STABILIZED LEVEL-SET METHOD

The updated interface is given by the level-set equation wherein the scalar level-set field is driven by the velocity field facilitated by the incompressible Navier-Stokes equations. Since the level-set equation is a non-dissipative and non-dispersive advection equation, it requires a stabilizing technique to yield accurate numerical solution. The computed level-set field is checked to ensure that it satisfies the criterion of the signed distance field. In case of deviation, a re-initialization process [11] that is governed by the Eikonal equation is invoked. If the numerical solution of the hyperbolic system induces dissipation of mass, a mass conservation algorithm [144] is invoked to preserve physics associated with the inertial effects.

We consider the fine-scale level-set advection equation (3.16)

$$\left(\psi', \boldsymbol{v}\cdot\nabla\phi'\right) = -\left(\psi', \dot{\phi} + \boldsymbol{v}\cdot\nabla\bar{\phi}\right) = \left(\psi', r_{\text{LSA}}\right) \tag{3.31}$$

where $-r_{\text{LSA}} = \dot{\phi} + \boldsymbol{v}\cdot\nabla\bar{\phi}$ is the residual of the Euler-Lagrange equation of the coarse-scale level-set equation. We expand the fine-scale weighting function and trial solution in (3.12) by element-wise bubble functions as

$$\psi' = b^e\xi \quad \text{and} \quad \phi' = b^e\eta \tag{3.32}$$

Substituting (3.32) into (3.31), and following along [25] the fine-scale model can be extracted as

$$\phi' = \tau_{\text{LSA}} r_{\text{LSA}} \tag{3.33}$$

where τ_{LSA} is the stabilization parameter, derived in our earlier work [113].

$$\tau_{\text{LSA}} = \frac{b^e \int_{\Omega^e} b^e \, d\Omega}{\int_{\Omega^e} \left((\Delta t)^{-1} \left(b^e \right)^2 + b^e \bar{\boldsymbol{v}} \cdot \nabla b^e \right) d\Omega} \tag{3.34}$$

Substituting ϕ' from (3.33) in (3.14) leads to stabilized form for advection equation that can be written as

$$\begin{aligned} \boxed{\mathcal{B}_{\text{Gal}}(\psi;\boldsymbol{v},\phi) + \mathcal{B}_{\text{VMS}}(\psi;\boldsymbol{v},\phi) = 0} \\ \mathcal{B}_{\text{Gal}}(\psi;\boldsymbol{v},\phi) = \left(\psi, \frac{\partial \phi}{\partial t} + \boldsymbol{v} \cdot \nabla \phi \right) \\ \mathcal{B}_{\text{VMS}}(\psi;\boldsymbol{v},\phi) = \left(\tau \boldsymbol{v} \cdot \nabla \psi, \frac{\partial \phi}{\partial t} + \boldsymbol{v} \cdot \nabla \phi \right) - \left(\psi, \tau \boldsymbol{v} \cdot \nabla \frac{\partial \phi}{\partial t} \right) \end{aligned} \tag{3.35}$$

Remark. For the derivation of the stabilized method for the advection-diffusion equation, see [113]. For time-dependent fine-scales, interested reader is referred to the derivation in [30].

3.4. STRUCTURE OF THE INTERFACE STABILIZATION TERMS

We now focus on the two interfacial terms in (3.28) that are defined over Ω_I in the subdomain that contains the embedded interface Γ_I. To keep the problem simple, we have dropped the superposed bar on the coarse-scale quantities: $\bar{\boldsymbol{w}}$, $\bar{\boldsymbol{v}}$ and $\bar{\phi}$ (within the coarse-scale residual of level-set advection equation). These terms (i.e. interface stabilization 1 and 2) are only present in the interior of the elements that are traversed by the boundary Γ_I.

$$
\begin{aligned}
&\left(\boldsymbol{w},\left(\rho_{+}-\rho_{-}\right)\delta_{\Gamma_I}\phi'\left(\dot{\boldsymbol{v}}+\boldsymbol{v}\cdot\nabla\boldsymbol{v}-\boldsymbol{f}\right)\right)_{\Omega_I}+\left(\nabla\boldsymbol{w},2\left(\eta_{+}-\eta_{-}\right)\delta_{\Gamma_I}\phi'\,\nabla^{s}\boldsymbol{v}\right)_{\Omega_I}\\
&=\left(\boldsymbol{w},\rho^{-1}\left(\rho_{+}-\rho_{-}\right)\delta_{\Gamma_I}\phi'\nabla\cdot\boldsymbol{\sigma}\right)_{\Omega_I}+\left(\nabla\boldsymbol{w},2\left(\eta_{+}-\eta_{-}\right)\delta_{\Gamma_I}\phi'\,\nabla^{s}\boldsymbol{v}\right)_{\Omega_I}\quad\text{(via governing eqn.)}\\
&=-\left(\nabla\boldsymbol{w},\rho^{-1}\left(\rho_{+}-\rho_{-}\right)\delta_{\Gamma_I}\phi'\boldsymbol{\sigma}\right)_{\Omega_I}+\left(\nabla\boldsymbol{w},2\left(\eta_{+}-\eta_{-}\right)\delta_{\Gamma_I}\phi'\,\nabla^{s}\boldsymbol{v}\right)_{\Omega_I}\quad\text{(via Gauss theorem)}\\
&=\left(\nabla\boldsymbol{w},2\left(\eta_{+}-\eta_{-}-\frac{\eta}{\rho}\left(\rho_{+}-\rho_{-}\right)\right)\delta_{\Gamma_I}\phi'\,\nabla^{s}\boldsymbol{v}\right)_{\Omega_I}\quad\text{(combining the terms)}\\
&=\left(\nabla\boldsymbol{w},2\hat{\eta}\phi'\,\nabla^{s}\boldsymbol{v}\right)_{\Omega_I}\\
&=\left(\nabla\boldsymbol{w},\hat{\eta}\delta_{\Gamma_I}\tau_{\mathrm{LSA}}r_{\mathrm{LSA}}\nabla^{s}\boldsymbol{v}\right)_{\Omega_I}
\end{aligned}
\tag{3.36}
$$

where $\hat{\eta}$ is defined as the interfacial parameter given as

$$
\hat{\eta}=\eta_{+}-\eta_{-}-\frac{\eta}{\rho}\left(\rho_{+}-\rho_{-}\right)=\begin{cases}\rho_{-}\left(\nu_{+}-\nu_{-}\right) & \text{in}\quad\Omega_{+}\\ \rho_{+}\left(\nu_{+}-\nu_{-}\right) & \text{in}\quad\Omega_{-}\end{cases}
\tag{3.37}
$$

Since jump in the material properties occurs normal to the interface, this term in fact provides control over jump in the velocity gradient perpendicular to the interface. In the context of linear algebraic systems, such terms are invariably added to the system to control ill-conditioning in the elements that are cut by the interface as discussed in [23]. Furthermore, the jump in interface parameter $\hat{\eta}$ in (3.37) which becomes the source of jump in the velocity gradient only takes place in the direction normal to the interface Γ_I. The material parameters do not have jump in their value in the direction, which is parallel to the interface, therefore $\hat{\eta}=0$ in the tangential direction to the interface. Consequently, in the limit as the length parameter normal to the interface approaches zero thickness, we can approximate (3.36) as an interface-based term that controls the projection of the gradient field in the direction normal to the interface. Accordingly, the reduced form of this term at Γ_I in $\mathbb{R}^{n_{\mathrm{sd}}-1}$ can be written as

$$
\boxed{\left(\nabla\boldsymbol{w},2\hat{\eta}\phi'\nabla^{s}\boldsymbol{v}\right)_{\Omega_I}\ \cong\ \left(\nabla\boldsymbol{w}\cdot\boldsymbol{n}_I,2\hat{\eta}\phi'\nabla^{s}\boldsymbol{v}\cdot\boldsymbol{n}_I\right)_{\Gamma_I}}
\tag{3.38}
$$

whereas $\phi'=\tau_{\mathrm{LSA}}r_{\mathrm{LSA}}$ (as defined in Section 3), and $\nabla^{s}\boldsymbol{v}\cdot\boldsymbol{n}_I$ is the projection of the gradient of velocity in the direction perpendicular to Γ_I. From the structure of (3.38), it can be seen that for the case of zero

jump in the kinematic viscosity, this interfacial stabilization vanishes, thereby confirming its variational consistency.

Remark. In the numerical implementation of the method, we have opted for the full gradient method because of the ease of its implementation.

3.5. ANALYSIS OF THE INTERFACE STABILIZATION TERM

We assume that $\rho_w > \rho_a$, $\eta_w > \eta_a$ and the density of the two-phase fluid is a bounded function such that $\rho_a \le \rho(\phi) \le \rho_w$. Our objective is to show that the interface terms as in fact a stabilization terms that add to the overall stability of the method. We have two forms of interface stabilizations

$$\begin{aligned} \mathcal{B}_{\text{VMS}}^{\Omega_I}(\boldsymbol{w};\boldsymbol{v},\phi) &= \left(\nabla \boldsymbol{w}, 2\hat{\eta}\delta_{\Gamma_I(\phi)}\tau_{\text{LSA}} r_{\text{LSA}} \nabla^s \boldsymbol{v}\right)_{\Omega_I} = \left(\nabla \boldsymbol{w}, 2\hat{\eta}\phi' \nabla^s \boldsymbol{v}\right)_{\Omega_I} \\ \mathcal{B}_{\text{VMS}}^{\Gamma_I}(\boldsymbol{w};\boldsymbol{v},\phi) &= \left(\nabla \boldsymbol{w} \cdot \boldsymbol{n}_I, 2\hat{\eta}\phi' \nabla^s \boldsymbol{v} \cdot \boldsymbol{n}_I\right)_{\Gamma_I} \end{aligned} \tag{3.39}$$

We first establish two conditions:

1) $\hat{\eta}\phi' \ge 0 \quad \forall \boldsymbol{x} \in \Omega_I$

2) ϕ' is a bounded function, where $\phi' = \tau_{\text{LSA}} r_{\text{LSA}}$

For the second condition to hold, we also need to establish that τ_{LSA} is a bounded function.

PROPOSITION 1: The sign of the fine-scale level-set field ϕ' is such that

$$\begin{aligned} \phi' \le 0 \quad \text{in} \quad \Omega_+ = \left\{ \boldsymbol{x} \in \Omega_I \mid \phi(\boldsymbol{x}) > 0 \right\} \\ \phi' \ge 0 \quad \text{in} \quad \Omega_- = \left\{ \boldsymbol{x} \in \Omega_I \mid \phi(\boldsymbol{x}) < 0 \right\} \end{aligned} \tag{3.40}$$

PROOF: We consider two cases for the orientation of the level-set field ϕ.

Case 1: We assume the orientation of the signed distance field $\bar{\phi}(x)$ such that in the phase with higher density indicated as Ω_w, $\bar{\phi}(x) \ge 0$ (see Figure 3.2a).

Case 2: We flip the assumed orientation of the signed distance field as shown in Figure 3.2b, such that $\bar{\phi}(x) \ge 0$ in Ω_a.

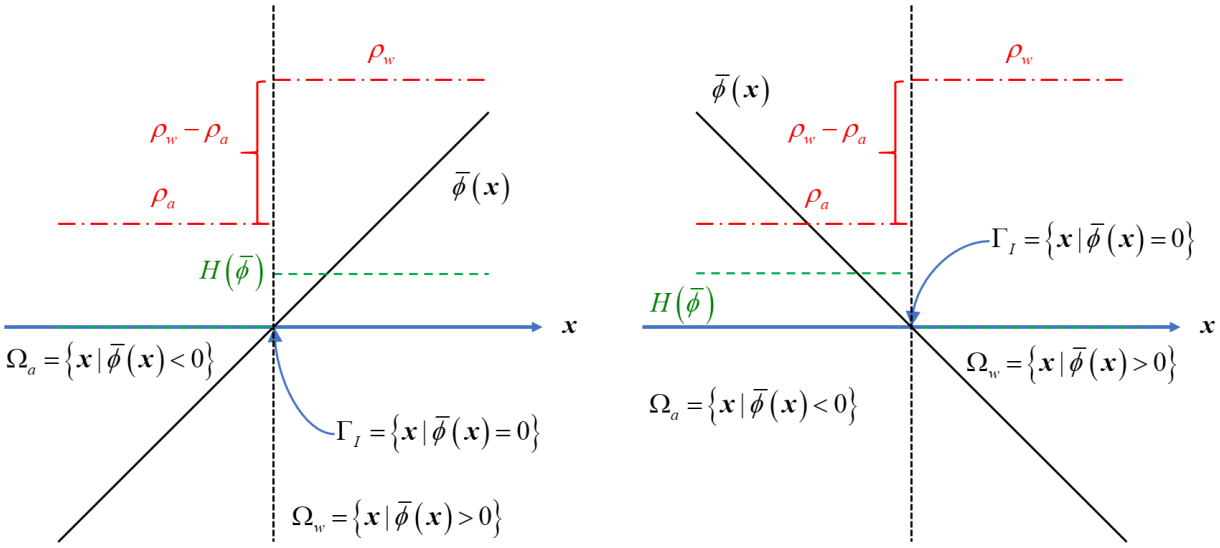

a) Case 1 b) Case 2

Figure 3.2 Possible orientations of the level-set field

In either case, the density ρ and dynamic viscosity η vary sharply across the phase boundary Γ_I which is marked by zero value of the level-set ϕ, while the jump in the value is defined via the Heaviside function $H(\phi)$.

$$\begin{aligned}\rho(\phi) &= \rho_+ H(\phi) + \rho_- (1 - H(\phi)) \\ &= \rho_- + (\rho_+ - \rho_-) H(\phi)\end{aligned} \tag{3.41}$$

For the simplicity of further analysis, we use a regularized Heaviside function $H_\varepsilon(\phi)$ that depends on the half width ε of Ω_I and the limit of the regularized Heaviside function approaches the sharp discontinuity, that is

$$\lim_{\varepsilon \to 0} |H_\varepsilon - H| = 0 \quad \forall \phi \in \mathbb{R} \tag{3.42}$$

We substitute ϕ in terms of its additively decomposed form (3.12), and employing Taylor series expansion on the regularized Heaviside function we can simplify the expression

$$\begin{aligned}\rho\left(\bar{\phi}+\phi'\right) &= \rho_- + \left(\rho_+ - \rho_-\right) H_\varepsilon\left(\bar{\phi}+\phi'\right) \\ &= \rho_- + \left(\rho_+ - \rho_-\right) H_\varepsilon\left(\bar{\phi}\right) + \left(\rho_+ - \rho_-\right) H_{\varepsilon,\phi}\left(\bar{\phi}\right)\phi' + O\left(\phi'^2\right) \quad \text{(Taylor Expansion)} \\ &\cong \rho\left(\bar{\phi}\right) + \left(\rho_+ - \rho_-\right) H_{\varepsilon,\phi}\left(\bar{\phi}\right)\phi' \qquad\qquad \text{(drop high-order terms)}\end{aligned} \tag{3.43}$$

We drop the higher order terms in ϕ'. It is important to note that $H_{,\phi}\left(\bar{\phi}\right)$ yields the Dirac delta function $\delta_{\Gamma_I(\bar{\phi})}$, which is defined along the embedded interface Γ_I that is marked by zero value of the signed distance field.

We follow the convention adopted in the description of the level-set field where $\bar{\phi}$ is the coarse level set, while the fine-scale level-set ϕ' is the perturbation that can also be viewed as a correction term to the level set field. Accordingly, $\rho\left(\bar{\phi}\right)$ is the density of the fluid in the subdomain Ω_+ and Ω_- as given by the coarse-scale signed distance field across the boundary Γ_I.

$$\rho(\phi) = \rho\left(\bar{\phi}\right) + \left(\rho_+ - \rho_-\right)\delta_{\Gamma_I}\left(\bar{\phi}\right)\phi' \tag{3.44}$$

In this context, the densities of the two discrete phases are the lower and upper bounds on the density that depends on the signed distance field.

$$\rho_a \le \rho\left(\bar{\phi}\right) + \left(\rho_+ - \rho_-\right)\delta_{\Gamma_I}\left(\bar{\phi}\right)\phi' \le \rho_w \tag{3.45}$$

Now we look at it in the context of cut FEM where one side of Γ_I is the void. This can be realized by setting $\rho_a = \nu_a = 0$.

<u>STEP 1</u>: We first consider the (3.45) within the region $\Omega_+ = \left\{\boldsymbol{x} \in \Omega_I \mid \phi\left(\boldsymbol{x}\right) > 0\right\}$

$$\begin{aligned} & 0 \le \rho_+ + \left(\rho_+ - \rho_-\right)\delta_{\Gamma_I}\left(\bar{\phi}\right)\phi' \le \rho_w \quad \left(\rho\left(\bar{\phi}\right)\Big|_{\varepsilon\to 0} = \rho_+\right) \\ \Rightarrow \quad & -\rho_+ \le \left(\rho_+ - \rho_-\right)\delta_{\Gamma_I}\left(\bar{\phi}\right)\phi' \le \rho_w - \rho_+ \qquad \left(\text{Subtract } \rho_+\right) \\ & -\frac{\rho_+}{\rho_w} \le \operatorname{sign}\left(\rho_+ - \rho_-\right)\delta_{\Gamma_I}\left(\bar{\phi}\right)\phi' \le 1 - \frac{\rho_+}{\rho_w} \quad \left(\text{divide } \rho_w = \left|\rho_+ - \rho_-\right|\right) \end{aligned} \tag{3.46}$$

$$\left.\begin{aligned} &\text{Case 1: Fig. 2a} \quad \rho_w = \rho_+ > \rho_- = 0 \quad \Rightarrow \quad -1 \le \delta_{\Gamma_I}\left(\bar{\phi}\right)\phi' \le 0 \\ &\text{Case 2: Fig. 2b} \quad \rho_w = \rho_- > \rho_+ = 0 \quad \Rightarrow \quad 0 \le -\delta_{\Gamma_I}\left(\bar{\phi}\right)\phi' \le 1 \end{aligned}\right\} \quad \Rightarrow \quad \phi' \le 0 \quad \text{in} \quad \Omega_+$$

STEP 2: We now consider (3.45) within $\Omega_- = \{\boldsymbol{x} \in \Omega_I \,|\, \phi(\boldsymbol{x}) < 0\}$

$$
\begin{aligned}
0 \le \rho_- + (\rho_+ - \rho_-)\delta_{\Gamma_I}(\bar{\phi})\phi' \le \rho_w \quad & \left(\rho(\bar{\phi})\big|_{\varepsilon\to 0} = \rho_-\right) \\
-\rho_- \le (\rho_+ - \rho_-)\delta_{\Gamma_I}(\bar{\phi})\phi' \le \rho_w - \rho_- \quad & (\text{Subtract } \rho_-) \\
-\frac{\rho_-}{\rho_w} \le \operatorname{sign}(\rho_+ - \rho_-)\delta_{\Gamma_I}(\bar{\phi})\phi' \le 1 - \frac{\rho_-}{\rho_w} \quad & (\text{divide } \rho_w = |\rho_+ - \rho_-|)
\end{aligned}
\tag{3.47}
$$

$$
\left.
\begin{array}{ll}
\text{Case 1: Fig. 2a} & \rho_w = \rho_+ > \rho_- = 0 \quad \Rightarrow \quad 0 \le \delta_{\Gamma_I}(\bar{\phi})\phi' \le 1 \\
\text{Case 2: Fig. 2b} & \rho_w = \rho_- > \rho_+ = 0 \quad \Rightarrow \quad -1 \le -\delta_{\Gamma_I}(\bar{\phi})\phi' \le 0
\end{array}
\right\} \quad \Rightarrow \quad \phi' \ge 0 \quad \text{in} \quad \Omega_-
$$

PROPOSITION 2: Magnitude and orientation of the interface parameter:

$$
\begin{aligned}
\hat{\eta} \le 0 \quad \text{in} \quad \Omega_+ = \{\boldsymbol{x} \in \Omega_I \,|\, \phi(\boldsymbol{x}) > 0\} \\
\hat{\eta} \ge 0 \quad \text{in} \quad \Omega_- = \{\boldsymbol{x} \in \Omega_I \,|\, \phi(\boldsymbol{x}) < 0\}
\end{aligned}
\tag{3.48}
$$

PROOF: The interface parameter defined in (3.37) can be specialized to the two cases

Case 1: Figure 3.2a $\Omega_+ = \Omega_w = \{\boldsymbol{x} \in \Omega_I \,|\, \rho(\boldsymbol{x}) = \rho_w\}$ and $\Omega_- = \Omega_a = \{\boldsymbol{x} \in \Omega_I \,|\, \rho(\boldsymbol{x}) = \rho_a\}$

$$
\hat{\eta} = \begin{cases}
\rho_+(\nu_+ - \nu_-) = \cancel{\rho_a}(\nu_w - \nu_a) \approx 0 \quad \text{in} \quad \Omega_+ \\
\rho_-(\nu_+ - \nu_-) = \rho_w(\nu_w - \cancel{\nu_a}) \approx \eta_w > 0 \quad \text{in} \quad \Omega_-
\end{cases}
\tag{3.49}
$$

Case 2: Figure 3.2b $\Omega_+ = \Omega_a$ and $\Omega_- = \Omega_w$

$$
\hat{\eta} = \begin{cases}
\rho_+(\nu_+ - \nu_-) = \rho_w(\cancel{\nu_a} - \nu_w) \approx -\eta_w < 0 \quad \text{in} \quad \Omega_+ \\
\rho_-(\nu_+ - \nu_-) = \cancel{\rho_a}(\nu_a - \nu_w) \approx 0 \quad \text{in} \quad \Omega_-
\end{cases}
\tag{3.50}
$$

where ν_a and ν_w are the dynamic viscosity of air and water, respectively

PROPOSITION 3: The product $\hat{\eta}\phi' \ge 0 \quad \forall \boldsymbol{x} \in \Omega_I$

PROOF: Combining (3.40) with (3.48) we get

$$
\hat{\eta}\,\phi'\big|_{\Omega_I} = \begin{cases}
\hat{\eta}\,\phi'\big|_{\Omega_+} \ge 0 \quad \text{in} \quad \Omega_+ = \{\boldsymbol{x} \in \Omega_I \,|\, \phi(\boldsymbol{x}) > 0\} \\
\hat{\eta}\,\phi'\big|_{\Omega_-} \ge 0 \quad \text{in} \quad \Omega_- = \{\boldsymbol{x} \in \Omega_I \,|\, \phi(\boldsymbol{x}) < 0\}
\end{cases}
\tag{3.51}
$$

PROPOSITION 4: τ_{LSA} is a bounded function

As stated in the derivation of the method, the fine scales are expanded in terms of bubble functions that are nonzero on the sum of element interior and vanish on inter element boundaries. Consequently, the bubble basis functions $\varphi \in B(K)$ satisfy

$$\begin{aligned} \varphi(\boldsymbol{x}) &\geq 0 \quad \forall \boldsymbol{x} \in K \\ \varphi(\boldsymbol{x}) &= 0 \quad \forall \boldsymbol{x} \in \partial K \end{aligned} \tag{3.52}$$

where $B(K)$ is the space of bubble function defined over a generic element K in the discretized domain $\mathcal{K}$ and $\max_{x} \varphi(x) = 1$ which is the standard property associated with interpolation functions. The fine scale solution is given by equation (3.33) where the value of the unknown coefficients is obtained as a function of the chosen bubble basis function φ, the data (ρ, η, and $\boldsymbol{f}$), and the residual of the Euler-Lagrange equation of the coarse scales.

We first establish some preliminary results:

1. We define the $L_2(\Omega)$ inner product $\mathcal{V} \times \mathcal{V} \to \mathbb{R}$

$$(u, v) = \int_{\Omega} uv d\Omega \tag{3.53}$$

The $L_2(\Omega)$ norm is defined as

$$\| v \|_{0,\Omega}^2 = \int_{\Omega} v^2 d\Omega \tag{3.54}$$

2. Poincare inequality

$$\| b^e \|^2 \leq C_1(\mathcal{K}) h^2 \| \nabla b^e \|^2 \tag{3.55}$$

where $C_1 = 1/2$

3. Inverse estimate

$$\| \nabla b^e \|_K \leq C_{\text{INV}} \, h^{-1} \| b^e \|_K \tag{3.56}$$

where C_{INV} is the constant of the inverse estimate.

4. For cubic bubbles we have:

$$\int_K \varphi d\Omega = C_{1K} h_K^2 \qquad \varphi\big|_K \in B(K), \qquad K \in \mathcal{K} \tag{3.57}$$

$$\| \varphi \|_{0,K} = C_{2K} h_K^2 \qquad \varphi\big|_K \in B(K), \qquad K \in \mathcal{K} \tag{3.58}$$

$$\| \nabla \varphi \|_{0,K} = C_{3K} \qquad \varphi\big|_K \in B(K), \qquad K \in \mathcal{K} \tag{3.59}$$

where C_{1K}, C_{2K}, and C_{3K} are positive constants, independent of the element parameter h_K.

Recall the definition of τ_{LSA} in (3.34)

$$\tau_{\text{LSA}}^e = \frac{b^e\left(b^e,1\right)}{\left(\Delta t\right)^{-1}\left(b^e,b^e\right)+\left(b^e,\boldsymbol{v}\cdot\nabla b^e\right)} \tag{3.60}$$

where Δt is a small positive constant given by the CFL condition $\Delta t \le C_{FL} h/|\boldsymbol{v}|$ and C_{FL} is the Courant number that depends on the time marching scheme.

We consider the mass type term

$$\begin{aligned}(\Delta t)^{-1}(b^e,b^e) &= (\Delta t)^{-1}\| b^e \|^2 \le C_{1K} h_K^2 (\Delta t)^{-1} \| \nabla b^e \|^2 \qquad \left(\text{Poincaré Inequality}\right) \\ &\le \frac{h_K^2}{2\Delta t}\| \nabla b^e \|^2\end{aligned} \tag{3.61}$$

Step 1: τ_{LSA}^e is bounded from below.

$$\hat{\tau}_{\text{LSA}}^e = \frac{\left(b^e,1\right)}{(\Delta t)^{-1}\| b^e \|^2} \ge \frac{\left(b^e,1\right)}{\frac{h_K^2}{2\Delta t}\| \nabla b^e \|^2} \tag{3.62}$$

Employing Poincaré inequality for the integrated expression for $\tau_{\text{LSA}}^e = \int_{\Omega^e} \tau_{\text{LSA}}^e \, d\Omega$

$$\tau_{\text{LSA}}^e = \frac{\| b^e \| \| b^e \|}{\frac{h_K^2}{2\Delta t}\| \nabla b^e \|^2} \ge \frac{C_{1K} h_K^2 C_{2K} h_K^2}{\left(\frac{h_K^2}{2\Delta t}\right) C_{3K}^2} = C_A h_K^2 \Delta t \tag{3.63}$$

where $C_A = 2C_{1K}C_{2K} / C_{3K}^2$

Step 2: τ_{LSA}^e bounded from above.

$$\hat{\tau}_{\text{LSA}}^e = \frac{(b^e,1)}{(\Delta t)^{-1}\| b^e \|^2} \le \frac{(b^e,1)\Delta t}{(C_{\text{INV}}^{-1} h_K)^2 \| \nabla b^e \|^2} \tag{3.64}$$

Employing inverse estimate for the integrated τ_{LSA}^e

$$\tau^e_{\text{LSA}} \;=\; \frac{\| b^e \| \| b^e \| \Delta t}{(C^{-1}_{\text{INV}} h_K)^2 \| b^e \|^2} \;=\; \frac{C_{1K} h_K^2 C_{2K} h_K^2}{\left(C^{-1}_{\text{INV}} h_K\right)^2 C_{3K}^2} \Delta t \;\le\; C_B h_K^2 \Delta t \tag{3.65}$$

where $C_B = (C_{1K} C_{2K} / C_{3K}^2) C_{\text{INV}}^2 = 1/2\, C_A C_{\text{INV}}^2$.

From (3.63) and (3.65) we have

$$\boxed{C_A h_K^2 \Delta t \;\le\; \tau^e_{\text{LSA}} \;\le\; C_B h_K^2 \Delta t} \tag{3.66}$$

LEMMA 1: $\mathcal{B}^{\Omega_I}_{\text{VMS}}(\boldsymbol{w};\boldsymbol{w},\phi)$ is positive definite.

$$\mathcal{B}^{\Omega_I}_{\text{VMS}}(\boldsymbol{w};\boldsymbol{w},\phi) \ge C^{\Omega_I}_{\text{VMS}} \left\|\nabla \boldsymbol{w}\right\|^2_{\Omega_I} \tag{3.67}$$

where $C^{\Omega_I}_{\text{VMS}}$ is a positive constant.

PROOF:

$$\begin{aligned} \mathcal{B}^{\Omega_I}_{\text{VMS}}(\boldsymbol{w};\boldsymbol{w},\phi) &= \left(\nabla \boldsymbol{w}, 2\hat{\eta}\phi' \nabla^s \boldsymbol{w}\right)_{\Omega_I} \qquad \forall \boldsymbol{w} \in \mathcal{V} \\ &= \sum_e \left(\nabla \boldsymbol{w}, 2\hat{\eta}\phi' \nabla^s \boldsymbol{w}\right)_{\Omega^e_I} \quad \text{(taking mean}\left(\hat{\eta}\phi'\right)\text{)} \\ &\ge \left|2\hat{\eta}\phi'\right| \left\|\nabla \boldsymbol{w}\right\|^2_{\Omega_I} \qquad \text{in} \quad \Omega_I \end{aligned} \tag{3.68}$$

LEMMA 2: $\mathcal{B}^{\Gamma_I}_{\text{VMS}}(\boldsymbol{w};\boldsymbol{w},\phi)$ is positive definite.

$$\mathcal{B}^{\Gamma_I}_{\text{VMS}}(\boldsymbol{w};\boldsymbol{w},\phi) \ge C^{\Gamma_I}_{\text{VMS}} \left\|\nabla \boldsymbol{w}^{\perp}\right\|^2_{\Omega_I} \tag{3.69}$$

where $C^{\Gamma_I}_{\text{VMS}}$ is a positive constant.

PROOF:

$$\begin{aligned} \mathcal{B}^{\Gamma_I}_{\text{VMS}}(\boldsymbol{w};\boldsymbol{w},\phi) &= \left(\nabla \boldsymbol{w} \cdot \boldsymbol{n}_I, 2\hat{\eta}\phi' \nabla^s \boldsymbol{w} \cdot \boldsymbol{n}_I\right)_{\Gamma_I} \qquad \forall \boldsymbol{w} \in \mathcal{V} \\ &= \sum_i \left(\nabla \boldsymbol{w}, 2\hat{\eta}\phi' \nabla^s \boldsymbol{w}\right)_{\Gamma^i_I} \qquad \text{(taking mean}\left(\hat{\eta}\phi'\right)\text{)} \\ &\ge \left|2\hat{\eta}\phi'\right| \left\|\nabla \boldsymbol{w}^{\perp}\right\|^2_{\Gamma_I} \qquad \text{on} \quad \Gamma_I \end{aligned} \tag{3.70}$$

Consequently, both forms of interface stabilization terms derived in Section 2 subtend a normed quantity that adds to the stability of the method.

3.6. NUMERICAL TESTS

Before the presentation of the numerical results, we briefly discuss the implementation of the interfacial stabilizations in (3.36) that we derived in Section 2. In the numerical test cases we have employed a regularized Heaviside function to numerically approximate the Dirac delta function. The Heaviside function $H(\phi)$ and its regularized form $H_\varepsilon(\phi)$ are defined as follows

$$H(\phi)=\begin{cases}0 & \text{if} \quad \phi<0\\ \frac{1}{2} & \text{if} \quad \phi=0\\ 1 & \text{if} \quad \phi>0\end{cases} \qquad H_\varepsilon(\phi)=\begin{cases}0 & \text{if} \quad \phi<-\varepsilon\\ \frac{1}{2}\left(1+\frac{\phi}{\varepsilon}+\frac{1}{\pi}\sin\left(\frac{\pi\phi}{\varepsilon}\right)\right) & \text{if} \quad |\phi|\le\varepsilon\\ 1 & \text{if} \quad \phi>\varepsilon\end{cases} \tag{3.71}$$

Parameter ε is a length scale perpendicular to the interface Γ_I. In the numerical implementation, this is taken as one element diameter on either side of Γ_I. Consequently, the regularized Dirac delta function is

$$\delta_\varepsilon(\phi)=\begin{cases}0 & \text{if} \quad \phi<-\varepsilon\\ \frac{1}{2\varepsilon}+\frac{1}{2\varepsilon}\cos\left(\frac{\pi\phi}{\varepsilon}\right) & \text{if} \quad |\phi|\le\varepsilon\\ 0 & \text{if} \quad \phi>\varepsilon\end{cases} \tag{3.72}$$

One advantage of the level set method is the implicit modeling of the interface or free-surface evolution without the need of interface-conforming meshes as is the case in ALE-based methods. We first present the convergence rate studies to show the consistency and stability of the proposed stabilized weak form for the level-set equation. Then we use a widely used numerical test case to verify conservation of mass during interface evolution, and the time-dependent correction that is facilitated via the fine-scales. Therefore, we present the interface stabilized Navier-Stokes equations and carry out convergence rate study with solitary wave problem that has an exact solution. Method is then tested on harder engineering problems of dam break, and free-falling water column and the attributes of the stabilization tensor are investigated. We close the section with 3D dam-break flow to show application of the method to a problem of engineering interest.

3.6.1. Shear Flow (Vortex in a Box)

Vortex-in-a-box [123] is a common benchmark problem to evaluate the performance of numerical schemes for the level set equation. We carry out the rate of convergence study with hexahedral and tetrahedral elements, employing two time-dependent test cases. In these problems the third dimension is constrained to create plane strain conditions.

The stream function φ for the prescribed vortex velocity field defined in a 2D unit square $\Omega = [0,1] \times [0,1]$ is given as

$$\varphi(x, y, t) = \frac{1}{\pi} \cos\left(\frac{\pi t}{T}\right) \sin^2(\pi x) \sin^2(\pi y) \tag{3.73}$$

This velocity field produced by (3.73) is divergence free. The zero contour of ϕ_0 is a circular interface located at (0.5, 0.75) with a radius of 0.15. The time-dependent VMS stabilized weak form in (3.35) is applied with backward Euler scheme as the time integrator. The $\Delta t / \Delta x$ ratio in the CFL number is set equal to 1, and the time duration is $T = 4$. A smooth initial condition is employed in this test case.

$$\phi_0(x, y) = \exp\left(-(x - 0.5)^2 - (y - 0.75)^2\right) - \exp\left(-0.15^2\right) \tag{3.74}$$

Figure 3.3a shows the planar view and warped view of the level set field and the zero intercept defines the object at $t = 0$. The rotational flow stretches the initial circular interface, and Figure 3.3b shows the planar view and warped profile for the computed level set field at $t = T / 2$. The flow is then reversed from time $T / 2$ to T. The computed profile is employed to evaluate the error in the scalar field with respect to the initial condition. The L_∞ norm of error between the computed solution $\phi(x, y, T)$ and the initial condition $\phi_0(x, y)$ is evaluated and linear rate of convergence is attained for both B8 and T4 elements, as shown in Figure 3.4. Nave *et al.* [123] show a cubic convergence rate in the L_∞ norm using Hermite cubic interpolation functions for this problem.

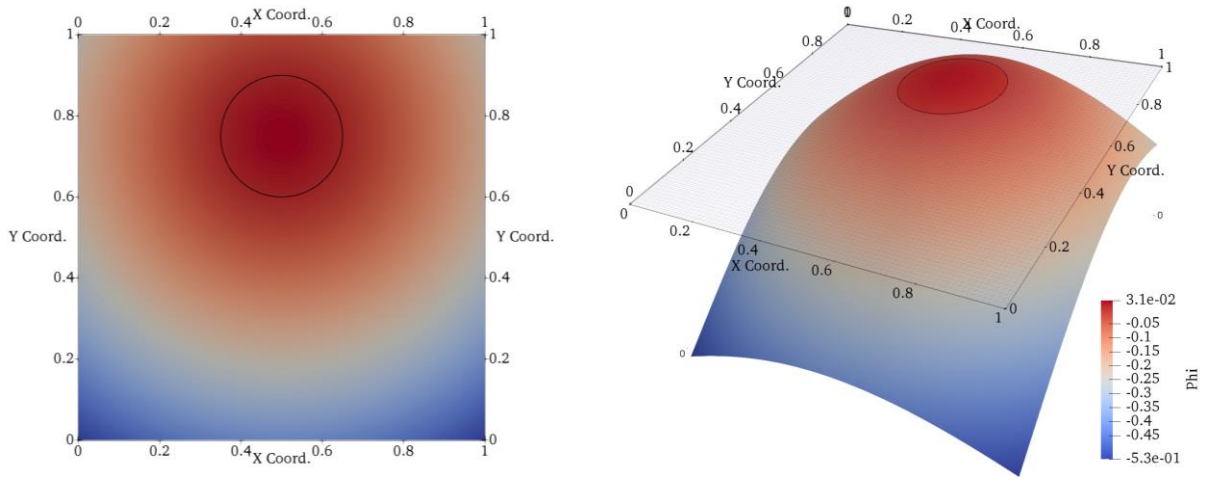

(a) Interface location and warped scalar field at t = 0s

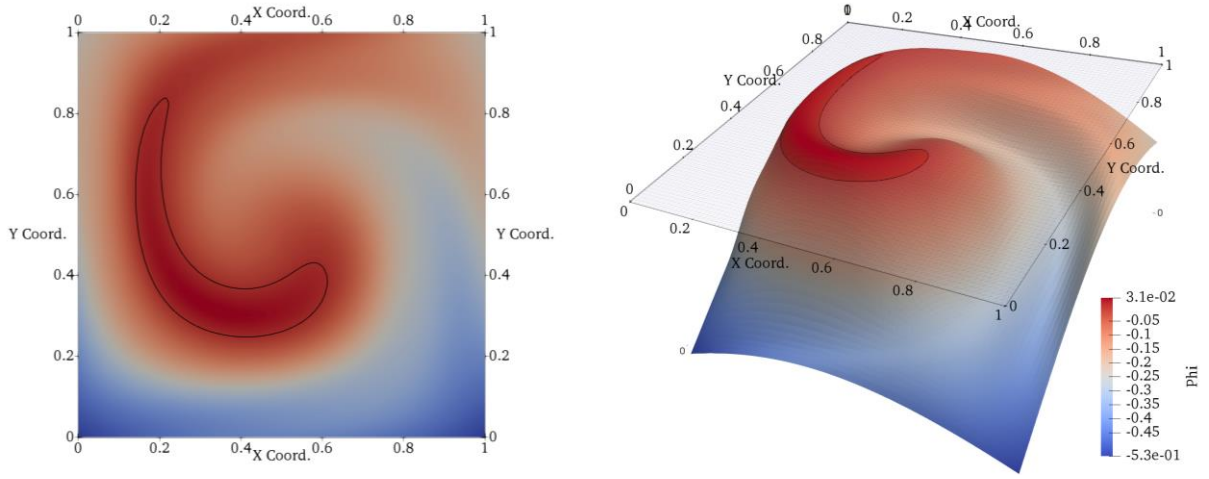

(b) Interface location and warped scalar field at t = 2s

Figure 3.3 Interface location at initial and intermediate stages of vortex-in-a-box test

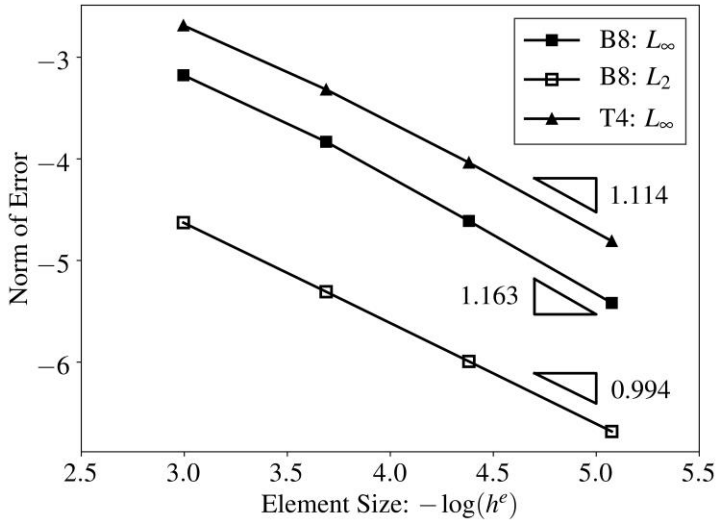

Figure 3.4 Convergence rates for uniform meshes with linear 3D elements

3.6.2. Shear Flow Reversal

This test case is a continuation of the problem presented in Sec 3.6.1. The circular interface is rotated around 2.25 times in a total time $T/2=4$. Subsequently, from $T/2$ to $T=8$, the vortex flow is reversed to bring the vortex back to its initial location. To check proposed stabilized weak form of level-set advection equation, re-initialization process or mass correction are not invoked. This test case investigates the effects of two time integration methods employing two consecutive meshes, i.e.: (i) 128×128 B8 elements with backward Euler method; (ii) 128×128 B8 elements with generalized alpha method; and (iii) 256×256 B8 elements with the generalized alpha method. The time increment in the first two cases is set equal to 0.01s, while it is 0.005s in the third case to maintain the CFL number. The location of the interface for all three cases at $T/2=4$ is shown in Figure 3.5a. Figure 3.5b shows the final shape of the interface which is compared with the exact solution given by the initial state. In the case with finer mesh (256×256), the numerical solution (blue line) is very close to the exact solution (black line). As indicated in Section 3, the time-dependent fine scales recover the errors induced due to limited mesh resolution, truncated interpolation space and the order of accuracy of the time integrator employed for the resolved scale. Such improvements in the accuracy of capturing the interface also contribute to the

reduction in mass loss during temporal evolution. In Figure 3.6, we plot the history of normalized mass (volume) of the region where signed distance field is positive. As noted in Herrmann [61], the standard level set method shows more than 30% mass loss on a 128×128 mesh. Desjardins *et al.* [41] show a level-set method together with a mass conservation algorithm that uses 5th order spatial interpolation scheme (HOUC5) and 2nd order time integrator (Crank-Nicolson) on a 128×128 mesh, and it still has 4% variation in mass. In our method, the case of 128×128 linear elements with the generalized alpha method results in mass change that is less than 5%. With a finer mesh 256×256, the mass loss in our method reduces to under 1%. We wish to point out that both test cases in the present work are carried out with linear elements without the re-initialization process and without any mass correction algorithm. These results can be further improved by *p*- and *h*- refinements and by using high-order time marching schemes.

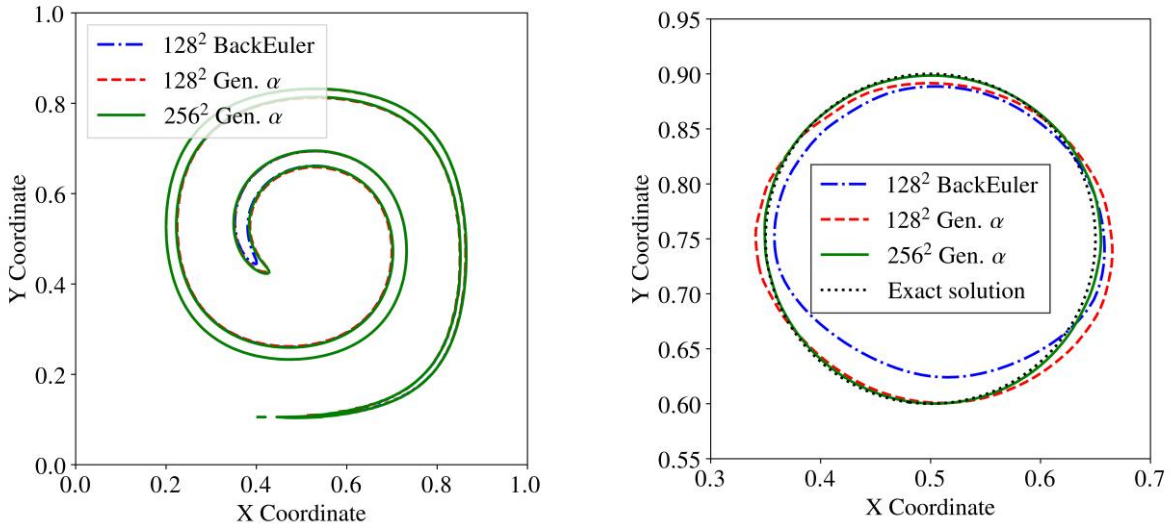

(a) Interface location at t = 4s

(b) Interface location at t = 8s

Figure 3.5 Comparative study: Location of the interface for shear flow test. Black: exact solution, Blue: time-dependent VMS (256×256, generalized α), Red: time-dependent VMS (128×128, generalized α), Green: time-dependent VMS (128×128, backward Euler)

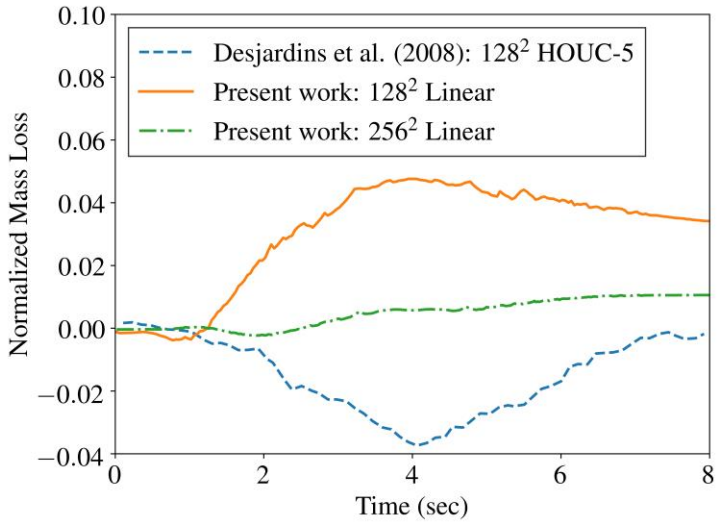

Figure 3.6 Time history of normalized mass (volume) loss in shear flow via the proposed stabilized method

3.6.3. Travelling of Solitary Wave

The test case is the classic free-surface flow problem involving propagation of a 2D solitary wave. A schematic description of the problem is shown in Figure 3.7.

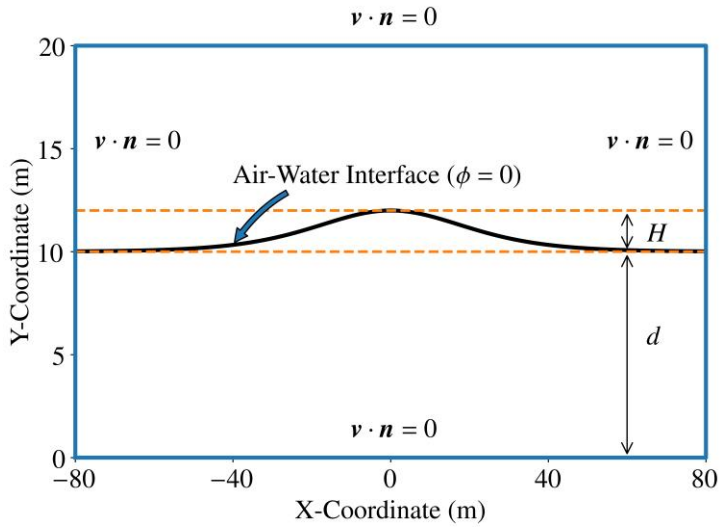

Figure 3.7 Schematics of the two-dimensional travelling solitary wave (units: m)

The initial velocity and location of the air-water interface is set according to the second order analytical approximation by Laitone [90], wherein the 2D velocity field (v_1, v_2) and height of the air-water interfaces $\eta(x)$ are given as follows

$$
\begin{aligned}
v_1 &= \sqrt{gd}\,\frac{H}{d}\operatorname{sech}^2\left(\sqrt{\frac{3H}{4d^3}}(x-ct)\right) \\
v_2 &= \sqrt{3gd}\left(\frac{H}{d}\right)^{3/2}\left(\frac{y}{d}\right)\operatorname{sech}^2\left(\sqrt{\frac{3H}{4d^3}}(x-ct)\right)\tanh\left(\sqrt{\frac{3H}{4d^3}}(x-ct)\right) \\
\eta &= d + H\operatorname{sech}^2\left(\sqrt{\frac{3H}{4d^3}}(x-ct)\right) \qquad c = \sqrt{gd\left(1+\frac{H}{2d}\right)}
\end{aligned}
\tag{3.75}
$$

The maximum amplitude of the solitary wave is $H = 2$, the depth of the still water body $d = 10$, the gravitational acceleration $g = 9.8$, and c is the speed of wave propagation. All parameters are in SI units. The size of the computational domain is $[-8d, 8d]\times[0, 2d]$ to minimize the effect of truncated left and right boundary on the solitary wave. The domain Ω is subdivided by the interface Γ_I into water-subdomain $\Omega_w = \{(x,y) \mid y < \eta(x)\}$ with density $1000\,\text{kg/m}^3$ and dynamic viscosity $1\times10^{-3}\,\text{Pa}\cdot\text{s}$, and air-subdomain $\Omega_a = \{(x,y) \mid y \geq \eta(x)\}$ with density $1\,\text{kg/m}^3$ and dynamic viscosity $1\times10^{-4}\,\text{Pa}\cdot\text{s}$. Slip boundary conditions are applied at all four boundaries of the computational domain. Convergence rate test employs four structured hierarchical meshes comprised of linear quadrilateral elements: 10×10, 20×20, 40×40, 80×80. A finer mesh with 160×160 elements is used for generating the reference solution. All test cases are run for 10 time-steps with a uniform time increment $0.01\,\text{s}$, which ensures a low CFL number for all the meshes to eliminate the accumulation of error from the time marching scheme. The L_2 norm of the error in the free-surface profile is defined as:

$$
|e|_2 = \sqrt{\int_{-8d}^{8d}\left(\eta^h(x) - \eta^{\text{exact}}(x)\right)^2 dx} \tag{3.76}
$$

A nearly optimal convergence rate is attained in this test as shown in Figure 3.8.

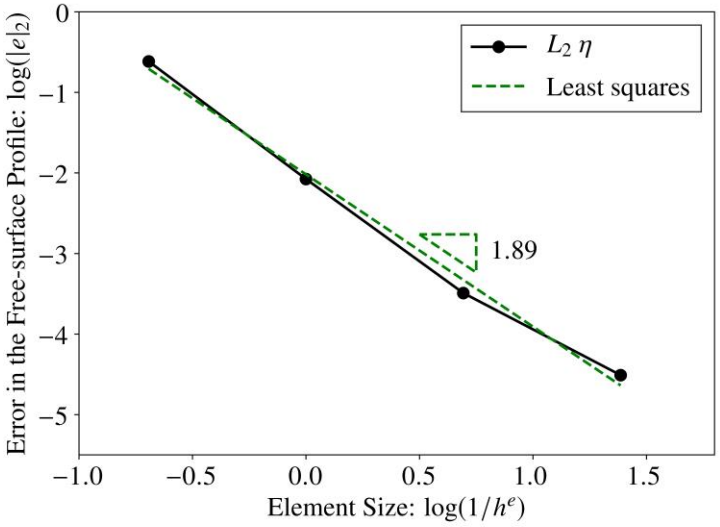

Figure 3.8. Spatial convergence of the travelling solitary wave

3.6.4. Free-Surface Sloshing Problem

This test case investigates the coupled response of the governing system of equations for the flow physics and the level-set method for the free-surface evolution. Since analytical solution is available for this 2D sloshing problem it serves as a good test case to numerically establish the consistency of the method and evaluate its accuracy for long-time simulations. The initial profile of the free-surface elevation is given by the following function.

$$\eta_0 = a\cos\left(\frac{2\pi}{W}\left(x+\frac{W}{2}\right)\right) \tag{3.77}$$

where $W=1$ is the width of the tank, and $a=0.01$ is the initial wave amplitude. A schematic description of the problem is presented in Figure 3.9.

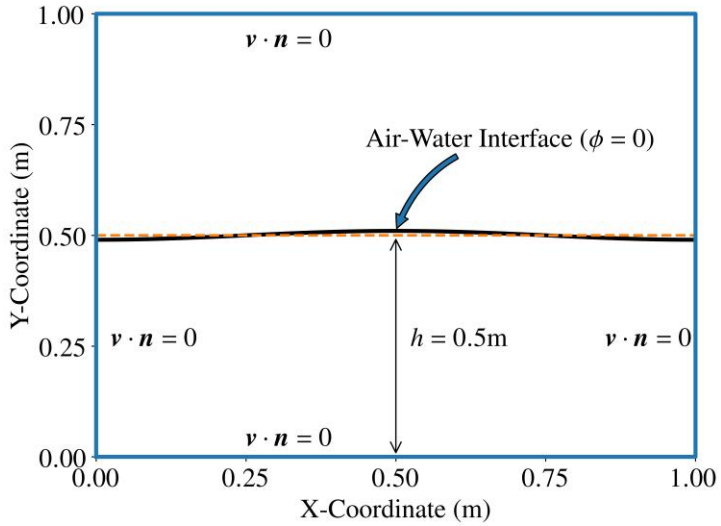

Figure 3.9 Schematics of the two-dimensional free sloshing problem (units: m)

The depth of liquid in the tank is $h = 0.5\,\mathrm{m}$ and the Reynolds number $\mathrm{Re} = h\sqrt{gh}/\nu$ is set equal to 100, 200 and 400. A relatively coarse mesh that is comprised of 40×52 elements and a time increment $\Delta t = 0.001s$ is used for all the three test cases. Each simulation is stopped when it reaches a non-dimensional time $t^* = t\sqrt{g/h} = 20$. The comparison of the normalized elevation of free-surface along the left edge with the analytical solution provided in [164] is shown in Figure 3.10. The amplitude of the damped periodic behavior of the analytical solution is accurately tracked by the numerical method for all the Reynolds numbers as shown in Figure 3.10. Only a small phase lag is observed after several cycles, which is attributed to the accumulation of error in the time marching scheme.

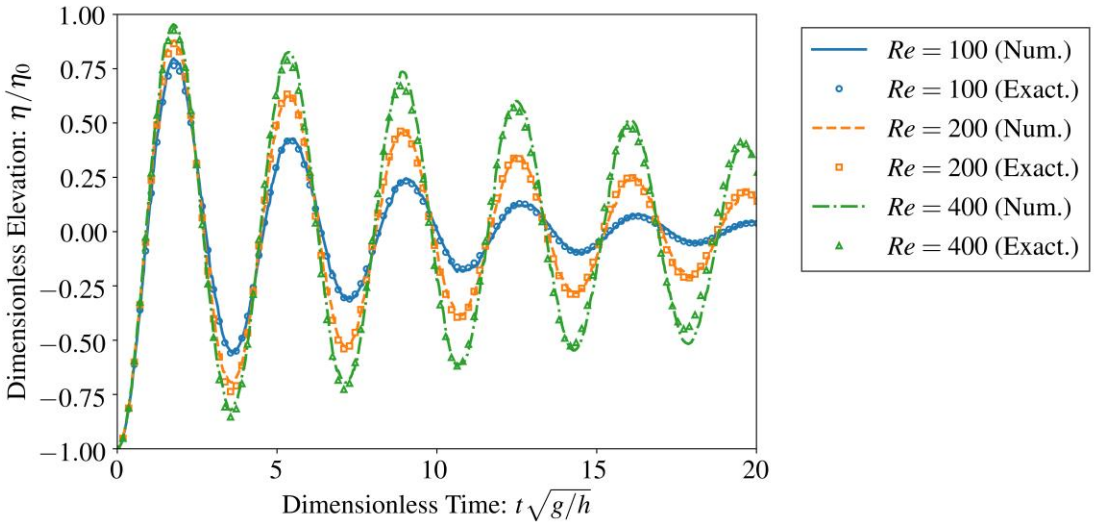

Figure 3.10 Time history of the normalized elevation of the liquid along the left edge: numerical and analytical results

3.6.5. Dam-Break Flow (2D)

The collapse of a water column in a tank is a widely-used benchmark problem to verify numerical methods for free-surface evolution because of the availability of experimental data [89,101]. A water column of height $2a$ is instantly released in a tank. It collapses under the effect of gravity and flows towards the opposite wall of the tank. The geometric description of this problem is shown in Figure 3.11. The computational domain is a box of dimensions $4a \times a \times 2.4a$, where a is a length parameter taken as a = 0.146m. The water column has dimensions $a \times a \times 2a$. The density of water is 1000 kg/m^3 and that of the air is 1 kg/m^3. The dynamic viscosity of water is 1.0×10^{-3} Pa·s and for air it is 1.0×10^{-5} Pa·s.

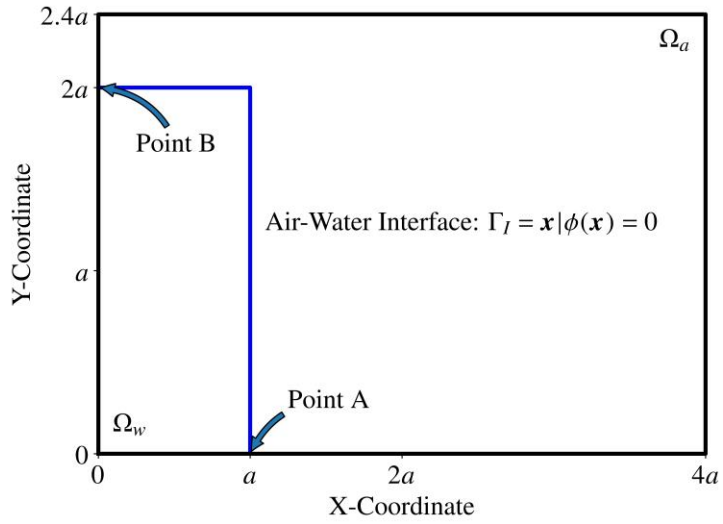

Figure 3.11 Two-dimensional dam-break problem

Because of the rapid change in the surface profile and large motion of the water column, all facets of the algorithm are invoked, i.e., the stabilized method for the two fluids, the time-dependent level-set method, and SUPG stabilization of time-dependent Eikonal equation. The mass loss from the proposed stabilized method for the level-set advection equation is very small and therefore mass conservation algorithm is not activated in this test case. In this sense this problem serves as a good test case to investigate the robustness of the method.

3.6.5.1. Boundness of τ and stability of the interfaces

We first present the numerical study of effectiveness of the proposed interfacial stabilization term and the boundness of stabilization parameter τ_e that has been analytically established in Sec. 4. Following the problem settings discussed above, two simulations are carried out employing a 40×20 mesh of linear elements. One simulation is with the interface stabilization term and the second one is without it. Figure 3.12a shows the free surface profile at time t = 0.19s for the case where interface stabilization is not invoked and numerical instability at the interface triggers non-physical surface profile. However, as the interface stabilization term is activated, a stable interface evolution can clearly be seen in Figure 3.12b.

In addition, Figure 3.12b also marks the narrow band around the interface where this term is active, and the edges of the band also can be seen to traverse through the elements, as does the interface.

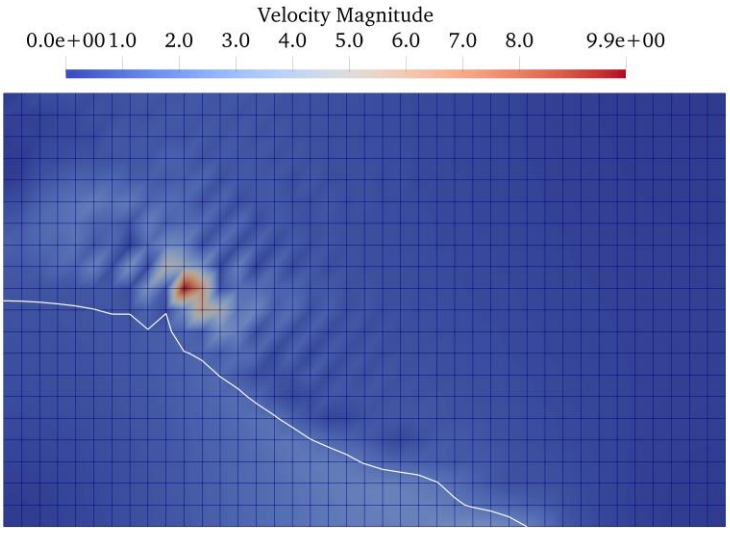

(a)

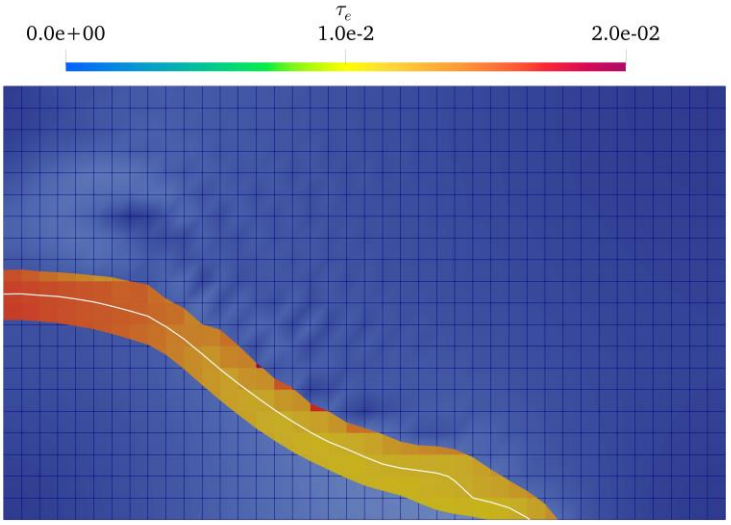

(b)

Figure 3.12 Interface location (white), velocity distribution and active region of interfacial stabilization term at t = 0.19s: (a) without interfacial stabilization and (b) with interfacial stabilization

To numerically verify the boundness of the stabilization parameter, in Figure 3.13 we plotted the value of τ^e_{LSA} in terms of the magnitude of velocity at the center of the element. Figure 14 presents the histograms of τ^e_{LSA} at various of time points during the simulation. As time evolves and the entire system

gets accelerated by the gravitational force, the distribution of the stabilization tensor also evolves into a Gaussian distribution. It is important to note that all through the simulation, element-wise constant τ^e_{LSA} is positive and it stays bounded.

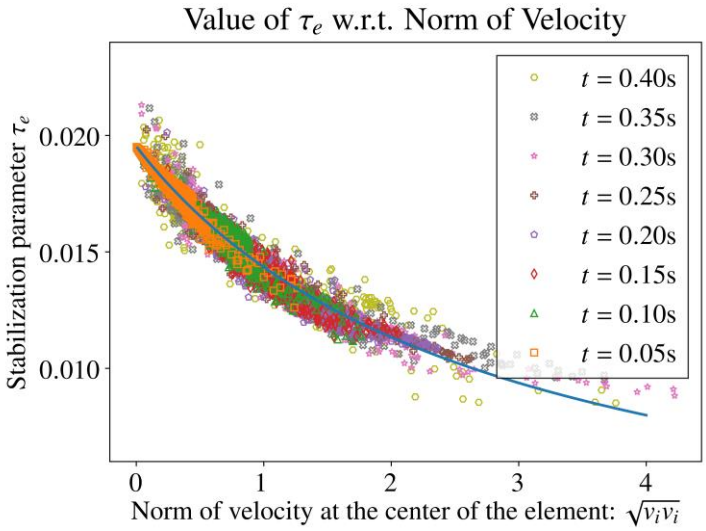

Figure 3.13 Stabilization tensor vs. norm of velocity and its histograms

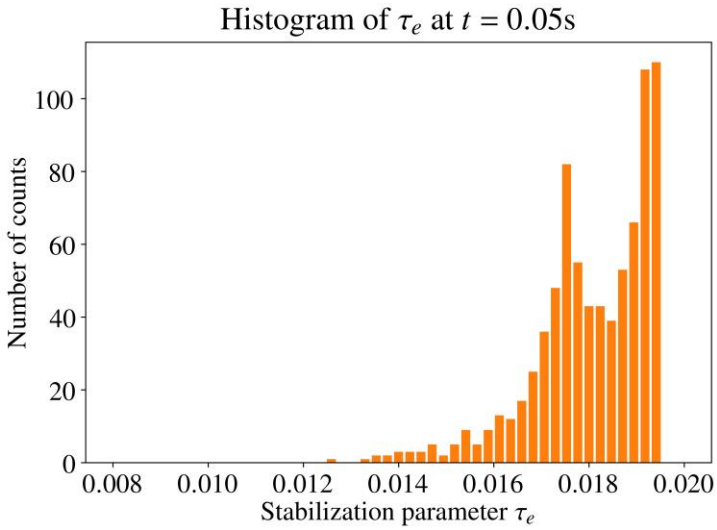

Figure 3.14 Histograms of stabilization tensor

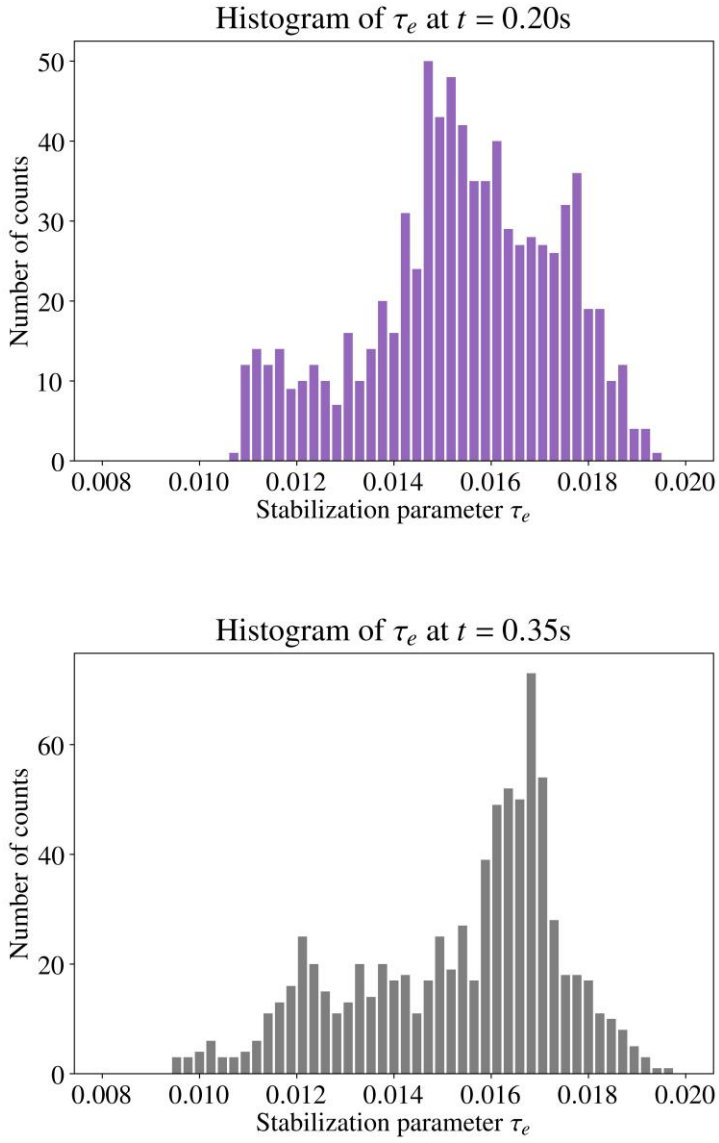

Figure 3.14 (cont.)

3.6.5.2. Validation of the evolution of free-surface profile

We now test the two versions of the formulation; one in which a term associated with *div*-stabilization on the interior of the elements is added in the entire domain, and this test case is simulated with an 80×40 mesh. The second version of the formulation does not invoke *div*-stabilization term and rather employs the variationally derived ghost-penalty terms that are active only in the elements that are traversed by the interface. This simulation is carried out with a 40×20 mesh. It is interesting to note that

even though this mesh is considerably cruder, the numerical solution from interface stabilization method compares very well with the numerical data published in [82]. In both the cases the time increment Δt corresponding to the two meshes is adjusted to maintain the same CFL number across both the simulations. Both simulations is stopped at t = 0.4s when the front of the interface reaches the upper right corner. Although the top of the tank in the experimental setup is open, for numerical simulations the top edge of the mesh becomes an artificial edge of the computational domain for the two-phase flow.

We keep track of the motion of point A that lies at the toe of the water column and slides along the floor of the tank, and point B that is at the top of the water column and slides down along the left wall of the tank. The location of both points A and B is normalized with the characteristic length a and the simulation time is normalized by characteristic time $\sqrt{2g/a}$ to eliminate the dimensional effects. Figure 3.15a shows the sliding motion of point A in terms of dimensionless length traversed versus the dimensionless time. Likewise Figure 3.15b shows the time evolution of the sliding motion of point B along the left wall. In both the cases, good agreement is attained with the published experimental [89,101] and simulated data [43,82].

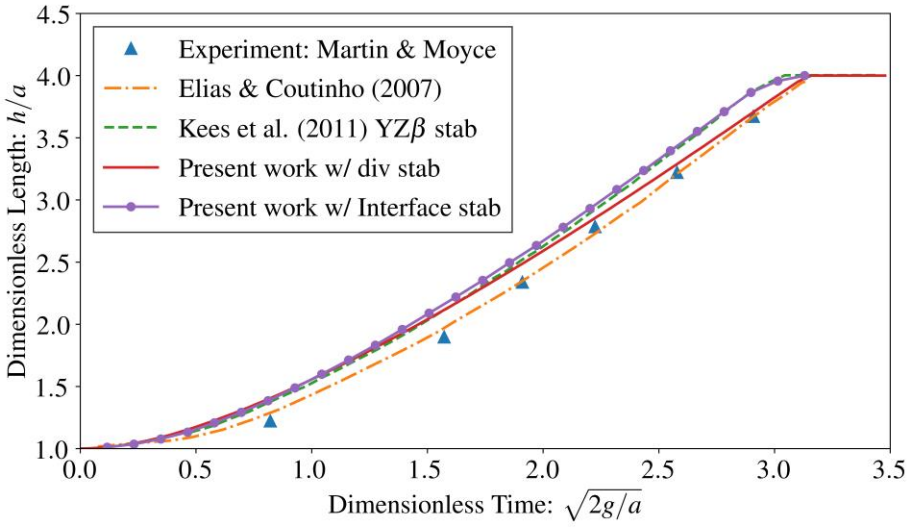

(a) Time evolution of point A at the toe of the advancing column

Figure 3.15 Two-dimensional dam-break flow: location of water front vs. time

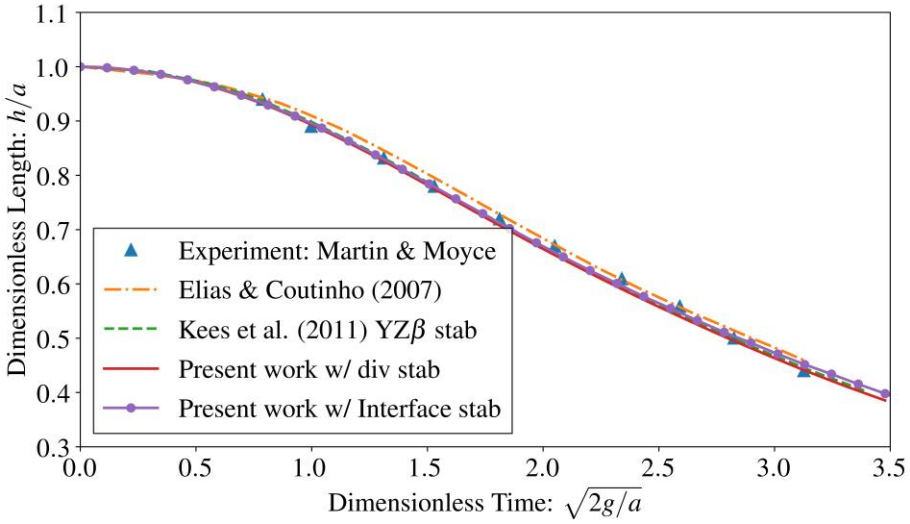

(b) Time evolution of point B collapsing along the left wall

Figure 3.15 (cont.)

3.6.6. Free Overfall Under the Effect of Gravity

This test case investigates interfacial stability of an open channel flow that evolves into a freely falling water column under the effect of gravity. The schematic diagram of the test problem is represented in Figure 3.16. The Weber number in this test problem is greater than 1.5 and therefore the influence of surface tension is negligible. The channel has a width of 0.1m and a length of 0.3m, while the dimension of the rectangular domain is 0.5m × 0.4m. The domain is discretized with a structured mesh comprising 4600 bilinear elements. The size of element is 0.01m × 0.005m. A uniformly distributed inflow velocity field $\boldsymbol{v} = [v_x, 0]$ m/s is prescribed at the left boundary, and open boundary condition is set at the bottom of the domain which also serves as the outflow boundary. Except for the inflow and outflow boundaries, slip boundary conditions are applied at all the other surfaces. The domain is initially filled with air and a layer of water with depth of $Y_n^* = 0.075$m is injected in the domain. The location of air-water interface at the inflow boundary is marked by the signed distance field and it is held fixed, thereby splitting the inflow into air and water inflow region, as shown in Figure 3.16.

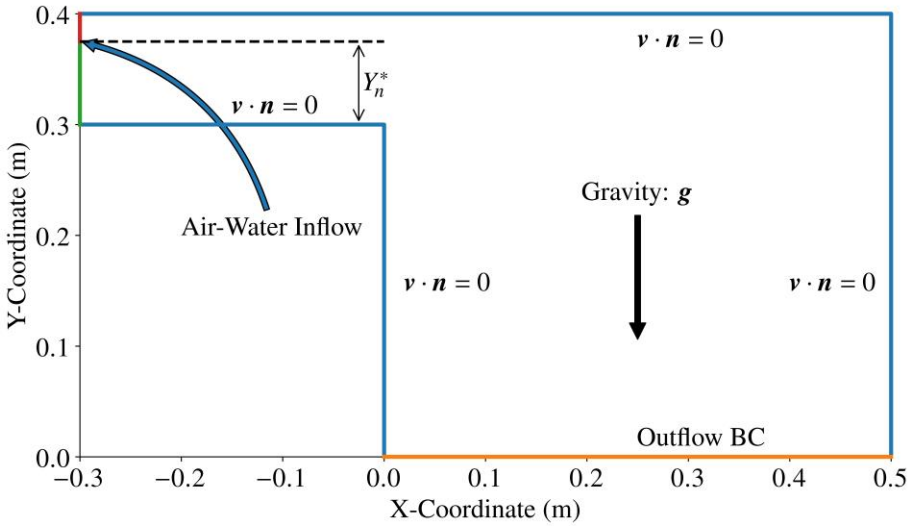

Figure 3.16 Schematic diagram of the free overfall problem (units: m)

A non-dimensional depth Y_n is used to quantify the problem through the critical depth Y_c^* and the definitions are as follows,

$$Y_n = \frac{Y_n^*}{Y_c^*} \quad \text{and} \quad Y_c^* = \sqrt[3]{\left(v_x Y_n^*\right)^2 / g} \tag{3.78}$$

Three test cases with different Y_n (1.0, 0.68 and 0.49) are simulated using the same mesh and the corresponding inflow velocity v_x is calculated via (3.78) for a fixed value of $Y_n^* = 0.075$. According to the reported work [100], $Y_n = 1.0$ results in a subcritical state and the other two choices of Y_n are supercritical states.

We first investigate the subcritical case with $Y_n = 1.0$. Figure 3.17 shows the air-water interface, the pressure distribution in the water body and streamlines for the entire domain that is colored by the magnitude of vorticity at various time points. The simulation is continued until the system reaches a statistically steady-state. It is important to note that the system would not reach an absolute steady state due to the Rayleigh-Taylor instability that can arise because of the discrete density jump across the interface. In Figure 3.18, we compare the statistical steady-state air-water interface with the reported experimental data [100] and numerical results reported in [8] that employ an adaptive mesh technique

with 33,301 triangular elements. Despite a relatively crude spatial discretization the computed free surface profile with our method compares well with the experimental data and the numerical reference obtained on much finer mesh resolutions.

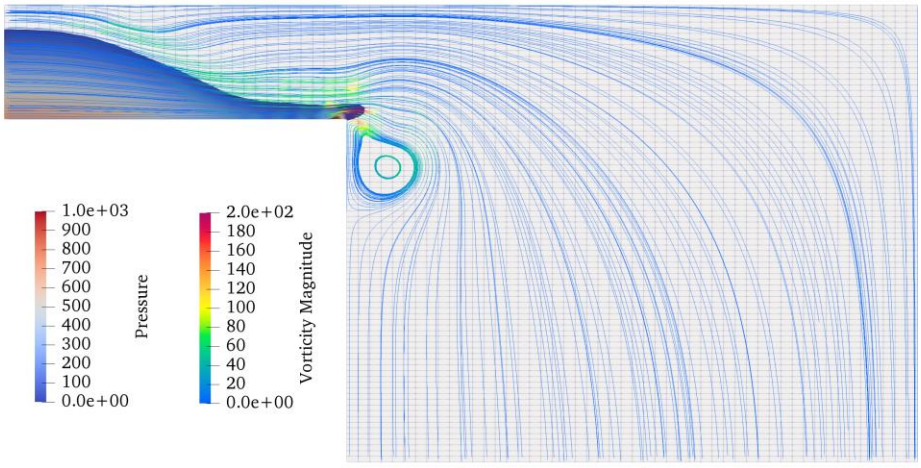

(a) t = 0.2s

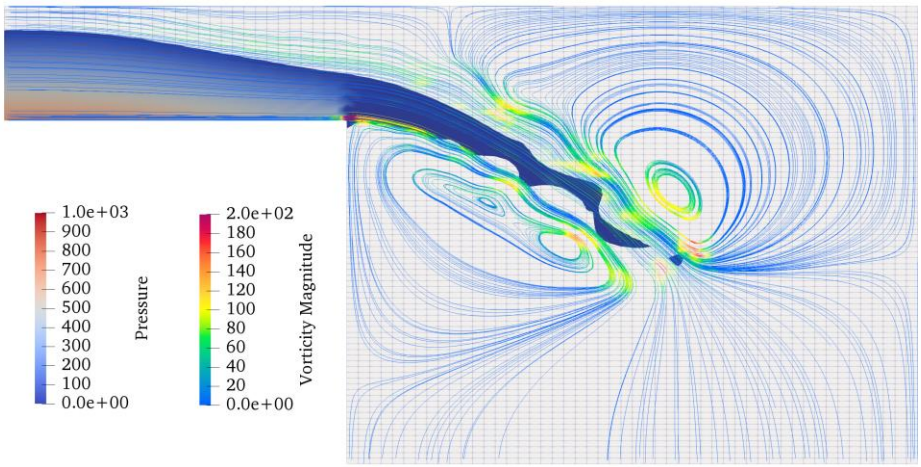

(b) t = 0.4s

Figure 3.17 Free overfall: air-water interface, pressure distribution, streamlines and magnitude of vorticity at various time points: (a) t = 0.2s, (b) t = 0.4s, (c) t = 0.6s and (d) t = 0.8s

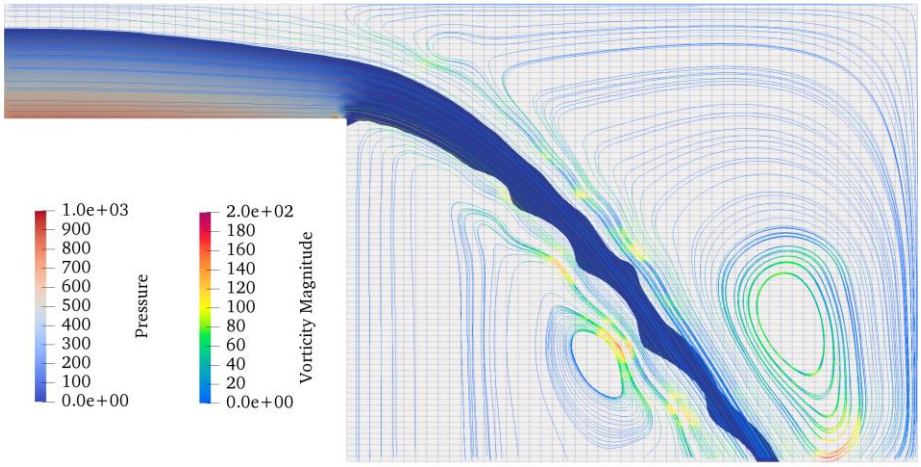

(c) t = 0.6s

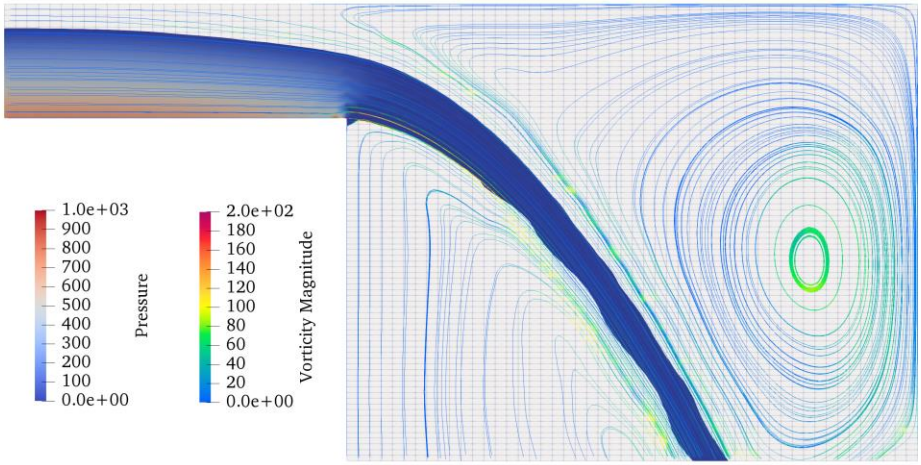

(d) t = 0.8s

Figure 3.17 (cont.)

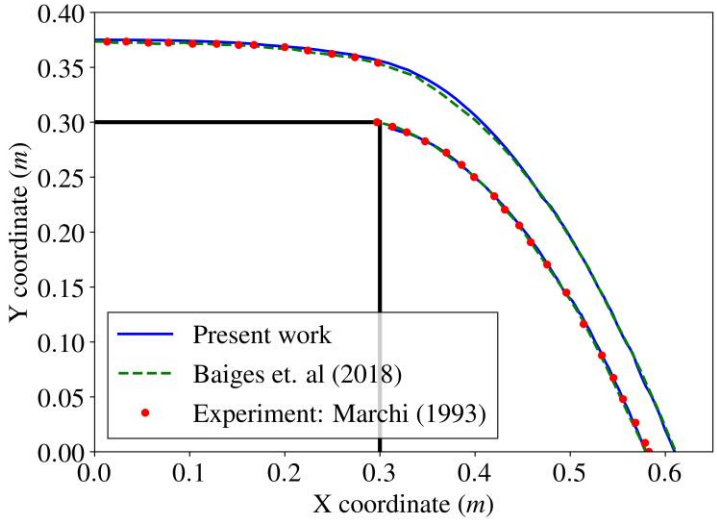

Figure 3.18 Comparison of the air-water interface profiles

We next focus on the supercritical cases with $Y_n = 0.68$ and $Y_n = 0.49$. We compare the statistical steady-state air-water interface profile from our simulation with the experimental data reported in [100]. Figure 3.19(a, b) shows the top and bottom air-water interface profiles and a good comparison with the experimental data is attained.

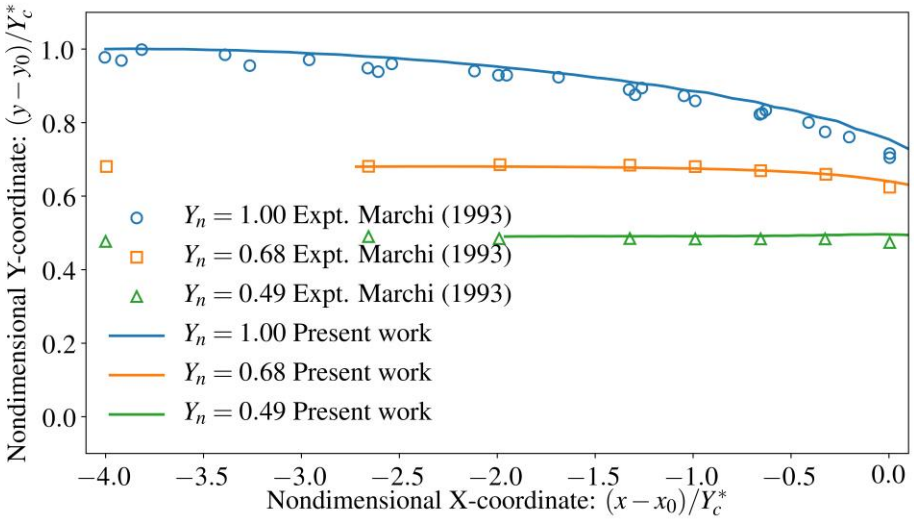

Figure 3.19 Comparison of open channel and lower air-water interface with various non-dimensional depths Y_n

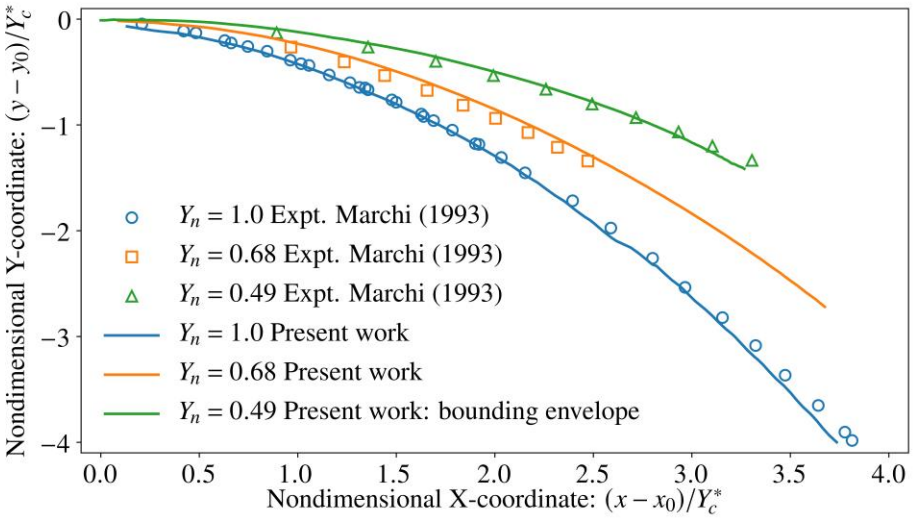

Figure 3.19 (cont.)

For the supercritical case with $Y_n = 0.49$, due to the larger inflow velocity, the lower air-water interface does not reach a stable state as is the situation in the other two cases. Rather the typical Kelvin-Helmholtz interfacial instability arises along the lower air-water interface and can be seen in Figure 3.20. In addition, Figure 3.20 also shows the Q-criterion color contours that show the physical instability along the lower air-water interface. The bounding lines show good agreement with the experimental results from Figure 3.20.

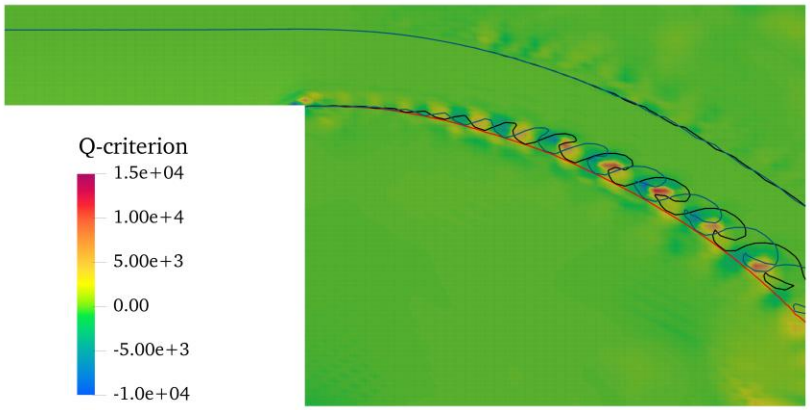

Figure 3.20 Instantaneous lower profile and enveloping line of supercritical case $Y_n = 0.49$

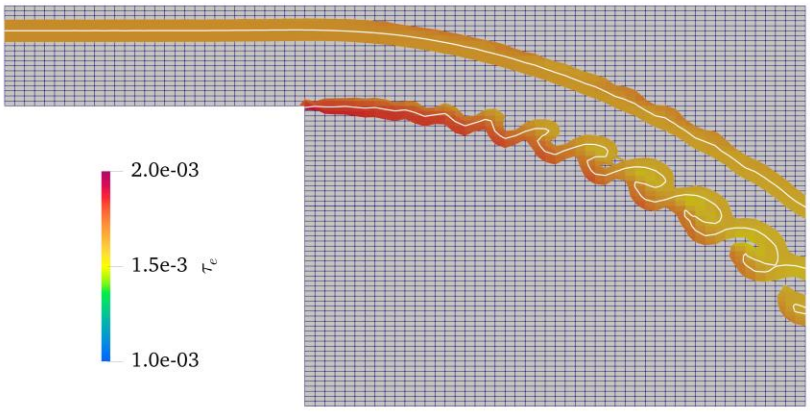

Figure 3.20 (cont.)

3.6.7. Three-dimensional Dam-break Flow with an Obstacle

This test case investigates the proposed method on 3D two-phase flows with rapidly evolving interfaces. The computational domain has dimensions $3.22\,\mathrm{m} \times 1.0\,\mathrm{m} \times 1.0\,\mathrm{m}$ in X, Y and Z direction, respectively. An obstacle of dimension $0.161\,\mathrm{m} \times 0.161\,\mathrm{m} \times 0.403\,\mathrm{m}$ is placed at $x = 2.315\,\mathrm{m}$ from the left end ($x = 0$) and it lies symmetric in the spanwise direction, as shown in Figure 3.21. We have employed 8-node brick elements for both the Navier-Stokes equations as well as the time-dependent level set equation. Numerical quadrature of sufficiently high order is used to evaluate all integrals. In 3D the air-water interface is a 2D surface that is invariably quite complex as shown in Figure 3.22. Although the geometry and the initial conditions for the problem are symmetric, due to the highly nonlinear nature of the flow physics that is further compounded by the very erratic free surface evolution, the discrete system is not symmetric. This non-symmetry is enhances as the advancing front hits the obstacle thereby making the subsequent flow further non-symmetric. Consequently, the computed interface or zero iso-surface of the level set is not uniformly connected, as it is at the start of the problem, and there is propensity for deviation from the strict definition of the signed distance field. This requires using the Eikonal equation to reinitialize the signed distance function which has also been implemented using 8-node brick elements.

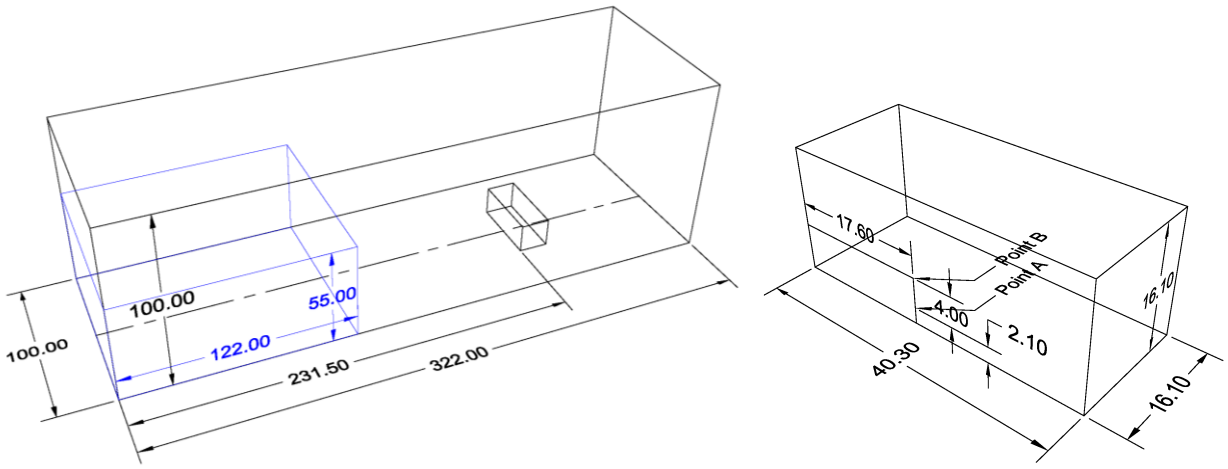

Figure 3.21 Schematics of the three-dimensional dam-break problem (units: cm)

To solve this problem, we generated a structured mesh with resolution of $64\times32\times32$ hexahedral elements. The obstacle is comprised of $3\times12\times5$ elements that are removed from the system. Figure 3.22 shows the 3D contour plots of the free surface evolution at different time points, and they are color coded with the pressure field. The advancing wave hits the obstacle at around 0.5 sec, giving rise to rapid change in the elevation of the free surface. Very intricate free surface elevation patterns can be seen with water jumping over the obstacle, followed by the merging of the two advancing fronts around the obstacle as shown in Figure 3.22a to Figure 3.22c. After hitting the right wall the reflected wave travels back and the advancing front can be seen in Figure 3.22d and Figure 3.22e. The pressure is high when the wave hits the obstacle and the distribution of pressure at the obstacle as well as at the right wall can be seen in Figure 3.23a and Figure 3.23b. From these plots we see that the right wall has higher wall normal pressure than even the obstacle. This is attributed to the momentum gained by the falling water column as it jumps over the obstacle before it hits the wall.

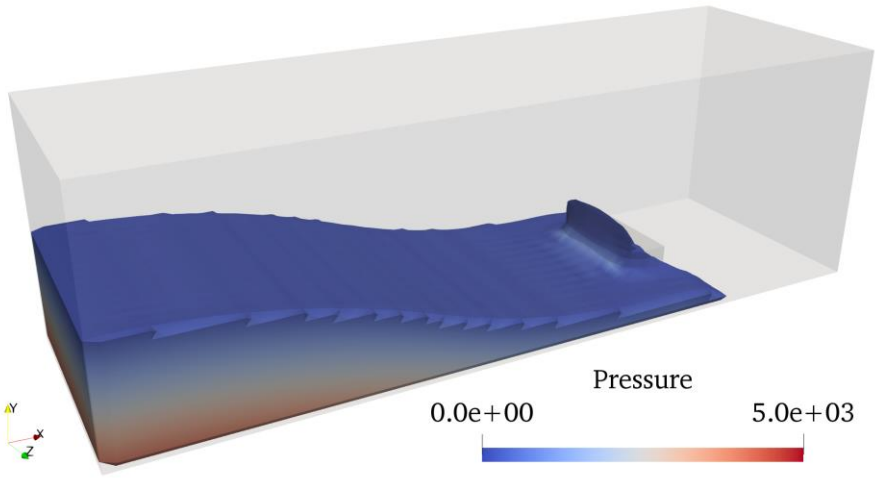

(a) t = 0.5s

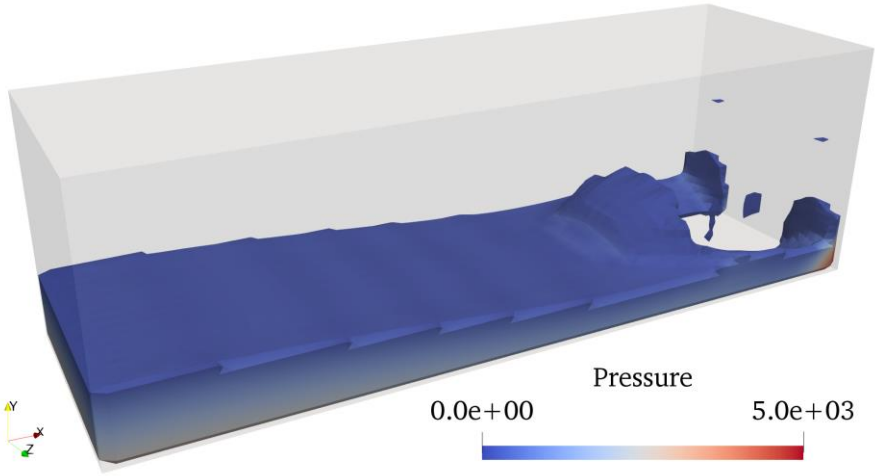

(b) t = 1.0s

Figure 3.22 Three-dimensional dam-break flows with obstacle: Interface location

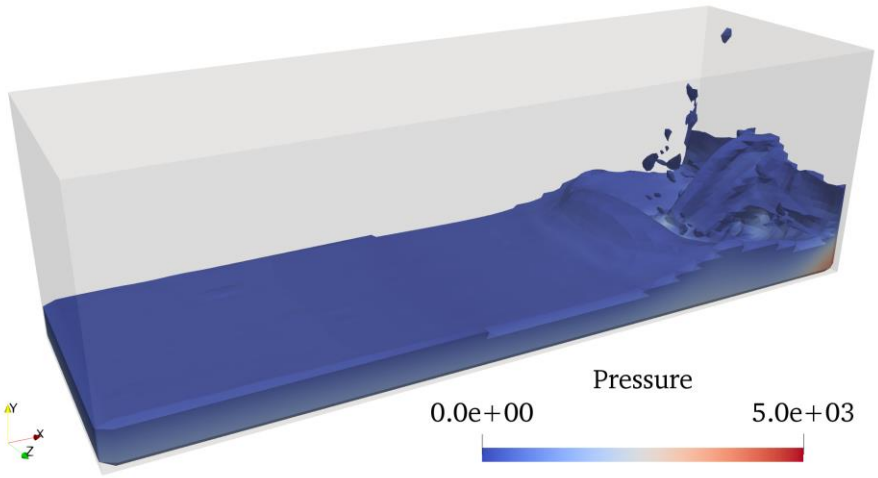

(c) t = 1.5s

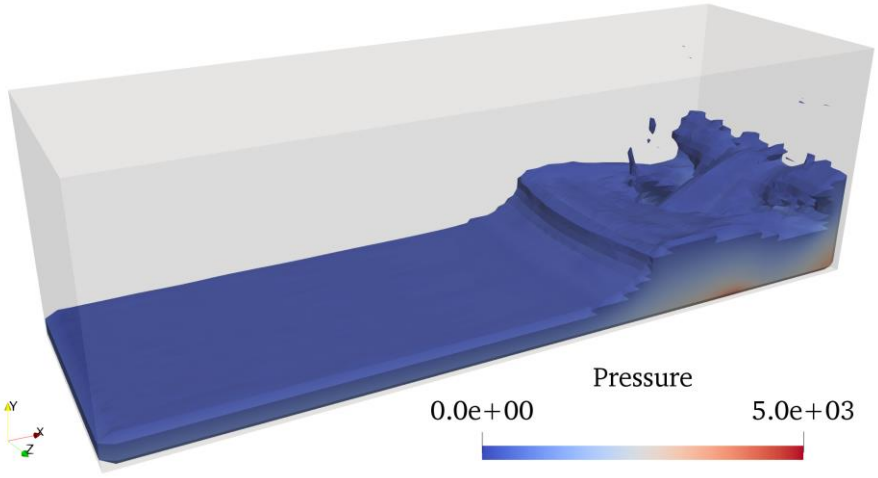

(d) t = 2.0s

Figure 3.22 (cont.)

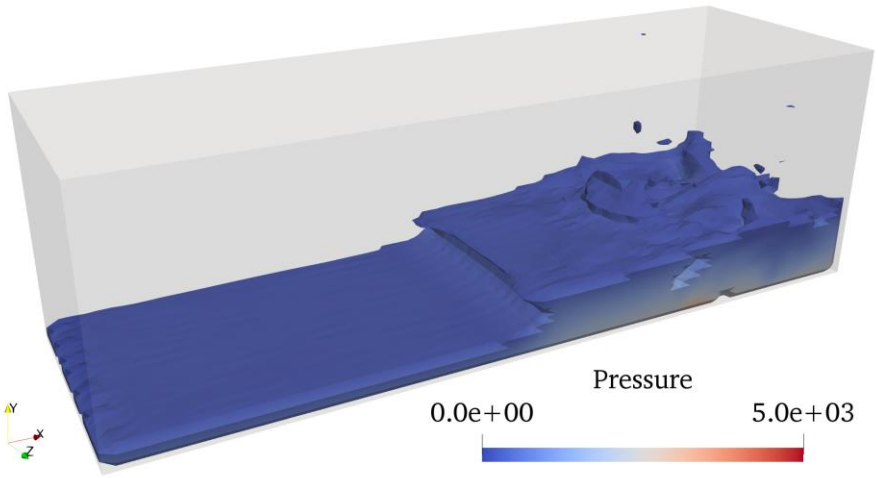

(e) t = 2.5s

Figure 3.22 (cont.)

To quantify the numerical results for the 3D dam-break flow, we present the time history of pressure at points A and B located on the obstacle (see Figure 3.24) and the time history of water height at two locations in the domain with coordinates (0.582,0.5,0) and (1.732,0.5,0) (see Figure 3.25). Once again we compare our results with experimental data [87] and reported numerical results [82,96]. Our numerical simulation accurately captures the time history of pressure at both the locations, and a good correlation is attained with the reported experimental and numerical data. The numerical results show a higher-pressure pulse at around 0.4 second when the water front hits the obstacles, as compared to the reported experimental data. This is potentially due to the reason that the obstacle is modeled as a rigid body by prescribing Dirichlet boundary conditions on the surface of the obstacle, thus enhancing the incompressibility effects in the flow.

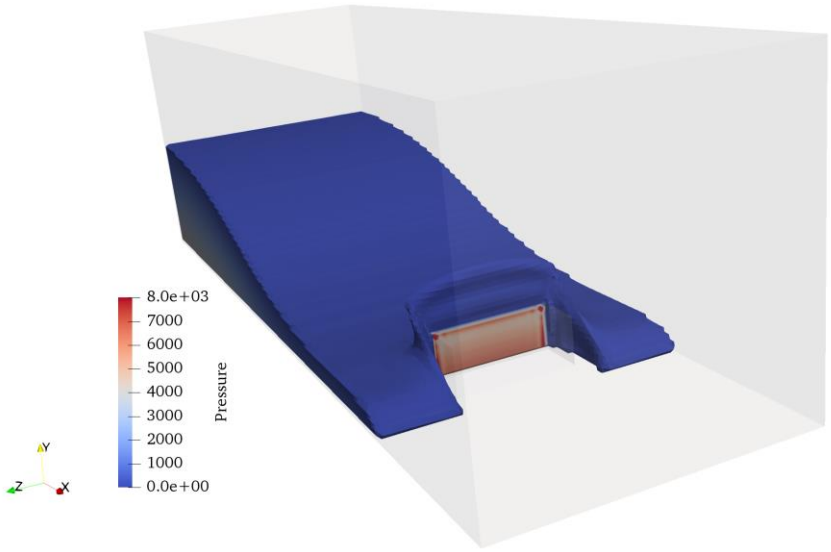

(a) Pressure profile: t = 0.50s

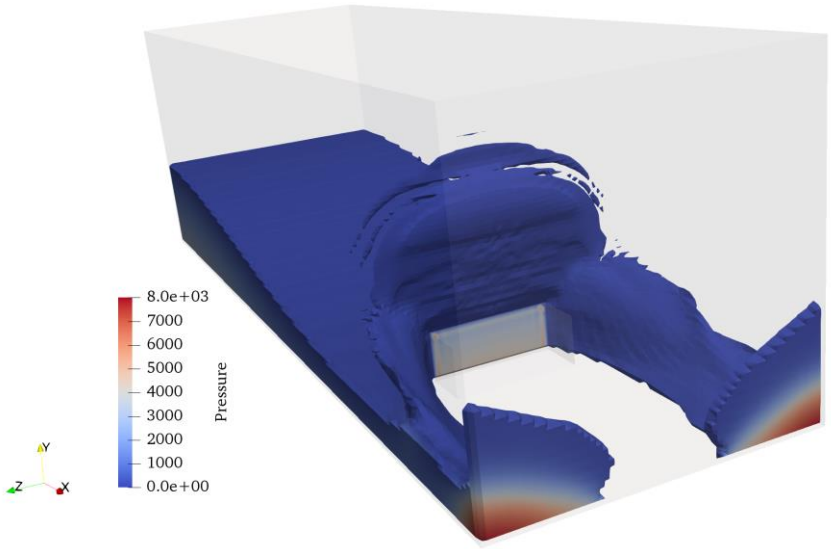

(b) Pressure profile: t = 0.75s

Figure 3.23 Three dimensional dam-break flow with obstacle: pressure profile at the obstacle

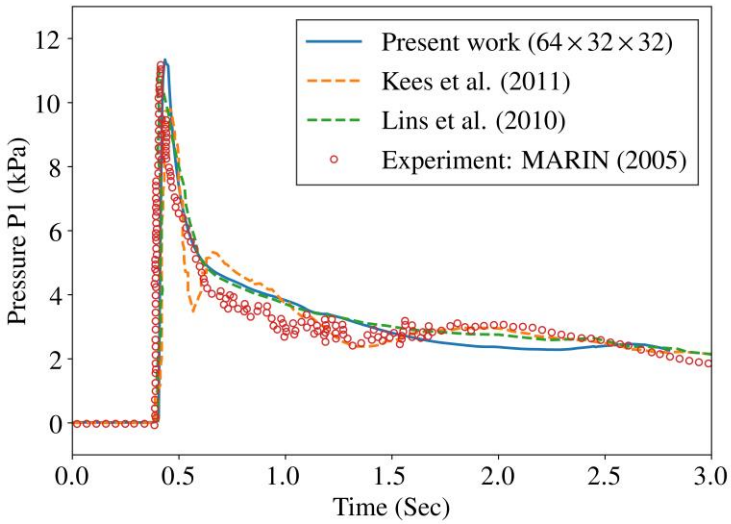

(a) Pressure time history at point A.

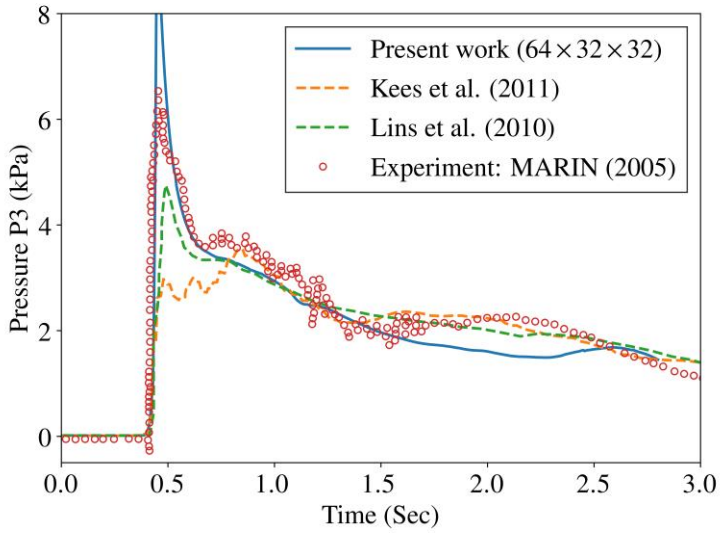

(b) Pressure time history at point B.

Figure 3.24 Pressure history at the obstacles: comparison with experimental and numerical data

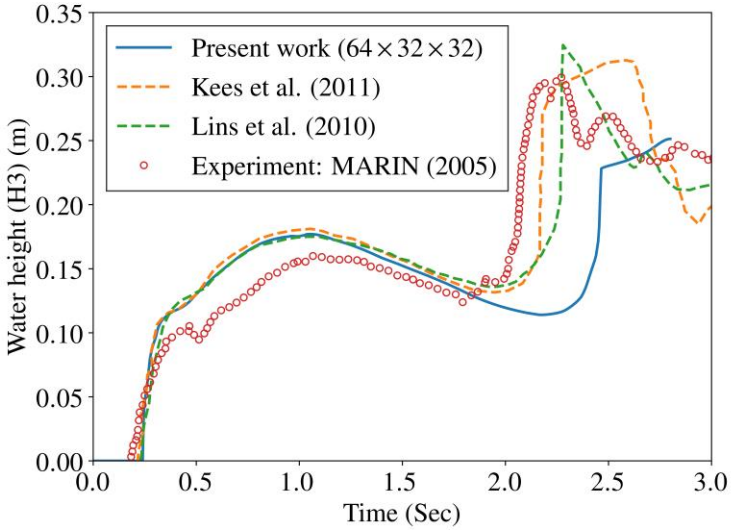

(a) Water elevation history at point $(x,y,z) = (0.582,0.5,0)$.

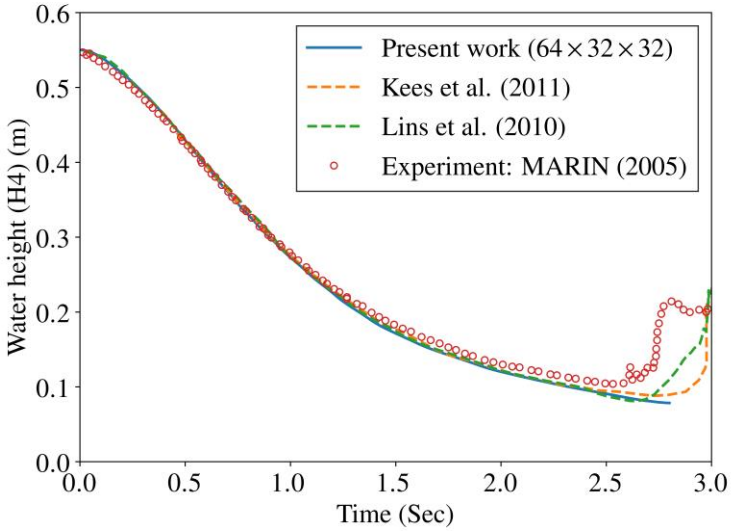

(b) Water elevation history at point (x,y,z) = (1.732,0.5,0).

Figure 3.25 Water elevation history at two locations: Comparison with experimental and numerical data

3.7. CONCLUSIONS

We have presented a stabilized interface formulation for the surface flows on fixed Eulerian meshes where the motion of the interface is tracked via the level-set advection equation. The evolution of

the interface is consistently represented in the governing system via dependence of density and viscosity on the level set field which is driven by the velocity field furnished by the Navier-Stokes equations. Application of VMS method to the coupled systems of equations gives rise to interfacial terms that have a structure which is similar to the Ghost penalty terms reported in the literature. These interfacial terms do not appear naturally if VMS-based stabilization is applied individually to each of the two PDEs. Representing the location of the interface via dependency of the mechanical material coefficients on the level-set also provides an avenue to variationally account for sub-grid effects engendered by the deforming interface. The variationally consistent derivation presented here not only provides the necessary stabilization for the sources of instability in convective free-surface flows, it also shows the variational basis of the ghost penalty term as a stabilizing term.

The proposed method gives rise to two forms of stabilization terms: (i) full gradient form, and (ii) interface form that is operational at the domain boundary between the phases. A significant attribute of the current method is the derivation of the interfacial stabilization parameter that varies spatially as well as temporally as the interfacial physics evolves. Mathematical analysis reveals that this parameter is bounded and positive definite which is numerically confirmed on several test cases presented in the numerical section. Consequently, the interfacial term is a bounded term that adds to interfacial stability, thereby controlling nonphysical interfacial modes that may get triggered due to jumps in density and viscosity of the fluids across the moving and deforming interfaces.

Benchmark problems in 2D are presented to highlight the salient features of the proposed method. Shear flow in a box presents a circular interface that is convected via a vortex velocity field and computed results show linear convergence in the L norm for both linear hexahedral and linear tetrahedral elements. The response for the linear sloshing problem is compared with the analytical solution and the period as well as the amplitude are uniformly preserved for various Reynolds number flows. Method is then applied to 2D dam break problem and good comparison with the experimentally observed data as well as with the published computed results is attained. Simulation of free overfall of open channel under gravity with discrete air-water interface shows stable and convergent solution even on relatively cruder discretization.

The 3D dam break problem with obstacle presents large free-surface motions and shows the enhanced stability and accuracy of the method to model breaking waves and complex flow patterns of practical interest in engineering.

CHAPTER 4: RESIDUAL-BASED TURBULENCE MODELS AND ARBITRARY LAGRANGIAN-EULERIAN FRAMEWORK FOR FREE SURFACE FLOWS[*]

4.1. INTRODUCTION

Modeling of fluid flows with free surfaces is an essential ingredient in the design and analysis of off-shore structures such as oil platforms and off-shore wind turbine farms in which the dynamics of free surface waves plays an important role. Accurate representation of free surfaces is also important to model the effect of waves on coastal structures. These applications are gaining attention due to the growing interest in new energy resources, and the need to build structures that can survive possible environmental hazards caused by climate change. Another area where free surface wave dynamics is important is fluid sloshing inside storage tanks. Although sloshing fluid can have undesirable destabilization effects during fluid transportation, it can also be carefully modulated to have stabilizing effects by serving as energy sinks that mitigate earthquake effects on built structures. Other problems where free surface flows are important are flows in rivers and channels, and in the modeling of ship hydrodynamics. In all these cases, accurate modeling of free surface effects is crucial for evaluating wave and current action on the structures.

Several approaches have been reported in the literature to study free surface flows. The interface tracking techniques model the evolution of free surfaces via a set of nodes or particles with time evolving spatial locations that track the geometry of the free surface. First applications of the interface tracking methods were based on the Arbitrary Lagrangian-Eulerian (ALE) methods [65,71] where the ALE frame of reference enables the motion of the boundaries and the nodal coordinates. The main advantage of this approach is a precise description of the evolving interface, and therefore an accurate modeling of flow physics that is associated with the evolution of the interface. However, a limitation of such methods is that under conditions of large free surface motions, the computational mesh needs to be redefined in order

[*] This chapter has been adapted from "Calderer, R., Zhu, L., Gibson, R. and Masud, A., 2015. Residual-based turbulence models and arbitrary Lagrangian–Eulerian framework for free surface flows. *Mathematical Models and Methods in Applied Sciences*, 25(12), pp.2287-2317". The copyright owner has provided written permission to reprint the work.

to avoid excessive mesh distortions. Particle methods are another sub-class of interface tracking methods that are based on a Lagrangian description of the fluid, namely, the Particle Finite Element Method (PFEM) [126,132]. These methods effectively overcome the mesh distortion issues. The Lagrangian description of the fluid and the fact that a contiguous mesh is not needed makes these methods suitable for problems with very large deformations of the free surfaces. Despite their versatility, particle methods are computationally expensive due to the need for determining a tessellation at each time step to compute the interaction between the particles. The ALE/Lagrangian method [132] is a compromise between the two approaches. The region near the free surfaces is modeled employing a particle method that enables the free surface to undergo large deformations, and the remaining part of the domain is modeled using an ALE frame. Space-time methods for free surface problems [110,156,157] also fall in the category of interface tracking methods because the space-time domains evolve along the time axes to accommodate the motion of the moving free surfaces. A formal equivalence between the deforming space-time domain techniques and ALE based techniques is presented in [110].

A second family of methods that is used to study free surface flows is based on interface capturing techniques. In this approach, the computational mesh is fixed and the location of the free surface is traced employing an additional scalar field. One of the first applications of this method is the Volume of Fluids (VOF) technique [43,62,96], which uses a scalar field that represents the fraction of fluid in each of the mesh elements. Another interface capturing technique is the Level Set method [4,82,94,149] in which an additional field is introduced to capture the evolving interface. In interface capturing techniques, the additional scalar field is invariably governed by a time-dependent advection equation [37].

A mixed approach is also possible for problems with free surfaces and moving solid objects. In these methods, the free surface can be represented by an interface-capturing approach, and the fluid-solid interfaces can be represented by an interface-tracking approach. This family of methods, which is known as Mixed Interface-Tracking/Interface-Capturing Technique (MITICT) was first presented in [154] and then used for free-surface flow and fluid-object interaction in [2].

The present paper develops a residual-based turbulence model for flows with free surfaces. To accommodate free surfaces motions the formulation is cast in an ALE frame of reference [29,84]. Underlying idea of the residual-based turbulence models is the VMS method [13,30,50,66,124] wherein the solution fields are decomposed in components of overlapping scales, namely, the coarse and the fine scales. The fine scales are modeled in terms of the residuals of the Euler-Lagrange equations of the coarse scales, and are variationally embedded in the coarse-scale equations. In the present work we extend the formulation presented in [30] on turbulence models for domains with moving boundaries, to free surface flows. In [108], we presented a model based on three-level hierarchical decomposition of the velocity and pressure fields. We used linear shape functions to represent the coarse-scale fields, and hierarchical bubbles for the two levels of fine scales. Use of bubble functions helps in confining the fine-scale problems to element interiors, thereby facilitating a convenient way to extract models for fine scales that are functions of the residuals of the Euler-Lagrange equations for the coarse scales. This has been shown in a variety of turbulent flow problems over fixed [30,107] and moving domains [108]. In the present paper we extend [108] to problems with free surfaces and show the applicability of the proposed method via application to two sets of turbulent free surface flow problems.

A literature review reveals that other authors have also explored multiscale methods. For example, Collis [36] and Gravemeier et al. [50] have proposed three-scale methods using the VMS approach. Our method also proposes three-scale decomposition. However in our case, the smallest scales are solved using bubble function approach [17,19] that is applied to element interiors and it yields an analytical expression for the level-three scales. The terms modeling level-three scales are substituted in the level-two system of equations and it results in a model for the finer turbulence scales that is free of user-defined parameters. This sequential and variationally consistent nesting of models from the finer levels into the equations at the coarser levels provides a mathematically consistent and computationally inexpensive model for turbulent flows

The remaining part of the paper is organized as follows. In Sec. 2, the incompressible Navier-Stokes equations are presented in an ALE frame of reference. In Sec. 3, a residual-based method for

turbulent free surface flows is presented. In Sec. 4, we apply the proposed method for turbulent flows with free surfaces to two open channel problems. First, we study the flow in a flat open channel. The turbulent features of the flow are the driving mechanism that causes the free surfaces to evolve in time. We investigate the flow with two different slopes of the channel, and mesh refinement study is carried out to show the convergence of computed physics. The second problem studied is a channel with an undulated bottom surface. Multiple flow conditions are analyzed and the results are compared with experimental [9] and numerical results [170]. Also presented are numerical results for a thin channel with wavy bottom surface. Turbulence generated at the bottom surface interacts with the free surface. This leads to evolving irregular free surface elevations. Conclusions are drawn in Sec. 5.

4.2. THE INCOMPRESSIBLE NAVIER-STOKES EQUATIONS

Let $\Omega_t \subset \mathbb{R}^3$ be a connected, open, bounded region with time-dependent piecewise smooth boundary Γ_t. The incompressible Navier-Stokes equations written in an Arbitrary Lagrangian-Eulerian (ALE) frame are:

$$\left.\frac{\partial \boldsymbol{u}}{\partial t}\right|_{\boldsymbol{Y}} + (\boldsymbol{u} - \boldsymbol{u}_M) \cdot \nabla \boldsymbol{u} - 2\nu \nabla \cdot \boldsymbol{\varepsilon}(\boldsymbol{u}) + \nabla p = \boldsymbol{f} \tag{4.1}$$

$$\nabla \cdot \boldsymbol{u} = 0 \quad \text{in } \Omega_t \times]0,T[\tag{4.2}$$

$$\boldsymbol{u} = \boldsymbol{g} \quad \text{on } \Gamma_g|_t \times]0,T[\tag{4.3}$$

$$(2\nu \boldsymbol{\varepsilon}(\boldsymbol{u}) - p\boldsymbol{I}) \cdot \boldsymbol{n}_t = \boldsymbol{h} \quad \text{on } \Gamma_h|_t \times]0,T[\tag{4.4}$$

$$(2\nu \boldsymbol{\varepsilon}(\boldsymbol{u}) - p\boldsymbol{I}) \cdot \boldsymbol{n}_t = \boldsymbol{0} \quad \text{on } \Gamma_f|_t \times]0,T[\tag{4.5}$$

$$(\boldsymbol{u} - \boldsymbol{u}_M) \cdot \boldsymbol{n}_t = 0 \quad \text{on } \Gamma_f|_t \times]0,T[\tag{4.6}$$

$$\boldsymbol{u}(\boldsymbol{x},0) = \boldsymbol{u}_0 \quad \text{on} \quad \Omega_0 \times \{0\} \tag{4.7}$$

where $\boldsymbol{u}$ is the velocity vector, p is the kinematic pressure, $\boldsymbol{f}$ is the body force (per unit of mass), ν is the kinematic viscosity ($\nu>0$), $\boldsymbol{u}_M$ is the fluid mesh velocity, $\left.\frac{\partial \boldsymbol{u}}{\partial t}\right|_Y$ is the time derivative of the velocity field in the ALE frame, $\boldsymbol{I}$ is the identity tensor, $\boldsymbol{n}_t$ is the exterior normal to the boundary Γ_t, $\boldsymbol{u}_0$ is the initial condition for the velocity field, $\boldsymbol{\varepsilon}(\boldsymbol{u})=\nabla^s\boldsymbol{u}$ is the strain rate tensor, $\boldsymbol{g}:\Gamma_g\big|_t\to\mathbb{R}^3$ is the Dirichlet boundary condition, and $\boldsymbol{h}:\Gamma_h\big|_t\to\mathbb{R}^3$ is the Neumann boundary condition. Without loss of generality, the surface tension on the free surface of the fluid $\Gamma_f\big|_t$ is assumed to be negligible, i.e. Eq. (4.5). In addition, the free surface boundary moves to satisfy the continuum condition that the flux of fluid across the free surface is zero, i.e. Eq. (4.6).

The standard weak form of the problem (4.1)-(4.7) is: find $\boldsymbol{u}(\boldsymbol{x},t)\in\boldsymbol{\mathcal{S}}$ and $p(\boldsymbol{x},t)\in\mathcal{P}$ such that for all $\boldsymbol{w}(\boldsymbol{x})\in\boldsymbol{\mathcal{V}}$ and . $q(\boldsymbol{x})\in\mathcal{Q}$.,

$$(\boldsymbol{w},\frac{\partial \boldsymbol{u}}{\partial t})+(\boldsymbol{w},(\boldsymbol{u}-\boldsymbol{u}_M)\cdot\nabla\boldsymbol{v})+(\nabla^s\boldsymbol{w},2\nu\nabla^s\boldsymbol{u})-(\nabla\cdot\boldsymbol{w},p)=(\boldsymbol{w},\boldsymbol{f}) \tag{4.8}$$

$$(q,\nabla\cdot\boldsymbol{u})=0 \tag{4.9}$$

where $(\bullet,\bullet)=\int_\Omega(\bullet)d\Omega$ is the $L^2(\Omega)$ -inner product. The functions $\boldsymbol{w}(\boldsymbol{x})\in\boldsymbol{\mathcal{V}}=\left(H_0^1(\Omega)\right)^3$ and $q(\boldsymbol{x})\in\mathcal{Q}=C^0(\Omega)\bigcap L^2(\Omega)$ are the weighting functions for the velocity and the pressure fields, respectively, and $\boldsymbol{\mathcal{S}}$ and $\mathcal{P}$ are the time-dependent spaces of trial solutions for the velocity and the pressure fields, respectively.

The variational problem can be expressed in a compact abstract form as:

$$\mathcal{L}(\boldsymbol{w};\boldsymbol{u},p;\boldsymbol{u}_M)=\varphi(\boldsymbol{w}) \tag{4.10}$$

$$\mathcal{H}(q;\boldsymbol{u})=0 \tag{4.11}$$

where the functional $\mathcal{L}(\boldsymbol{w};\boldsymbol{u},p;\boldsymbol{u}_M)$ contains the terms from the left hand side of (4.8), $\varphi(\boldsymbol{w})=(\boldsymbol{w},\boldsymbol{f})$ and $\mathcal{H}(q;\boldsymbol{u})=(q,\nabla\cdot\boldsymbol{u})$.

4.3. RESIDUAL-BASED TURBULENCE MODELS FOR FREE SURFACE FLOWS

The variational problem (4.10)-(4.11) is a mixed-field problem. It needs to be stabilized to (i) account for the convective effects, and (ii) enable the use of arbitrary interpolations for the velocity and pressure fields. To address these issues, VMS ideas were introduced and it was later realized that these ideas actually extend to the development of turbulence models where larger features can be numerically resolved while finer features can be modeled. In addition, these residual-based approaches automatically take care of the issues enumerated above. To derive a formulation that successfully encompasses all these attributes we employ the VMS framework, which decomposes the solution fields into components of different scales. In the following section we present a synopsis of the method that we derived in [108] and we extend it to the treatment of the free surface condition that is considered in the present work.

4.3.1. Multiscale Decomposition

We assume a multiscale decomposition of the solution fields into overlapping hierarchical scales termed as coarse and fine scales.

$$\boldsymbol{u}(\boldsymbol{x},t) = \underbrace{\bar{\boldsymbol{u}}(\boldsymbol{x},t)}_{\text{coarse scale}} + \underbrace{\boldsymbol{u}'(\boldsymbol{x},t)}_{\text{fine scale}} \tag{4.12}$$

$$p(\boldsymbol{x},t) = \underbrace{\bar{p}(\boldsymbol{x},t)}_{\text{coarse scale}} + \underbrace{p'(\boldsymbol{x},t)}_{\text{fine scale}} \tag{4.13}$$

Similarly, we also decompose the weighting functions $\boldsymbol{w}$ and q into coarse and fine scales:

$$\boldsymbol{w}(\boldsymbol{x}) = \underset{\text{coarse scale}}{\bar{\boldsymbol{w}}(\boldsymbol{x})} + \underset{\text{fine scale}}{\boldsymbol{w}'(\boldsymbol{x})} \tag{4.14}$$

$$q(\boldsymbol{x}) = \underset{\text{coarse scale}}{\bar{q}(\boldsymbol{x})} + \underset{\text{fine scale}}{q'(\boldsymbol{x})} \tag{4.15}$$

Remark. We assume that the coarse and fine-scale components admit a unique decomposition, which is important for the stability and consistency of the method. From a computational perspective this condition is easily satisfied by the discretized formulations via the use of linearly independent interpolations.

Substituting (4.12)-(4.15) in the variational problem (4.10)-(4.11) and employing the fact that the operators $\mathcal{L}$, φ and $\mathcal{H}$ are linear with respect to their weighting functions, the problem can be decomposed in two sub-problems:

Coarse-scale sub-problem

$$\mathcal{L}\left(\bar{\boldsymbol{w}};\, \bar{\boldsymbol{u}}+\boldsymbol{u}',\, \bar{p}+p';\, \boldsymbol{u}_M\right)=\varphi\left(\bar{\boldsymbol{w}}\right) \tag{4.16}$$

$$\mathcal{H}\left(\bar{q};\, \bar{\boldsymbol{u}}+\boldsymbol{u}'\right)=0 \tag{4.17}$$

Fine-scale sub-problem

$$\mathcal{L}\left(\boldsymbol{w}';\, \bar{\boldsymbol{u}}+\boldsymbol{u}',\, \bar{p}+p';\, \boldsymbol{u}_M\right)=\varphi\left(\boldsymbol{w}'\right) \tag{4.18}$$

$$\mathcal{H}\left(q';\, \bar{\boldsymbol{u}}+\boldsymbol{u}'\right)=0 \tag{4.19}$$

In our earlier work on the Navier-Stokes equations [23, 7] we had only assumed a multiscale decomposition of the velocity field, while the pressure field was not decomposed. In our subsequent developments [28] we showed that the continuity condition (4.2) is better enforced if the final formulation has a *div*-stabilization term. This term was injected in the method developed in [107], while in [30] it was systematically derived by assuming a multiscale decomposition of the pressure field. Although this second approach has superior mass conservation properties, it gives rise to a fine-scale problem that itself is a mixed-field problem, whereas the fine-scale problem that corresponds to the first approach is a single field problem. This difference in the two formulations also gets manifested in the numerical evaluation of the fine-scale models. While the former approach is computationally less intensive, the later approach possesses superior attributes even in the very small time-step range.

The method employed to solve the coupled coarse and fine-scale problems, is summarized as follows. First, a model for the fine scales $\boldsymbol{u}'$ and p' is extracted from fine-scale problem (4.18)-(4.19) in terms of the residuals of the Euler-Lagrange equations for the coarse scales $\bar{\boldsymbol{u}}$ and $\bar{p}$. Then, the model is substituted in the coarse-scale problem (4.16)-(4.17). This variationally consistent embedding of the fine-scale model in the coarse-scale formulation amounts to a variational projection of the fine scales onto the

coarse-scale space. As a consequence, the resulting formulation is only expressed in terms of the coarse-scales, and the effects of the fine scales are accounted for via the projected fine-scale model.

Remark. The fine-scale problem (18)-(19) is a mixed field problem, and therefore it needs to be stabilized to (i) account for the fine convective terms, and (ii) have the flexibility to use arbitrary interpolations for the fine-scale velocity and pressure fields. We carry out a hierarchical application of VMS ideas [30,109] that leads to another overlapping split of the fine-scale fields. Objective of this split is to derive a stabilized formulation for the fine-scale system represented by equations (18)-(19).

Remark. The level-three scales are used to stabilize the level two scales and make the level-two model free of any constraints on the combination of interpolation functions, as well as any assumption on the order of the pressure field, or any restriction on the structure of the stabilization tensor. Numerical tests show that if there are less constraints on the level-two model, its modeling capacity and capability is tremendously increased which is reflected via the higher Reynolds number flows that it can resolve.

4.3.2. Solution of the Fine-Scale Problem

The fine-scale problem (4.18)-(4.19) is a mixed field problem, and therefore it needs to be stabilized to (i) account for the fine convective terms, and (ii) have the flexibility to use arbitrary interpolations for the fine-scale velocity and pressure fields. We carry out a hierarchical application of VMS ideas [30,109] that lead to another overlapping split of the fine-scale fields. Objective of this split is to derive a stabilized formulation for the fine-scale problem (4.18)-(4.19). Figure 1 shows a schematic diagram of the hierarchical approach. Accordingly, we assume a multiscale decomposition of the velocity field in two overlapping components termed as fine-scale level-I and level-II:

$$\boldsymbol{u}'(\boldsymbol{x},t) = \underbrace{\boldsymbol{u}'_I(\boldsymbol{x},t)}_{\text{level-I scale}} + \underbrace{\boldsymbol{u}'_{II}(\boldsymbol{x};t)}_{\text{level-II scale}} \tag{4.20}$$

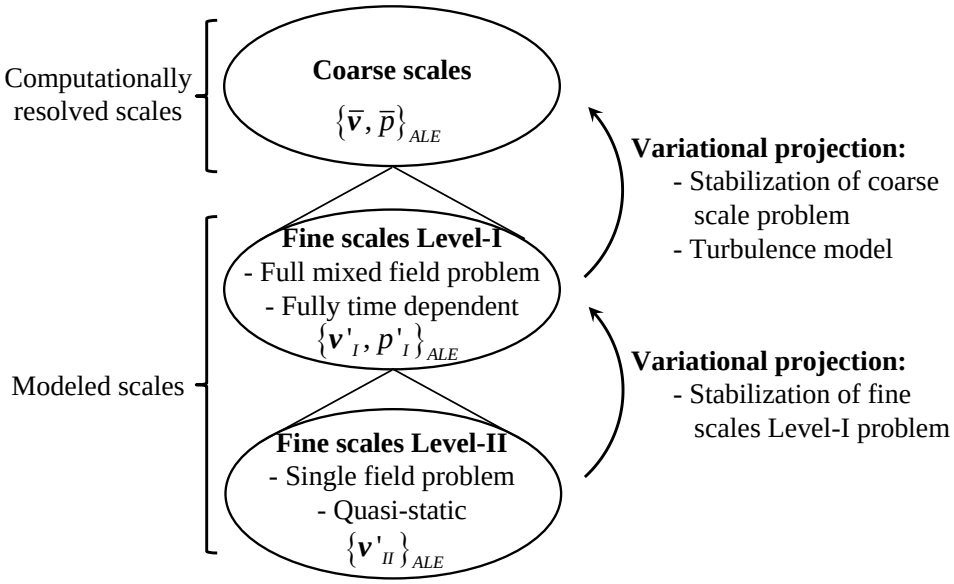

Figure 4.1 Schematic diagram of telescopic depth in scales

Consistency and stability of the method necessitate that the decomposition of level-I and level-II scales, as stipulated in (4.20), is unique. Because of the scale split in (4.20), we can limit any modeling assumptions to the level-II velocities $\boldsymbol{u}'_{II}$ with no presumptions on level-I velocities $\boldsymbol{u}'_{I}$. Since $\boldsymbol{u}'_{II}$ are sufficient to stabilize the level-I scales, we do not assume a multiscale decomposition of the fine-scale pressure field:

$$p'(\boldsymbol{x},t) = \underbrace{p'_I(\boldsymbol{x},t)}_{\text{level-I scale}} \tag{4.21}$$

Likewise we decompose the fine-scale component of the weighting velocity field into level-I and level-II components, but we do not decompose the fine-scale pressure weighing function:

$$\boldsymbol{w}'(\boldsymbol{x}) = \underbrace{\boldsymbol{w}'_I(\boldsymbol{x})}_{\text{level-I scale}} + \underbrace{\boldsymbol{w}'_{II}(\boldsymbol{x})}_{\text{level-II scale}} \tag{4.22}$$

$$q'(\boldsymbol{x}) = \underbrace{q'_I(\boldsymbol{x})}_{\text{level-I scale}} \tag{4.23}$$

We then substitute the decompositions (4.20)-(4.23) in the fine-scale problem (4.18)-(4.19), and employing the linearity with respect to the weighting functions $\boldsymbol{w}'$ and q', we further split the fine-scale problem into two sub-problems:

Fine-scale problem I

$$\mathcal{L}\left(\boldsymbol{w}'_I;\, \bar{\boldsymbol{u}}+\boldsymbol{u}'_I+\boldsymbol{u}'_{II},\, \bar{p}+p'_I;\, \boldsymbol{u}_M\right)=\boldsymbol{\varphi}\left(\boldsymbol{w}'_I\right) \tag{4.24}$$

$$\mathcal{H}\left(q'_I;\, \bar{\boldsymbol{u}}+\boldsymbol{u}'_I+\boldsymbol{u}'_{II}\right)=0 \tag{4.25}$$

Fine-scale problem II

$$\mathcal{L}\left(\boldsymbol{w}'_{II};\, \bar{\boldsymbol{u}}+\boldsymbol{u}'_I+\boldsymbol{u}'_{II},\, \bar{p}+p'_I;\, \boldsymbol{u}_M\right)=\boldsymbol{\varphi}\left(\boldsymbol{w}'_{II}\right) \tag{4.26}$$

Remark. The present approach results in an homogeneous multiscale framework [116] as the same operators $\mathcal{L}$ and $\mathcal{H}$ govern the three nested problems involved in the hierarchical decomposition, i.e. problems (4.16)-(4.17), (4.24)-(4.25) and (4.26).

We extract $\boldsymbol{u}'_{II}$ from (4.26) in terms of the residual of level-I scales and the residual of the Euler Lagrange equations of the coarse scales. To do so, we employ bubble functions to interpolate the level-II velocity field. Because of their definition and construction, bubble functions help localize (4.26) to sum of these terms over the element interiors. In the numerical tests presented in Sec. 4, we have used forth order polynomial bubble functions for $\boldsymbol{u}'_{II}$. This leads to a model for $\boldsymbol{v}'_{II}$ that can be expressed in an abstract form as follows:

$$\boldsymbol{v}'_{II} = \mathcal{M}_{II}\left(\bar{\boldsymbol{v}},\, \bar{p},\, \boldsymbol{u}'_I,\, p'_I\right) \tag{4.27}$$

We variationally project the model for $\boldsymbol{u}'_{II}$ onto the level-I problem (4.24)-(4.25), which can be expressed as:

$$\mathcal{L}\left(\boldsymbol{w}'_I;\, \bar{\boldsymbol{u}}+\boldsymbol{u}'_I+\mathcal{M}_{II}\left(\bar{\boldsymbol{u}},\, \bar{p},\, \boldsymbol{u}'_I,\, p'_I\right),\, \bar{p}+p'_I;\, \boldsymbol{u}_M\right)=\boldsymbol{\varphi}\left(\boldsymbol{w}'_I\right) \tag{4.28}$$

$$\mathcal{H}\left(q'_I;\, \bar{\boldsymbol{u}}+\boldsymbol{u}'_I+\mathcal{M}_{II}\left(\bar{\boldsymbol{u}},\, \bar{p},\, \boldsymbol{u}'_I,\, p'_I\right)\right)=0 \tag{4.29}$$

Equations (4.28)-(4.29) depend only on the coarse-scales and the level-I fine scales. Using a second set of bubble functions that is linearly independent of the first set of bubbles employed to derive the model (4.27), we can solve (4.28)-(4.29) and derive a model for the level-I scales in terms of the coarse-scale fields:

$$\begin{bmatrix} \boldsymbol{u}'_I \\ p'_I \end{bmatrix} = \mathcal{M}_I\left(\bar{\boldsymbol{u}},\, \bar{p}\right) \tag{4.30}$$

Revisiting the objective underlying the hierarchical decomposition of scales we see that the level-II scales were primarily used to stabilize the fine-scale variational problem (4.18)-(4.19), and the level-I scales served as the model for the turbulent scales. Solution of the nested up-scaling equations (4.28)-(4.29) yields $\left\{\boldsymbol{u}'_I, p'_I\right\}$ with $\boldsymbol{v}'_{II}$ embedded, and therefore the fine-scales can be approximated by the level-I solutions:

$$\begin{bmatrix} \boldsymbol{u}' \\ p' \end{bmatrix} \simeq \begin{bmatrix} \boldsymbol{u}'_I \\ p'_I \end{bmatrix} \tag{4.31}$$

4.3.3. The Variational Multiscale Turbulence Model

The model for the fine-scale fields (4.31) is substituted in the coarse-scale problem (4.16)-(4.17). The resulting formulation can be written in an abstract form as:

$$B_{Gal}\left(\bar{\boldsymbol{w}}, \bar{q}\,;\, \bar{\boldsymbol{u}}, \bar{p}, \boldsymbol{v}_M\right) + B^{Turb}_{VMS}\left(\bar{\boldsymbol{w}}\,, \bar{q}\,;\, \bar{\boldsymbol{u}}\,, \boldsymbol{u}'\,, p', \boldsymbol{v}_M\right) = F_{Gal}\left(\bar{\boldsymbol{w}}\right) \tag{4.32}$$

where

$$\begin{aligned} B_{Gal}\left(\bar{\boldsymbol{w}}, \bar{q}\,;\, \bar{\boldsymbol{u}}, \bar{p}, \boldsymbol{v}_M\right) \;=\; & (\bar{\boldsymbol{w}}, \frac{\partial \bar{\boldsymbol{u}}}{\partial t}) + (\bar{\boldsymbol{w}}, \left(\bar{\boldsymbol{u}} - \boldsymbol{u}_M\right)\cdot\nabla\bar{\boldsymbol{u}}) + (\nabla^s\bar{\boldsymbol{w}}, 2\nu\nabla^s\bar{\boldsymbol{u}}) \\ & - (\nabla\cdot\bar{\boldsymbol{w}}, \bar{p}) + (\bar{q}, \nabla\cdot\bar{\boldsymbol{u}}) \end{aligned} \tag{4.33}$$

Equation (4.33) comprises all the terms that appear on the left hand side of the standard variational form (4.8)-(4.9),

$$F_{Gal}\left(\bar{\boldsymbol{w}}\right) = (\bar{\boldsymbol{w}}, \boldsymbol{f}) \tag{4.34}$$

is the right hand side of (4.8).

$$\begin{aligned} B^{Turb}_{VMS}\left(\bar{\boldsymbol{w}}\,, \bar{q}\,;\, \bar{\boldsymbol{u}}\,, \boldsymbol{u}'\,, p', \boldsymbol{v}_M\right) \;=\; & (\bar{\boldsymbol{w}}, \frac{\partial \boldsymbol{u}'}{\partial t}) - (\,(\bar{\boldsymbol{u}} - \boldsymbol{u}_M)\cdot\nabla\bar{\boldsymbol{w}} - \bar{\boldsymbol{w}}\nabla\cdot\boldsymbol{u}_M \\ & - \bar{\boldsymbol{w}}\cdot\nabla^T\bar{\boldsymbol{u}} + \nabla\bar{q} + 2\nu\Delta^s\bar{\boldsymbol{w}}, \boldsymbol{u}') \\ & - (\nabla\cdot\bar{\boldsymbol{w}}, \boldsymbol{u}'\otimes\boldsymbol{u}') - (\nabla\cdot\bar{\boldsymbol{w}}, p') \end{aligned} \tag{4.35}$$

The right hand side of (4.35) contains terms that arise due to the *a-priori* assumption of the existence of fine scales. These terms serve two purposes: they provide stability to the mixed field problem, and they serve as the turbulence model.

Remark: Since the fine-scale fields (4.30) depend on the residuals of the Euler-Lagrange equations of the coarse-scales, the final formulation (4.32) only depends on the coarse-scale fields $\bar{\boldsymbol{u}}$ and $\bar{p}$.

4.3.4. Free Surface Condition

The turbulence model (4.32) is complemented by the condition that enforces zero flux across the free surface (4.6). Several techniques have been proposed in the literature to enforce this condition [65,161]. In this work we impose this condition in a weak form which can be written as follows:

$$\int_{\Gamma_t^{fs}} \eta \, (\boldsymbol{u} - \boldsymbol{u}_M) \cdot \boldsymbol{n}_t \, d\Gamma = 0 \tag{4.36}$$

where η is an arbitrary weighting function, $\boldsymbol{v}$ is the fluid velocity on the free surface, $\boldsymbol{u}_M$ is the mesh velocity, Γ_t^{fs} is the time dependent free surface boundary, and $\boldsymbol{n}_t$ is the time evolving unit normal vector on Γ_t^{fs}.

Imposing the zero-flux condition in a weak sense has two advantages. Firstly, the global mass of the fluid is conserved because local errors due to the free surface discretization are compensated for. Secondly, the unit normal $\boldsymbol{n}_t$ vector has to be computed only at the Gauss points, where the normal is uniquely defined. This is a significant advantage as compared to imposing the zero-flux condition strongly at the nodal points in which case the normal needs to be computed at the nodal points. In general the normal at the nodal points is non-unique due to C^0 continuity of the fields, and this is especially true for simplical elements.

Formulation (4.36) needs to be solved iteratively because the normal $\boldsymbol{n}_t$ depends on the displacement field associated with the free surface. In the numerical tests presented in Sec. 4 we have solved (4.36) using a fixed-point iteration approach. To obtain the updated free surface geometry, $\boldsymbol{n}_t$ has

been computed using the most current configuration of the free surface. For the benchmark problems presented in Sec. 4, the free surface is well resolved in two to three iterations.

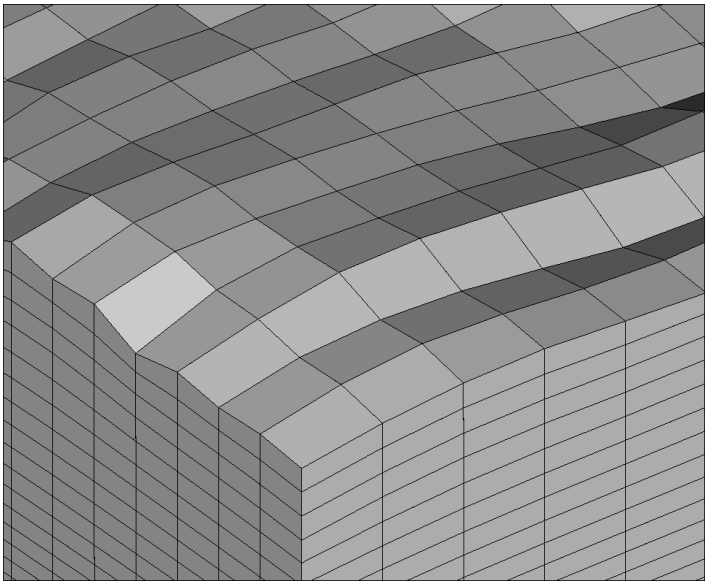

(a)

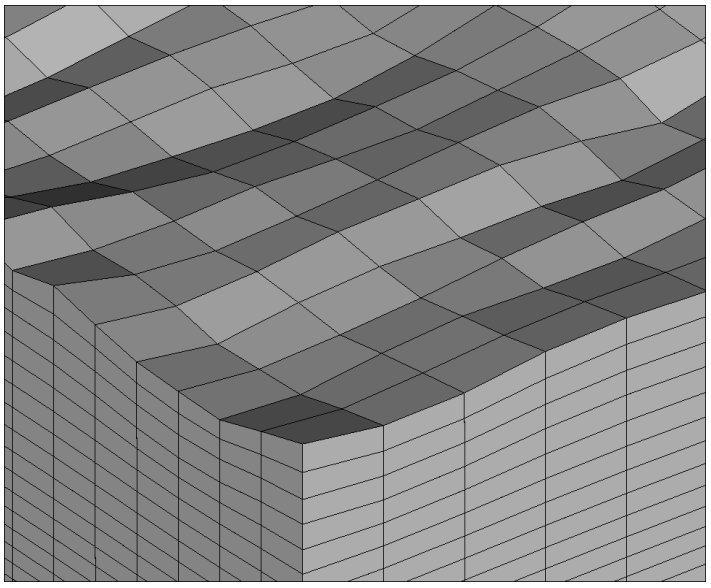

(b)

Figure 4.2 Detailed view of the free surface at two different time instants

Remark: The evolving free surfaces determine the boundaries of the computational domain. In the following section we use a mesh moving scheme to adapt the mesh to the evolving domain boundaries.

4.3.5. Mesh Moving Scheme

Once the location of the nodes on the free surface has been determined, the location of the interior nodes needs to be updated to maintain a good quality mesh for subsequent calculations. To update the mesh we use the method proposed by Masud and co-workers [80,104,110], in which the displacement of the nodal coordinates is determined by solving equation:

$$\nabla \bullet \left(\left[1 + \alpha^e \right] \nabla \boldsymbol{d} \right) = 0 \quad \text{in } \Omega_t \tag{4.37}$$

$$\boldsymbol{d} = \boldsymbol{g}(\boldsymbol{x},t) \qquad \text{on } \Gamma_t^m \tag{4.38}$$

$$\boldsymbol{d} = \boldsymbol{0} \qquad \text{on } \Gamma^f \tag{4.39}$$

where $\boldsymbol{d}(\boldsymbol{x},t)$ is the displacement field of the mesh, Γ^f is the part of the boundary that is fixed, Γ_t^m is the free surface boundary, and $\boldsymbol{g}(\boldsymbol{x},t)$ is the instantaneous displacement of the free surface. From the standpoint of the mesh moving scheme, $\boldsymbol{g}(\boldsymbol{x},t)$ is a Dirichlet boundary condition that is specified to match the geometry of the free surface obtained in Sec. 3.4.

The parameter α^e controls the relative deformation of the elements. The value of α^e depends on the volume V_e of element *e*, the volume of the smallest element of the mesh $V_{\min}$, and the volume of the largest element of the mesh $V_{\max}$ as follows:

$$\alpha^e = \frac{1 - V_{\min}/V_{\max}}{V_e/V_{\max}} \tag{4.40}$$

Via equation (4.40) the larger elements are assigned a lower value of α^e than the smaller elements. This process introduces a relative stiffening effect throughout the mesh that is inversely proportional to the size of the elements. Consequently, smaller elements in the vicinity of the free-surface behave stiffer and therefore maintain their aspect ratio during the mesh rezoning process. This transfers the large amplitude deformations induced by the oscillating free surface on to the larger elements that are in the interior of the domain. This process is not deleterious for the interior elements because the percentage of relative

distortion as measured in terms of change in element jacobian before and after deformation is fairly uniform all across the mesh. For details, interested reader is referred to [80,104].

Remark: The formulation for the fluid equations (4.32) and the formulation that models the evolution of the free surface are coupled. We solve them in an iterative fashion using the algorithm described in Box 4.1.

Box 4.1 Algorithmic form of the solution procedure

Initialize the algorithm: $i=1,\ n=1,\ t=0,\ \boldsymbol{u}_i^n=\boldsymbol{u}_0,\ \left.\frac{\partial \boldsymbol{u}}{\partial t}\right|_i^n=\boldsymbol{0},\ p_i^n=0$ and $\left(\boldsymbol{u}_M\right)_i^n=\boldsymbol{0}$.

1. Time step loop: Update time level, $t \leftarrow t+\Delta t$ and the time step counter, $n \leftarrow n+1$.
2. Compute the predictor variables: $\boldsymbol{u}_i^n=\boldsymbol{u}^{n-1},\ p_i^n=p^{n-1},\ \left.\frac{\partial \boldsymbol{u}}{\partial t}\right|^n=\frac{\gamma-1}{\gamma}\left.\frac{\partial \boldsymbol{u}}{\partial t}\right|_i^{n-1}$ and $\left(\boldsymbol{u}_M\right)_i^n=\left(\boldsymbol{u}_M\right)^{n-1}$, and reset the iteration counter, $i=1$
   a. Nonlinear iteration loop: Compute the fine-scales level-I $\boldsymbol{v}'$ and p' using eq. (4.31) and (4.27).
   b. Employing eq. (4.32), compute the element consistent tangent matrices $(\boldsymbol{K}^e)_i^n$ and element residual vectors $(\boldsymbol{R}^e)_i^n$ and assemble them to form the linearized system $\boldsymbol{K}_i^n \Delta \boldsymbol{d}_i=\boldsymbol{R}_i^n$, where $\Delta \boldsymbol{d}_i=\left[\Delta \boldsymbol{v}_i^n, \Delta p_i^n\right]^T$.
   c. Apply the Dirichlet boundary conditions to the linear system of equations formed in step b.
   d. Solve the linear system formed in steps b and c.
   e. Update the solution vectors: $\left[\boldsymbol{u}_{i+1}^n, p_{i+1}^n\right]^T=\left[\boldsymbol{u}_i^n, p_i^n\right]^T+\left[\Delta \boldsymbol{u}_i^n, \Delta p_i^n\right]^T$ and $\left.\frac{\partial \boldsymbol{u}}{\partial t}\right|_{i+1}^n=\left.\frac{\partial \boldsymbol{u}}{\partial t}\right|_i^n+\frac{1}{\gamma\,\Delta t}\Delta \boldsymbol{u}_i^n$.
   f. Update the free surface geometry using eq. (4.36) employing the velocity field obtained in step e.
   g. Update the mesh nodal coordinates by solving problem (4.37)-(4.39) and compute the updated mesh velocity $\left(\boldsymbol{u}_M\right)_{i+1}^n$.
3. End of nonlinear iteration loop: If convergence criterion is not satisfied, update the nonlinear iteration counter, $i \leftarrow i+1$, and go to step 2.a. Else, continue with step 4.
4. Update the converged solution: $\boldsymbol{u}^n=\boldsymbol{u}_{i+1}^n,\ p^n=p_{i+1}^n,\ \left.\frac{\partial \boldsymbol{u}}{\partial t}\right|^n=\left.\frac{\partial \boldsymbol{u}}{\partial t}\right|_{i+1}^n$ and $\left(\boldsymbol{u}_M\right)^n=\left(\boldsymbol{u}_M\right)_{i+1}^n$.

End of time step loop: If *n* is the last time step stop, else go to step 1.

4.4. NUMERICAL TESTS

Literature review reveals that there are only a handful of benchmark test cases for validating turbulence models for problems with free surfaces. A common test case is a confined turbulent channel flow under body force generated due to gravity where flow is confined between two parallel fixed walls. For this test case reference DNS results were reported by Moser and co-workers [121] for various Reynolds number flows.

We first present the case of regular deep sea waves for which analytical solution is available [47], and therefore it serves as a good benchmark problem to verify the accuracy and stability of the method. Then we present two sets of numerical tests. First set considers a turbulent channel that has a fixed bottom surface, while the top surface is free to evolve. The flow is driven by the gravity force. The Reynolds number $Re_T = 395$. Two different slopes of the bottom boundary are analyzed. The second set of problems is inspired by [9,170], and it consists of an open channel flow with a non-flat bottom surface. We employ same geometric configuration as is used in [170], and we compare our results with the experimental data reported in [9], and LES results reported in [170]. For this problem, we also consider a configuration with reduced depth of the channel wherein turbulence generated at the bottom boundary interacts with the evolving free surface and gives rise to more complex free surface flow patterns than are reported in [170].

All the numerical tests have been conducted using tri-linear hexahedral elements for the coarse-scale fields, quadratic bubble functions for the fine-scale level-I fields and fourth-order bubble functions for the fine-scale level-II fields. The element integrals are evaluated using full Gaussian quadrature and the generalized-alpha method with $\rho_\infty = 0$ is used for time integration.

4.4.1. Regular Waves

This test case investigates a regular wave of height 10m, period T=10 sec and wave length λ=159m in a water depth of 120m. Body force is -981 and fluid viscosity is 0.01. The results of the numerical simulations are compared to the analytical Stokes V solution, which is the solution of fifth

order Stokes theory as presented in reference [47]. Fig 3 shows a schematic description of the problem where the inflow velocity $U_x(x=0, y, t) = \partial\Phi/\partial x$, and $\Phi(x, y, t)$ is defined by as follows.

$$\begin{aligned}\Phi(x, y, t) = &\left(\frac{g}{k^3}\right)^{1/2} \varepsilon\, e^{ky} \sin k(x - c\,t) \\ &- \frac{1}{2}\left(\frac{g}{k^3}\right)^{1/2} \varepsilon^3\, e^{ky} \sin k(x - c\,t) + \frac{1}{2}\left(\frac{g}{k^3}\right)^{1/2} \varepsilon^4\, e^{ky} \sin k(x - c\,t) \\ &+ \varepsilon^5 \left(\frac{g}{k^3}\right)^{1/2} \left(\frac{-37}{24} e^{ky} \sin k(x - c\,t) + \frac{1}{12} e^{3ky} \sin 3k(x - c\,t)\right) \\ &- \frac{2\pi}{T\sqrt{gk}} + 1 + \frac{1}{2}\left(\frac{kH}{2}\right)^2 + \frac{1}{8}\left(\frac{kH}{2}\right)^4 = 0\end{aligned} \tag{4.41}$$

where $\varepsilon = k\,H/2$, $c = 2\pi/k\,T$, H is the wave height, and T is the wave period.

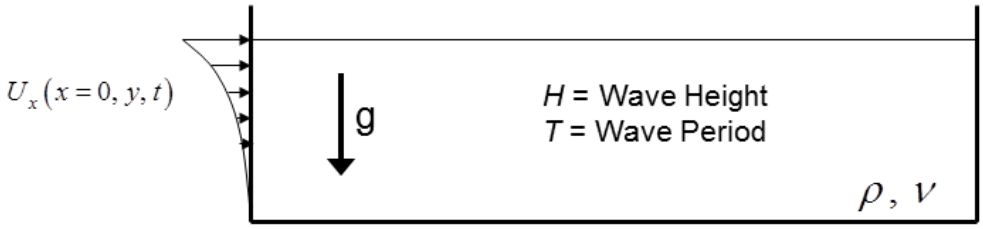

Figure 4.3 Schematic diagram of the problem description with inflow profile [13]

The computational domain is two dimensional with 1025 nodes in the horizontal direction and 258 nodes in the vertical. The upstream vertical boundary is forced with the solution of [47], whereas on the downstream vertical and lower boundaries a zero velocity condition is imposed. The length of the domain is 8000m, and hence, during the simulations reflected waves do not contaminate the wave field.

Figure 4 shows two representative snap-shots of the surface profile. In this simulation massless particles are seeded below the surface to highlight the near surface amplification of the particle motion due to the propagating free-surface waves. Fig. 5 shows the surface profile as a function of time at three locations within the domain. The figure shows that as expected a large wave develops at the front of the wave train, but that after this the wave crests and wave troughs are in good agreement with [47]. The figure also shows that there is no significant numerical dissipation of wave energy within the domain. Fig 6 compares the simulated surface profile over one wave length to the Stokes V solution. The plot shows

that the wave length and the elevation of both the wave crest and the wave trough are all in excellent agreement, but that there are some small differences in the shape of the wave profile.

In free surface flows, wave celerity is the velocity at which the free surface waves propagate. Fig 7 shows contours of surface elevation. The solid and dashed black lines represent the wave celerity group and deep water wave group celerity, respectively. The plot demonstrates that, as the solid black line overlies a wave crest, the waves are propagating at the correct nonlinear wave speed. This is also evident in Fig 5 as the wave profiles overlie one another.

Finally, Fig 8 shows the profile of horizontal velocity through depth over half a wave period. The results of the numerical simulation are compared to the Stokes V solution under the wave crest and can be seen to be in excellent agreement. The only unexpected feature evident in the simulation is a small positive kink in the velocities right at the water surface.

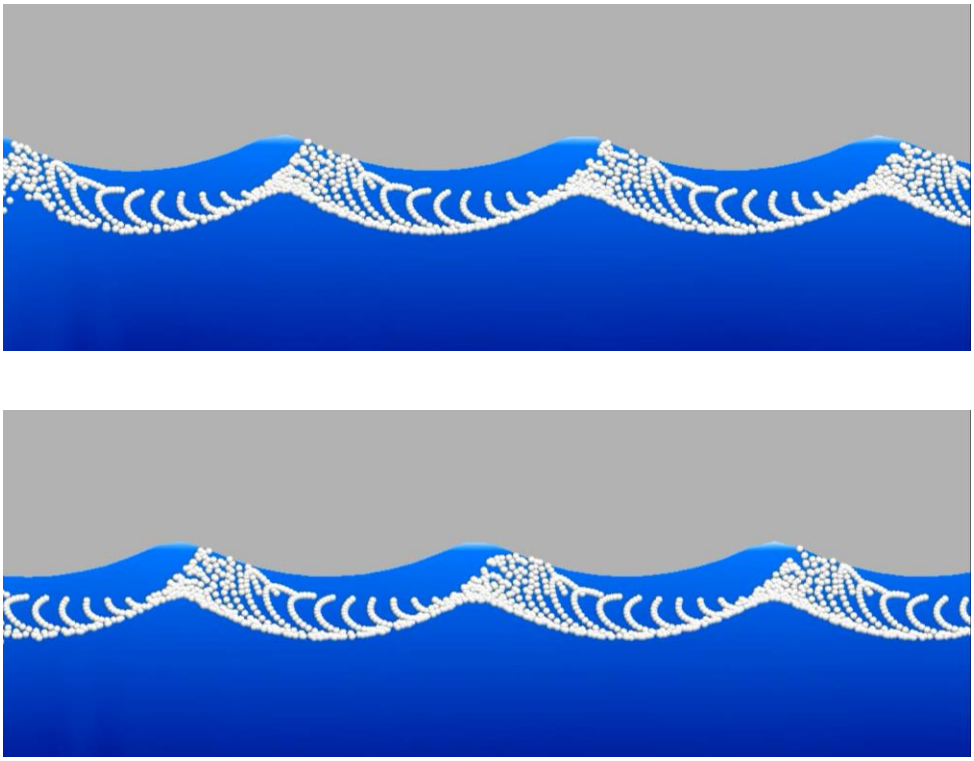

Figure 4.4 Two snapshots of free-surface waves with massless particles showing the near-surface motion of fluid particles

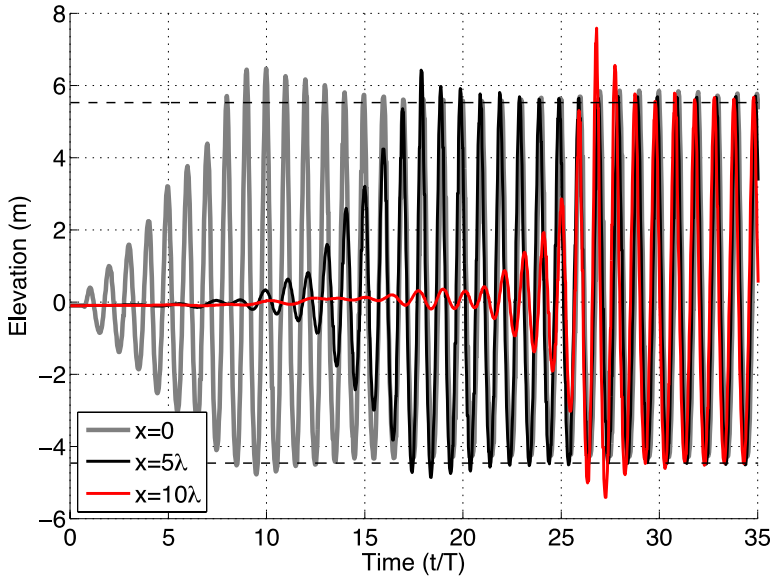

Figure 4.5 Variation in the surface profile in time at three locations within the domain. The horizontal dashed lines represent the elevation of the wave crest and wave trough using the analytical solution of [13]

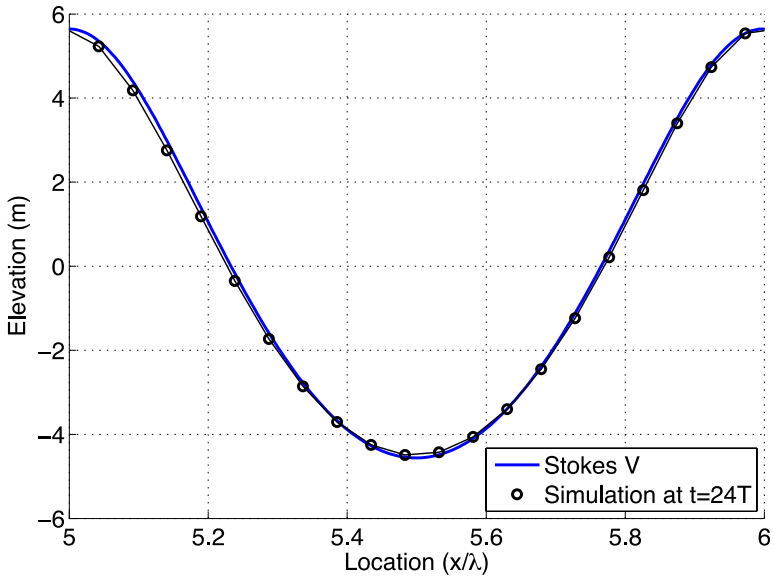

Figure 4.6 Surface profile over one wave length compared to a Stokes V solution [13]**.**

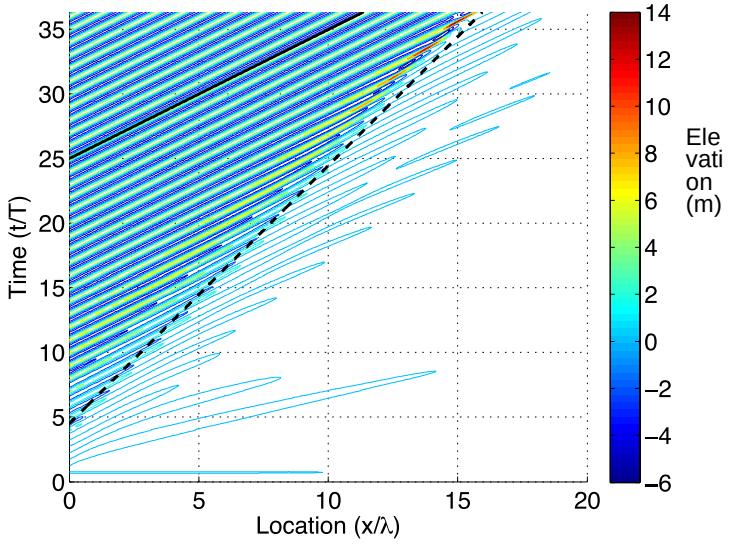

Figure 4.7 Contours of surface elevation. The solid black line represents the wave celerity, and the dashed black line the deep water wave group celerity**.**

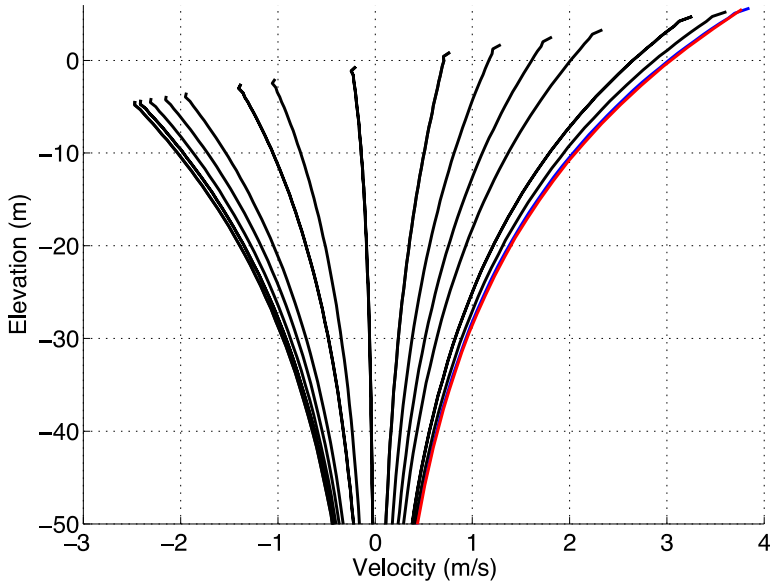

Figure 4.8 Horizontal velocities through a half wave period at x = 5λ and t = 24T. The blue line is the simulated velocity profile under the wave crest and the red line the corresponding Stokes V solution

4.4.2. Flat Open Turbulent Channel Flow

This test case models an open channel flow with a flat bottom surface. This problem was studied by Pan and Banerjeea [129] and Nagaosa [122] wherein they treated the free surface as a rigid wall with

free-slip boundary condition that precluded the deformation of the free surface. In this paper we use the formulation presented in the previous sections that considers the top surface as a freely evolving boundary, and we numerically compute the evolving free surface configurations.

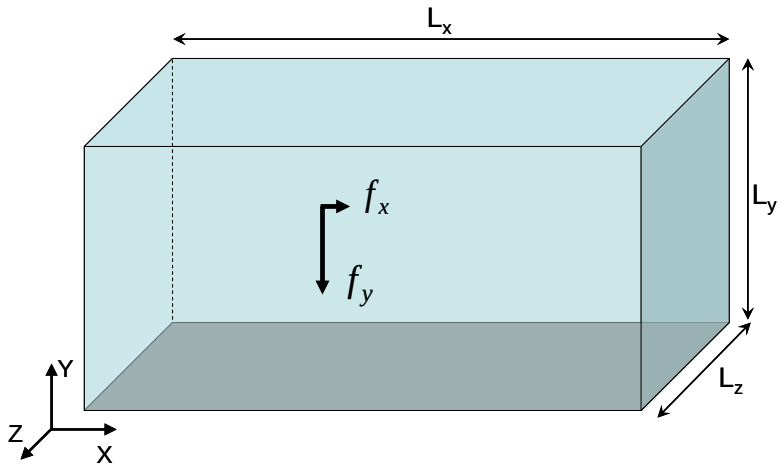

Figure 4.9 Schematic diagram of the channel problem with a flat bottom

The computational domain studied is schematically represented in Fig. 9. The length of the domain is $L_x = 6$, width $L_z = 4$, and height $L_y = 1$. We apply zero velocity on the bottom surface, while the top surface is considered to be a free surface. Periodic boundary conditions are applied on the lateral surfaces, and this assumption can be made because the flow is statistically uniform in the *x* and *z* directions. The viscosity of the fluid is set equal to 0.0001472. The problem is driven by a constant body force. The slope of the channel is set equal to $1/80$ and $1/40$ in Sec 4.2.1 and 4.2.2, respectively.

We study the flow using three meshes of $32 \times 32 \times 32$, $64 \times 32 \times 64$ and $64 \times 64 \times 64$ hexahedral elements. The elements are uniformly distributed in the *x* and *z* directions and graded on the *y* direction. The grading is obtained using a hyperbolic distribution that clusters more nodes near the fixed wall and is given by the following expression:

$$y_i = 1 - \frac{\tanh\left(\gamma\left(1 - i/N\right)\right)}{\tanh\left(\gamma\right)} \tag{4.42}$$

where γ is set equal to 1.5 for all the cases, N is the number of elements in the wall-normal direction and $i \in [0, N]$. The time step size Δt is set equal to 0.025 for all the test cases.

The flow is initialized with a stream-wise parabolic velocity field that is randomly perturbed in the x and z directions by less than 10% of the parabolic mean velocity. After a transitory regime in which the turbulence structures develop and the free surface starts to evolve, the flow reaches a statistically steady state regime. The solution field is then sampled every 10 time steps for a period of 5000 steps. The sampled solution is averaged over time and also in the stream-wise and span-wise directions. The statistics were computed on the mesh nodes and not on a background Eulerian mesh because of the complexity arising due to the evolving free-surface levels. This procedure is also consistent with the approach adopted in the reference results that are used for validation purpose [170]. Also as the reviewer points out, the "Eulerian" statistics are not straightforward to calculate near the free surface because the surface level evolves in time.

4.4.2.1. Channel with flatter slope

The first test case has a slope of the bottom surface equal to $1/80$ that gives rise to body force components $f_x = 0.00337204$ and $f_y = -0.2697632$. The y-axis is through the depth axis and has its origin at the bottom of the channel. The Reynolds number of the flow based on Taylor's micro-scales is 395.

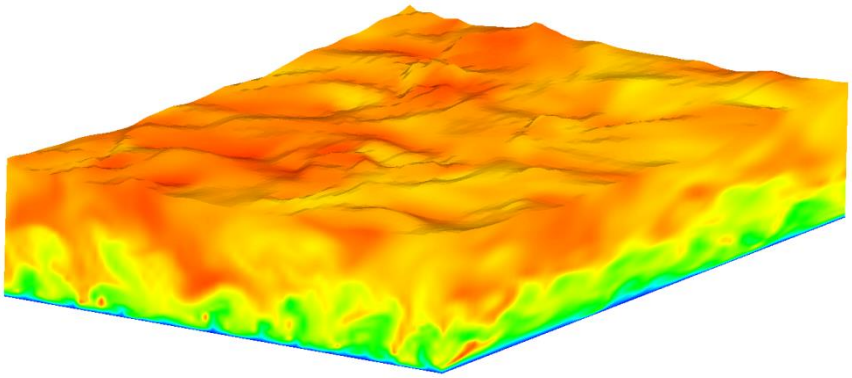

Figure 4.10 Instantaneous velocity field for the channel with slope $1/40$

For the channel with $1/40$ slope, Fig. 10 shows the geometry of the problem and velocity field at a typical time point.

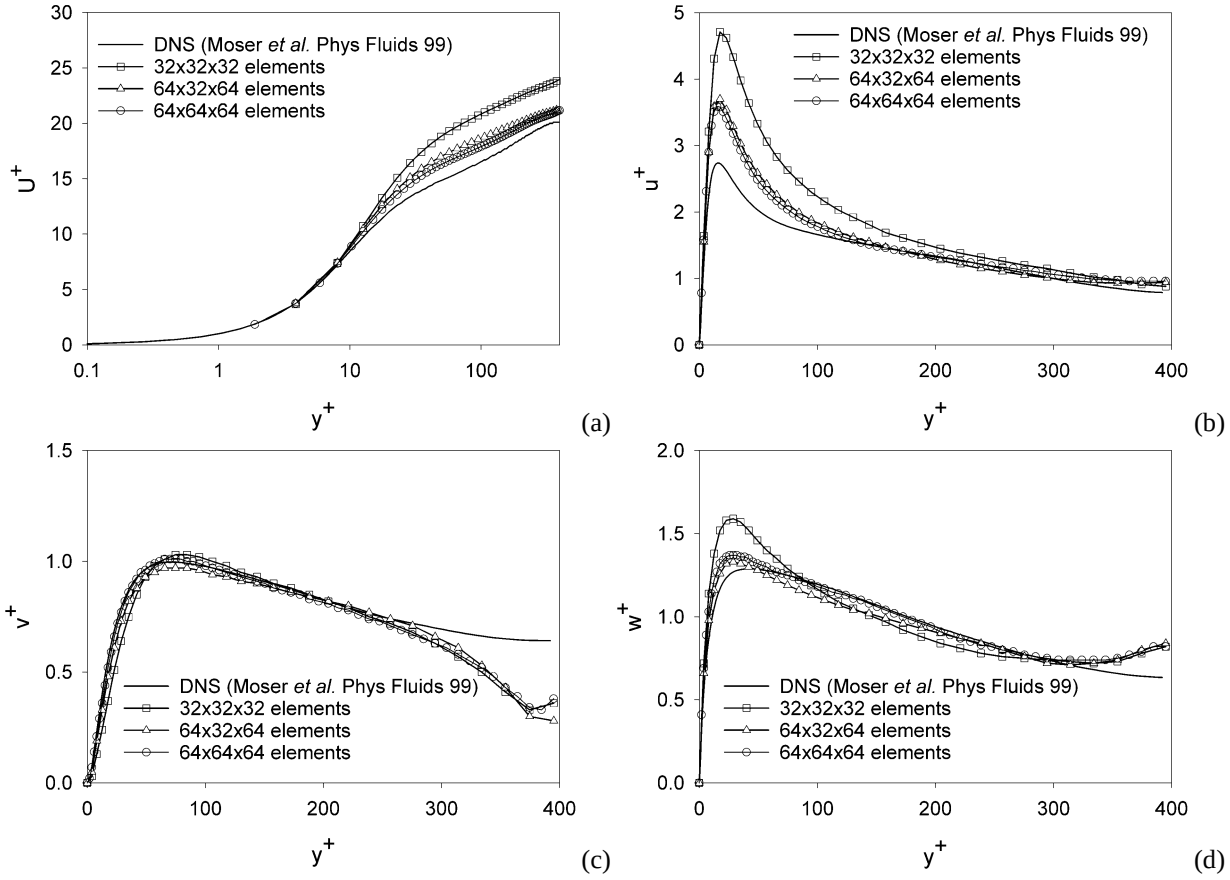

Figure 4.11 Mean velocity and RMS fluctuations along the wall normal direction for the channel with $1/80$ slope

Figure 11 shows the mean velocity and the root mean square of its fluctuations in each of the three spatial dimensions. In addition to showing the results obtained with each of the three meshes employed, Fig. 11 also shows the DNS results for the lower half part of an equivalent confined turbulent channel flow [121].

Near the wall, the statistics of the confined channel are very close to the statistics of the open channel. This is due to the fact that the effects of the free surface diminish with depth. Closer to the free surface, the results from the confined channel are different from the results for the open channel because

open channel has a free surface, while the confined channel has fluid domain in the top half of the channel above the pseudo free surface. The effect of the free surface is clearly evident in the fluctuations of the velocity field in the wall-normal and span-wise directions, i.e., Fig. 11(c) and Fig. 11(d), respectively. All the results presented in Fig. 11 are expressed employing wall units [134]. The second column of Table 1 shows the Froude number of the flow, which is a measure of the ratio between inertial and gravity forces, and is defined as

$$Fr = \frac{U_O}{\sqrt{f_y L_y}} \tag{4.43}$$

where U_O is the mean velocity of the free surface, f_y is the vertical component of the body force vector, and L_y is the depth of the channel. For the uniform channel problem, $L_y = 1$.

Table 4.1 Froude number of the flat open channel flow

Mesh	Lowest slope	Highest slope
$32 \times 32 \times 32$	2.68	3.87
$64 \times 32 \times 64$	2.39	3.46
$64 \times 64 \times 64$	2.37	3.34

4.4.2.2. Channel with steeper slope

The same study was carried out for a channel with stepper slope of $1/40$. The components of the body force are set to $f_x = 0.00337204$ and $f_y = -0.134882$. The Reynolds number of flow based on Taylor's micro-scales is 395. Figure 12 shows the statistics of the flow in which the computed solution shows similar features as in the previous case. While near the wall the results are similar to the statistics of the confined turbulent channel, the effects of the free surface are more pronounced near the upper surface. The third column of Table 1 shows the Froude number obtained with each of the three meshes. As expected, Froude number is higher than in the previous case because the channel is steeper, and therefore inertial force is more significant than the gravitational force.

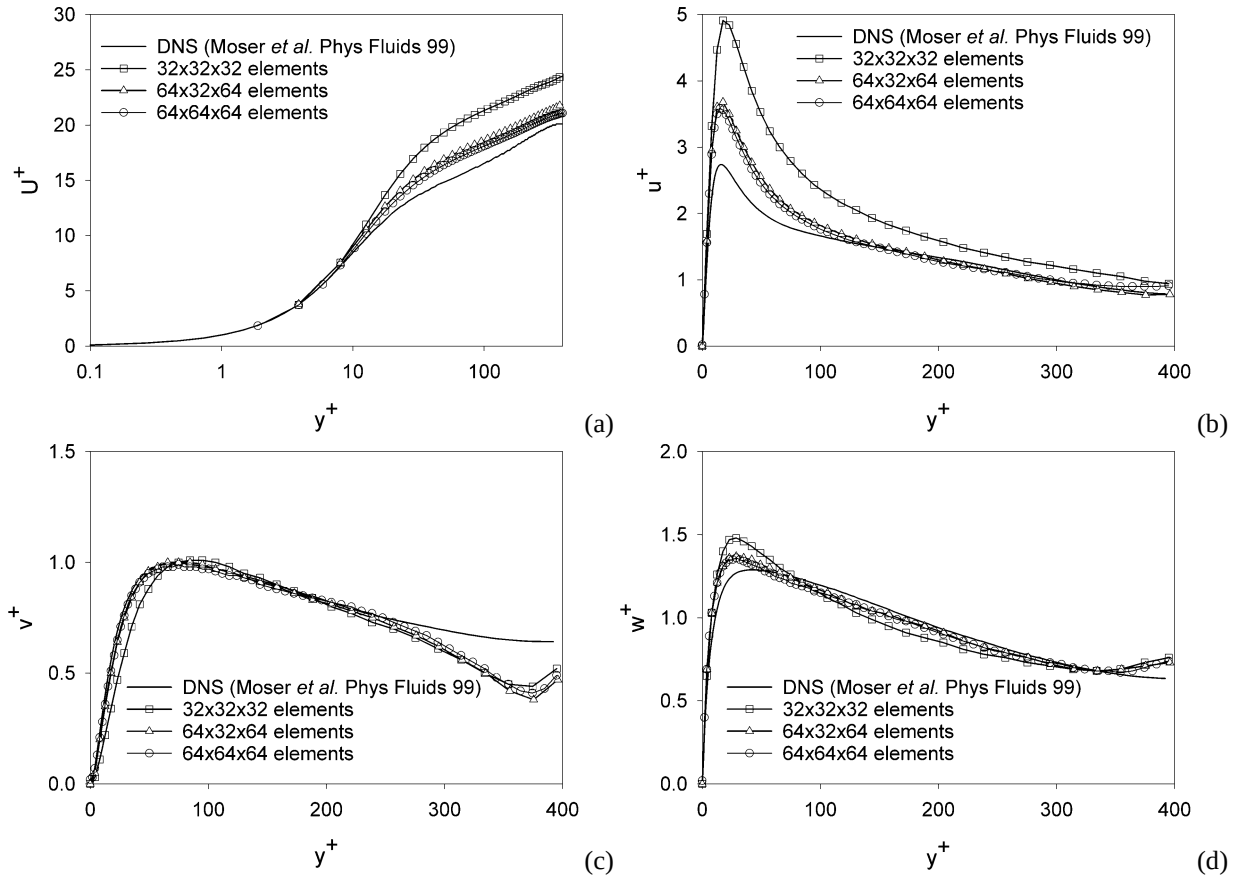

Figure 4.12 Mean velocity and RMS fluctuations along the wall normal direction for the channel with $1/40$ slope

We use the consistent tangent tensor for the fluid problem. Since the flow features induced by surface motions are relatively less intense as compared to the complexity of the turbulent flow, the convergence rate is close to being quadratic. Table 2 shows the evolution of the residual as a function of the iteration number for the flat open channel flow problem at higher Froude number. The results shown in the table correspond to the mesh that has $64 \times 64 \times 64$ elements. Depending on the time level considered, the solution converges in 4 iterations levels.

Table 4.2 Residual reduction in Newton-Raphson scheme for the flat open channel flow at higher Froude number. The residual is reported at the end of each fluid iteration.

Iteration number	t = 827.15	t = 829.40	t = 831.65
1	2.040×10^{-1}	2.038×10^{-1}	2.098×10^{-1}
2	1.131×10^{-4}	1.112×10^{-4}	1.218×10^{-4}
3	8.789×10^{-8}	8.508×10^{-8}	8.786×10^{-8}
4	2.523×10^{-11}	2.378×10^{-11}	4.461×10^{-12}
5	2.693×10^{-14}	3.660×10^{-14}	-

4.4.3. Turbulent Channel Flow with Wavy Bed

This test problem is also an open channel flow, however with a non-flat bed. The bottom of the channel has a shape that resembles a fixed sand dune. This problem was proposed by Balachandar and Patel [3] who studied deep water flows experimentally, and by Yue and co-workers [170], who analyzed the problem computationally. We consider the same problem specifications as in these references and compare our results with the published data. In addition, we also analyze this problem at a higher Froude number to show the applicability of the present method to problems where free surface undergoes larger and irregular deformations due to the interaction of bottom generated turbulence with the top free surface.

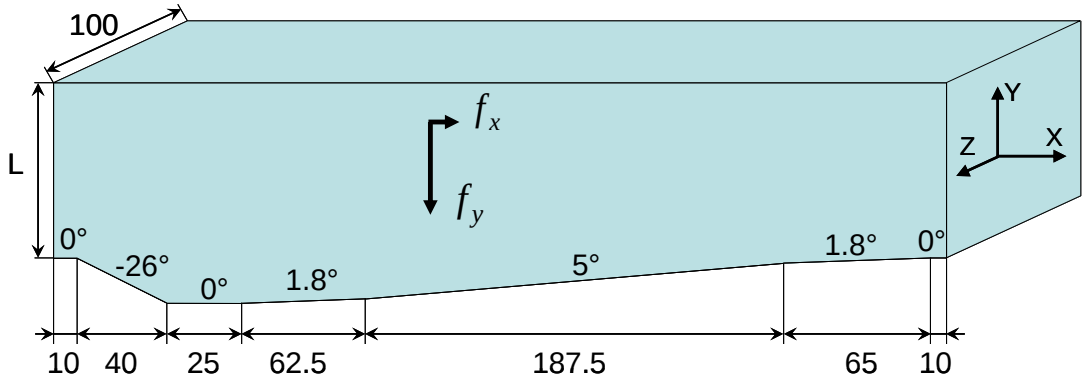

Figure 4.13 Schematic diagram of the channel problem with a wavy bottom surface

The computational domain employed in our studies is schematically represented in Fig. 13, and the precise locations of its key sections are given in Table 3. The bottom boundary surface approximates the shape of a sand dune, with no-slip boundary conditions imposed. On the lateral walls, periodic boundary conditions are applied, and this assumption can be made because the flow is statistically

uniform in the x and z directions. The top boundary is located at a distance L from the crest of the dune and is considered to be a free surface. The viscosity of the fluid is set equal to 1.

Table 4.3 Coordinates of key locations of the bottom surface of the wavy channel

x-coordinate	*y*-coordinate	Comment
0	0	Periodic boundary
10	0	Change of slope
50	-20	Change of slope
75	-20	Change of slope
137.5	-18.1174	Change of slope
325	-1.95791	Change of slope
390	0	Change of slope
400	0	Periodic boundary

4.4.3.1. Lower Froude number flow

With the goal of comparing our results with the existing data [43, 3], we set the depth $L=132$, and apply a gravitational body force of magnitude 981. The channel is inclined at a mean angle of 2.56° that results in body force components $f_x=0.7651799$ and $f_y=-980.9997$. The domain is discretized using $80\times64\times64$ hexahedral elements that are evenly distributed in the *x* and *z* directions. As shown in Fig. 14, the elements are graded through the depth of the channel in the *y* direction. The top 5 layers of elements have a height of $4/5$, the remaining elements are distributed using a hyperbolic function (4.44), in which $\gamma=1.75, L=132$, and *N*=59.

$$y_i=\left[1-\frac{\tanh\left(\gamma\left(1-i/N\right)\right)}{\tanh\left(\gamma\right)}\right](L-4) \tag{4.44}$$

The time step size Δt is set equal to 0.015.

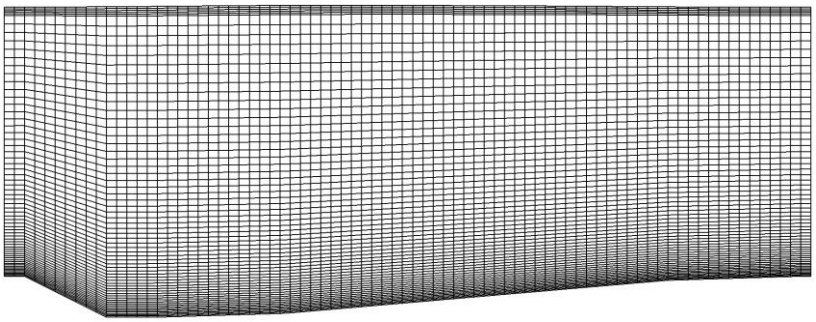

Figure 4.14 Transversal view of the mesh for the wavy channel with depth L=132

The problem is initialized from at rest conditions and it evolves until it reaches a statistically steady state regime. Figure 15 shows the fully developed velocity field. It can be observed that the motion of the free surface is relatively small. To compute the statistics of the flow, we sample the solution every 10 time steps over a period of 5,000 steps. In addition to averaging the solution over all the sampled time steps, we average it along the span-wise direction. Figure 16 shows the averaged geometry and velocity fields, and the mean velocity streamlines. The mean flow has a recirculation zone downstream of the dune, which starts at $x = 10$ and ends at $x = 104$. The length of the recirculation zone agrees well with the LES-based result of $\Delta x = 90$, reported by Yue and co-workers [170]. The Froude number based on the mean velocity of the free surface at $x = 0$ is 0.42. Figure 17 shows the mean velocity of the flow at 6 vertical cross sections along the length of the channel. The results are compared with the experimental data reported by Balachandar and Patel [3] and the computed results on a similar mesh reported by Yue *et al.* [43] employing a dynamic Smagorinsky model. Our results agree well with the existing data. The LES results [43] are plotted beyond $y/L = 1$ because they considered a layer of air on top of the open channel. The results show that the layer of air, which adds to the inertia at the free surface, still does not have a significant effect on the results for the case under consideration. Figure 18 shows the root mean square of the fluctuations of the velocity field in the stream-wise direction at several cross sections. In this case, a very good agreement with previously published results is also observed.

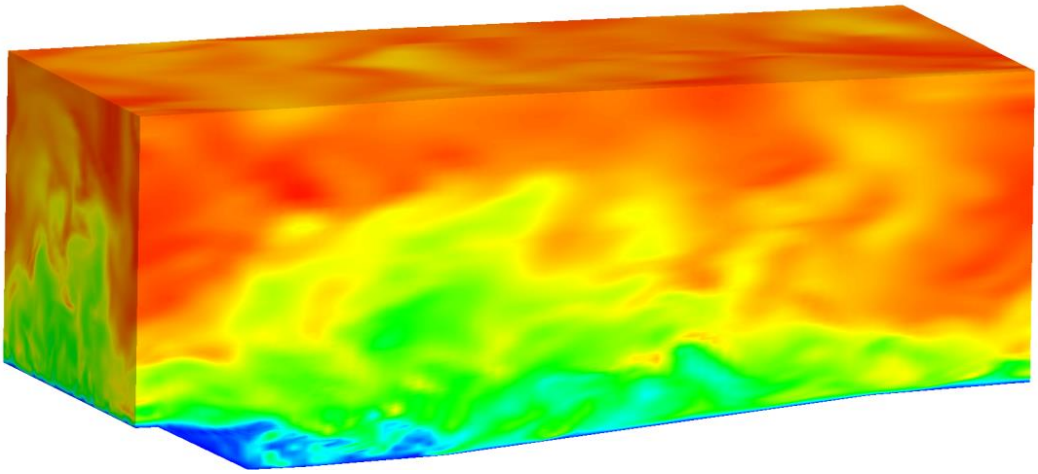

Figure 4.15 Instantaneous velocity field for channel with depth L=132

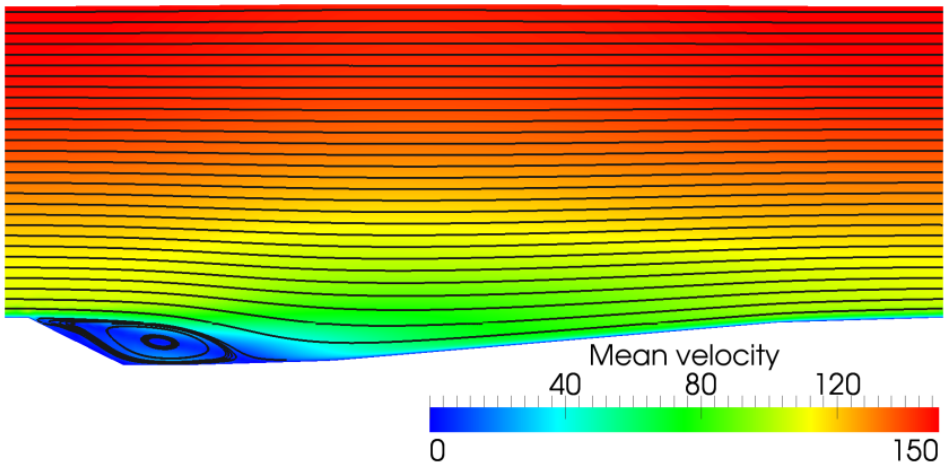

Figure 4.16 Mean velocity field for channel with depth L=132

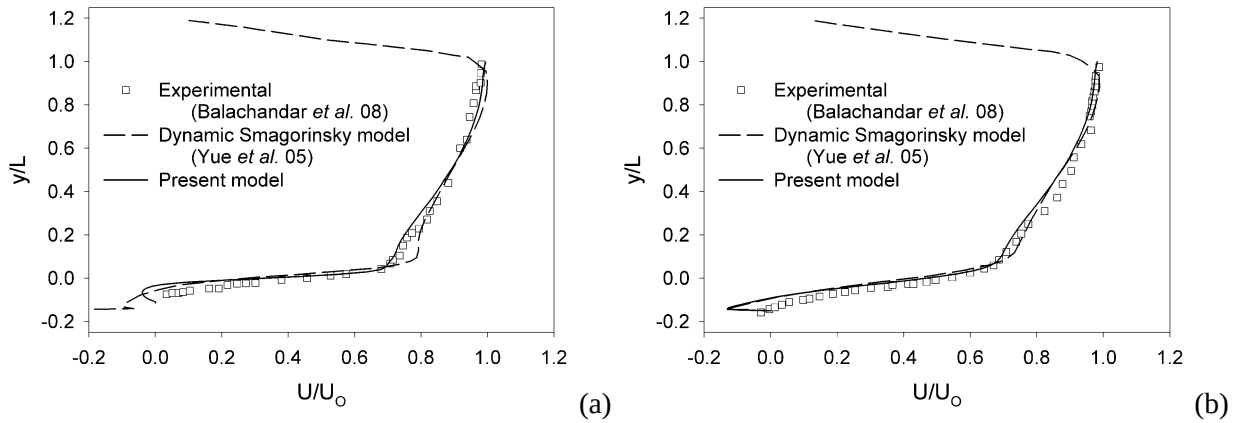

Figure 4.17 Mean velocity along the y-coordinate for channel with depth L=132, (a) x =40, (b) x=80, (c) x =100, (d) x =120, (e) x =240 and (f) x =360

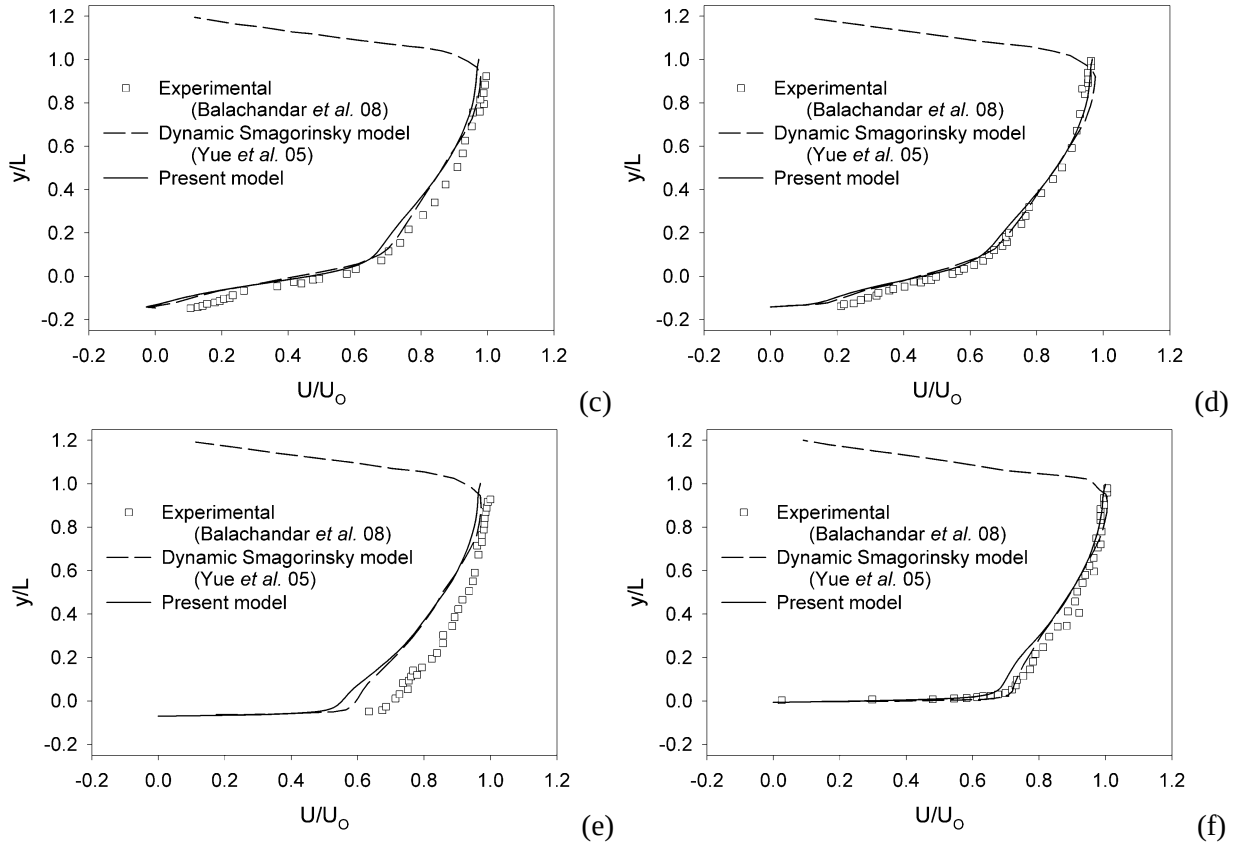

Figure 4.17 (cont.)

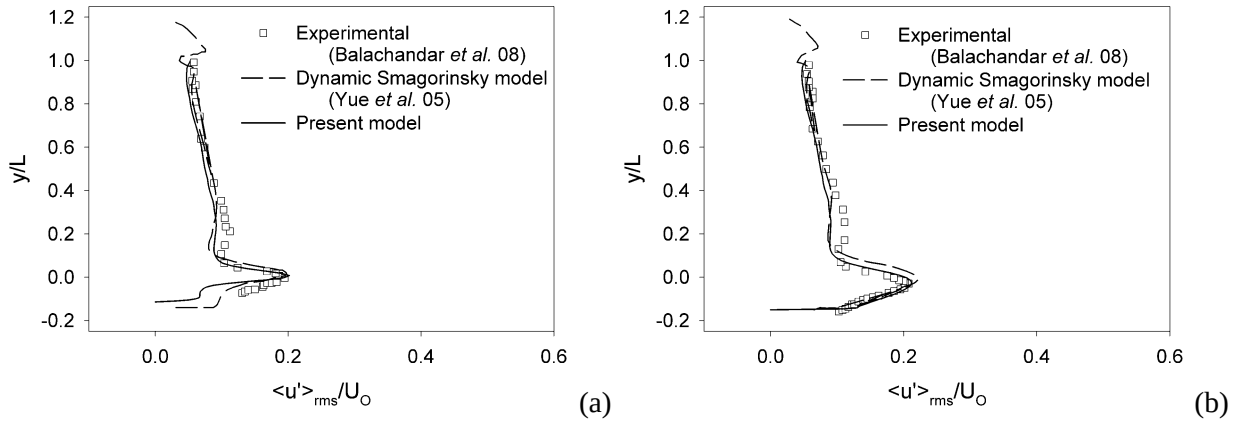

Figure 4.18 RMS fluctuations of the steam-wise velocity field along the y-coordinate for channel with depth L=132, (a) x =40, (b) x=80, (c) x =100, (d) x =120, (e) x =240 and (f) x =360

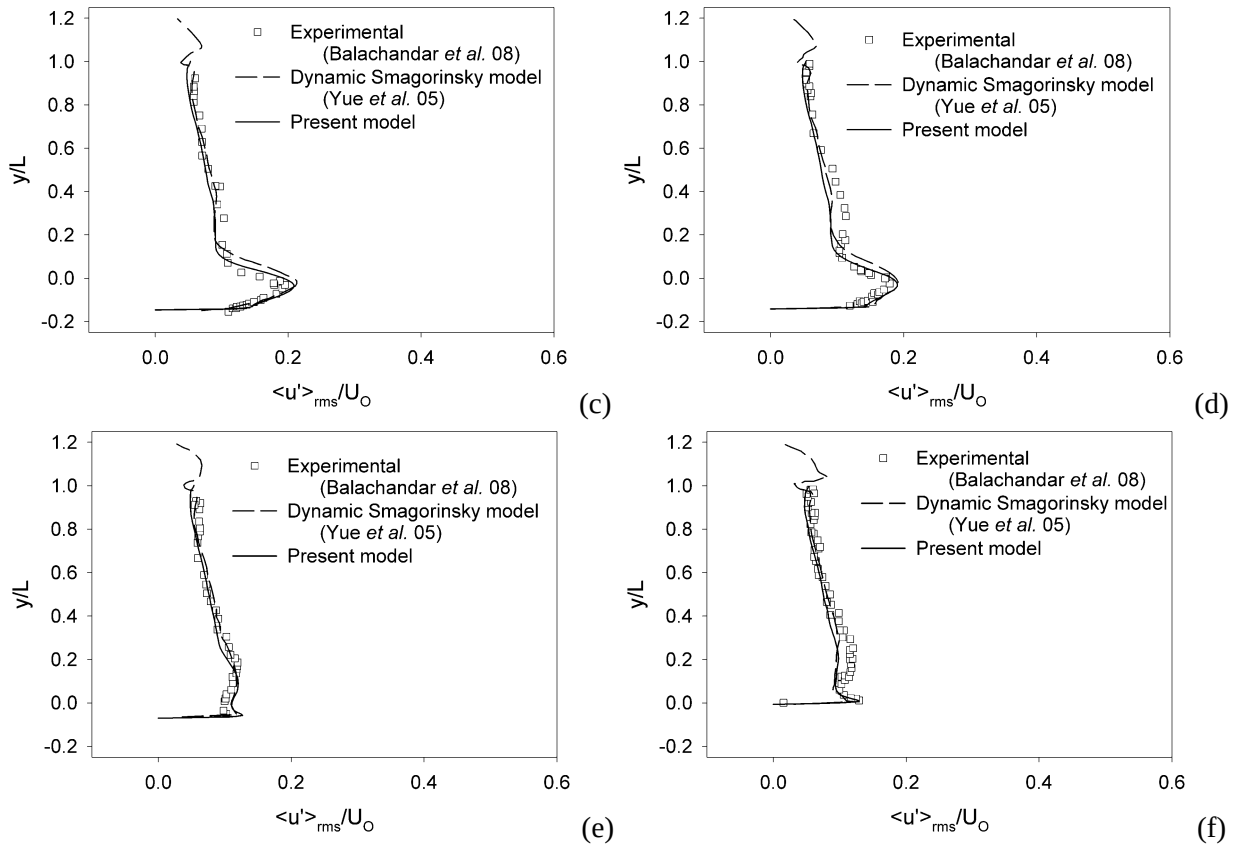

Figure 4.18 (cont.)

4.4.3.2. Higher Froude number flow

The next problem that we analyze is a harder problem as it has shallower depth and a steeper slope. Due to the shallower depth the turbulence generated at the bed of the channel interacts with the free surface thereby causing irregular and chaotic free surface motion. Furthermore, steeper slope leads to higher Froude number flow. We set the depth of the channel L equal to 20, along with a mean inclination of the channel at 13.39°. The components of the body force are $f_x = 4.0$ and $f_y = -980.992$. Other parameters of the problem are same as in the previous case. The mesh employed in the present test is developed following the same guidelines as in the previous test case, and it is comprised of $80 \times 54 \times 48$ hexahedral elements. The time step size is set equal to 0.01. Figure 19 shows the velocity field in the fully developed regime. In this test case, the free surface undergoes larger motions. As can be seen in Fig. 19b, the fluid accelerates downstream from the sand dune, and therefore the depth of the fluid column

decreases locally. Further downstream of this region, fluid velocity slows down because of the obstruction in the form of a gradual sand dune. Consequently, in this region the depth of the channel increases.

The statistically averaged solution is represented in Fig. 20, in which the streamlines of the velocity field also show the presence of a recirculation region downstream of the first dune. The Froude number based on the computed flow is 0.69. Vertical profiles of the stream-wise velocity field and its fluctuations are represented in Figs. 21 and 22, respectively.

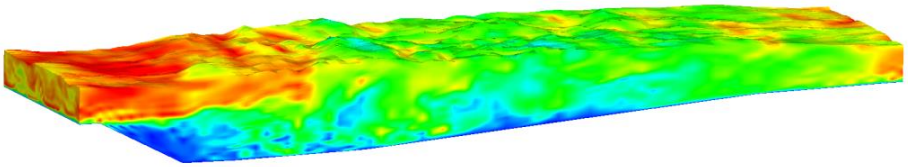

(a)

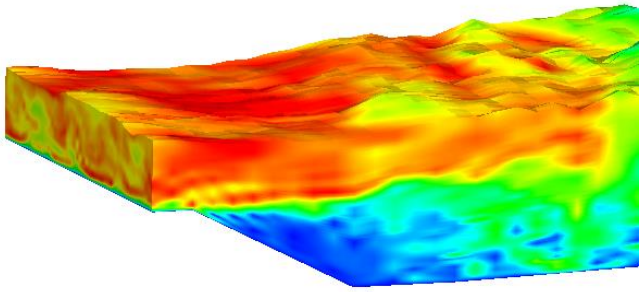

(b)

Figure 4.19 Instantaneous velocity field for channel with depth L=20

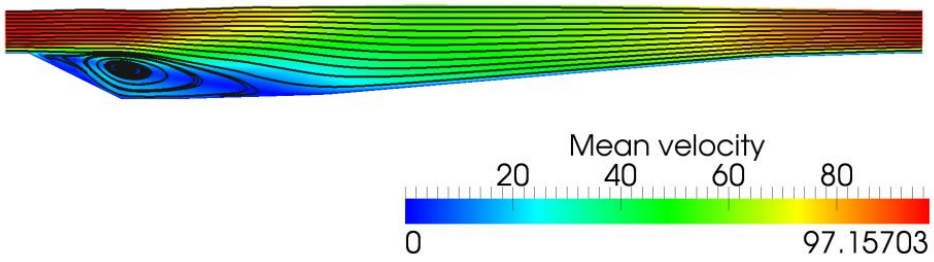

Figure 4.20 Mean velocity field for channel with depth L=20

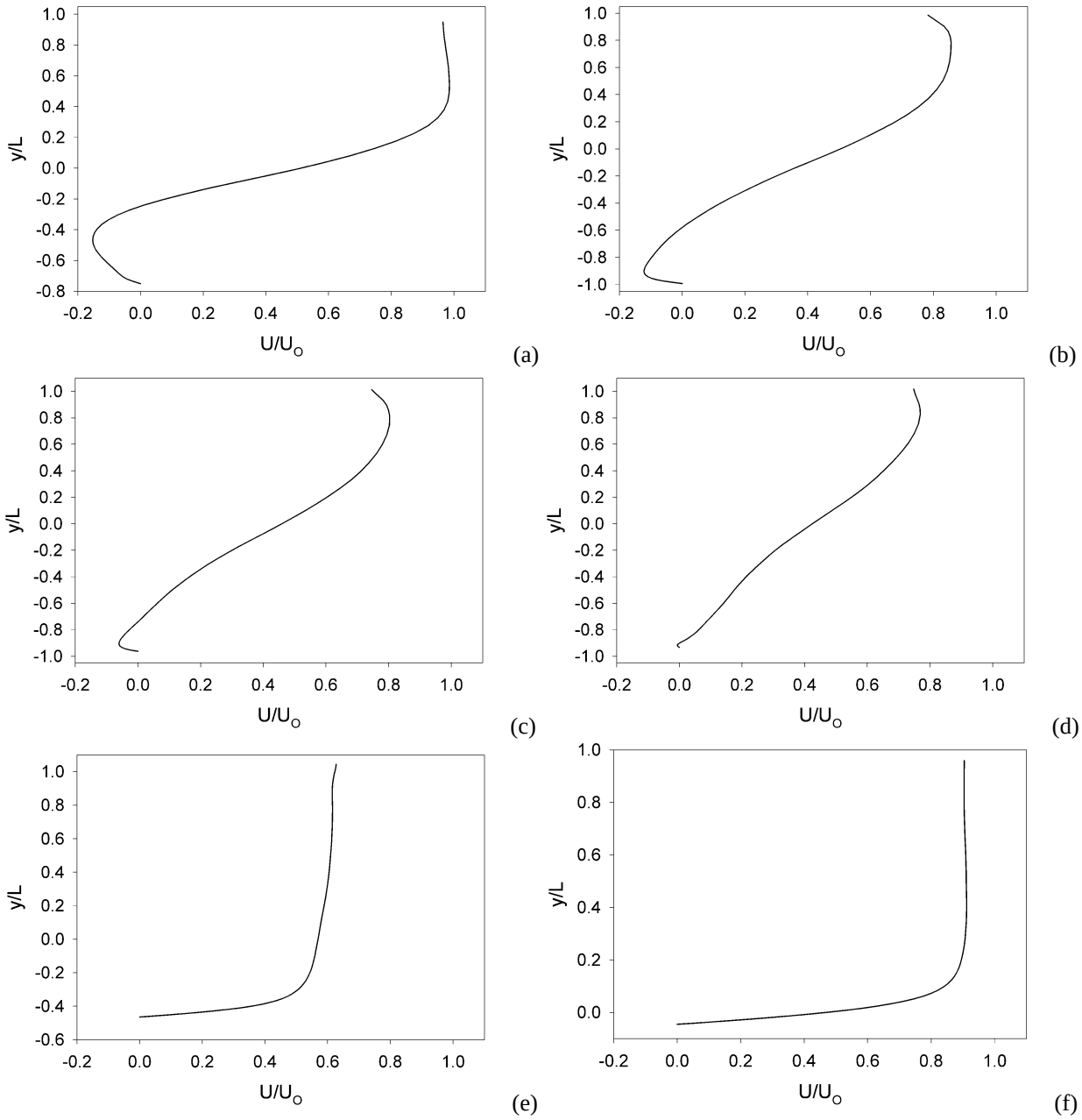

Figure 4.21 Mean velocity along the *y*-coordinate for channel with depth *L*=20, (a) *x* =40, (b) *x*=80, (c) *x* =100, (d) *x* =120, (e) *x* =240 and (f) *x* =360

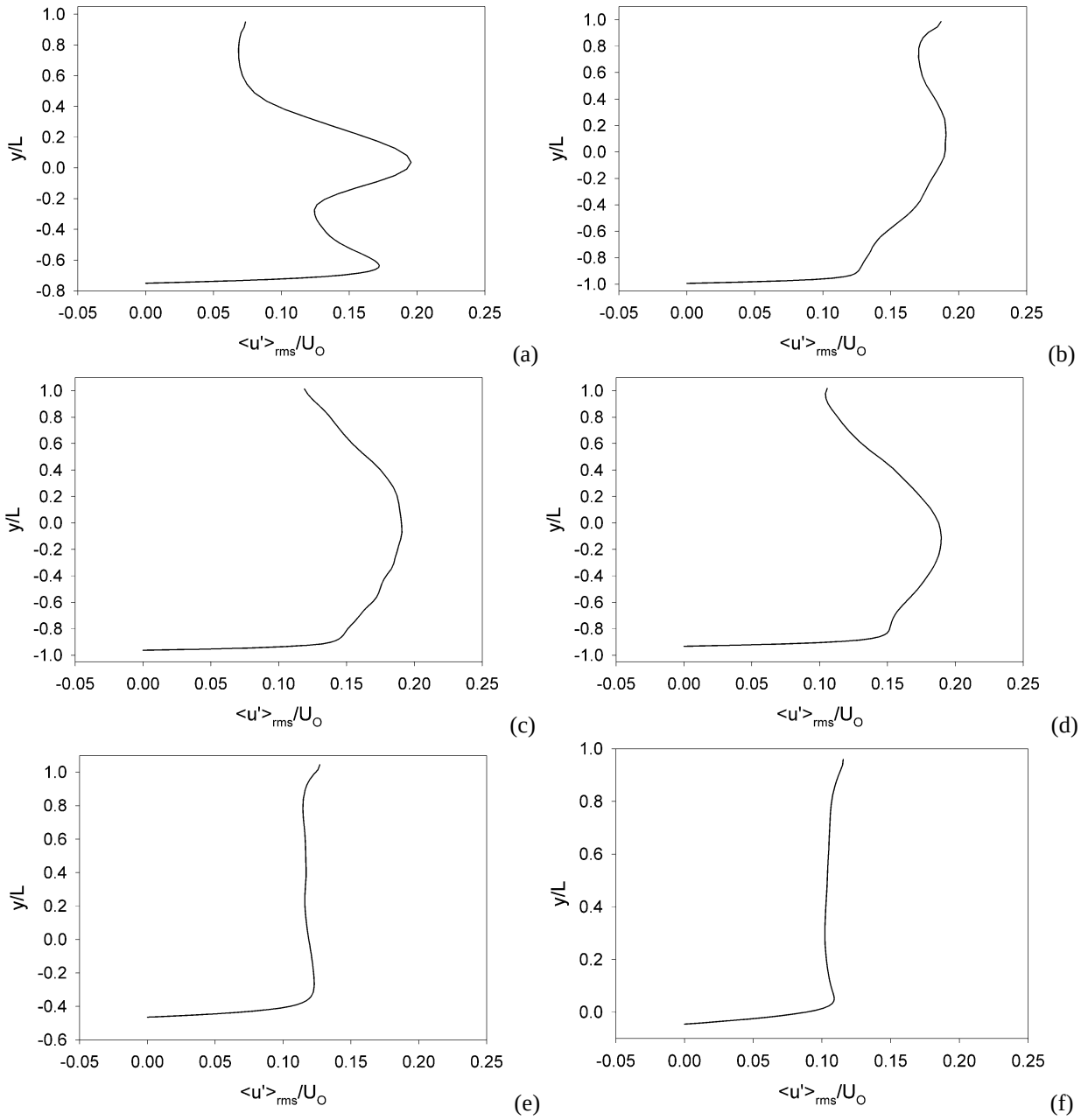

Figure 4.22 RMS fluctuations of the steam-wise velocity field along the *y*-coordinate for channel with depth *L*=20, (a) *x* =40, (b) *x*=80, (c) *x* =100, (d) *x* =120, (e) *x* =240 and (f) *x* =360

4.5. CONCLUSIONS

We have presented an extension of our previous work on residual-based turbulence models for problems with moving boundaries [108] to a formulation that is able to accommodate free surface problems. The method has been derived assuming a multiscale decomposition of the velocity and pressure fields into coarse and fine scales. This leads to two coupled mixed-field problems. The mixed-field fine-

scale problem is stabilized by a further decomposition of the fine-scale velocity field into level-I and level-II fine scales. The problem governing level-II scales is modeled using forth order bubble functions, and its solution is variationally embedded in the problem that governs the level-I scales. The stabilized level-I fine scale problem is solved using quadratic bubble functions as interpolation functions for the level-I velocity and pressure fields. The derived level-I model that approximates the fine-scale fields is variationally embedded in the coarse-scale problem and these terms model the effects of the sub-grid scales on the resolved scales. The bubble function approach employed to model the two fine-scale problems leads to a formulation that does not have any embedded or tunable parameters. The formulation is applied to study two free surface flow problems to show the applicability of the method. The first test case is a flat open channel with a fixed boundary on the flat bottom surface, periodic boundaries on the lateral walls, while the top boundary is a free surface. The flow is driven by a gravitational body force. Two different inclinations of the channel are considered, and the mean velocity field and its root mean square fluctuations are reported over the depth of the channel. The second problem investigated is an open channel flow with a wavy bottom boundary. Two different depths of the channel are investigated, and the results obtained are compared with the experimental and numerical results reported in the literature [9,170]. These numerical tests show the stability and accuracy of the proposed formulation for modeling free surface flows. Specifically the wavy bed problem that involves interaction of interior turbulence with free surface elevation shows the robustness of the method for irregular free surface flows.

CHAPTER 5: MULTILEVEL VARIATIONAL MULTISCALE LARGE-EDDY TURBULENCE MODEL FOR ISOTHERMAL FLUID

5.1. INTRODUCTION

Boundary layer theory and flow separation are now well understood. However, these phenomena in the presence of turbulence are still open-ended research issues. Main issue is that turbulence precludes the use of any simplifying assumptions and necessitates the solution of NSE in all generality, thereby leading to DNS. In order to economize DNS calculations, a common practice is to inject ad hoc models into NSE that induce high wave-number dissipation. These models in turn introduce artificial length scales and modeling parameters that are applicable only in certain scenarios. This issue of ad hoc or intuitive models has been the bottleneck in the modeling of turbulence.

A literature review reveals Subgrid-Scale (SGS) Models for Large Eddy Simulation (LES), wherein the equations for LES are derived from NS equations with low-pass spatial filters [52,140]. The discretization filtering operator is called implicit filter. The flow motion is then divided into two parts: the resolved motion and the subfilter-scale motion (SFS). The scale of the flow motion smaller than the grid size is referred to the unresolved SFS motion, or subgrid-scale (SGS) motion. For the SGS motion, a closure model is required to link the SGS motion effect to the resolved SFS. In most of the engineering applications, the implicit filter is the only one filter used in the LES modeling. However, the filter width, filter shape, and filter resolution are free parameters in LES and narrowing them down for a problem at hand is neither easy nor straightforward.

In light of these limitations, modern fluid mechanics calls for theoretical and mathematical developments for deriving high-fidelity numerical methods with enhanced stability properties to be able to explain the complex behavior of turbulent flows.

In this paper we present the derivation of closure model for LES that is based on the notion of the Variational MultiScale (VMS) method [17,66,67]. VMS was introduced by Hughes as a framework to develop stable and accurate numerical approximations of partial differential equations, preventing

numerical instabilities that arise when the standard Galerkin Finite Element (FE) method is used. In the context of the incompressible Navier–Stokes equations there are two well-known instabilities. First, there is the need to satisfy a compatibility between velocity and pressure approximation spaces, i.e., the inf–sup condition [16], which is not satisfied when equal order interpolation is used. Second, we have the instabilities that appear when convective dominated flows [20] are simulated, which can be solved by adding some kind of extra dissipation to the problem. There is also a much less known loss of accuracy in the discrete velocity due to poor mass conservation which can be linked to a poor resolution of the pressure typical of mixed interpolations that satisfy the inf–sup condition.

We have developed residual based turbulence models for LES. It is based on exploiting the fine-scale variational structure facilitated by the VMS framework and then embedding ideas from the Residual-Free Bubbles (RFB) method [84,107,108] directly at the fine-scale level. This merger of RFB with VMS results in a new and more powerful method that facilitates great flexibility in variationally deriving LES type models for turbulence. A significant attribute of the new approach is that it does not need filter functions that invariably cause problems near the walls of the computational domain. Furthermore, contrary to the ad hoc models employed in traditional LES techniques, residual based turbulence models are consistent with the Navier-Stokes equations in the sense that if coarse-scales represent all the features of the flow, then the fine-scale terms vanish uniformly. From a numerical implementation perspective, the residual based turbulence models only involve element level computations thereby resulting in substantial ease in terms of implementation in existing CFD codes.

Flexibility of RFB yields many options for the derivation of the closure models that can then be variationally embedded in the mean solution in a mathematically consistent fashion. In this method there are no empirical or tunable parameters. This means there are no filter functions to be used anywhere in the mesh. Methods work for Tetrahedral and Hexahedral elements, and for fixed and moving meshes. Since there are no empirical models involved, the method can be viewed as DNS on cruder meshes, or as LES models but without an empirical induction of intuitive ideas.

In the numerical section we apply this method to several problems of engineering interest that possess an increasing degree of complexity. In particular, our turbulent flow studies have shown that: (i) our method is able to predict the correct energy decay in the sub-inertial range which is a desirable property for any LES method, (ii) model can accurately predict the behavior of wall-bounded flows, and (iii) our method can also be applied to more complex flows involving flow separation and reattachment, giving rise to flow reversals and separation bubbles. Computed results also compare very well with some of the state-of-the art LES models proposed in the literature.

5.2. INCOMPRESSIBLE NAVIER-STOKES EQUATIONS

The Navier-Stokes equations for the isothermal incompressible flows are

$$\frac{\partial \boldsymbol{u}}{\partial t} + \boldsymbol{u}\cdot\nabla\boldsymbol{u} - \nabla\cdot\left(2\nu\nabla^s\boldsymbol{u}\right) + \nabla p = \boldsymbol{f} \quad \text{in} \quad \Omega \tag{5.1}$$

$$\nabla\cdot\boldsymbol{u} = 0 \quad \text{in} \quad \Omega \tag{5.2}$$

where $\boldsymbol{u}:\Omega\times]0,T[\to\mathbb{R}^3$ is the velocity field and $p:\Omega\times]0,T[\to\mathbb{R}$ is the kinematic pressure field, $\nu>0$ is the kinematic viscosity, $\boldsymbol{f}:\Omega\times]0,T[\to\mathbb{R}^3$ is the body force (per unit of mass), and the symmetric gradient operator ∇^s is defined as $\nabla^s = 1/2(\nabla+\nabla^T)$. The domain $\Omega\in\mathbb{R}^3$ is connected, open and bounded with piecewise smooth boundary Γ. Eqn.(5.1) is the momentum balance equation and Eqn.(5.2) is the mass conservation equation in the form of incompressibility condition. The Dirichlet and Neumann boundary conditions, and initial condition are defined as

$$\boldsymbol{u} = \boldsymbol{g} \quad \text{on} \quad \Gamma_g \tag{5.3}$$

$$\left(2\nu\nabla^s\boldsymbol{u} - p\boldsymbol{I}\right)\cdot\boldsymbol{n} = \boldsymbol{h} \quad \text{on} \quad \Gamma_h \tag{5.4}$$

$$\boldsymbol{u}(\boldsymbol{x},0) = \boldsymbol{u}_0 \tag{5.5}$$

where $\Gamma = \Gamma_g \bigcup \Gamma_h$ and $\varnothing = \Gamma_g \bigcap \Gamma_h$, $\boldsymbol{g}$ is the Dirichlet boundary condition, $\boldsymbol{h}$ is the Neumann boundary condition and $\boldsymbol{u}_0$ is the initial solenoidal velocity field (i.e., $\nabla\cdot\boldsymbol{u}_0 = 0$).

Let $\boldsymbol{w}$ and q represent the weighting function for the velocity $\boldsymbol{u}$ and pressure q. The standard weak form of (5.1) and (5.2) with appropriate boundary conditions (5.3) and (5.4) and initial condition (5.5) is: Find $\boldsymbol{u}(\boldsymbol{x},t)\in\mathcal{W}_t$ and $p(\boldsymbol{x},t)\in\mathcal{Q}_t$, such that $\forall\boldsymbol{w}(\boldsymbol{x})\in\mathcal{W}$ and $\forall q(\boldsymbol{x})\in\mathcal{Q}$,

$$\left(\boldsymbol{w},\frac{\partial\boldsymbol{u}}{\partial t}\right)+(\boldsymbol{w},\boldsymbol{u}\cdot\nabla\boldsymbol{u})+(\nabla\boldsymbol{w},2\nu\nabla^s\boldsymbol{u})-(\nabla\cdot\boldsymbol{w},p)=(\boldsymbol{w},\boldsymbol{f})+(\boldsymbol{w},\boldsymbol{h})_{\Gamma_h} \tag{5.6}$$

$$(q,\nabla\cdot\boldsymbol{u})=0 \tag{5.7}$$

where $(\bullet,\bullet)_\Omega=\int_\Omega(\bullet)d\Omega$ is the $L^2(\Omega)$ product. $\mathcal{W}=\left(H_0^1(\Omega)\right)^3$ and $\mathcal{Q}=C^0(\Omega)\bigcap L^2(\Omega)$ are the function space of weighting functions, and $\mathcal{W}_t$ and $\mathcal{Q}_t$ are the time-dependent counterparts for trial solutions. For the simplicity of illustration, we denote the variational forms (5.6) and (5.7) in abstract forms as

$$\mathcal{B}(\boldsymbol{w},q;\boldsymbol{v},p)=\mathcal{L}(\boldsymbol{w}) \tag{5.8}$$

where $\mathcal{B}(\boldsymbol{w},\boldsymbol{v})$ is the summation of left-hand side of (5.6) and the left-hand side of (5.7) and $\mathcal{L}(\boldsymbol{w})$ is the right-hand side of (5.6).

The conventional large eddy simulation (LES) approaches model the contribution of the sub-grid scale (SGS) fields by diffusion. This analogy is rational from the perspective of energy cascade nature of turbulence and the modelling propose is henceforth simplified as the estimation of the turbulent viscosity. Dynamic Smagorinksy model, which follows this methodology, is the most popular LES model that provides a local and dynamic model for the turbulent viscosity. On the basis of the split of resolved and sub-grid scales, it further makes uses the finest resolved wave to represent the SGS behavior.

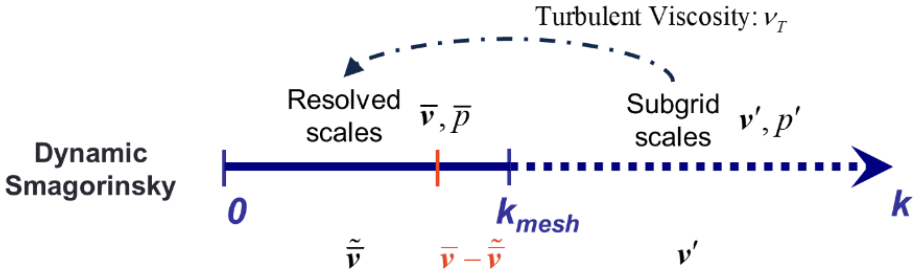

Figure 5.1 Methodology of conventional LES approaches

Remark. why do we call it a closure model: The flow motion is then divided into two parts: the resolved motion and the subfilter-scale motion (SFS). The scale of the flow motion smaller than the grid size is referred to the unresolved SFS motion, or subgrid-scale (SGS) motion. For the SGS motion, a closure model is required to link the SGS motion effect to the resolved SFS.

5.3. RESIDUAL-BASED VARIATIONAL MULTISCALE TURBULENCE MODEL

Variational Multi-Scale (VMS) framework assumes an overlapping decomposition of the unknown solution fields along with their corresponding weighting functions into coarse and fine scales. In the context of turbulence modeling, coarse scales represent the larger features in the flow. From a mathematical perspective, the coarse scale features belong to a finite dimensional space. The fine scales, on the other hand, represent the higher modes that correspond to the higher wave numbers along the wave-number axis as shown in Figure 5.1, and they belong to an infinite dimensional space.

Our work extends the VMS turbulent model by further decompose the fine scales into two levels: fine scale level-I and fine scale level-II. In a hierarchy structure of the variational formulation, we managed to project the solution of finer scales to the coarser scales and to push the modelling part into the fine-scale level-II. Consequently, there is no modelling element in the coarse-scale variational formulation. Term-wise, the proposed formulation provides a comprehensive LES model, including the SGS Reynolds stress representing the fluctuation and the Leonard stresses representing the forward- and back- scatter of energy. Compared to two-level VMS model, it provides a model of SGS/fine-scale pressure to enforce the fine-scale mass conservation, which is the div stabilization term in the context of stabilization method.

The mixed-field formulation (5.6) and (5.7) is constraint by the inf-sup condition that prevents using equal order interpolation of velocity and pressure fields. Also, due to the convection term in the momentum balance equation (5.6) in the Eulerian frame of refence, stabilization formulation is needed. VMS framework is utilized in the literature to address these numerical instabilities and further extended to large-eddy turbulence model by adding the Reynolds stress to the weak form, whereas the fine-scale or

subgrid-scale velocity is derived in the residual-driven form by resolving the fine-scale sub-problems with bubble function as local support.

5.3.1. Variational Multiscale Decomposition

We assume an overlapping and additive decomposition of the trial solutions (velocity and pressure) into coarse and fine scales, where coarse scale represents the physics resolved by the given mesh resolution and fine scale represents the subgrid-scale physics that is filtered by the spatial and temporal resolution, such as

$$\begin{aligned} \boldsymbol{u}(\boldsymbol{x},t) &= \underbrace{\bar{\boldsymbol{u}}(\boldsymbol{x},t)}_{\text{Coarse scale}} + \underbrace{\boldsymbol{u}'(\boldsymbol{x},t)}_{\text{Fine scale}} \\ p(\boldsymbol{x},t) &= \underbrace{\bar{p}(\boldsymbol{x},t)}_{\text{Coarse scale}} + \underbrace{p'(\boldsymbol{x},t)}_{\text{Fine scale}} \end{aligned} \tag{5.9}$$

The spaces of functions for the coarse scales are defined to be linearly independent of the spaces used to represent the fine scales. For a detailed discussion on the spaces of functions, see [107,108,173]. Similarly, we can assume an additive decomposition of the weighting functions:

$$\begin{aligned} \boldsymbol{w}(\boldsymbol{x}) &= \bar{\boldsymbol{w}}(\boldsymbol{x}) + \boldsymbol{w}'(\boldsymbol{x}) \\ q(\boldsymbol{x}) &= \bar{q}(\boldsymbol{x}) + q'(\boldsymbol{x}) \end{aligned} \tag{5.10}$$

Substituting the VMS decomposition (5.9) and (5.10) into the variational form (5.8) and segregate the weighting functions in coarse and fine scales, the problems can be split into sub-problems in two scales:

Coarse-scale sub-problems:

$$\mathcal{B}(\bar{\boldsymbol{w}},\bar{q};\bar{\boldsymbol{u}}+\boldsymbol{u}',\bar{p}+p') = \mathcal{L}(\bar{\boldsymbol{w}}) \tag{5.11}$$

Fine-scale sub-problems:

$$\mathcal{B}(\boldsymbol{w}',q';\bar{\boldsymbol{u}}+\boldsymbol{u}',\bar{p}+p') = \mathcal{L}(\boldsymbol{w}') \tag{5.12}$$

5.3.2. Solution of the Fine-Scale Sub-Problems

To attain the solution of the fine-scale sub-problem, we first linearize the nonlinear form (5.12) with respect to the fine-scale fields through a linearization operator defined as

$$\mathcal{L}\left(R\left(\boldsymbol{w}',q';\bar{\boldsymbol{u}},\boldsymbol{u}',\bar{p},p'\right)\right)=\frac{d}{d\varepsilon}R\left(\boldsymbol{w}',q';\boldsymbol{u}+\varepsilon\delta\boldsymbol{u}',p+\varepsilon\delta p'\right)\Big|_{\varepsilon\to 0} \tag{5.13}$$

Applying the operator (5.13) to the fine-scale sub-problem (5.12), we get the linearized fine-scale problems in abstract residual-driven form as

$$\mathcal{B}^{L}\left(\boldsymbol{w}',q';\boldsymbol{u},\boldsymbol{u}',p'\right)=-\left(\mathcal{B}\left(\boldsymbol{w}',q';\boldsymbol{u},p\right)-\mathcal{L}_{M}\left(\boldsymbol{w}'\right)\right)=-\left(\boldsymbol{w}',\boldsymbol{r}_{M}\right)-\left(q',r_{C}\right) \tag{5.14}$$

$$\begin{aligned}\mathcal{B}^{L}\left(\boldsymbol{w}',q';\boldsymbol{u};\boldsymbol{u}',p'\right):=&\left(\boldsymbol{w}',\boldsymbol{u}'_{,t}\right)+\left(\boldsymbol{w}',\boldsymbol{u}\cdot\nabla\boldsymbol{u}'\right)+\left(\boldsymbol{w}',\boldsymbol{u}'\cdot\nabla\boldsymbol{u}\right)+\left(\nabla\boldsymbol{w}',2\nu\nabla^{s}\boldsymbol{u}'\right)\\&-\left(\nabla\cdot\boldsymbol{w}',p'\right)+\left(q',\nabla\cdot\boldsymbol{u}'\right)\end{aligned} \tag{5.15}$$

$$\boldsymbol{r}_{M}\left(\boldsymbol{u},p\right):=\boldsymbol{u}_{,t}+\boldsymbol{u}\cdot\nabla\boldsymbol{u}-\nabla\cdot\left(2\nu\nabla^{s}\boldsymbol{u}\right)+\nabla p-\boldsymbol{f} \tag{5.16}$$

$$r_{C}\left(\boldsymbol{u}\right):=\nabla\cdot\boldsymbol{u} \tag{5.17}$$

where $\mathcal{B}^{L}\left(\boldsymbol{w}',q';\boldsymbol{u};\boldsymbol{u}',p'\right)$ represents the linearized Navier-Stokes equation, $\boldsymbol{r}_{M}$ is the Euler-Lagrange of the momentum balance equation and r_{C} is the Euler-Lagrange of the incompressibility condition.

5.3.2.1. Multi-level decomposition on the fine scale

The fine-scale sub-problems defined in (5.14) is a mixed-field problems as (5.8). Objective at this point is to resolve the fine-scale sub-problem locally to extract expressions for the fine-scale velocity and pressure fields. However, the fine-scale problem lies in an infinite dimensional space. Accordingly, some simplifications need to be made to make the problem tractable. In addition, (12) is a mixed field problem and therefore subject to the inf-sup condition imposed by the Babuska-Brezzi theorem. In order to convert the problem into an unconstrained problem, we employ VMS-based stabilization concepts. Similar to the original weak form, we use VMS as the remedy again for those numerical issues. Here, the fine-scale velocity field are further decomposed into fine-scale level-I and fine-scale level-II,

$$\boldsymbol{u}'\left(\boldsymbol{x},t\right)=\underbrace{\boldsymbol{u}'_{I}\left(\boldsymbol{x},t\right)}_{\text{Intermediate scale}}+\underbrace{\boldsymbol{u}'_{II}\left(\boldsymbol{x},t\right)}_{\text{Finest scale}} \tag{5.18}$$

$$\boldsymbol{w}'(\boldsymbol{x},t)=\boldsymbol{w}'_I(\boldsymbol{x},t)+\boldsymbol{w}'_{II}(\boldsymbol{x},t) \tag{5.19}$$

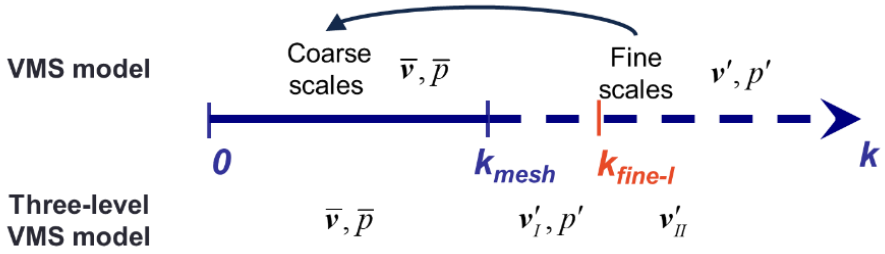

Figure 5.2 Methodology of VMS approaches

The level-II velocity field will help develop stabilized form for level-I fine-scale problem, thus making it an unconstrained problem thereby facilitating analytical extracting of the fine-scale models. We employ a multiscale decomposition of the velocity field and its weighting function, and it is sufficient to derive a stabilized formulation. Therefore, we do not assume a multiscale decomposition of the fine-scale pressure field and its weighting function. Therefore, we do not assume a multiscale decomposition of the fine-scale pressure field and its weighting function. Consequently,

$$\begin{aligned} p'(\boldsymbol{x},t)&=p'_I(\boldsymbol{x},t)\\ q'(\boldsymbol{x},t)&=q'_I(\boldsymbol{x},t)\end{aligned} \tag{5.20}$$

Substituting the fine-scale VMS decomposition (5.18) and (5.19) into the fine-scale formulation (5.14), we can separate the fine-scale sub-problems into fine-scale level-I sub-problems and fine-scale level-II sub-problem.

Fine-scale level-I sub-problems

$$\mathcal{B}^L(\boldsymbol{w}'_I,q';\boldsymbol{u},\boldsymbol{u}'_I+\boldsymbol{u}'_{II},p')=-\left(\boldsymbol{w}'_I,\boldsymbol{r}_M(\boldsymbol{u},p)\right)-\left(q',r_C(\boldsymbol{u})\right) \tag{5.21}$$

Fine-scale level-II sub-problem

$$\mathcal{B}^L(\boldsymbol{w}'_{II},q';\boldsymbol{u},\boldsymbol{u}'_I+\boldsymbol{u}'_{II},p')=-\left(\boldsymbol{w}'_{II},\boldsymbol{r}_M(\boldsymbol{u},p)\right) \tag{5.22}$$

5.3.2.2. Solution of fine-scale level-II

By pushing all terms depends on fine-scale level-I trial solution of velocity field $\boldsymbol{u}_I'$ to the right-hand side, the fine-scale level-II sub-problem can be rewritten as follows

$$\mathcal{B}^L\left(\boldsymbol{w}_{II}', q'; \boldsymbol{u}, \boldsymbol{u}_{II}', p'\right) = -\left(\boldsymbol{w}_{II}', \boldsymbol{r}_M'\left(\boldsymbol{u}_I', p'\right)\right) - \left(\boldsymbol{w}_{II}', \boldsymbol{r}_M\left(\boldsymbol{u}, p\right)\right) \tag{5.23}$$

$$\boldsymbol{r}_M'\left(\boldsymbol{u}', p'\right) = \boldsymbol{u}_{,t}' + \boldsymbol{u}\cdot\nabla\boldsymbol{u}' + \boldsymbol{u}'\cdot\nabla\boldsymbol{u} - \nabla\cdot\left(2\nu\nabla^s\boldsymbol{u}'\right) + \nabla p' \tag{5.24}$$

where $\boldsymbol{r}_M'\left(\boldsymbol{u}', p'\right)$ is the perturbed Euler-Lagrange of momentum balance equation. Now that the right-hand side of (5.23) are only depends on coarse-scale trial solutions and the left-hand side is irrelevant to this field, we can numerically solve (5.23) by choosing basis function and time-marching schemes. We can denote the solution of fine-scale level-II velocity field in the abstract form as

$$\boldsymbol{u}_{II}'\left(\boldsymbol{u}, \boldsymbol{u}_{II}', p, p'\right) = -\boldsymbol{\tau}'\left(\boldsymbol{u}, p\right)\left(\boldsymbol{r}_M + \boldsymbol{r}_M'\right) \tag{5.25}$$

Remark. At this stage, the fine-scale level-II velocity field has been fully represented by coarse-scale and fine-scale level-I fields.

5.3.2.3. Solution of fine-scale fields

We first rewrite the formulation of fine-scale level-I (5.21) by separating the terms that depend on the fine-scale level-II velocity field $\boldsymbol{u}_{II}'$ from other terms,

$$\mathcal{B}^L\left(\boldsymbol{w}_I', q'; \boldsymbol{u}, \boldsymbol{u}_I', p'\right) + \left(\boldsymbol{\chi}\left(\boldsymbol{w}_I', q'\right), \boldsymbol{u}_{II}'\right) = -\left(\boldsymbol{w}_I', \boldsymbol{r}_M\left(\boldsymbol{u}, p\right)\right) - \left(q', r_C\left(\boldsymbol{u}\right)\right) \tag{5.26}$$

where the weighting function $\boldsymbol{\chi}$ derived from the adjoint operator of linearized Navier-Stokes equation is defined as follows

$$\boldsymbol{\chi}\left(\boldsymbol{w}, q\right) = \boldsymbol{w}\cdot\nabla^T\boldsymbol{u} - \boldsymbol{u}\cdot\nabla\boldsymbol{w} - \nu\left(\nabla\left(\nabla\cdot\boldsymbol{w}\right) + \Delta\boldsymbol{w}\right) - \nabla q \tag{5.27}$$

Substituting the fine-scale level-II solution (5.25) onto (5.26) yields the stabilized fine-scale formulation as

$$\mathcal{B}^L\left(\boldsymbol{w}', q'; \boldsymbol{u}, \boldsymbol{u}', p'\right) - \left(\boldsymbol{\chi}\left(\boldsymbol{w}', q'\right), \boldsymbol{\tau}'\left(\boldsymbol{u}, p\right)\boldsymbol{r}_M'\right) = -\left(\boldsymbol{w}' - \boldsymbol{\chi}\left(\boldsymbol{w}', q'\right), \boldsymbol{r}_M\right) - \left(q', r_C\right) \tag{5.28}$$

The solution of the fine-scale fields can be represented as

$$\begin{bmatrix} \boldsymbol{u}'(\boldsymbol{u},p) \\ p'(\boldsymbol{u},p) \end{bmatrix} = -\boldsymbol{\tau}(\boldsymbol{u},p) \begin{bmatrix} \boldsymbol{r}_M \\ r_C \end{bmatrix} \tag{5.29}$$

Remark. All fine-scale level-II terms in (5.28) are eliminated through the projection. Thus, the subscript of fine-scale level is dropped henceforth for the simplicity. In other words, we use the enriched fine-scale level-I fields as the estimated fine-scale solutions, that is

$$\begin{bmatrix} \boldsymbol{v}' \\ p' \end{bmatrix} \cong \begin{bmatrix} \boldsymbol{v}'_I \\ p' \end{bmatrix} \tag{5.30}$$

5.3.3. The Multi-Level Fine-Scale Variational Multiscale Turbulence Model

We reorganize the coarse-scale variational formulation (5.11) as follows,

$$\underbrace{\mathcal{B}(\bar{\boldsymbol{w}},\bar{q};\bar{\boldsymbol{u}},\bar{p}) - \mathcal{L}(\bar{\boldsymbol{w}})}_{\text{Galerkin}} + \underbrace{\left(\boldsymbol{\chi}(\bar{\boldsymbol{w}},\bar{q}),\boldsymbol{u}'\right) - \left(\nabla\cdot\bar{\boldsymbol{w}},p'\right)}_{\text{Stabilization}} + \underbrace{\left(\bar{\boldsymbol{w}},\boldsymbol{u}'\cdot\nabla\boldsymbol{u}'\right)}_{\text{LES model}} = 0 \tag{5.31}$$

The stabilization part in (5.31) consists of all the terms that is linearly dependent on the fine-scale fields $\boldsymbol{u}'$ and p', while the LES model part (i.e., Reynolds stress) is split from the nonlinear convection term.

Remark. First ever method to variationally derive closure models for turbulence. (turbulence is the research frontier in fluid mechanics today).

Remark. From theoretical perspective, the new method is developed by integrating the RFB method from Brezzi directly at the fine-scale variational level in the VMS method from Hughes. This has resulted in a powerful method where fine-scale (or centered fluctuations) level is the perturbation part of the total solution while coarse-scale is the mean solution.

Remark. Flexibility of RFB yields many options for the derivation of the closure models that can then be variationally embedded in the mean solution in a mathematically consistent fashion.

5.4. NUMERICAL RESULTS

5.4.1. Taylor Green Vortex at Re = 1600

Taylor-Green Vortex is a popular test case to study the generation of small-scale vorticity from a smooth initial condition under the influence of vortex stretching. It is a simple test case to set up because of the relatively simple setting of initial conditions and the homogeneous nature of the computed turbulence scales. The initial conditions are

$$u_0(\boldsymbol{x}) = \begin{bmatrix} \sin(x)\cos(y)\cos(z) \\ -\cos(x)\sin(y)\cos(z) \\ 0 \end{bmatrix} \tag{5.32}$$

where all the kinematic energy stays in the largest wave mode of the domain as shown in Figure 5.7. The computational domain is $\Omega = [0,\pi]^3$ and all six boundaries are applied with no normal flow condition and slip boundary condition. Two uniformly structured meshes were created with number of nodes 33^3 and 65^3 to conduct *h*-refinement study with the method. The domain is discretized with B8 and B27 elements for the purpose of *p*-refinement tests. We compare results with DNS data presented reference [136] that was obtained via pseudo-spectra method on 768^3 nodes in a $[0,2\pi]^3$ domain. We also compare our results with other two-level VMS method that employs NURBS basis functions reported in van Opstal *et al.* in [127] and Evans *et al.* [45]. We have employed the generalized alpha method with step size dt=0.01s for 32-cubed mesh and dt=0.005s for the 64-cubed mesh to keep the same CFL number.

Figure 5.3 shows the time history of kinetic energy and we notice that 64-cubed meshes show uniformly better accuracy as compared with the 32-cubed meshes thereby confirming the h-refinement feature. Secondly, for given number of nodes, quadratic bricks show better accuracy as compared with the linear bricks, thus confirming the p-refinement feature of the method. Figure 5.4 shows the decay rate of kinetic energy. Both element types and both meshes attain nearly similar peak decay rate as compared with the DNS data, and show closer comparison with DNS as compared with the C1 and C3 B-splines. We perform a h- and p- refinement study with the energy decay rate and mesh refinement uniformly presents better comparison with the DNS data for both element types as shown in Figure 5.5. Our results

of 64^3 accurately predicts the trend the kinetic energy and its decaying rate in the turbulent stage (t > 10s). Also, we observe that high order interpolation also helps improve the results in Figure 5.5. The energy spectra of different mesh resolutions and different interpolation orders at t = 10s are plotted in Figure 5.6. The slope of energy spectra are consistent with the Kolmogorov -5/3 law.

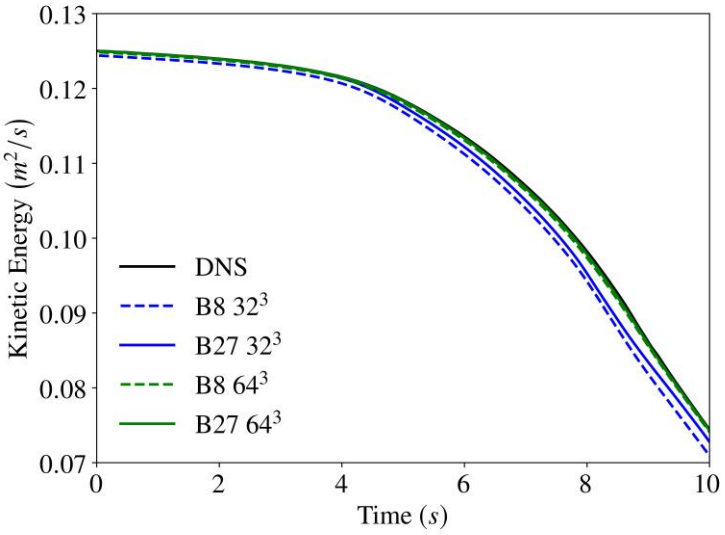

Figure 5.3 History of kinetic energy of Taylor-Green vortex

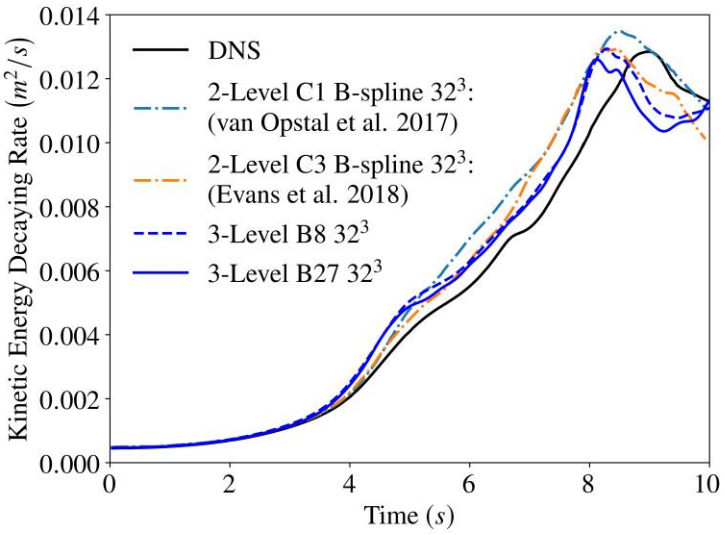

Figure 5.4 History of kinetic energy decaying rate of Taylor-Green vortex: comparison between two-level VMS and three-level VMS

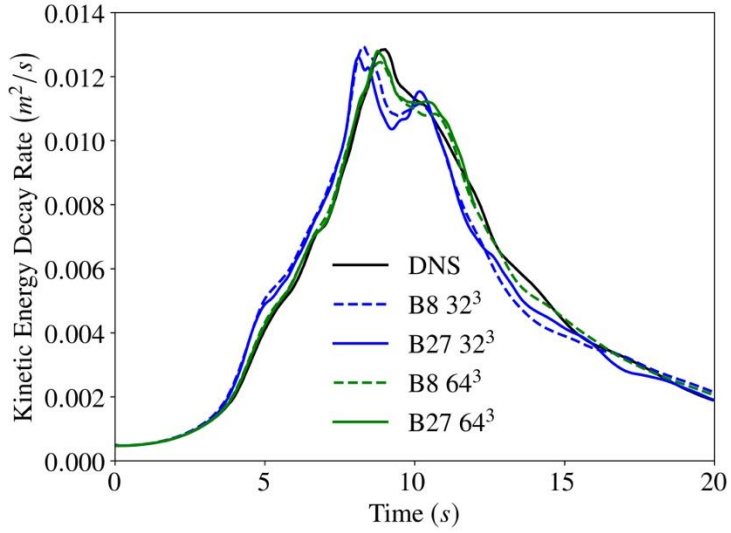

Figure 5.5 History of kinetic energy decaying rate of Taylor-Green vortex: h- and p- refinement of three-level VMS

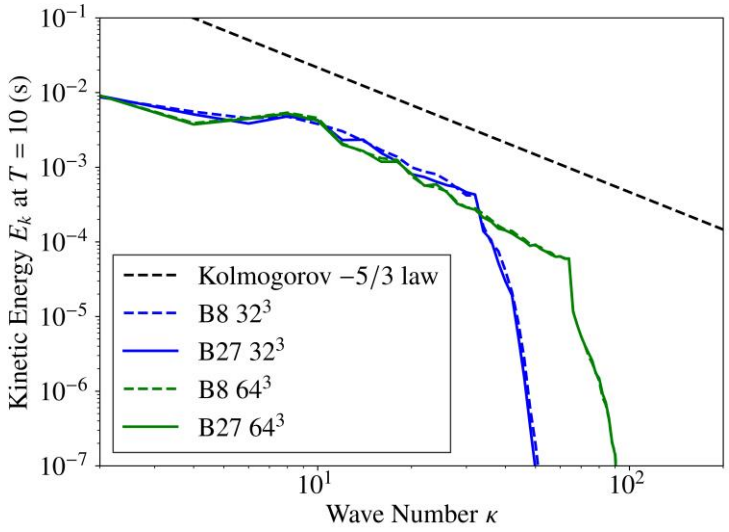

Figure 5.6. Energy spectra vs wave numbers at t = 10s.

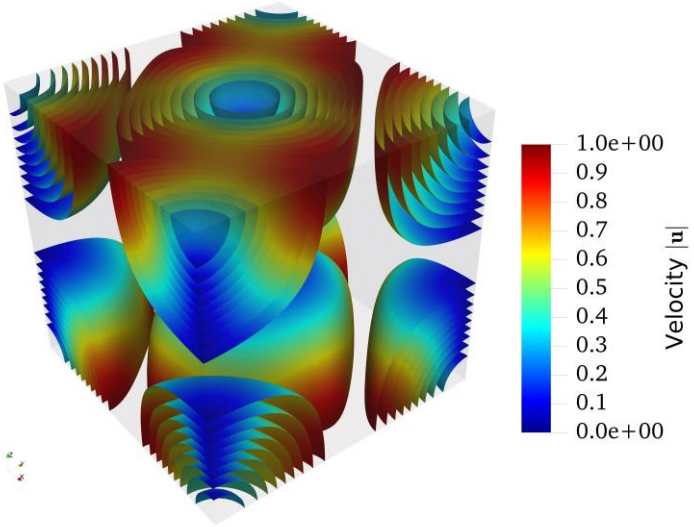

(a)

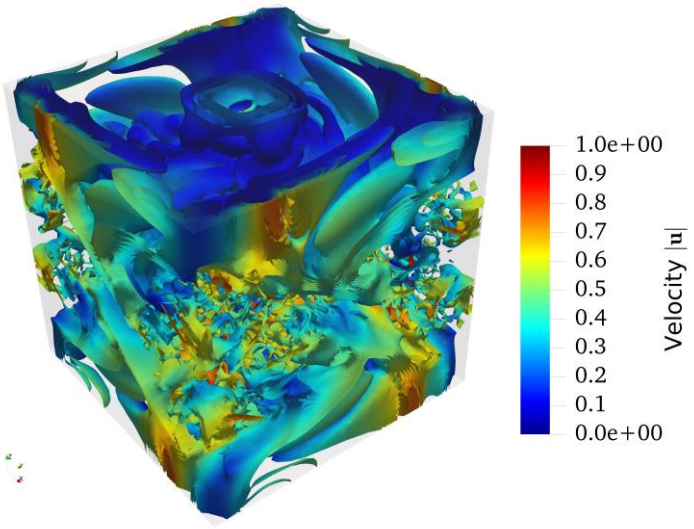

(b)

Figure 5.7 Iso-contours of Q criterion: (a) initial condition and (b) at t = 10s when dissipation is in progress.

5.4.2. Turbulent Channel Flow

Turbulent channel flow is a standard benchmark problem for statistically stationary turbulence. We test our method for three different friction Reynolds number Re_τ flows: 395, 590 and 950. The problem is driven by a constant pressure gradient in streamwise direction and the kinematic viscosity is appropriately adjusted for create the relevant friction Reynolds number flow. The geometric description of the various mesh settings are given in Table 1. The simulation results is compared with DNS reference

in [121] (395 and 590) and [64], and with reported two-level VMS results in [13,14,50,107]. T10 result of three-level VMS is reported in [30]

Table 5.1 Simulations settings of turbulent channel flow

Re_τ	$L_x \times L_z$	dP/dx	ν	Δt	$\Delta y^+_{\min}$	*Mesh res.*
395	2π×2π/3	3.37204e-3	1.472e-4	0.025	1.313	32×33×32
590	2π×π	1.0	1.6949e-3	0.0015	0.903	64×65×64
950	4π×4π/3	2.63099e-3	5.3992e-5	0.01	1.455	64×65×64

5.4.2.1. Friction Reynolds number 395

The first test case is Re=395. The mesh is comprised of 32-cubed nodes, which are appropriately connected to create 8-node and 27-node hexahedral elements. The mesh is graded in the wall normal direction such that $y(j) = -\tanh\left(\gamma\left(1-2j/N_y\right)\right)\Big/\tanh(\gamma)$ where $\gamma = 2.75$ is the stretch coefficient and j is the node numbering in wall-normal direction. Figure 5.8 shows the schematics of the channel problem. Periodic boundary conditions are applied in the streamwise direction of the flow as well in the span-wise direction, while no slip conditions are imposed on the top and bottom walls. We have employed the generalized-α method for time integration at both coarse-scale as well as at the fine-scale levels. Time step employed in the study is shown in Table 1. In addition, we employed Additive Schwarz preconditioner and Bi-Conjugate Gradient Stabilized method for the solution of the system of equations.

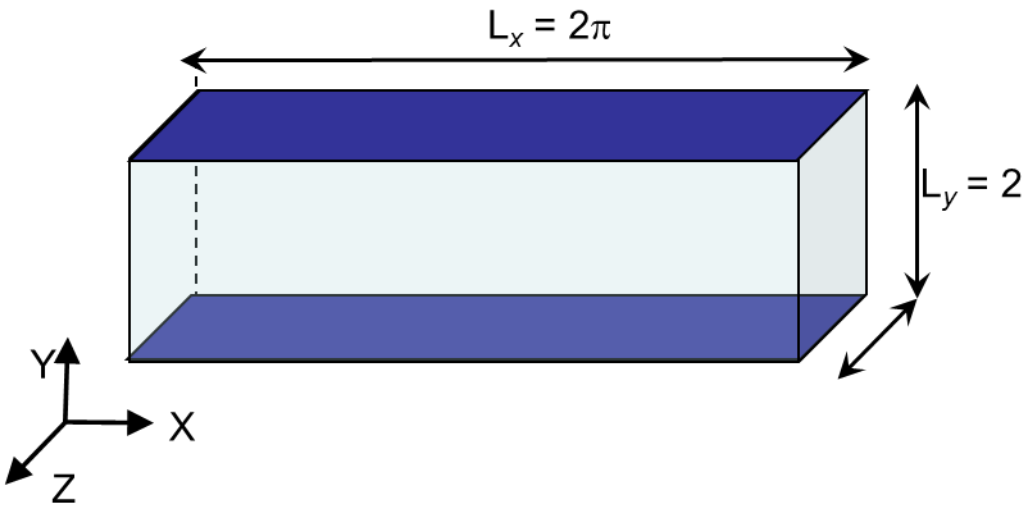

Figure 5.8 Schematics of the problem description of the channel problem

Figure 5.9 **(cont.)** shows the streamwise mean flow, and the flow fluctuations in the streamwise direction, wall-normal direction, and spanwise direction. Computed results are compared with DNS data reported in [121] and was obtained via a pseudo-spectral method with 256×193×192 nodes. Hexahedral elements with the current three-level VMS constructs perform better than the quadratic triangles with three level VMS constructs [30]. In addition, linear bricks with three-level VMS constructs perform better than the linear bricks with two level VMS constructs [107], thus providing the numerical manifestation of the underlying variational structure of the residual-based LES model. We have also compared our data with C1 continuous B-splines reported [13].

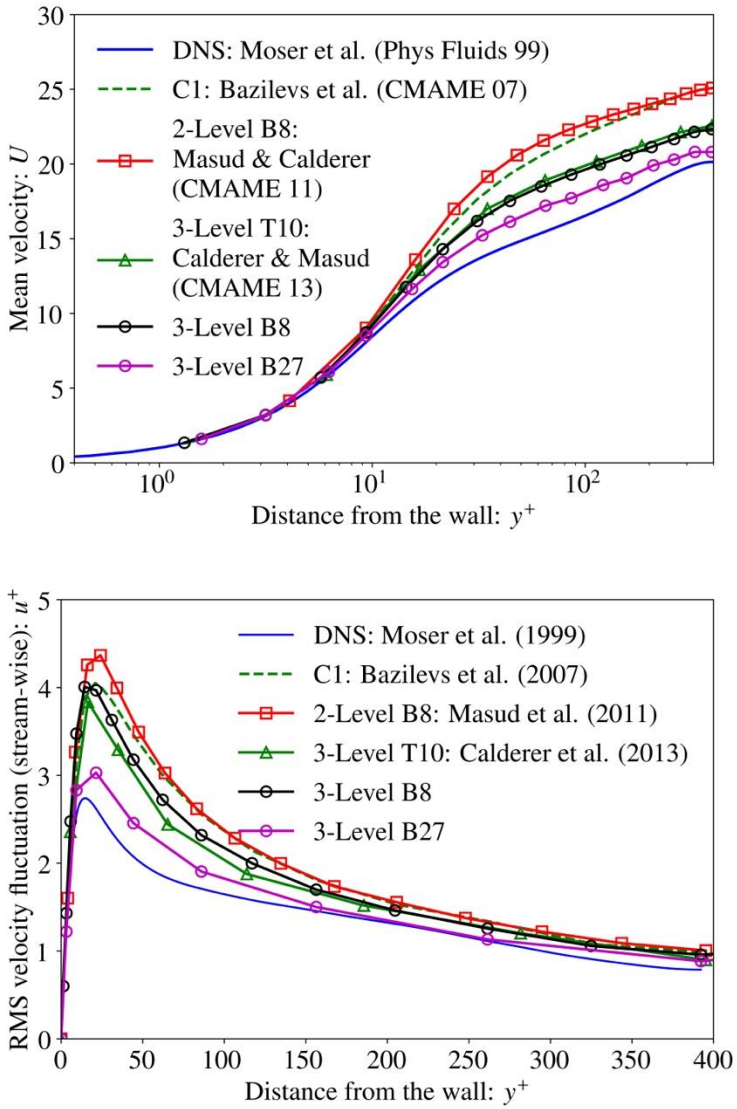

Figure 5.9 Streamwise mean, Streamwise fluctuation, wall-normal fluctuation, spanwise fluctuation 395

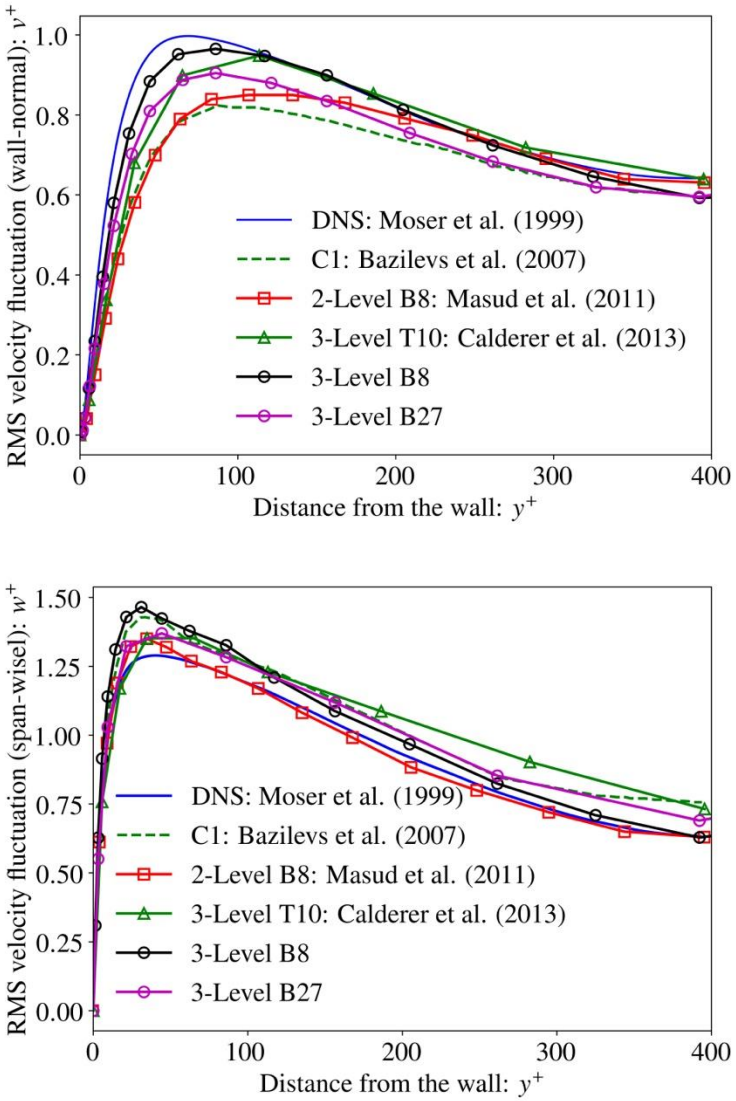

Figure 5.9 (cont.)

5.4.2.2. Friction Reynolds number 590

This section presents numerical test case of $\mathrm{Re}_\tau = 590$. The domain's dimensions are presented in Table 1 and it is discretized with 64-cubed nodes that are appropriately connected to make meshes of 8-node bricks, employing the three-level VMS model. We compare our results with published DNS data [121] and some published data [30,50,107] in the literature. Linear bricks with enhanced fine-scale model facilitated via the variational embedding of fine-scale physics which is preserved because of the higher-order functions employed at the fine-scale level are able to produce a closer approximation to the DNS

data as compared to quadratic tetrahedral elements or linear-hexahedra. A similar trend is seen in all the fluctuations as well.

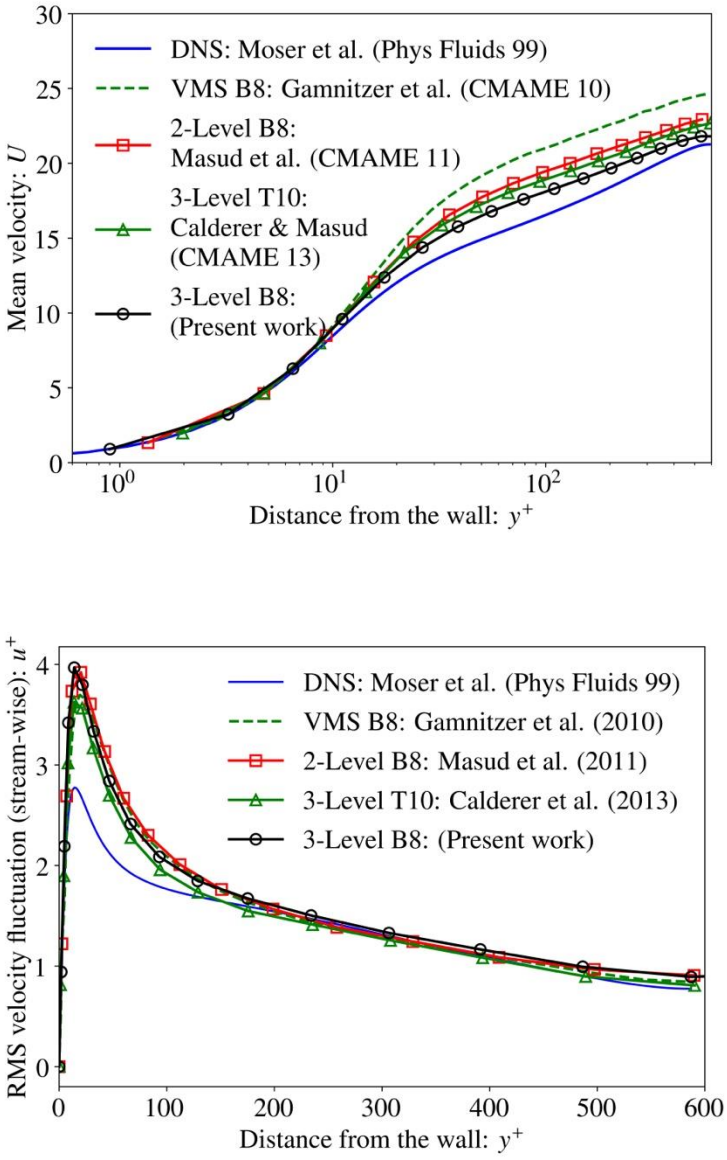

Figure 5.10 Streamwise mean, Streamwise fluctuation, wall-normal fluctuation, spanwise fluctuation 590

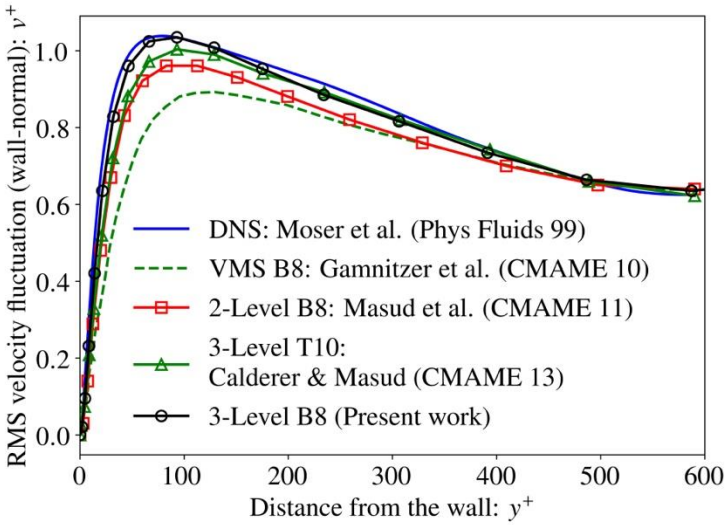

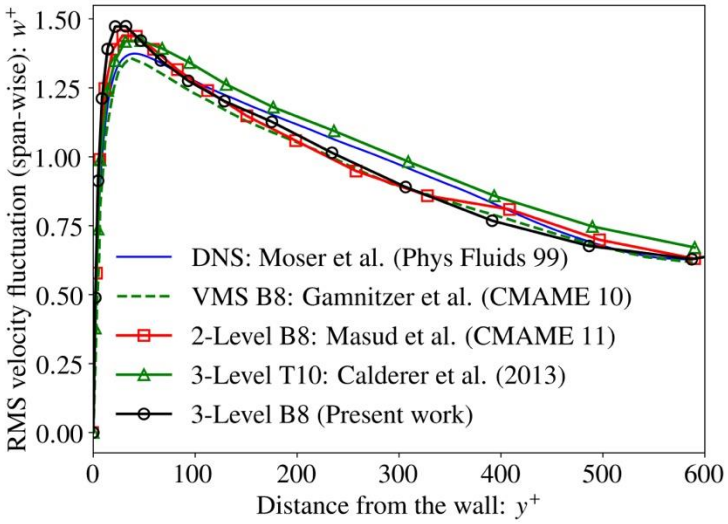

Figure 5.10 (cont.)

5.4.2.3. Friction Reynolds number 950

The third test case is $\mathrm{Re}_\tau = 950$ and the geometric and material parameters for this test case are presented in Table 1. We compare our results with DNS data from Hoyes and Jimenez [64] and C1 continuous B-splines in Bazilevs et al [14].

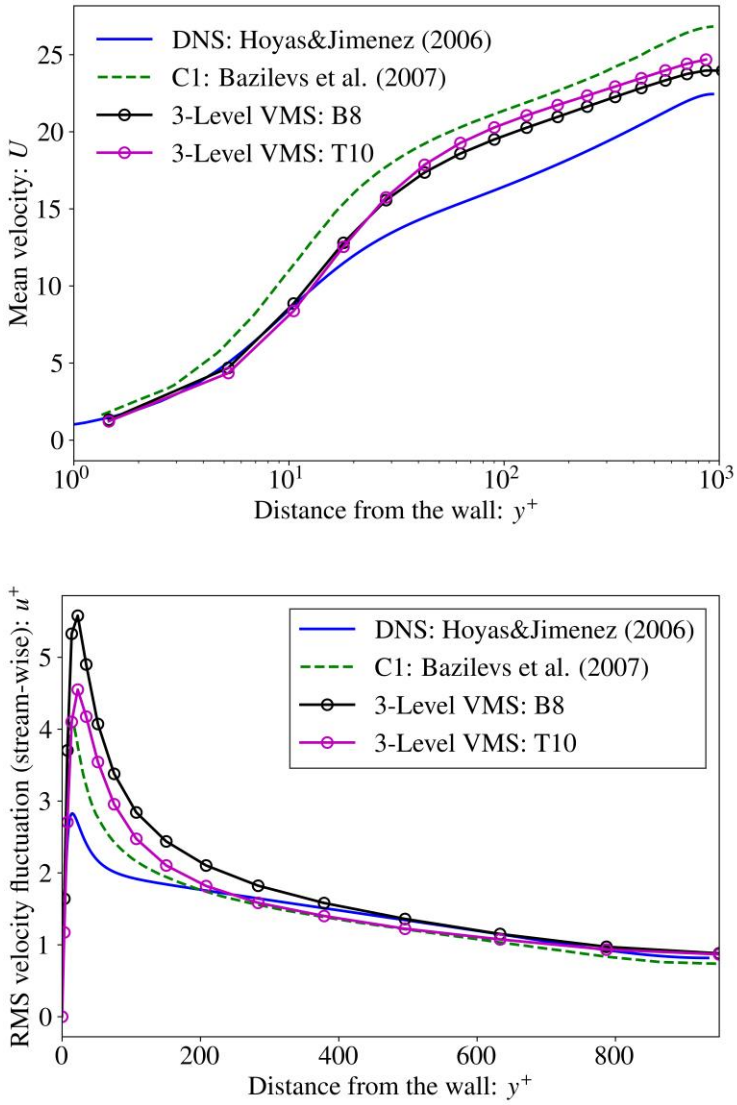

Figure 5.11 Streamwise mean, Streamwise fluctuation, wall-normal fluctuation, spanwise fluctuation 950

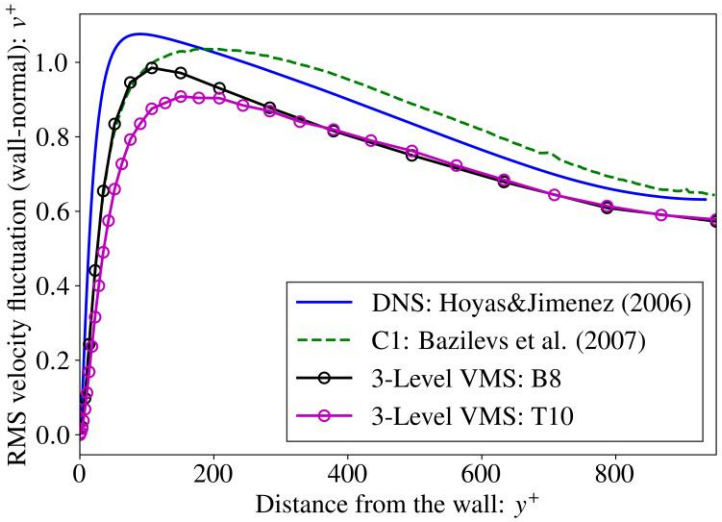

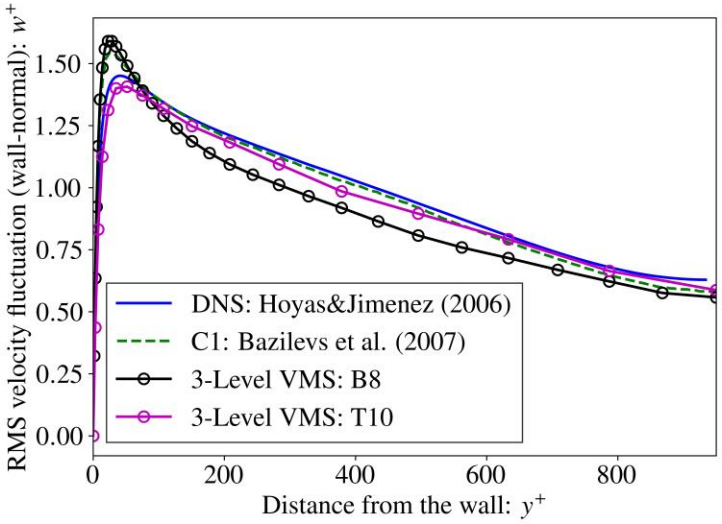

Figure 5.11 (cont.)

5.4.3. Flow over flat plate

Flow over a flat plate is a standard transition problem where a laminar boundary layer gets detached and grows into turbulent flow. Two cases are investigated that represent two ends of the spectrum: In one case the leading edge is circular while in the other there is a sharp corner. In both cases, we only simulate the half of the domain due to the fact that the flat plate is infinitely long.

5.4.3.1. Flow over flat plate with smooth leading edge

In the first numerical study, we set the leading edge of the flat plate as a smooth semicircle. The Reynolds number defined based on the radius of the circle is 1725. The dimensions and boundary conditions are illustrated in Figure 5.12. To reduce the computational cost, the semi-disk shape of the domain is set in $k_{\max}$ the regime of the laminar flow before being perturbed by the flat plate. A uniform inflow velocity is applied on the left side of the domain. Slip and no-penetration boundary conditions are applied on the top and symmetric boundaries. No slip conditions are applied on the plate and periodic boundary conditions are applied in the spanwise direction (z-axis). An outflow boundary condition is implemented to prevent the backflow. We have employed 8-node brick elements and 10-node tetrahedral elements for this simulation with a structured mesh: $181\times 65\times 40$. The simulation is initialized with static flow and gradually increase the inflow velocity to the designated magnitude. The turbulence is self-initialized without any synthetic turbulence embedded in the inflow. Once the flow reaches the statistically steady state, we collecting data for around 10 flow-through time.

Once the flow reaches the leading edge of the flat plate, the laminar flow is perturbed, and a recirculation bubble develops due to the separation effect. To verify the results, we average the velocity field in time and homogeneous space dimension and extract the parameters of the structures of the bubble. These parameters includes: l_r length of reattachment, h_r height of recirculation bubble, Δx_c center of recirculation, θ separation angle, $k_{\max}$ maximum turbulent kinetic energy, $\Delta x_{\min}$ location of maximum backflow and $U_{\min}$ maximum of backflow. These values are compared with DNS results [91] in Table 2. An instantaneous flow field is shown in Figure 5.13 and the space and time averaged 2D flow field is presented in Figure 5.14. To further validate our simulation results, we extract velocity fields in six different locations within and outside the recirculation bubble and compare the distribution of mean and fluctuation along wall-normal direction with other LES simulations [92,169] utilizing other turbulence model with finer mesh in Figure 5.15 and Figure 5.16. In each case we get a very good correlation with the published data.

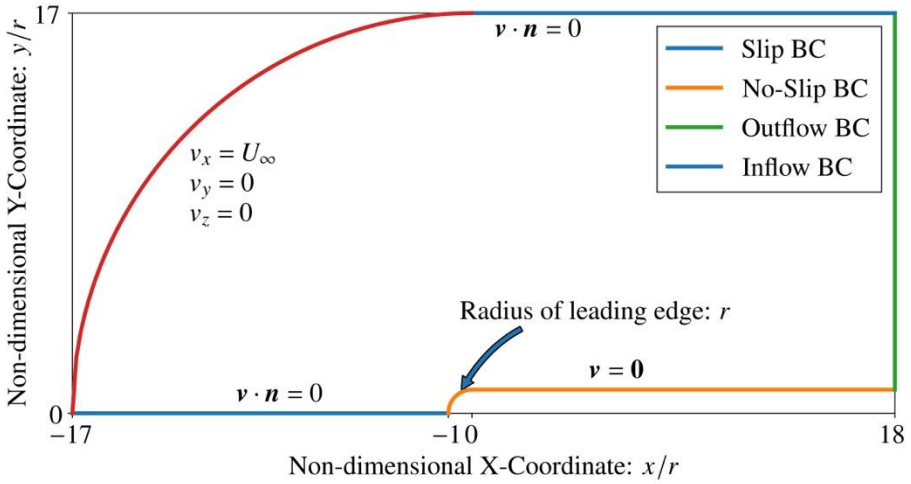

Figure 5.12 Schematic diagram of domain dimensions and boundary condition for boundary layer separation with smooth leading edge

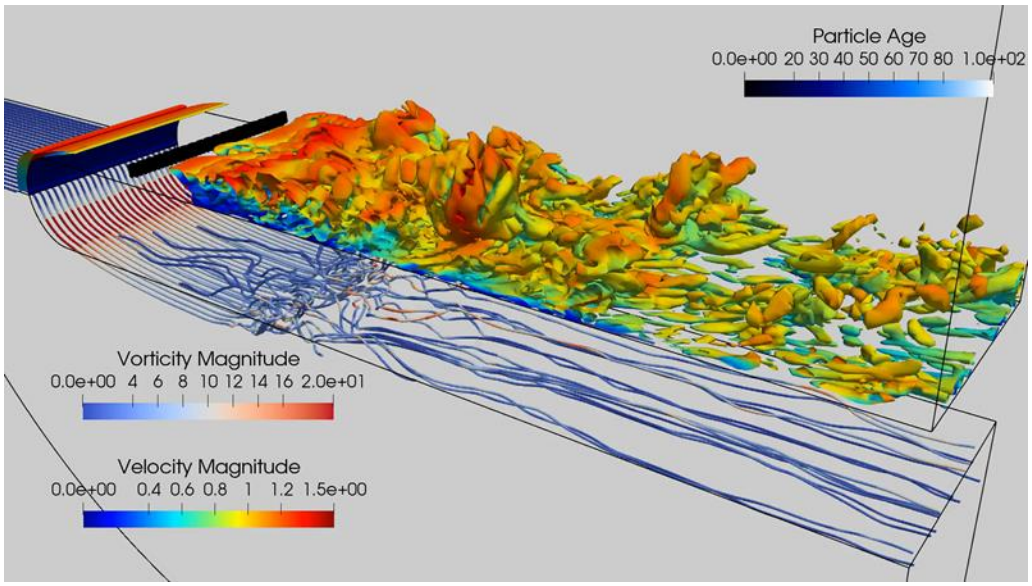

Figure 5.13 Streamlines of velocity and iso-contours of Q-criterion: laminar, transitional and turbulent regimes

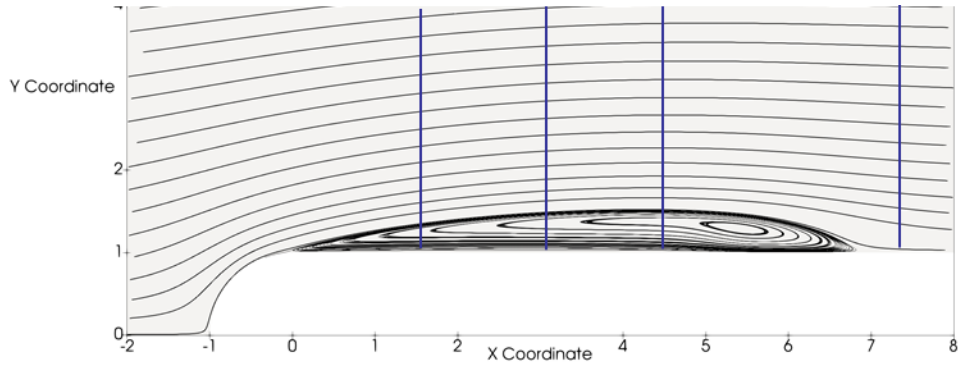

Figure 5.14 Streamlines of time and space averaged velocity field

Table 5.2. Comparison of attributes of recirculation bubble

	l_r	h_r	$\Delta x_c / l_r$	θ	$k_{\max}$	$\Delta x_{\min}$	$U_{\min}$
DNS w/ noise	4.7	0.43	0.76	15	0.11	2.9	-0.23
DNS w/o noise	7.6	0.61	0.82	16	0.11	4.9	-0.25
LES	7.09	0.53	0.82	17	0.1040	4.66	-0.24

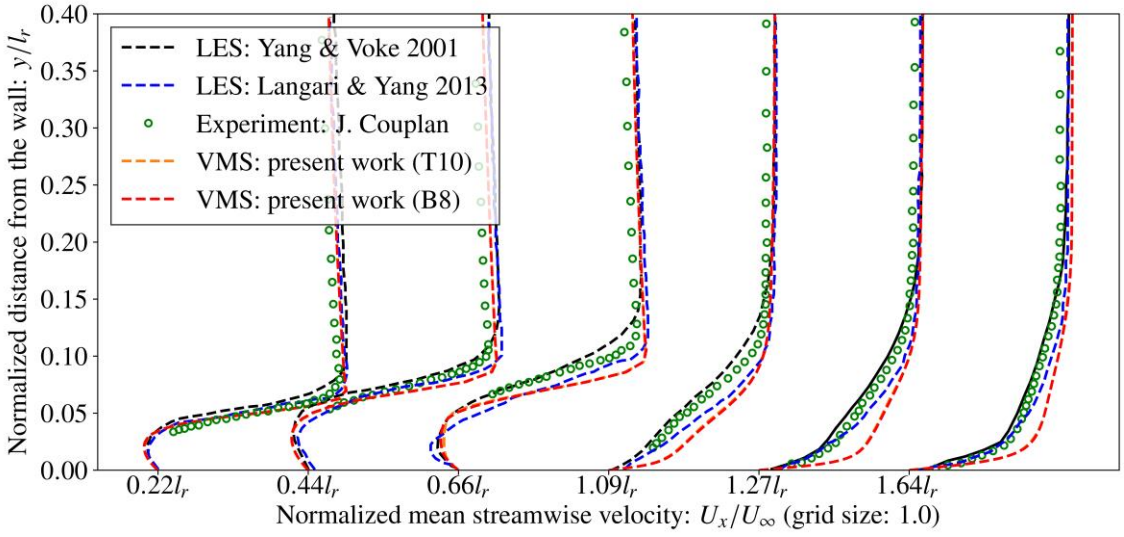

Figure 5.15 Mean streamwise velocity field

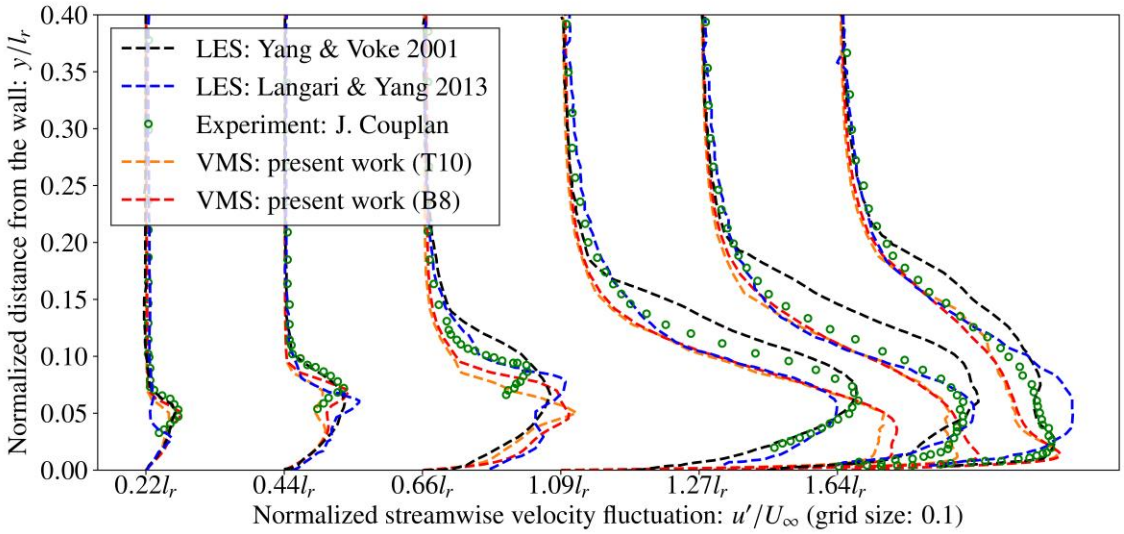

Figure 5.16 Fluctuation of streamwise velocity field

5.4.3.2. Flow over flat plate with blunt leading edge

The problem setting of this test case is very similar to the previous one except for the blunt leading edge of the flat plate. The Reynolds number defined through the thickness of the place is 7500. Like previous test case, we start the simulation with static flow field and gradually increase the inflow velocity to the designated level. The turbulence is self-initialized without any input noise. A snapshot of iso-contours of Q criterion at the stage when the flow is fully developed is shown in Figure 5.17.

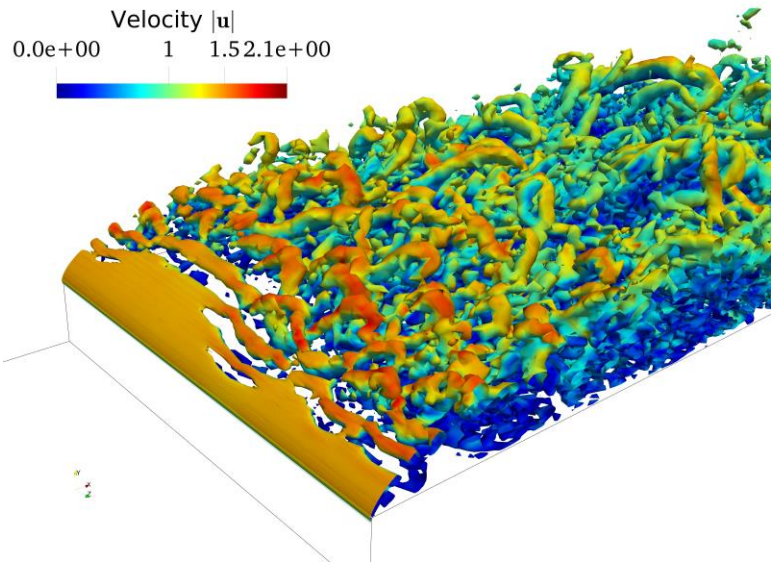

Figure 5.17 Iso-contours of Q criterion (value: 5)

Through time and space averaging, we measure the length of reattachment as $l_r = 3.86$, which is consistent with 3.38~3.68 from other LES results [153]. The height of the recirculation bubble is measured as $y_r / H = 0.52$, which is very close to 0.53 from reported LES results [153]. To further verify the proposed turbulence model, we first compare the distribution of wall mean pressure coefficient and its root-mean-square values from our simulation with experimental data [35,86,142] and reported LES simulation results [153] in Figure 5.18. From Figure 5.19 to Figure 5.22, the distribution of mean and fluctuation of averaged velocity field at various locations along wall-normal direction from our simulation are compared with reported LES results [153] and experimental data [142].

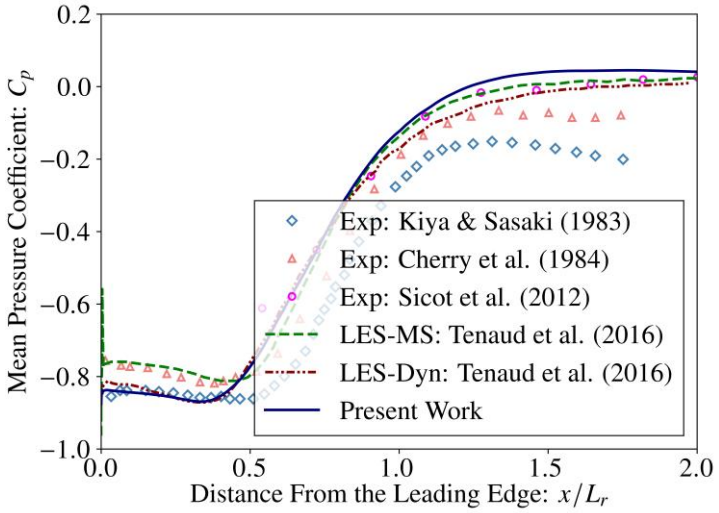

(a)

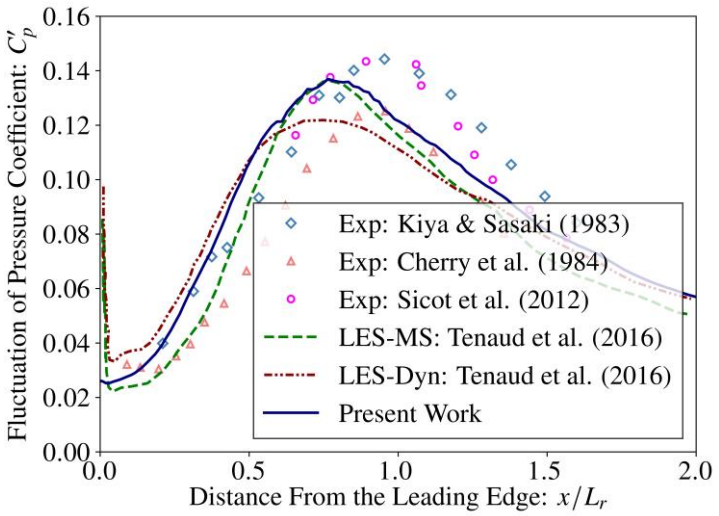

(b)

Figure 5.18 Streamwise wall pressure distribution (mean and fluctuation)

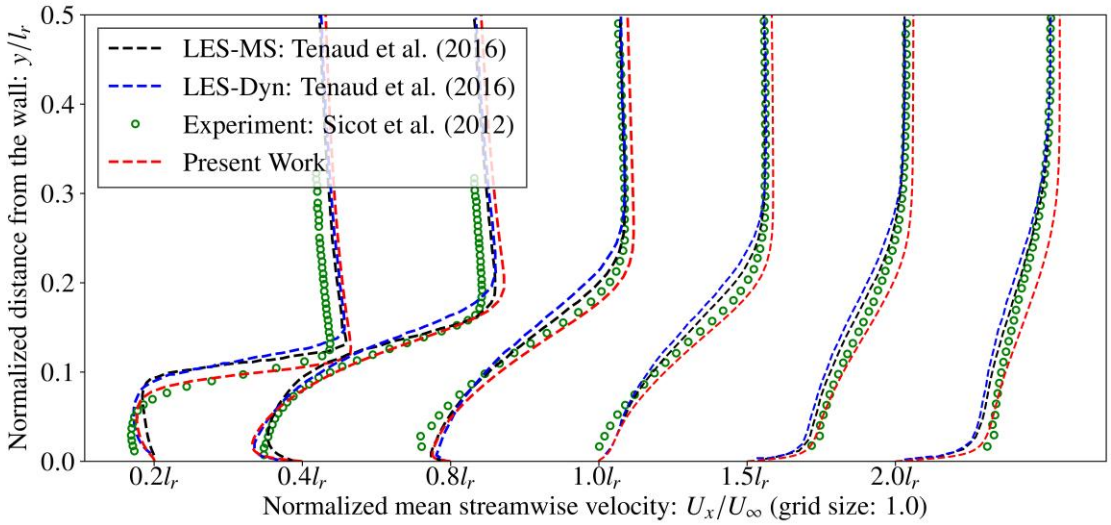

Figure 5.19 Streamwise mean velocity distribution

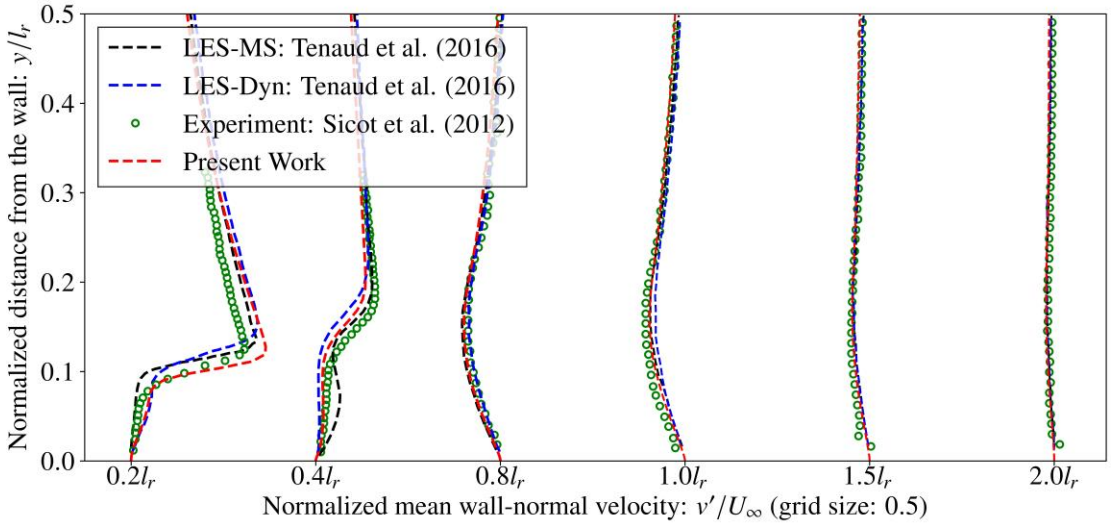

Figure 5.20 Wall normal mean velocity distribution

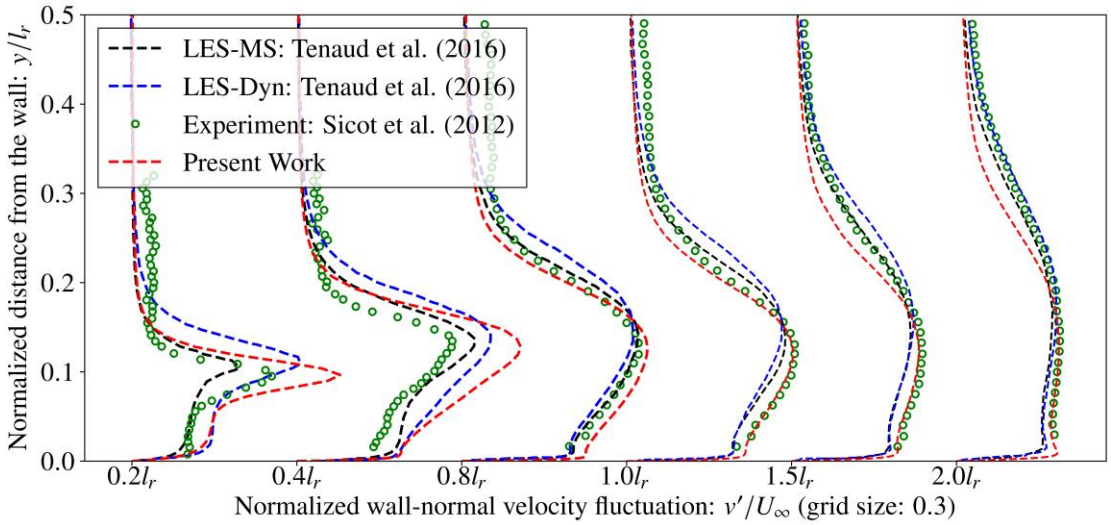

Figure 5.21 Streamwise velocity fluctuation distribution

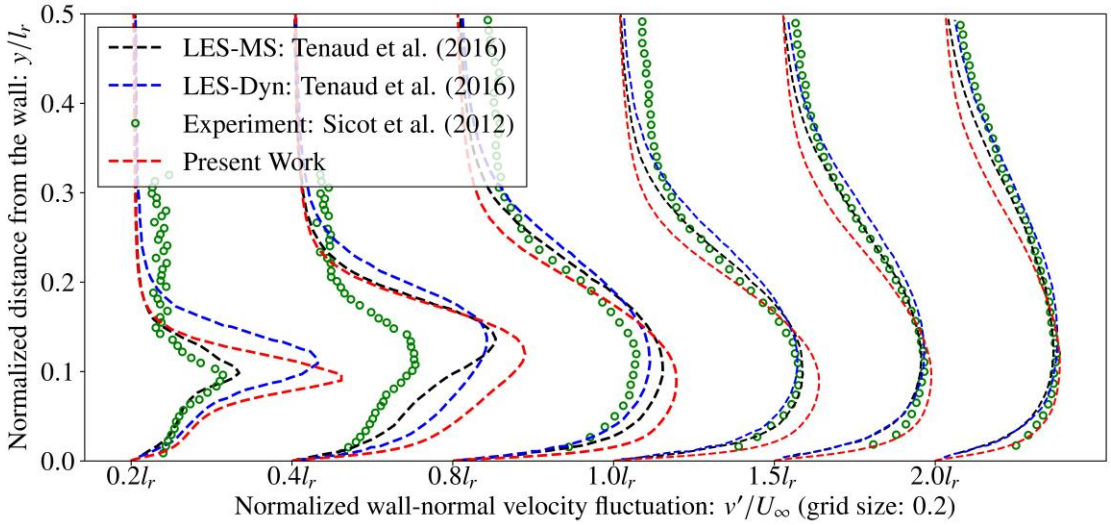

Figure 5.22 Wall normal velocity fluctuation distribution

5.5. CONCLUSIONS

In this work, we have presented a residual-based isothermal turbulence model based on the multi-level fine-scale variational multiscale method. In the present work, the fine or subgrid scales are solved from a linearized transient form of incompressible Navier-Stokes equations. The mixed form of fine-scale sub-problems are stabilized via the VMS method through utilizing the decomposition of the fine scales. Thus, the unknown fields are decomposed into three levels: coarse-scale, fine-scale level-I and fine-scale

level-II. This multi-level nested formulation features a variationally consistent forward and backward scatter between various scales, thus it pioneered a new method for deriving closure models for Turbulence.

From theoretical perspective, the new method is developed by integrating the RFB method from Brezzi directly at the fine-scale variational level in the VMS method from Hughes. This has resulted in a powerful method where fine-scale (or centered fluctuations) level is the perturbation part of the total solution while coarse-scale is the mean solution. Flexibility of RFB yields many options for the derivation of the closure models that can then be variationally embedded in the mean solution in a mathematically consistent fashion. Methods work for Tetrahedral and Hexahedral elements, and for fixed and moving meshes. Since there are no empirical models involved, the method can be viewed as DNS on very fine meshes, or as LES models but without an empirical induction of intuitive ideas.

To validate the proposed methods, we carried out a serious of numerical studies of canonical flows with increasing challenges on turbulence model. The first test case is the Taylor-Green vortex problem, where the energy budget and decaying rate are compared with DNS results, and a h- and p-refinement study for hexahedral and tetrahedral elements. Then we use the code to run the turbulent channel flow with friction Reynolds number up to 950. Finally, the method is utilized with boundary layer separations of flows over a plate with a smooth or a blunt leading edge.

CHAPTER 6: LARGE-EDDY RESIDUAL-BASED TURBULENCE MODEL FOR INCOMPRESSIBLE FLOW WITH DENSITY STRATIFICATION

6.1. INTRODUCTION

Amongst various fluid physics problems, the incompressible flows coupled with a scalar field are the underlying governing system. Via Reynolds transport theorem, one can attain a hyperbolic partial differential equation (PDE) for the scalar field in the form of the advection-diffusion equation, where the velocity field is furnished by the solution of the incompressible Navier-Stokes equations for fluid dynamics. The scalar field is also in turn involved in the conservation of momentum. Therefore, the scalar field is often referred to as an "active" scalar field [140] due to the two-way coupling nature of the system. The scalar field could be the concentration of chemical constituents [15] for simulation of combustion, the magnetic field in stellar astrophysics [171], or the temperature field of stratification in natural water bodies (e.g., lake and ocean), etc. In particular, density stratification is the dominant physics in various engineering and environmental applications. Natural plumes [163] due to stratifications are widely observed in different scales of space, time, and intensities, including eruptions of volcanos and sudden release of carbon dioxide bubbles in the lakes. The studies on phytoplankton blooms [6] have revealed that the hydrothermal effect plays a vital role in the stimulation of large reproduction of the microalgae. Another environmental flow that needs to consider the density stratification is the tropical cyclones, where the winded forced ocean circulation has a strong correlation with the intensity of the hurricanes [56]. Apart from these environmental or geophysical flows, one industrial application of stratification is the storage of heat energy, which becomes the major concern in the renewable energy industry [52] due to the unsteady characteristics in those energy sources (e.g., solar and wind farms). To maximize the efficiency of the heat storage and exchange devices, the stratification effects need to be taken into account in the design of overall systems [52]. Apparently, a robust computational fluid dynamics (CFD) tool is necessary not only to understand the role of density stratification in physical

processes, including the production and dissipation of turbulence [7,77,133], but also to help the design of energy-efficient devices.

CFD methods for simulation of stratified turbulence can be classified by the resolution and determinacy into Reynolds-averaged Navier-Stokes (RANS), large-eddy simulations (LES), and direct numerical simulation (DNS) [134]. LES [140] is a relatively ideal choice of numerical methods for the purpose that we have covered previously due to the balance of accuracy and computational cost. The closure problem (i.e., the gap between filtered and unfiltered nonlinear convection) becomes more complicated than that in the isothermal incompressible flows due to additional nonlinear convection in the conservation of energy. Besides, the stratified turbulence also results in anisotropy in small scales, which is examined through DNS [51,98,145]. Thus, an isothermal LES model needs to be extended to the stratified turbulence, and a dynamically and locally adaptive LES model is required to address the anisotropy in the unresolved scales. The dynamic strategy to determine the turbulence viscosity, first proposed in [53] for isothermal flows, has been utilized for LES of stably and unstably stratified turbulence [83,137,162]. Remmler and Hickel [137] uses the adaptive local deconvolution method (ALDM) to construct an efficient scheme for implicit LES, and Khani and Waite [83] investigate the appropriate filter scales to capture the fundamental features in stratified turbulence. Specifically, the dynamic strategy may result in a negative value of the Smagorinsky coefficient that eventually leads to instability [119]. Another path following a similar hypothesis is to use the renormalization group (RNG) theory [167] to derive the turbulent viscosity and diffusivity, which has been extended from isothermal flows [118] to turbulent thermal convection [160].

Apart from the LES models based on the turbulent viscosity, variational multiscale (VMS) framework [3,13,31,66,72–74,107] suggests an alternative approach to turbulence modeling that does not rely on any hypothesis on the unresolved scales. The VMS modeling of isothermal turbulence is originated by Hughes and his colleagues [72], then implemented with pseudo-spectral method [73,74], and further extended to finite-element methods [3,13,31,107]. A thorough review of the VMS method of incompressible turbulence modeling can be seen in [1]. Recently, the VMS method is used for the

coupled system of incompressible flow with an active scalar field [165,166,168], including stably stratified turbulence [168], thermal convection [165] and particle-laden flows [166]. Yan and his colleagues [166,168] designed a new fine-scale model by tweaking the coupling in the fine-scale inertia while the advection and diffusion of fine-scale velocity and temperature were left uncoupled. The incompressible turbulence model is directly used in [165] for thermal convection. In the context of the VMS framework, two major classes of fine-scale modeling exist: the Green's function [3,13,165,166,168] and residual-free bubbles [31,107]. The latter method preserves the transient linearized fine-scale sub-problems without any approximation, which is suitable for the extension of the turbulence model for addressing additional physics. In this work, the VMS large-eddy turbulence model is derived based on the idea of multi-level fine-scale modeling [31,58] and VMS method for a coupled system [173], which results in a fully-coupled turbulence model for stratified turbulence. No *ad hoc* devices or parameters are needed.

An outline of the paper is as follows. The coupled system of incompressible flow with density stratification is established in Section. 6.2. The derivation of the three-level VMS turbulence model is presented in Section. 6.3. A set of numerical test cases is carried out to validate the proposed method and exhibit a wide range of applications in Section. 6.4. Conclusions are drawn at last.

6.2. INCOMPRESSIBLE THERMAL FLUID WITH BOUSSINESQ BUOYANCY

6.2.1. Strong Form

The influence of the spatiotemporally varying active scalar field (e.g., temperature) $T(\boldsymbol{x},t)$ leads to the variation of density $\rho(\boldsymbol{x},t)$. In the context of incompressible Newtonian fluids, the effect of the density variation is accounted for by introducing a buoyancy force to the momentum balance equation, while the continuity equation satisfies the incompressibility condition. A background gradient in addition to local heat source is the driving mechanism for the thermal phase. With these assumptions, we have the classic equation for density-stratified flows known as the Boussinesq equations [42].

$$\frac{\partial \boldsymbol{u}}{\partial t} + \boldsymbol{u} \cdot \nabla \boldsymbol{u} = -\nabla p + \nabla \cdot \left(2\nu \nabla^s \boldsymbol{u} \right) - \boldsymbol{g}\beta\theta + \boldsymbol{f}_b \tag{6.1}$$

$$\nabla \cdot \boldsymbol{u} = 0 \tag{6.2}$$

$$\frac{\partial \theta}{\partial t} + \boldsymbol{u} \cdot \nabla \theta - \nabla \cdot \left(\alpha \nabla \theta \right) = f \tag{6.3}$$

where $\boldsymbol{u}$ and p is the velocity and kinematic pressure fields, respectively; $\theta = T - T_0$ is the relative temperature, T is the absolute temperature and T_0 is the reference temperature; ν is the kinematic viscosity of the fluid, β is the thermal expansion coefficient, $\boldsymbol{g}$ is the gravitational acceleration vector, and α is the thermal diffusivity; $\boldsymbol{f}_b$ is the non-gravitational body force (e.g., Lorentz force) and f is the heat source/sink. (6.1) is the momentum balance equation with a buoyancy term accounting for the thermal effects, (6.2) is the continuity equation to enforce the incompressible condition, and (6.3) is the energy conservation in the form of the convection-diffusion of the relative temperature field.

The initial conditions in the domain Ω and boundary conditions on the domain boundary $\Gamma = \partial\Omega$ are:

$$\boldsymbol{u}(\boldsymbol{x}, 0) = \boldsymbol{u}_0(\boldsymbol{x}) \quad \text{in} \quad \Omega \times \{0\} \tag{6.4}$$

$$\theta(\boldsymbol{x}, 0) = \theta_0(\boldsymbol{x}) \quad \text{in} \quad \Omega \times \{0\} \tag{6.5}$$

$$\boldsymbol{u}(\boldsymbol{x}, t) = \boldsymbol{g}_M \quad \text{on} \quad \Gamma_g^M \tag{6.6}$$

$$\theta(\boldsymbol{x}, t) = g_E \quad \text{on} \quad \Gamma_g^E \tag{6.7}$$

$$\boldsymbol{\sigma} \cdot \boldsymbol{n} = \left(2\nu \nabla^s \boldsymbol{u} - p\boldsymbol{I} \right) \cdot \boldsymbol{n} = \boldsymbol{h}_M \quad \text{on} \quad \Gamma_h^M \tag{6.8}$$

$$\boldsymbol{\phi} \cdot \boldsymbol{n} = \alpha \nabla \theta \cdot \boldsymbol{n} = h_E \quad \text{on} \quad \Gamma_h^E \tag{6.9}$$

where $\boldsymbol{u}_0$ and θ_0 are the initial conditions for velocity and relative temperature fields, respectively, $\boldsymbol{g}_M$ and g_E are the Dirichlet boundary conditions for the mechanical and thermal phases, $\boldsymbol{h}_M$ and h_E are the Neumann boundary conditions of mechanical and thermal phases. $\boldsymbol{\sigma}$ is the total stress in the fluid and $\boldsymbol{\phi}$

is the heat flux. $\boldsymbol{n}$ is the normal vector directed outwards at the boundary. Specifically, these boundaries satisfy the following conditions: $\Gamma_g^M \bigcap \Gamma_h^M = 0$, $\Gamma_g^M \bigcup \Gamma_h^M = \Gamma$, $\Gamma_g^E \bigcap \Gamma_h^E = 0$ and $\Gamma_g^E \bigcup \Gamma_h^E = \Gamma$.

6.2.2. Dimensionless Parameters

By introducing the characteristic length scale L_0 that is the distance between the hot and cold wall, temperature scale ΔT and velocity scale U_0, the classic non-dimensional numbers are defined as,

$$\mathrm{Pr} = \frac{\nu}{\alpha} \qquad \text{(Prandtl Number)} \tag{6.10}$$

$$\mathrm{Ra} = \frac{\beta \Delta T L_0^3 |\boldsymbol{g}|}{\nu \alpha} \qquad \text{(Rayleigh Number)} \tag{6.11}$$

$$\mathrm{Fr} = \frac{U_0}{N_0 L_0} \qquad \text{(Fronde Number)} \tag{6.12}$$

where $N_0 = \sqrt{\boldsymbol{g} d\theta / d\boldsymbol{x}}$ is the Brunt-Vaisala frequency. The Prandtl number defined in (6.10) represents the ratio between fluid kinematic viscosity and thermal diffusivity. The case when $\mathrm{Pr} = 0.71$ has gained wide interests in the literature because it corresponds to the flow of air.

6.2.3. Standard Weak Form

Let $\boldsymbol{w}(\boldsymbol{x}) \in \mathcal{W} = (H_0^1(\Omega))^{n_{sd}}$, $q(\boldsymbol{x}) \in \mathcal{Q} = C^0(\Omega) \bigcap L^2(\Omega)$, and $\eta(\boldsymbol{x}) \in \mathcal{H} = H_0^1(\Omega)$ be the weighting functions for the velocity $\boldsymbol{u}$, kinematic pressure p, and relative temperature θ fields, the standard weak form of the problem is:

Find $\boldsymbol{V} = (\boldsymbol{u}, p, \theta) \in \mathcal{W}_t \times \mathcal{Q}_t \times \mathcal{H}_t$, such that, $\forall \boldsymbol{W} = (\boldsymbol{w}, q, \eta) \in \mathcal{W} \times \mathcal{Q} \times \mathcal{H}$

$$(\boldsymbol{w}, \boldsymbol{u}_{,t}) + (\boldsymbol{w}, \boldsymbol{u} \cdot \nabla \boldsymbol{u}) + (\nabla \boldsymbol{w}, 2\nu \nabla^s \boldsymbol{u}) - (\nabla \cdot \boldsymbol{w}, p) + (\boldsymbol{w}, \boldsymbol{g} \beta \theta) = (\boldsymbol{w}, \boldsymbol{h}_M)_{\Gamma_h^M} + (\boldsymbol{w}, \boldsymbol{f}_b) \tag{6.13}$$

$$(q, \nabla \cdot \boldsymbol{u}) = 0 \tag{6.14}$$

$$(\eta, \theta_{,t}) + (\eta, \boldsymbol{u} \cdot \nabla \theta) + (\nabla \eta, \alpha \nabla \theta) = (\eta, h_E)_{\Gamma_h^E} + (\eta, f) \tag{6.15}$$

6.2.4. Closure Problems in Density-Stratified Flows

Compared to isothermal incompressible flow, there is one more nonlinear convection term $\boldsymbol{u}\cdot\nabla\theta$ that appears in the strong and weak forms of energy conservation equation. In the context of convectional LES, the gap between the filtered and unfiltered nonlinear convection term (i.e., $\left(\bar{\boldsymbol{w}},\boldsymbol{u}\cdot\nabla\boldsymbol{u}\right)-\left(\bar{\boldsymbol{w}},\bar{\boldsymbol{u}}\cdot\nabla\bar{\boldsymbol{u}}\right)$ in (6.13) and $\left(\bar{\eta},\boldsymbol{u}\cdot\nabla\theta\right)-\left(\bar{\eta},\bar{\boldsymbol{u}}\cdot\nabla\bar{\theta}\right)$ in (6.15)) needs to be closed, which is also known as the "closure problem". Therefore, the LES turbulence model needs to be extended from incompressible isothermal flows to incompressible flows with density stratification. Employing the VMS method for the system of weak forms, we describe the process of deriving the fully coupled residual-based turbulence model.

Remark. In the context of VMS framework, the basis functions for the coarse-scale trial solutions and weighting functions are viewed as filters or projectors in the conventional LES formulation.

6.3. VARIATIONAL MULTISCALE METHOD

6.3.1. Variational Multiscale Decomposition

We discretize the bounded domain Ω into n_{el} non-overlapping elements with subdomain Ω^e and its boundary $\Gamma^e=\partial\Omega^e$, where $e=1,2,\ldots,n_{el}$ is the element numbering. Henceforth, we can construct the union of element interiors $\Omega'=\bigcup_1^{n_{el}}\left(\text{int}\right)\Omega^e$ and element boundaries $\Gamma'=\bigcup_1^{n_{el}}\Gamma^e$. We further assume an additive decomposition of the unknown fields $\left[\boldsymbol{u},p,\theta\right]^T$ and their corresponding weighting functions $\left[\boldsymbol{w},q,\eta\right]$ as

$$\begin{aligned}\boldsymbol{u}\left(\boldsymbol{x},t\right)&=\bar{\boldsymbol{u}}\left(\boldsymbol{x},t\right)+\boldsymbol{u}'\left(\boldsymbol{x},t\right)\\ p\left(\boldsymbol{x},t\right)&=\bar{p}\left(\boldsymbol{x},t\right)+p'\left(\boldsymbol{x},t\right)\\ \theta\left(\boldsymbol{x},t\right)&=\bar{\theta}\left(\boldsymbol{x},t\right)+\theta'\left(\boldsymbol{x},t\right)\end{aligned}\tag{6.16}$$

$$\begin{aligned}\boldsymbol{w}\left(\boldsymbol{x}\right)&=\bar{\boldsymbol{w}}\left(\boldsymbol{x}\right)+\boldsymbol{w}'\left(\boldsymbol{x}\right)\\ q\left(\boldsymbol{x}\right)&=\bar{q}\left(\boldsymbol{x}\right)+q'\left(\boldsymbol{x}\right)\\ \eta\left(\boldsymbol{x}\right)&=\bar{\eta}\left(\boldsymbol{x}\right)+\eta'\left(\boldsymbol{x}\right)\end{aligned}\tag{6.17}$$

An assumption is made that the fine-scale fields vanishes at the element boundaries, that is

$$\begin{aligned} \boldsymbol{u}' = \boldsymbol{0} \quad p' = 0 \quad \theta' = 0 \quad \text{on} \quad \Gamma' \\ \boldsymbol{w}' = \boldsymbol{0} \quad q' = 0 \quad \eta' = 0 \quad \text{on} \quad \Gamma' \end{aligned} \tag{6.18}$$

We now introduce the appropriate function spaces for coarse-scale and fine-scale unknown fields by specifying a direct sum decompositions as $\mathcal{V} = \bar{\mathcal{V}} \oplus \mathcal{V}'$, $\mathcal{Q} = \bar{\mathcal{Q}} + \mathcal{Q}'$ and $\mathcal{H} = \bar{\mathcal{H}} + \mathcal{H}'$, where $\bar{\mathcal{V}}$, $\bar{\mathcal{Q}}$ and $\mathcal{H}$ are the spaces for the coarse-scale velocity, pressure and temperature fields that obey C^0 continuity over the entire domain with element-wise support of complete polynomials of orders determined by shape functions. On the other hand, the function spaces of fine-scale fields $\mathcal{V}'$, $\mathcal{Q}'$ and $\mathcal{H}'$ are infinite dimensional. We utilize bubble functions to discretize the fine scales, which satisfies the assumption (6.18).

By substituting the splits of weighting functions defined in (6.17) to the standard Galerkin weak forms (6.13)-(6.15), we have

$$\begin{aligned} \left(\bar{\boldsymbol{w}} + \boldsymbol{w}', \boldsymbol{u}_{,t}\right) + \left(\bar{\boldsymbol{w}} + \boldsymbol{w}', \boldsymbol{u} \cdot \nabla \boldsymbol{u}\right) + \left(\nabla\left(\bar{\boldsymbol{w}} + \boldsymbol{w}'\right), 2\nu\nabla^s \boldsymbol{u}\right) - \left(\nabla \cdot \left(\bar{\boldsymbol{w}} + \boldsymbol{w}'\right), p\right) \\ + \left(\bar{\boldsymbol{w}} + \boldsymbol{w}', \boldsymbol{g}\beta\theta\right) = \left(\bar{\boldsymbol{w}} + \boldsymbol{w}', \boldsymbol{h}_M\right)_{\Gamma_h^M} + \left(\bar{\boldsymbol{w}} + \boldsymbol{w}', \boldsymbol{f}_b\right) \end{aligned} \tag{6.19}$$

$$\left(\bar{q} + q', \nabla \cdot \boldsymbol{u}\right) = 0 \tag{6.20}$$

$$\left(\bar{\eta} + \eta', \theta_{,t}\right) + \left(\bar{\eta} + \eta', \boldsymbol{u} \cdot \nabla\theta\right) + \left(\nabla\left(\bar{\eta} + \eta'\right), \alpha\nabla\theta\right) = \left(\bar{\eta} + \eta', h_E\right)_{\Gamma_h^E} + \left(\bar{\eta} + \eta', f\right) \tag{6.21}$$

Because of the linearity of the additively decomposed weighting functions in (6.17), we can split the weak form into coarse-scale and fine-scale sub-problems as follows,

Coarse-scale sub-problems

$$\left(\bar{\boldsymbol{w}}, \boldsymbol{u}_{,t}\right) + \left(\bar{\boldsymbol{w}}, \boldsymbol{u} \cdot \nabla \boldsymbol{u}\right) + \left(\nabla\bar{\boldsymbol{w}}, 2\nu\nabla^s \boldsymbol{u}\right) - \left(\nabla \cdot \bar{\boldsymbol{w}}, p\right) + \left(\bar{\boldsymbol{w}}, \boldsymbol{g}\beta\theta\right) = \left(\bar{\boldsymbol{w}}, \boldsymbol{h}_M\right)_{\Gamma_h^M} + \left(\bar{\boldsymbol{w}}, \boldsymbol{f}_b\right) \tag{6.22}$$

$$\left(q, \nabla \cdot \boldsymbol{u}\right) = 0 \tag{6.23}$$

$$\left(\bar{\eta}, \theta_{,t}\right) + \left(\bar{\eta}, \boldsymbol{u} \cdot \nabla\theta\right) + \left(\nabla\bar{\eta}, \alpha\nabla\theta\right) = \left(\bar{\eta}, h_E\right)_{\Gamma_h^E} + \left(\bar{\eta}, f\right) \tag{6.24}$$

Fine-scale sub-problems

$$\left(\boldsymbol{w}', \boldsymbol{u}_{,t}\right) + \left(\boldsymbol{w}', \boldsymbol{u} \cdot \nabla \boldsymbol{u}\right) + \left(\nabla\boldsymbol{w}', 2\nu\nabla^s \boldsymbol{u}\right) - \left(\nabla \cdot \boldsymbol{w}', p\right) + \left(\boldsymbol{w}', \boldsymbol{g}\beta\theta\right) = \left(\boldsymbol{w}', \boldsymbol{h}_M\right)_{\Gamma_h^M} + \left(\boldsymbol{w}', \boldsymbol{f}_b\right) \tag{6.25}$$

$$\left(q', \nabla \cdot \boldsymbol{u}\right) = 0 \tag{6.26}$$

$$\left(\eta', \theta_{,t}\right) + \left(\eta', \boldsymbol{u} \cdot \nabla \theta\right) + \left(\nabla \eta', \alpha \nabla \theta\right) = \left(\eta', h_E\right)_{\Gamma_h^E} + \left(\eta', f\right) \tag{6.27}$$

6.3.2. Linearization of Fine-scale Sub-problems

The fine-scale problems summarized in (6.25)-(6.27) are a mixed nonlinear coupled systems. We first introduce the linearization operator with respect to all the fine-scale trial solution fields: $\boldsymbol{V}' = \{\boldsymbol{u}', p', \theta'\}$, that is

$$\mathcal{L}\left(R\left(\boldsymbol{u}', \theta'\right)\right) = \frac{d}{d\varepsilon} R\left(\boldsymbol{u}' + \varepsilon \delta \boldsymbol{u}', p' + \varepsilon \delta p', \theta' + \varepsilon \delta \theta'\right)\Big|_{\varepsilon = 0} \tag{6.28}$$

Applying the above linearization operator to the fine-scale sub-problems in (6.25)-(6.27), we get the linearized fine-scale problems as

$$\begin{aligned} &\left(\boldsymbol{w}', \delta \boldsymbol{u}'_{,t}\right) + \left(\boldsymbol{w}', \delta \boldsymbol{u}' \cdot \nabla \boldsymbol{u}\right) + \left(\boldsymbol{w}', \boldsymbol{u} \cdot \nabla \delta \boldsymbol{u}'\right) + \left(\nabla \boldsymbol{w}', 2\nu \nabla^s \delta \boldsymbol{u}'\right) - \left(\nabla \cdot \boldsymbol{w}', \delta p'\right) + \left(\boldsymbol{w}', \boldsymbol{g} \beta \delta \theta'\right) \\ &= -\left(\boldsymbol{w}', \boldsymbol{u}_{,t}\right) - \left(\boldsymbol{w}', \boldsymbol{u} \cdot \nabla \boldsymbol{u}\right) - \left(\nabla \boldsymbol{w}', 2\nu \nabla^s \boldsymbol{u}\right) + \left(\nabla \cdot \boldsymbol{w}', p\right) - \left(\boldsymbol{w}', \boldsymbol{g} \beta \theta\right) + \left(\boldsymbol{w}', \boldsymbol{f}_b\right) = -\left(\boldsymbol{w}', \boldsymbol{r}_M\right) \end{aligned} \tag{6.29}$$

$$\left(q', \nabla \delta \boldsymbol{u}'\right) = -\left(q', r_C\right) \tag{6.30}$$

$$\begin{aligned} &\left(\eta', \delta \theta'_{,t}\right) + \left(\eta', \delta \boldsymbol{u}' \cdot \nabla \theta\right) + \left(\eta', \boldsymbol{u} \cdot \nabla \delta \theta'\right) + \left(\nabla \eta', \alpha \nabla \delta \theta'\right) \\ &= -\left(\eta', \theta_{,t}\right) - \left(\eta', \bar{\boldsymbol{u}} \cdot \nabla \theta\right) - \left(\nabla \eta', \alpha \nabla \theta\right) + \left(\eta', f\right) = -\left(\eta', r_E\right) \end{aligned} \tag{6.31}$$

where $\boldsymbol{r}_M$, r_C and r_E are the residuals of the Euler-Lagrange equations of the coarse-scale conservation laws, including momentum, mass and energy, respectively, and are defined as

$$\boldsymbol{r}_M\left(\boldsymbol{u}, p, \theta\right) = \boldsymbol{u}_{,t} + \boldsymbol{u} \cdot \nabla \boldsymbol{u} + \nabla p - \nabla \cdot \left(2\nu \nabla^s \boldsymbol{u}\right) + \boldsymbol{g} \beta \theta - \boldsymbol{f}_b \tag{6.32}$$

$$r_C\left(\boldsymbol{u}\right) = \nabla \cdot \boldsymbol{u} \tag{6.33}$$

$$r_E\left(\boldsymbol{u}, \theta\right) = \theta_{,t} + \boldsymbol{u} \cdot \nabla \theta - \nabla \cdot \left(\alpha \nabla \theta\right) - f \tag{6.34}$$

Remark. The linear operator (6.28) is to eliminate the fine-scale Reynolds stress $\left(\boldsymbol{w}', \boldsymbol{u}' \cdot \nabla \boldsymbol{u}'\right)$ and fine-scale Reynolds flux $\left(\eta', \boldsymbol{u}' \cdot \nabla \theta'\right)$, while it preserves the coupling between mechanical and thermal phases.

In the earlier work of the senior author on isothermal incompressible turbulence model [31], a similar treatment was suggested.

Remark. The notation δ in the terms containing perturbed fine scales are dropped in following derivations.

6.3.3. Variational Multiscale Decomposition in Fine Scales

We decompose the fine-scale trial solution and weighting function into fine-scale level-I and fine-scale level-II. The purpose of applying VMS framework at the fine scale level is to derive a stabilized fine-scale formulation for the fine-scale inf-sup condition and the advection of fine-scale velocity $\boldsymbol{u}'$ and θ'. Therefore only these two fields and their corresponding weighting functions are subjected to a further additive split

$$\boldsymbol{u}'(\boldsymbol{x},t)=\boldsymbol{u}'_I(\boldsymbol{x},t)+\boldsymbol{u}'_{II}(\boldsymbol{x},t) \quad \text{and} \quad \theta'(\boldsymbol{x},t)=\theta'_I(\boldsymbol{x},t)+\theta'_{II}(\boldsymbol{x},t) \tag{6.35}$$

$$\boldsymbol{w}'(\boldsymbol{x})=\boldsymbol{w}'_I(\boldsymbol{x})+\boldsymbol{w}'_{II}(\boldsymbol{x}) \quad \text{and} \quad \eta(\boldsymbol{x})=\eta_I(\boldsymbol{x})+\eta_{II}(\boldsymbol{x}) \tag{6.36}$$

By segregating the terms in the weight functions corresponding to different levels in the fine-scale, we obtain the fine-scale level-I and fine-scale level-II problems:

Fine-scale level-I problems

$$\left(\boldsymbol{w}'_I,\boldsymbol{u}'_{,t}\right)+\left(\boldsymbol{w}'_I,\boldsymbol{u}'\cdot\nabla\boldsymbol{u}\right)+\left(\boldsymbol{w}'_I,\boldsymbol{u}\cdot\nabla\boldsymbol{u}'\right)+\left(\nabla\boldsymbol{w}'_I,2\nu\nabla^s\boldsymbol{u}'\right)-\left(\nabla\cdot\boldsymbol{w}'_I,p'\right)+\left(\boldsymbol{w}'_I,\boldsymbol{g}\beta\theta'\right)=-\left(\boldsymbol{w}'_I,\boldsymbol{r}_M\right) \tag{6.37}$$

$$\left(q'_I,\nabla\boldsymbol{u}'\right)=-\left(q'_I,r_C\right) \tag{6.38}$$

$$\left(\eta'_I,\theta'_{,t}\right)+\left(\eta'_I,\boldsymbol{u}'\cdot\nabla\theta\right)+\left(\eta'_I,\boldsymbol{u}\cdot\nabla\theta'\right)+\left(\nabla\eta'_I,\alpha\nabla\theta'\right)=-\left(\eta'_I,r_E\right) \tag{6.39}$$

Fine-scale level-II problems

$$\left(\boldsymbol{w}'_{II},\boldsymbol{u}'_{,t}\right)+\left(\boldsymbol{w}'_{II},\boldsymbol{u}'\cdot\nabla\boldsymbol{u}\right)+\left(\boldsymbol{w}'_{II},\boldsymbol{u}\cdot\nabla\boldsymbol{u}'\right)+\left(\nabla\boldsymbol{w}'_{II},2\nu\nabla^s\boldsymbol{u}'\right)-\left(\nabla\cdot\boldsymbol{w}'_{II},p'\right)+\left(\boldsymbol{w}'_{II},\boldsymbol{g}\beta\theta'\right)=-\left(\boldsymbol{w}'_{II},\boldsymbol{r}_M\right) \tag{6.40}$$

$$\left(\eta'_{II},\theta'_{,t}\right)+\left(\eta'_{II},\boldsymbol{u}'\cdot\nabla\theta\right)+\left(\eta'_{II},\boldsymbol{u}\cdot\nabla\theta'\right)+\left(\nabla\eta'_{II},\alpha\nabla\theta'\right)=-\left(\eta'_{II},r_E\right) \tag{6.41}$$

6.3.4. Modelling of Fine-scale Level-II

Our aim in this section is to extract the solution of fine-scale level-II velocity $\boldsymbol{u}'_{II}$ and temperature θ'_{II}. These solutions will be substituted in the fine-scale level-I and will result in a stabilized formulation for the fine-scale problems. We rearrange the fine-scale level-II problems in (6.40) and (6.41) by splitting the different level of fine-scale trail solutions as,

$$\begin{aligned}
&\left(\boldsymbol{w}'_{II},\boldsymbol{u}'_{II,t}\right)+\left(\boldsymbol{w}'_{II},\boldsymbol{u}'_{II}\cdot\nabla\boldsymbol{u}\right)+\left(\boldsymbol{w}'_{II},\boldsymbol{u}\cdot\nabla\boldsymbol{u}'_{II}\right)+\left(\nabla\boldsymbol{w}'_{II},2\nu\nabla^{s}\boldsymbol{u}'_{II}\right)+\left(\boldsymbol{w}'_{II},\boldsymbol{g}\beta\theta'_{II}\right)\\
&=-\left(\boldsymbol{w}'_{II},\boldsymbol{u}'_{I,t}\right)-\left(\boldsymbol{w}'_{II},\boldsymbol{u}'_{I}\cdot\nabla\boldsymbol{u}\right)-\left(\boldsymbol{w}'_{II},\boldsymbol{u}\cdot\nabla\boldsymbol{u}'_{I}\right)-\left(\nabla\boldsymbol{w}'_{II},2\nu\nabla^{s}\boldsymbol{u}'_{I}\right)\\
&+\left(\nabla\cdot\boldsymbol{w}'_{II},p'\right)-\left(\boldsymbol{w}'_{II},\boldsymbol{g}\beta\theta'_{I}\right)-\left(\boldsymbol{w}'_{II},\boldsymbol{r}_{M}\right)\\
&=-\left(\boldsymbol{w}'_{II},\boldsymbol{r}'_{M}\right)-\left(\boldsymbol{w}'_{II},\boldsymbol{r}_{M}\right)
\end{aligned}\tag{6.42}$$

$$\begin{aligned}
&\left(\eta'_{II},\delta\boldsymbol{u}'_{II,t}\right)+\left(\eta'_{II},\delta\boldsymbol{u}'_{II}\cdot\nabla\theta\right)+\left(\eta'_{II},\bar{\boldsymbol{u}}\cdot\nabla\delta\theta'_{II}\right)+\left(\nabla\eta'_{II},\alpha\nabla\delta\theta'_{II}\right)\\
&=-\left(\eta'_{II},\delta\boldsymbol{u}'_{I,t}\right)-\left(\eta'_{II},\delta\boldsymbol{u}'_{I}\cdot\nabla\theta\right)-\left(\eta'_{II},\bar{\boldsymbol{u}}\cdot\nabla\delta\theta'_{I}\right)-\left(\nabla\eta'_{II},\alpha\nabla\delta\theta'_{I}\right)-\left(\eta'_{II},r_{E}\right)\\
&=-\left(\eta'_{II},r'_{E}\right)-\left(\eta'_{II},r_{E}\right)
\end{aligned}\tag{6.43}$$

where $\boldsymbol{r}'_{M}$ is the residual of the Euler-Lagrange equation of the linearized fine-scale level-I conservation of momentum, while r'_{E} is the residual of the Euler-Lagrange equation of the linearized fine-scale energy equation.

$$\begin{aligned}
\boldsymbol{r}'_{M}&=\boldsymbol{u}'_{I,t}+\underbrace{\boldsymbol{u}'_{I}\cdot\nabla\boldsymbol{u}+\boldsymbol{u}\cdot\nabla\boldsymbol{u}'_{I}+\nabla p'-\nabla\cdot\left(2\nu\nabla^{s}\boldsymbol{u}'_{I}\right)+\boldsymbol{g}\beta\theta'_{I}}_{\boldsymbol{r}'^{SS}_{M}}\\
r'_{E}&=\theta'_{I,t}+\underbrace{\boldsymbol{u}'_{I}\cdot\nabla\theta+\boldsymbol{u}\cdot\nabla\theta'_{I}-\nabla\cdot\left(\alpha\nabla\theta'_{I}\right)}_{r'^{SS}_{E}}
\end{aligned}\tag{6.44}$$

We use bubble functions to interpolate the fine-scale trial solutions and weighting functions as follows,

$$\begin{aligned}
\boldsymbol{u}'_{II}&=b^{e}_{II}\boldsymbol{u}'^{e}_{II}\quad\text{and}\quad\theta'_{II}=b^{e}_{II}\theta'^{e}_{II}\\
\boldsymbol{w}'_{II}&=b^{e}_{II}\boldsymbol{w}'^{e}_{II}\quad\text{and}\quad\eta'_{II}=b^{e}_{II}\eta'^{e}_{II}
\end{aligned}\tag{6.45}$$

For the time marching scheme, we have employed generalized-alpha method [78] for the first-order system, where the inertial term is evaluated at $n+\alpha_{m}$ while other terms are evaluated at $n+\alpha_{f}$ as marching from time-step n to $n+1$. For a generic time-dependent filed $(\bullet)$, its temporal discretization through generalized-α method can be represented as

$$
\begin{aligned}
\left.\frac{\partial(\bullet)}{\partial t}\right|_{n+1} &= \frac{(\bullet)_{n+1}-(\bullet)_n}{\gamma\Delta t}+\frac{\gamma-1}{\gamma}\left.\frac{\partial(\bullet)}{\partial t}\right|_n = \frac{1}{\gamma\Delta t}(\bullet)_{n+1} \\
\left.\frac{\partial(\bullet)}{\partial t}\right|_{n+\alpha_m} &= \alpha_m\left.\frac{\partial(\bullet)}{\partial t}\right|_{n+1}+(1-\alpha_m)\left.\frac{\partial(\bullet)}{\partial t}\right|_n = \frac{\alpha_m}{\gamma\Delta t}(\bullet)_{n+1} \\
(\bullet)\big|_{n+\alpha_f} &= \alpha_f(\bullet)\big|_{n+1}+(1-\alpha_f)(\bullet)\big|_n = \alpha_f(\bullet)\big|_n
\end{aligned}
\tag{6.46}
$$

By applying the chosen spatial and temporal discretization to (6.42) and (6.43), we obtain a linear system as.

$$
\underbrace{\left(b_{II}^e, b_{II}^e\right)\boldsymbol{I}_{4\times4}}_{\boldsymbol{M}''_{4\times4}}\begin{bmatrix}\boldsymbol{u}''^e_{II,t}\\ \theta''^e_{II,t}\end{bmatrix}_{n+\alpha_m}+\underbrace{\begin{bmatrix}\hat{\boldsymbol{\tau}}_M & \hat{\boldsymbol{\tau}}_{ME}\\ \hat{\boldsymbol{\tau}}_{EM} & \tau_E\end{bmatrix}}_{\boldsymbol{K}''_{4\times4}}\begin{bmatrix}\boldsymbol{u}''^e_{II}\\ \theta''^e_{II}\end{bmatrix}_{n+\alpha_f}=-\left(b^e,1\right)\boldsymbol{I}_{4\times4}\begin{bmatrix}\boldsymbol{r}'_M+\boldsymbol{r}_M\\ r'_E+r_E\end{bmatrix}_{n+\alpha_f}
\tag{6.47}
$$

$$
\begin{aligned}
\hat{\tau}_M\left(b_{II}^e\right) &= \int_{\Omega^e}\left(b_{II}^e\boldsymbol{u}\cdot\nabla b_{II}^e+\left(b_{II}^e\right)^2\cdot\nabla^T\boldsymbol{u}+\nu\nabla b_{II}^e\cdot\nabla b_{II}^e+\nu\nabla b_{II}^e\otimes\nabla b_{II}^e\right)d\Omega \\
\hat{\tau}_E\left(b_{II}^e\right) &= \int_{\Omega^e}\left(b_{II}^e\boldsymbol{u}\cdot\nabla b_{II}^e+\alpha\nabla b_{II}^e\cdot\nabla b_{II}^e\right)d\Omega \\
\hat{\tau}_{ME}\left(b_{II}^e\right) &= \int_{\Omega^e}\boldsymbol{g}\beta\left(b_{II}^e\right)^2\,d\Omega \\
\hat{\tau}_{EM}\left(b_{II}^e\right) &= \int_{\Omega^e}\left(b_{II}^e\right)^2\nabla\theta\,d\Omega
\end{aligned}
\tag{6.48}
$$

where $\hat{\tau}_M$, including cross-scale advection term, skew advection term and symmetric diffusion terms, is in fact the standard linear system of linearized fine-scale Navier-Stokes equation that is derived in our earlier work [106,173]. $\hat{\tau}_E$ represents the cross-scale advection-diffusion in the thermal phase and is exactly similar to our earlier work [114,173]. The coupling terms (i.e., $\hat{\tau}_{ME}$ and $\hat{\tau}_{EM}$) of mechanical phase and thermal phase are also admitted in the fine-scale problems. Consequently, a full $\left(n_{sd}+1\right)\times\left(n_{sd}+1\right)$ matrices are derived from the discretized linear system in (6.47). Henceforth, the fine-scale level-II velocities and temperature are written in the residual-driven form

$$
\begin{bmatrix}\boldsymbol{u}'_{II}\\ \theta'_{II}\end{bmatrix}_{n+1}=b_{II}^e\begin{bmatrix}\boldsymbol{u}''^e_{II}\\ \theta''^e_{II}\end{bmatrix}_{n+1}=-\underbrace{\frac{\alpha''_f b_{II}^e\int_{\Omega^e}b_{II}^e\,d\Omega}{\dfrac{\alpha''_m}{\gamma''\Delta t}\boldsymbol{M}''+\alpha''_f\boldsymbol{K}''}}_{\boldsymbol{\tau}'}\begin{bmatrix}\boldsymbol{r}'_M+\boldsymbol{r}_M\\ r'_E+r_E\end{bmatrix}_{n+1}=-\boldsymbol{\tau}'\begin{bmatrix}\boldsymbol{r}'_M+\boldsymbol{r}_M\\ r'_E+r_E\end{bmatrix}_{n+1}
\tag{6.49}
$$

Remark. The time dependent terms $(\bullet)_n$ and their time derivative $\partial(\bullet)_n / \partial t$ of level-II fine scale are neglected (i.e., $(\bullet)_n = 0$ and $\partial(\bullet)/\partial t\big|_n = 0$). To ensure the unconditionally stability, α_m, α_f and γ are determined by a constant ρ_∞ [78].

Remark. To avoid the issue of orthogonality of standard bubble function and its derivatives, the advection parts in (6.48) are enriched with advection bubble, as suggested in senior author's previous work [106,114].

6.3.5. Modelling of Fine-scale Level-I

Applying the VMS decomposition to the fine-scales (6.35) on the combined fine-scale level-I sub-problems (6.37)-(6.39) and utilizing divergence theorem, we have

$$\begin{aligned}
&\left(\boldsymbol{w}', \boldsymbol{u}'_{,t}\right) + \left(\boldsymbol{w}', \boldsymbol{u}' \cdot \nabla \boldsymbol{u}\right) + \left(\boldsymbol{w}', \boldsymbol{u} \cdot \nabla \boldsymbol{u}'\right) + \left(\nabla \boldsymbol{w}'_I, 2\nu \nabla^s \boldsymbol{u}'\right) - \left(\nabla \cdot \boldsymbol{w}', p'\right) + \left(\boldsymbol{w}', \boldsymbol{g}\beta\theta'\right) \\
&\quad + \left(q', \nabla \boldsymbol{u}'\right) + \left(\eta', \theta'_{,t}\right) + \left(\eta', \boldsymbol{u}' \cdot \nabla \theta\right) + \left(\eta', \boldsymbol{u} \cdot \nabla \theta'\right) + \left(\nabla \eta', \alpha \nabla \theta'\right) \\
&\quad - \left(\left[\boldsymbol{\chi}'_M, \boldsymbol{\chi}'_E\right], \boldsymbol{\tau}'\left[\boldsymbol{u}'_{,t}; \theta'_{,t}\right]\right) - \left(\left[\boldsymbol{\chi}'_M, \boldsymbol{\chi}'_E\right], \boldsymbol{\tau}'\left[\boldsymbol{r}'^{SS}_M; r'^{SS}_E\right]\right) \\
&\quad = -\left(\boldsymbol{w}'_I, \boldsymbol{r}_M\right) - \left(q'_I, r_C\right) - \left(\eta'_I, r_E\right) + \left(\left[\boldsymbol{\chi}'_M, \boldsymbol{\chi}'_E\right], \boldsymbol{\tau}'\left[\boldsymbol{r}_M, \boldsymbol{r}_E\right]^T\right)
\end{aligned} \tag{6.50}$$

where weighting functions $\boldsymbol{\chi}'_M$ and $\boldsymbol{\chi}'_E$ are defined as,

$$\begin{aligned}
\boldsymbol{\chi}'_M &= \frac{\alpha''_m}{\gamma'' \Delta t} \boldsymbol{w}' + \boldsymbol{w}' \cdot \nabla^T \boldsymbol{u} - \boldsymbol{u} \cdot \nabla \boldsymbol{w}' - \nu\left(\nabla\left(\nabla \cdot \boldsymbol{w}'\right) + \Delta \boldsymbol{w}'\right) - \nabla q' + \eta' \nabla^T \theta \\
\boldsymbol{\chi}'_E &= \frac{\alpha''_m}{\gamma'' \Delta t} \eta' + \beta \boldsymbol{w}' \cdot \boldsymbol{g} - \boldsymbol{u} \cdot \nabla \eta' - \alpha \Delta \eta'
\end{aligned} \tag{6.51}$$

The basis function for the fine-scale weighting function and trial solution is bubble function, that is

$$\begin{aligned}
&\boldsymbol{u}' = b^e \boldsymbol{u}'^e; \quad p' = b^e p'^e; \quad \theta' = b^e \theta'^e; \\
&\boldsymbol{w}' = b^e \boldsymbol{w}'^e; \quad q' = b^e q'^e; \quad \eta' = b^e \eta'^e;
\end{aligned} \tag{6.52}$$

Using the spatial discretization defined in (6.52) and generalized-α method (6.46) as time marching scheme, the discrete system of stabilized fine-scale weak form is

$$
\underbrace{\left\{\left(b^e,b^e\right)\begin{bmatrix}\boldsymbol{I}_{n_{sd}} & & \\ & 0 & \\ & & 1\end{bmatrix}-\frac{\partial^2\left(\left[\boldsymbol{\chi}'_M,\boldsymbol{\chi}'_E\right],\boldsymbol{\tau}'\left[\boldsymbol{u}';\theta'\right]\right)}{\partial \boldsymbol{V}^e\partial \boldsymbol{W}^e}\right\}}_{\boldsymbol{M}'}\frac{\alpha'_m}{\gamma'\Delta t}\begin{bmatrix}\boldsymbol{u}'^e\\0\\\theta'^e\end{bmatrix}_{n+1}
$$

$$
+\underbrace{\left\{\begin{bmatrix}\hat{\boldsymbol{\tau}}_M\left(b^e\right) & -\left(\nabla\cdot b^e,b^e\right) & \hat{\boldsymbol{\tau}}_{ME}\left(b^e\right)\\ \left(b^e,\nabla b^e\right) & 0 & 0\\ \hat{\boldsymbol{\tau}}_{EM}\left(b^e\right) & 0 & \tau_E\left(b^e\right)\end{bmatrix}-\frac{\partial^2\left(\left[\boldsymbol{\chi}'_M,\boldsymbol{\chi}'_E\right],\boldsymbol{\tau}'\left[\boldsymbol{r}'^{SS}_M;r'^{SS}_E\right]\right)}{\partial \boldsymbol{V}^e\partial \boldsymbol{W}^e}\right\}}_{\boldsymbol{K}'}\alpha'_f\begin{bmatrix}\boldsymbol{u}'^e\\p'^e\\\theta'^e\end{bmatrix}_{n+1} \tag{6.53}
$$

$$
=-\alpha'_f\underbrace{\frac{\partial\left(\left[\boldsymbol{w}'_I,q'_I,\eta'_I\right]-\left[\boldsymbol{\chi}'_M,\boldsymbol{\chi}'_E\right]\boldsymbol{\tau}',1\right)}{\partial \boldsymbol{W}^e}\boldsymbol{I}_{n_{sd}+2}}_{\boldsymbol{F}'}\left(1,\left[\boldsymbol{r}_M,r_C,r_E\right]^T\right)
$$

where $\boldsymbol{V}^e=\left[\boldsymbol{u}'^e,p'^e,\theta'^e\right]^T$ and $\boldsymbol{W}^e=\left[\boldsymbol{w}'^e,q'^e,\eta'^e\right]$ are the fine-scale trial solution and weighting function, respectively. Henceforth, the fine-scale velocities, pressure and temperature are solved as

$$
\begin{bmatrix}\boldsymbol{u}'\\p'\\\theta'\end{bmatrix}_{n+1}=b^e\begin{bmatrix}\boldsymbol{u}'^e\\p'^e\\\theta'^e\end{bmatrix}_{n+1}=-\underbrace{\frac{\alpha'_f b^e\boldsymbol{F}'}{\frac{\alpha'_m}{\gamma'\Delta t}\boldsymbol{M}'+\alpha'_f\boldsymbol{K}'}}_{\boldsymbol{\tau}}\begin{bmatrix}\boldsymbol{r}_M\\r_C\\r_E\end{bmatrix}_{n+1}=-\boldsymbol{\tau}\begin{bmatrix}\boldsymbol{r}_M\\r_C\\r_E\end{bmatrix}_{n+1} \tag{6.54}
$$

Remark. The stabilized fine-scale sub-problems are now fully addressed in fine-scale level-I. For the simplicity of derivation, the subscript $_I$ is dropped.

Remark. The coefficients α_m , α_f and γ for the time integration in (6.54)&(6.49) are not necessarily the same.

6.3.6. Residual-based turbulence model

By substituting the VMS decomposition (6.16) into the coarse-scale sub-problems (6.22)-(6.24) and grouping these terms by the dependency of fine-scale fields, we have

$$
\begin{aligned}
&\left(\bar{\boldsymbol{w}},\bar{\boldsymbol{u}}_{,t}\right)+\left(\bar{\boldsymbol{w}},\bar{\boldsymbol{u}}\cdot\nabla\bar{\boldsymbol{u}}\right)+\left(\nabla\bar{\boldsymbol{w}},2\nu\nabla^{s}\bar{\boldsymbol{u}}\right)-\left(\nabla\cdot\bar{\boldsymbol{w}},\bar{p}\right)+\left(\bar{\boldsymbol{w}},\boldsymbol{g}\beta\bar{\theta}\right)\\
&+\left(\bar{q},\nabla\cdot\bar{\boldsymbol{u}}\right)+\left(\bar{\eta},\bar{\theta}_{,t}\right)+\left(\bar{\eta},\bar{\boldsymbol{u}}\cdot\nabla\bar{\theta}\right)+\left(\nabla\bar{\eta},\alpha\nabla\bar{\theta}\right)\\
&+\left(\boldsymbol{\chi}_{M},\boldsymbol{u}'\right)+\left(\chi_{E},\theta'\right)+\left(\bar{\boldsymbol{w}},\boldsymbol{u}'\cdot\nabla\boldsymbol{u}'\right)+\left(\bar{\eta},\boldsymbol{u}'\cdot\nabla\theta'\right)\\
&=\left(\bar{\boldsymbol{w}},\boldsymbol{h}_{M}\right)_{\Gamma_{h}^{M}}+\left(\bar{\boldsymbol{w}},\boldsymbol{f}_{b}\right)+\left(\bar{\eta},h_{E}\right)_{\Gamma_{h}^{E}}+\left(\bar{\eta},f\right)
\end{aligned}
\tag{6.55}
$$

where the weighting functions are defined as

$$
\begin{aligned}
\boldsymbol{\chi}_{M}&=\frac{\alpha_{m}'}{\gamma'\Delta t}\bar{\boldsymbol{w}}-\boldsymbol{u}\cdot\nabla\bar{\boldsymbol{w}}+\bar{\boldsymbol{w}}\cdot\nabla^{T}\boldsymbol{u}-\nu\left(\nabla\left(\nabla\cdot\bar{\boldsymbol{w}}\right)+\Delta\bar{\boldsymbol{w}}\right)-\nabla q+\bar{\eta}\nabla^{T}\theta\\
\chi_{E}&=\frac{\alpha_{m}'}{\gamma'\Delta t}\bar{\eta}+\beta\boldsymbol{g}\cdot\bar{\boldsymbol{w}}-\boldsymbol{u}\cdot\nabla\bar{\eta}-\alpha\Delta\bar{\eta}
\end{aligned}
\tag{6.56}
$$

The stabilized nonlinear weak form is the derived VMS residual-based turbulence model for stratified turbulence. In abstract form, we rewrite (6.55) as follows,

$$
\mathcal{B}^{\mathrm{Gal}}\left(\boldsymbol{w},q,\eta;\boldsymbol{u},p,\theta\right)+\mathcal{B}^{\mathrm{VMS}}\left(\boldsymbol{w},q,\eta;\boldsymbol{u},p,\theta\right)+\mathcal{B}^{\mathrm{LES}}\left(\boldsymbol{w},q,\eta;\boldsymbol{u},p,\theta\right)=\mathcal{F}^{\mathrm{Gal}}\left(\boldsymbol{w},\eta\right)
\tag{6.57}
$$

where $\mathcal{B}^{\mathrm{Gal}}$ and $\mathcal{F}^{\mathrm{Gal}}$ are the Galerkin terms

$$
\begin{aligned}
\mathcal{B}^{\mathrm{Gal}}\left(\boldsymbol{w},q,\eta;\boldsymbol{u},p,\theta\right)&=\left(\boldsymbol{w},\boldsymbol{u}_{,t}\right)+\left(\boldsymbol{w},\boldsymbol{u}\cdot\nabla\boldsymbol{u}\right)+\left(\nabla\boldsymbol{w},2\nu\nabla^{s}\boldsymbol{u}\right)-\left(\nabla\cdot\boldsymbol{w},p\right)+\left(\boldsymbol{w},\boldsymbol{g}\beta\theta\right)\\
&\quad+\left(q,\nabla\cdot\boldsymbol{u}\right)+\left(\eta,\theta_{,t}\right)+\left(\eta,\boldsymbol{u}\cdot\nabla\theta\right)+\left(\nabla\eta,\alpha\nabla\theta\right)\\
\mathcal{F}^{\mathrm{Gal}}\left(\boldsymbol{w},\eta\right)&=\left(\boldsymbol{w},\boldsymbol{h}_{M}\right)_{\Gamma_{h}^{M}}+\left(\boldsymbol{w},\boldsymbol{f}_{b}\right)+\left(\eta,h_{E}\right)_{\Gamma_{h}^{E}}+\left(\eta,f\right)
\end{aligned}
\tag{6.58}
$$

$\mathcal{B}^{\mathrm{VMS}}$ is the stabilization terms,

$$
\mathcal{B}^{\mathrm{VMS}}\left(\boldsymbol{w},q,\eta;\boldsymbol{u},p,\theta\right)=\left(\boldsymbol{\chi}_{M},\boldsymbol{u}'\right)+\left(\chi_{E},\theta'\right)
\tag{6.59}
$$

And $\mathcal{B}^{\mathrm{LES}}$ is the large-eddy turbulence model.

$$
\mathcal{B}^{\mathrm{LES}}\left(\boldsymbol{w},q,\eta;\boldsymbol{u},p,\theta\right)=\left(\boldsymbol{w},\boldsymbol{u}'\cdot\nabla\boldsymbol{u}'\right)+\left(\eta,\boldsymbol{u}'\cdot\nabla\theta'\right)
\tag{6.60}
$$

Remark. We drop the superposed bar from the coarse-scale weighting function and trial solutions since the stabilized form (6.55) is fully represented in the terms of coarse-scale fields.

6.4. NUMERICAL TESTS

6.4.1. 2D Natural Convection: A Benchmark

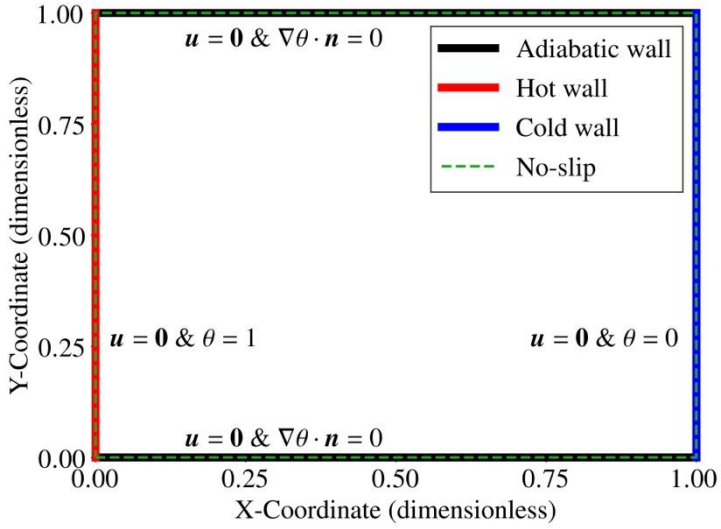

Figure 6.1 The schematics of natural convection problem

In this subsection, we carry out a convergence study to validate the accuracy of the proposed method through the classic Rayleigh-Bénard convection in a 2D bi-unit domain. The left and right walls are applied with Dirichlet boundary conditions on the relative temperature field to provide a constant background temperature gradient as the driving mechanism of the problem. The top and bottom are adiabatic walls. All four walls have no-slip condition, and a zero-pressure reference is applied at the left-bottom corner in order to filter out the constant pressure mode. The schematic diagram and boundary conditions are presented in Figure 6.1. The unit gravitational force is applied in the negative y-direction, and the thermal expansion coefficient is set as $\beta = 1$. The Prandtl number $\mathrm{Pr} = 0.71$ that represents the physics of air flows, and Rayleigh number is adjusted by proportionally changing the value of kinematic viscosity ν and thermal diffusivity α.

Though the exact solution for natural convection has derived by Chenoweth and Paulucci [34] for cases with $\mathrm{Ra} \to 0$, cases that are particularly concerned for engineering purposes with much larger Rayleigh number has no analytical solution. Therefore, the convergence study in this subsection is compared with reported numerical data [10,40,63,165], including maxima velocity, local and averaged Nusselt number.

6.4.1.1. Averaged Nusselt number

The averaged Nusselt number describes the averaged heat flux along a certain boundary, and it is defined as follows:

$$\overline{\mathrm{Nu}} = \frac{1}{A_H}\int_{\Gamma_H} \nabla\theta \cdot \boldsymbol{n}\, d\Gamma \tag{6.61}$$

Table 6.1 Reported averaged Nusselt number in the literature

Ra	***10^3***	***10^4***	***10^5***	***10^6***
***REF.** [40]*	1.118	2.243	4.519	8.800
***REF.** [63]*	--	2.24475	4.52164	8.82513
***REF.** [10]*	1.114	2.245	4.510	8.806
***REF.** [165]*	1.118	2.245	4.516	8.810
Present Work		2.24462	4.52021	8.81490

Amongst the reported data in the literature, Hortmann *et al.* [63] used a multigrid finite volume method and extrapolated the averaged Nusselt number through the finest mesh for various Rayleigh number with more significant figures than other available data. Therefore, these numbers are used as references for our convergence rate study about the error of the averaged Nusselt number (i.e., the relative difference between the computed and the reported $\overline{\mathrm{Nu}}$), as shown in Figure 6.2.

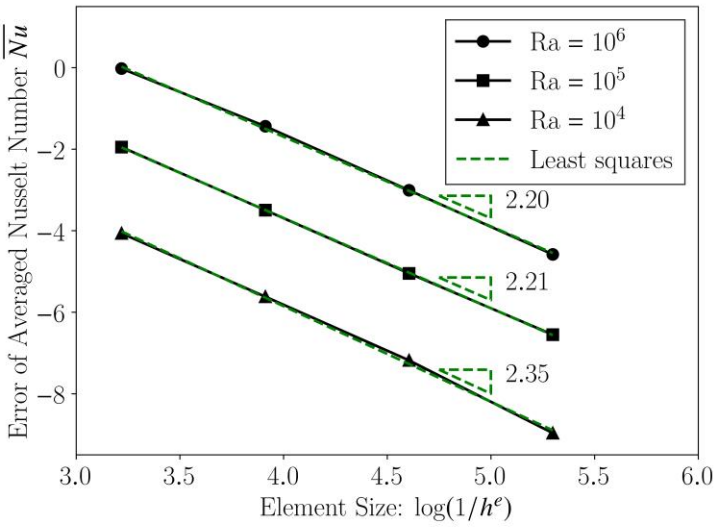

Figure 6.2 Convergence rate of averaged Nusselt number

6.4.1.2. Maxima of velocities

The maximum horizontal velocity $U_{\max}$ within the vertical middle line and the maximum vertical velocity $V_{\max}$ along the horizontal middle line are also reported in various literature [10,40,63,165]. We list these reported data in Table 6.2 and Table 6.3 as the references to validate the proposed method. As a comparison, the data are attained from the proposed method with a mesh of 200×200 B8 elements.

Table 6.2 Maximum horizontal velocity $U_{\max}$ at the vertical middle line

Ra	***10^3***	***10^4***	***10^5***	***10^6***
***REF.** [40]*	0.136	0.192	0.153	0.079
***REF.** [63]*	--	0.192	0.153	0.079
***REF.** [10]*	0.153	0.193	0.132	0.077
***REF.** [165]*	0.138	0.194	0.132	0.078
Present Work	--	0.192063	0.130386	0.0769102

Table 6.3 Maximum vertical velocity $V_{\max}$ at the horizontal middle line

Ra	10^3	10^4	10^5	10^6
***REF.** [40]*	0.138	0.234	0.261	0.262
***REF.** [63]*	--	0.233	0.261	0.262
***REF.** [10]*	0.155	0.234	0.258	0.262
***REF.** [165]*	0.139	0.235	0.259	0.263
Present Work	--	0.232963	0.257658	0.261474

6.4.2. Titled Square Enclosure with Pipes

Natural convective flows where the thermal effects on fluids are taken into account as buoyancy force is widely applied as the physical model for various engineering applications in energy, including solar collector and heat exchanger, where a pipe or a system of pipelines is arranged within an enclosure. The problem settings are illustrated in Figure 6.3, where a hot pipe goes through a square enclosure. In this numerical test, we are particularly interested in the heat exchange due to stratification between the cold wall of the square and the hot wall of the cylinder. Two design factors of the devices are considered, including the radius of the pipe and the orientation of the device.

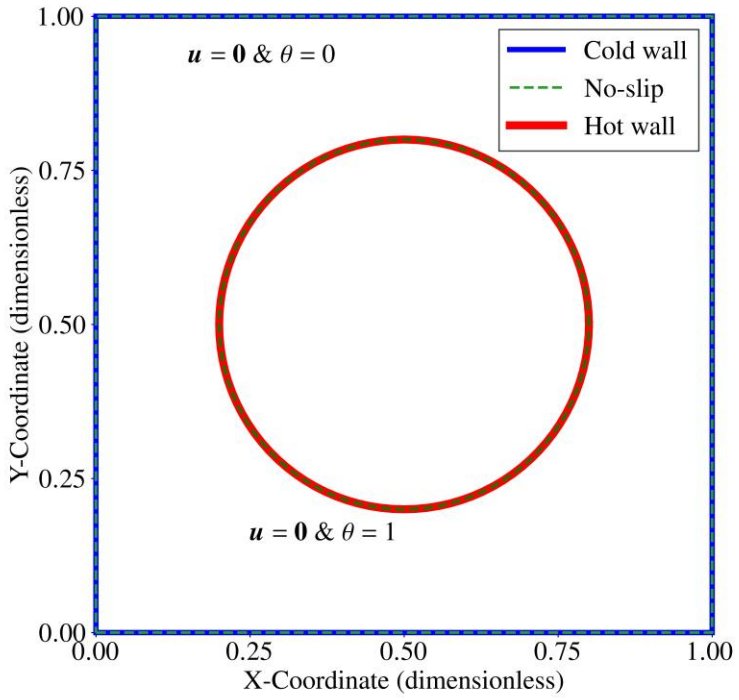

Figure 6.3 Schematics of natural convection in a 2D heat exchanger

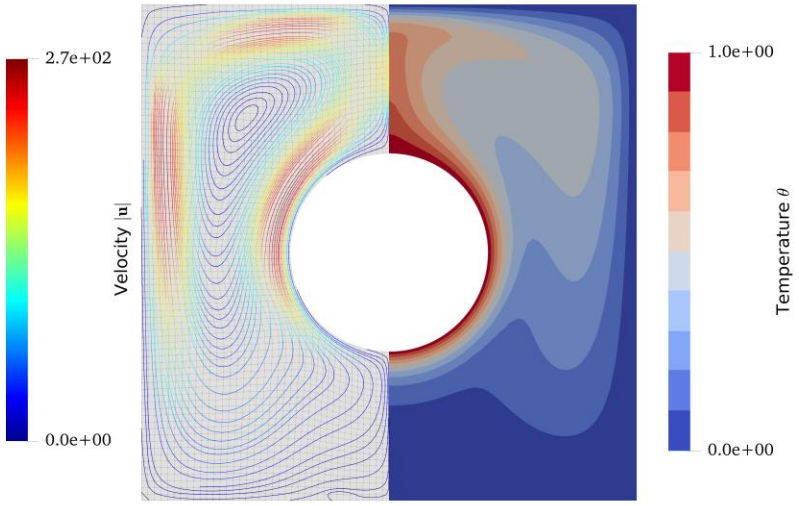

Figure 6.4 Velocity and relative temperature color rendering, streamlines of velocity and isothermal contours with background structured mesh (Ra = 10^6, r = 0.2, 1 cylinders)

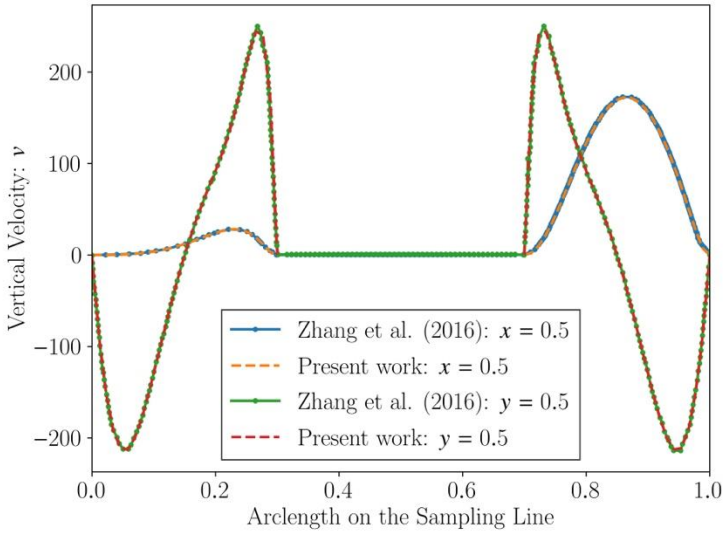

Figure 6.5 Vertical velocity distribution along x = 0.5 and y = 0.5 (Ra = 10^6 and r = 0.2)

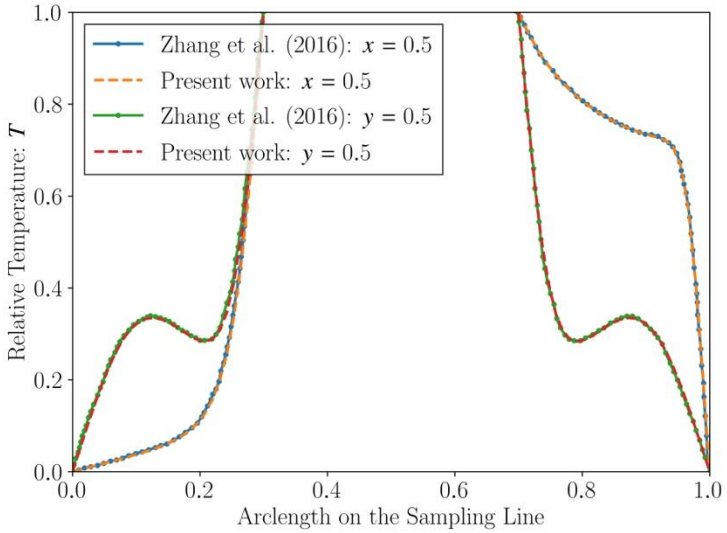

Figure 6.6 Temperature field distribution along x = 0.5 and y = 0.5 (Ra = 10^6 and r = 0.2)

The first test case that we considered is with radius $r = 0.2$, and gravity is perpendicular to the temperature gradient. The streamline of velocity and temperature contours are illustrated in Figure 6.4 to show the solution fields. To validate the numerical solution via the proposed method, we compare our simulated results with the reported computational results in [172], where the conventional uncoupled VMS stabilization is utilized with cubic spatial interpolation. In Figure 6.5 and Figure 6.6, the distribution of the two components of the velocity field along the horizontal and vertical centerline are presented,

respectively. Our results are attained from a structured mesh of 5408 nodes with linear quadrilateral elements, while the referred data is computed from 6379 nodes with cubic interpolation.

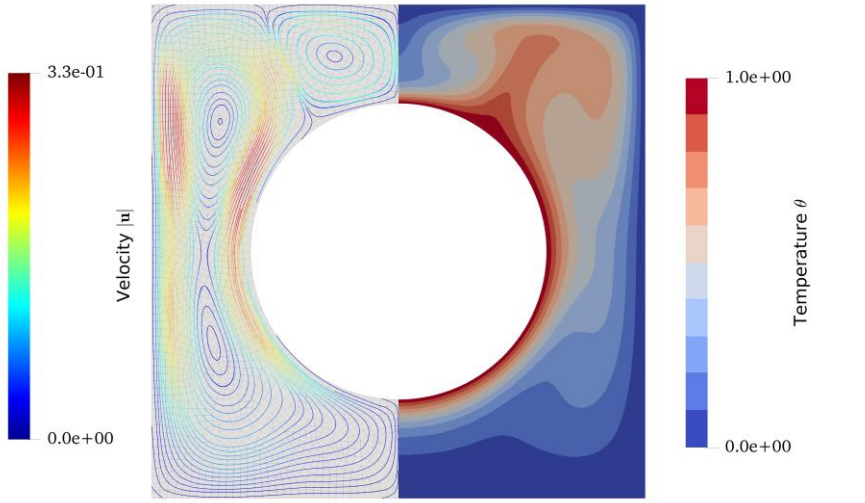

(a)

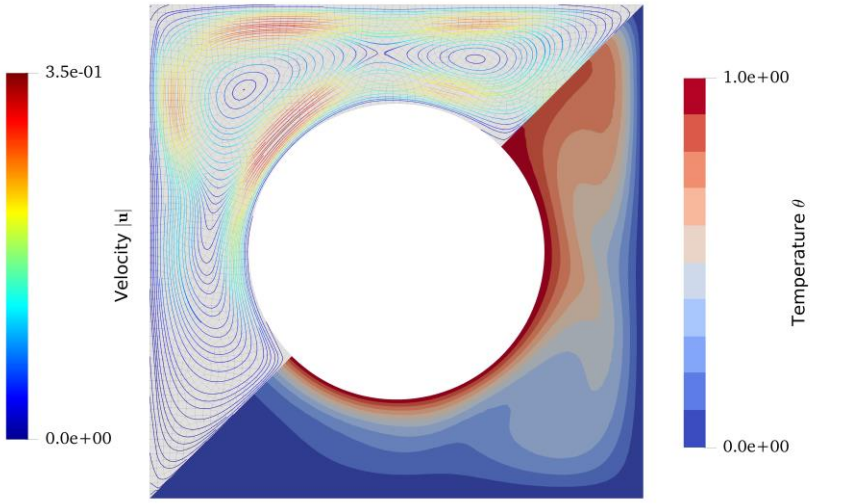

(b)

Figure 6.7 Velocity and relative temperature color rendering, streamlines of velocity and isothermal contours (Ra = 10^6, r = 0.3, 1 cylinder): (a) No inclination and (b) inclined: 45 degrees

Via variation of radius of the inner circle and the angle of inclination, we further test another two cases, where the radius is enlarged to $r = 0.3$ and the gravity is at $\pi / 4$ angle with the temperature gradient. To illustrate the solution fields, we present the streamlines of velocity and temperature contours

in Figure 6.7. For quantitative validation, we compare the distribution of local Nusselt number (heat flux) along the peripheral of the domain and inner circular boundaries with reported numerical data [130], where the solution is computed via finite volume method in a staggered grid, as shown in Figure 6.8.

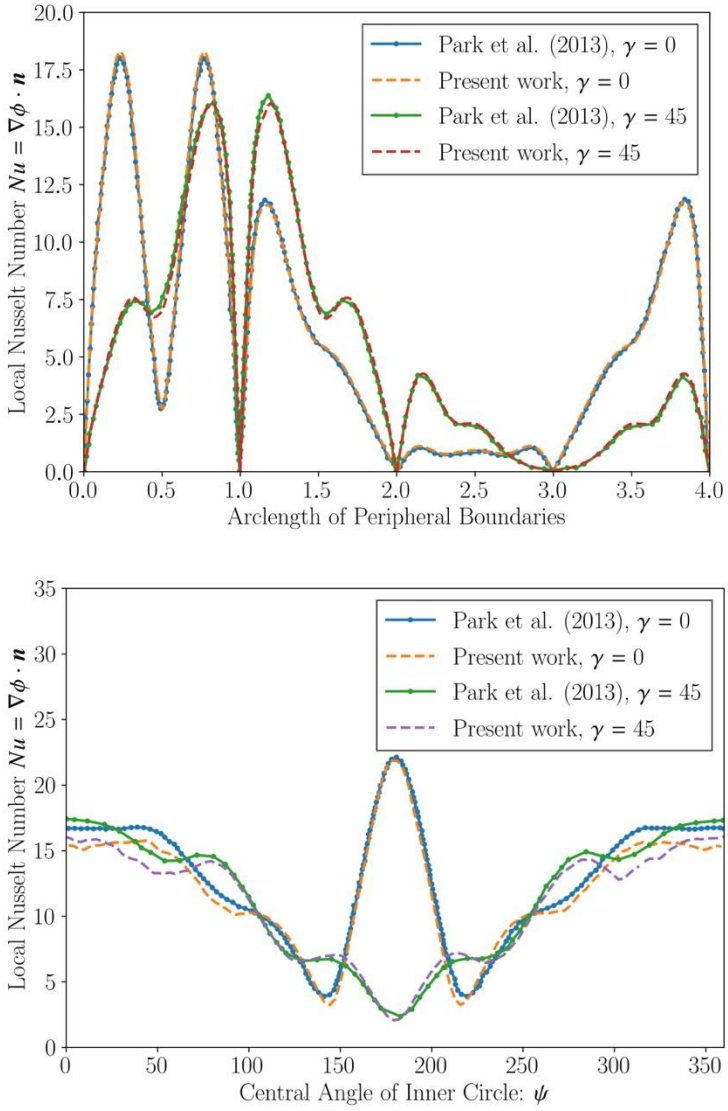

Figure 6.8 Distribution of local Nusselt number with respect to the arclength of peripheral boundaries and central angle of inner boundary

6.4.3. 3D Natural Convection

In this section, we extend the 2D natural convection to three dimensional, where the walls normal to the z-axis are adiabatic and imposed with no-slip boundary conditions. For consistency with

experimental settings [141], the dimension of the z axis is 0.32. The gravitational acceleration is still in the negative y-direction (i.e., $\boldsymbol{g}=[0,-1,0]$). The Rayleigh number is increased to $\mathrm{Ra}=1.5\times10^{9}$, which makes the flow physics fall in the turbulent regime. Due to the boundary layers in all three dimensions, a tensor-product Chebyshev grid $C_{x_n}\times C_{y_n}\times C_{z_n}$ is used, where the number of nodes in each dimension is: $x_n=y_n=51$ and $z_n=17$. Once the simulation reaches the statistical steady state, we carry out time averaging of the solution fields. To visualize the flow field, the streamlines of velocity and isosurfaces of temperature are plotted in Figure 6.9. In Figure 6.10, the time-averaged results are compared with the experimental data [141] and other reported results through DNS [141] and LES [165] with finer mesh, including the distribution of vertical velocity u_2 and temperature θ along the horizontal mid-line (i.e., $z=0.16$ and $y=0.5$), and distribution of horizontal velocity u_1 and temperature θ along the vertical mid-line, where good alignments are shown in these plots.

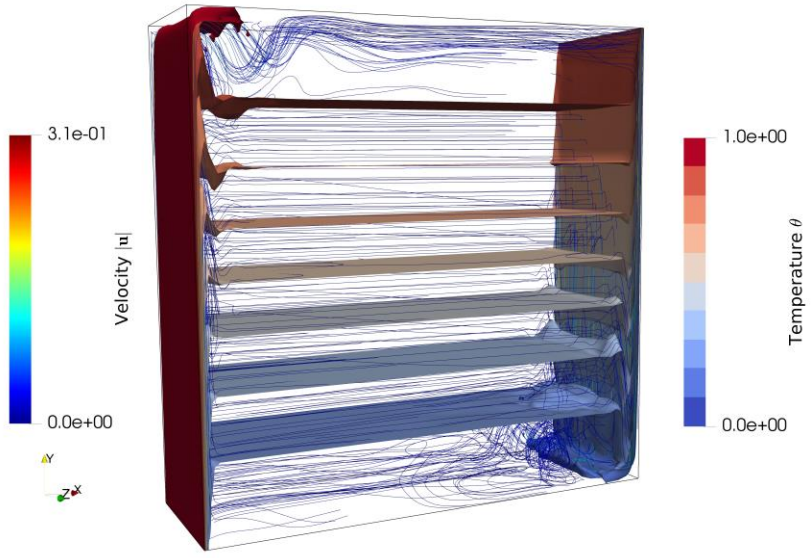

Figure 6.9 Time-averaged flow field: streamlines of velocity and iso-contours of temperature

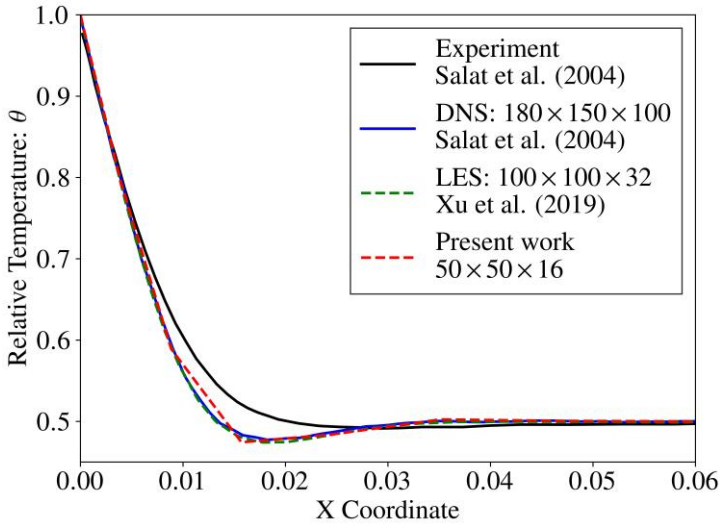

(a)

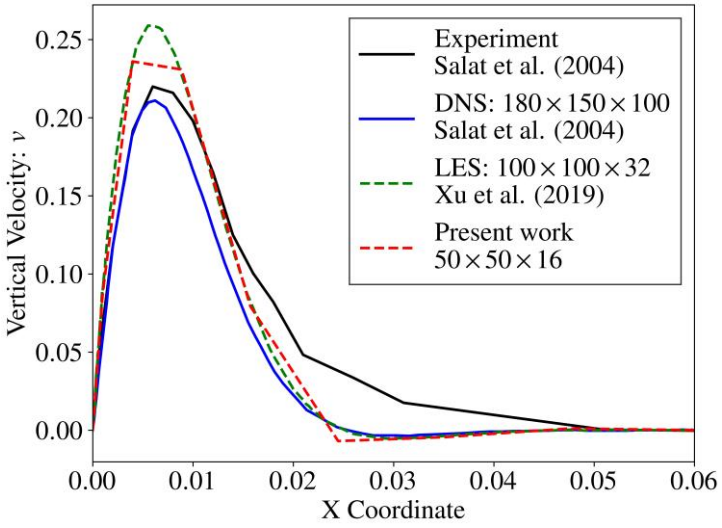

(b)

Figure 6.10 Mean profile comparisons for the present 3D simulations of natural convection: (a) temperature along the horizontal mid-line, (b) vertical velocity along the horizontal mid-line, (c) temperature along the vertical med-line and (d) horizontal velocity along the vertical med-line

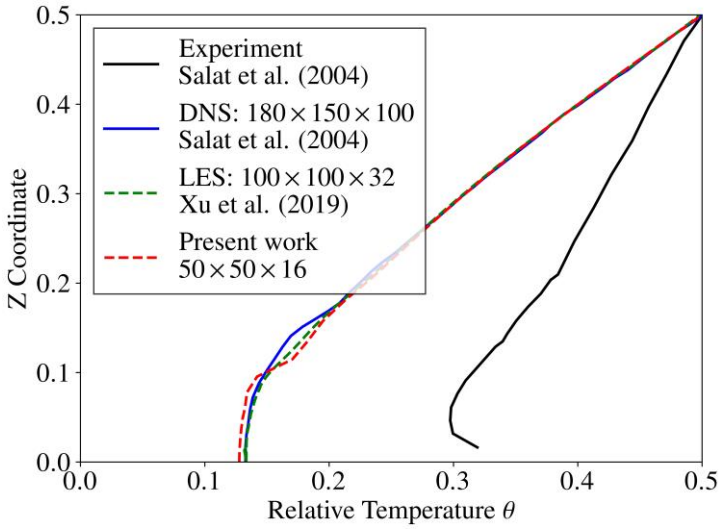

(c)

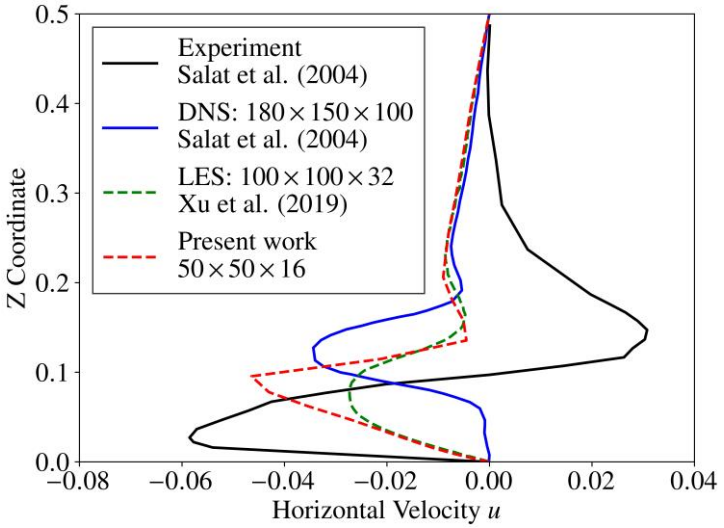

(d)

Figure 6.10 (cont.)

6.4.4. Rayleigh-Bénerd Convection

In this test, we use the proposed method to study the well-known Rayleigh-Bénard convection, where the gravity is in the same direction as temperature gradient. With such a setting, the buoyancy effect is opposed by the viscous damping effect, which results in the definition of the Rayleigh number in (6.11). Once the Rayleigh number reaches a certain level, Rayleigh-Bénard instability is triggered. Slip boundary conditions are applied on the top and bottom surfaces (i.e., $z = \pm 1$), where periodic boundary conditions for all fields are applied on the homogeneous directions (i.e., x and y). The Rayleigh number is

$\mathrm{Ra} = 10^8$ and Prandtl number is $\mathrm{Pr} = 1$. We initialize the problem with a static flow with zero-gradient temperature field. Once the flow reaches the statistical-steady state, the velocity fields and temperature fields are averaged over the two homogeneous directions (i.e., x and y) and time. We first compare the temporal evolution of total kinematic energy and total entropy with the DNS and LES results reported in [160] in Figure 6.11 and Figure 6.12. Due to the different initialization strategy, there are deviations in some extents. However, once the flow reaches the statistical-steady state, we observe a consistent trend of time histories. Next, we compare the distribution of the space-time averaged mean temperature and vertical velocity fluctuation with the reported DNS and LES results with a finer mesh [160] in Figure 6.13 and Figure 6.14, where good comparisons are observed. In Figure 6.15, we illustrate the iso-contours of temperature at two time-spots (12.5s and 50.0s). In Figure 6.15a, while the flow is developing from the static flow driven by the RB instability, the salt fingering mixing process is observed. Once the flow is fully developed, a more drastic mixing process can be seen in Figure 6.15b.

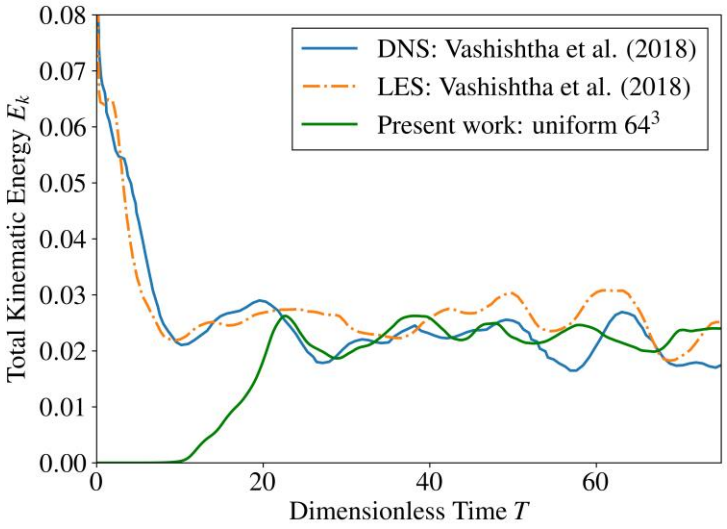

Figure 6.11 Time history of total kinetic energy

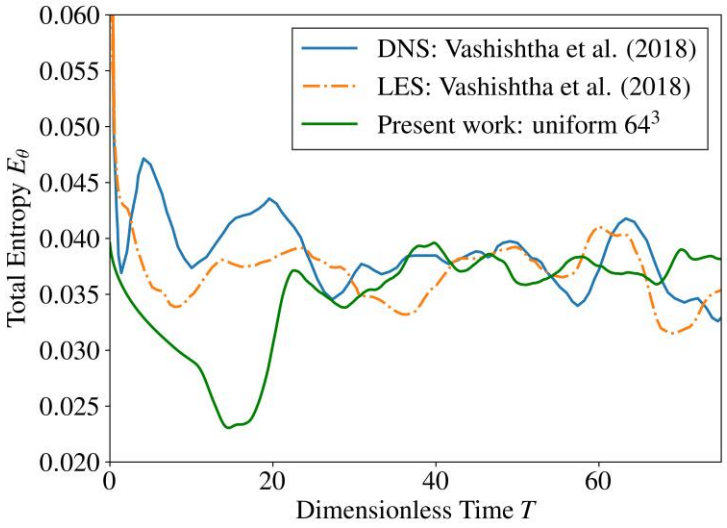

Figure 6.12 Time history of total entrolpy

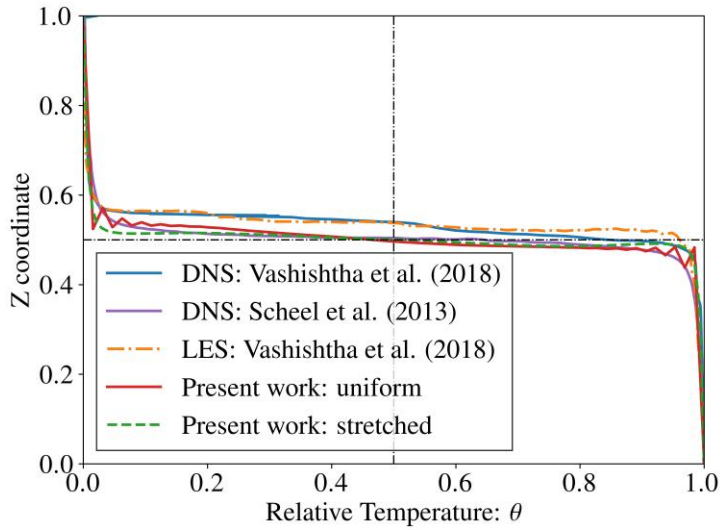

Figure 6.13 Space-time averaged mean profile of temperature field along the Z axis

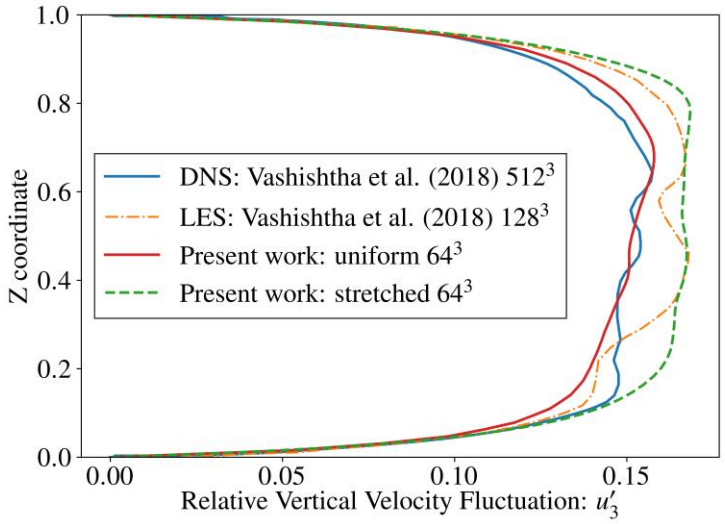

Figure 6.14 Fluctuation of vertical velocity along the Z axis

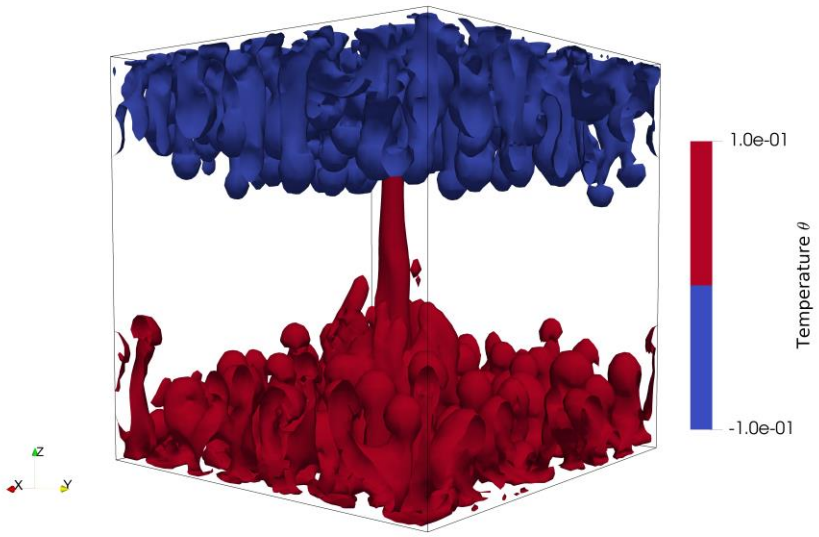

(a)

Figure 6.15 Iso-surfaces of temperature contours ($\theta = \pm 0.1$): (a) t = 12.5s and (b) t = 50.0s

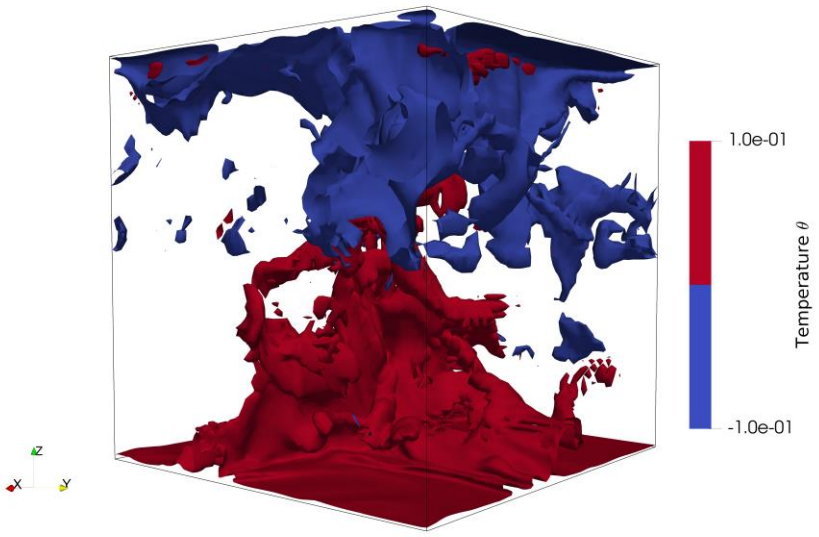

(b)

Figure 6.15 (cont.)

6.5. CONCLUSIONS

This paper has presented a VMS large-eddy turbulence model for the incompressible flow with density stratifications. The turbulence model is variationally derived through a hierarchical three-level VMS formulation where the fine-scale is further decomposed into fine-scale level-I and fine-scale level-II. In the context of stabilization methods, the resulting stabilized formulation overcomes the inf-sup condition, is essentially stable for advection-dominant flow, and yields a derived div-stab term, which further enhances the mass conservation. The Reynolds stress and flux arising from the two nonlinear advection terms are "closed" by the extended turbulence model, which is resolved through a discrete local system without any designed or artificial parameters. The fine-scale sub-problem is a transient coupled mixed formulation, which gives rise to a dynamic turbulence model that accommodates a wide range of flow problems. The proposed method is implemented with hexahedral and tetrahedral elements.

A benchmark problem of 2D laminar natural convection is used to validate the consistency of the proposed method. The proposed method is then tested with turbulent flows unstable stratifications, and the total energy and entropy budgets have consistent behavior as DNS results. Space and time averaged results are also compared with DNS or LES results with finer mesh.

CHAPTER 7: CONCLUDING REMARKS AND FUTURE DIRECTIONS

7.1. CONCLUDING REMARKS

The dissertation presents the variational multiscale methods for the coupled systems of incompressible flows with an active scalar field, of which two types of problems is detailed discussed: free-surface flows and stratified turbulence. By utilizing the VMS method for the coupled system instead of applying VMS method for a single PDE, the physics of additional nonlinearity is addressed, and the numerical challenges related to the additional physics are resolved.

The main conclusions of the present work are the following:

- A new stabilized weak form for advection-diffusion equation is constructed by taking the fine-scale time-dependency into account in the coarse scale. Compared to conventional VMS stabilized form for hyperbolic equation, a new stabilization term is derived, and it serves the purpose of reducing the numerical dissipation. In the application on the level-set method, the conservation of mass is largely improved.
- To ensure the robustness of long-time run of free-surface flows, a re-initialization process is added to the present framework. The Eikonal equation is transformed into pseudo time-dependent form and a stabilized form with SUPG/VMS type stabilization plus a residual-based shock-capturing term is used to solve this type of Hamilton-Jacobian equation.
- Following the previous two points, a stabilized framework of level-set method is established fully on the bubble-function based VMS method, as the first of its kind. Spatial and temporal refinement tests are carried with the proposed stabilized level-set method, and convergence rates are optimal for both hexahedral and tetrahedral elements.
- Conservation of mass is critical for the robustness and accuracy of long-time run of free-surface problems when the level-set method is the interface-capturing algorithm.
- Application of VMS method to the coupled systems of free-surfaces gives rise to interfacial terms that have a structure which is similar to the Ghost penalty terms reported in the literature. These

interfacial terms do not appear naturally if VMS-based stabilization is applied individually to each of the two PDEs. Representing the location of the interface via dependency of the mechanical material coefficients on the level-set φ also provides an avenue to variationally account for sub-grid effects engendered by the deforming interface. The variationally consistent derivation presented here not only provides the necessary stabilization for the sources of instability in convective free-surface flows, it also shows the variational basis of the ghost penalty term as a stabilizing term.

- The multilevel VMS LES turbulence model is further extended to hexahedral elements (linear and quadratic). A set of numerical tests with increasing complexities has performed to verify the proposed isothermal turbulences for general LES applications.
- The multilevel VMS LES turbulence modeling philosophy is adopted in the incompressible flows with density stratifications. A coupled fine-scale problem is resolved, of which the solution yields to the LES model of stratified turbulence, for both stable and unstable stratification.
- All the proposed methods are implemented with finite-element discretization. The codes are also parallelized for distributed-memory systems. The scalability is validated up to approximately 2000 CPUs.

7.2. FUTURE WORK

The dissertation has presented a methodology of numerical methods for coupled fluid dynamic systems where VMS is served as a mathematical bridge between coarse/resolved and fine/subgrid scales. This framework can be further utilized for other complex flows with additional physics.

The isothermal turbulence model can be extended for the Langmuir circulation by adding a surface stress on the top of the domain. The fine-scale sub-problems can automatically adapt to the modified driven mechanism in the governing PDE. Following this way of thinking, the stratified turbulence model can be extended to Rayleigh–Bénard–Marangoni convection.

Most of the applications within this dissertation employ incompressibility as low-Mach number approximation. Thus, the volumetric deformation is filtered out from the numerical methods. The turbulence model for incompressible flows can be further extend for low-Mach number variable-density flow, where the large amplitude of density and temperature variation is allowed. This model will serve for the combustions or chemical reactions and stellar hydrodynamics in astrophysics.

REFERENCES

[1] N. Ahmed, T.C. Rebollo, V. John, S. Rubino, A Review of Variational Multiscale Methods for the Simulation of Turbulent Incompressible Flows, Arch Computat Methods Eng. 24 (2017) 115–164.

[2] I. Akkerman, Y. Bazilevs, D.J. Benson, M.W. Farthing, C.E. Kees, Free-Surface Flow and Fluid-Object Interaction Modeling With Emphasis on Ship Hydrodynamics, J. Appl. Mech. 79 (2011) 010905–010905.

[3] I. Akkerman, Y. Bazilevs, V.M. Calo, T.J.R. Hughes, S. Hulshoff, The role of continuity in residual-based variational multiscale modeling of turbulence, Comput Mech. 41 (2008) 371–378.

[4] I. Akkerman, Y. Bazilevs, C.E. Kees, M.W. Farthing, Isogeometric analysis of free-surface flow, Journal of Computational Physics. 230 (2011) 4137–4152.

[5] S. Amdouni, K. Mansouri, Y. Renard, M. Arfaoui, M. Moakher, Numerical convergence and stability of mixed formulation with X-FEM cut-off, European Journal of Computational Mechanics. 21 (2012) 160–173.

[6] M. Ardyna, L. Lacour, S. Sergi, F. d'Ovidio, J.-B. Sallée, M. Rembauville, S. Blain, A. Tagliabue, R. Schlitzer, C. Jeandel, K.R. Arrigo, H. Claustre, Hydrothermal vents trigger massive phytoplankton blooms in the Southern Ocean, Nat Commun. 10 (2019) 1–8.

[7] V. Armenio, S. Sarkar, An investigation of stably stratified turbulent channel flow using large-eddy simulation, Journal of Fluid Mechanics. 459 (2002) 1–42.

[8] J. Baiges, R. Codina, A. Pont, E. Castillo, An adaptive Fixed-Mesh ALE method for free surface flows, Computer Methods in Applied Mechanics and Engineering. 313 (2017) 159–188.

[9] R. Balachandar, V.C. Patel, Flow over a fixed rough dune, Canadian Journal of Civil Engineering. (2008).

[10] G. Barakos, E. Mitsoulis, D. Assimacopoulos, Natural convection flow in a square cavity revisited: Laminar and turbulent models with wall functions, International Journal for Numerical Methods in Fluids. 18 (1994) 695–719.

[11] C. Basting, D. Kuzmin, J.N. Shadid, Optimal control for reinitialization in finite element level set methods, International Journal for Numerical Methods in Fluids. 84 (2017) 292–305.

[12] K.-J. Bathe, Finite element procedures, Klaus-Jurgen Bathe, 2006.

[13] Y. Bazilevs, V.M. Calo, J.A. Cottrell, T.J.R. Hughes, A. Reali, G. Scovazzi, Variational multiscale residual-based turbulence modeling for large eddy simulation of incompressible flows, Computer Methods in Applied Mechanics and Engineering. 197 (2007) 173–201.

[14] Y. Bazilevs, C. Michler, V.M. Calo, T.J.R. Hughes, Weak Dirichlet boundary conditions for wall-bounded turbulent flows, Computer Methods in Applied Mechanics and Engineering. 196 (2007) 4853–4862.

[15] R.W. Bilger, Turbulent Diffusion Flames, Annual Review of Fluid Mechanics. 21 (1989) 101–135.

[16] D. Boffi, F. Brezzi, M. Fortin, others, Mixed finite element methods and applications, Springer, 2013.

[17] F. Brezzi, L.P. Franca, T.J.R. Hughes, A. Russo, b = ∝ g, Computer Methods in Applied Mechanics and Engineering. 145 (1997) 329–339.

[18] F. Brezzi, L.P. Franca, A. Russo, Further considerations on residual-free bubbles for advective-diffusive equations, Computer Methods in Applied Mechanics and Engineering. 166 (1998) 25–33.

[19] F. Brezzi, D. Marini, A. Russo, Applications of the pseudo residual-free bubbles to the stabilization of convection-diffusion problems, Computer Methods in Applied Mechanics and Engineering. 166 (1998) 51–63.

[20] A.N. Brooks, T.J.R. Hughes, Streamline upwind/Petrov-Galerkin formulations for convection dominated flows with particular emphasis on the incompressible Navier-Stokes equations, Computer Methods in Applied Mechanics and Engineering. 32 (1982) 199–259.

[21] E. Burman, Ghost penalty, Comptes Rendus Mathematique. 348 (2010) 1217–1220.

[22] E. Burman, S. Claus, P. Hansbo, M.G. Larson, A. Massing, CutFEM: Discretizing geometry and partial differential equations, International Journal for Numerical Methods in Engineering. 104 (2015) 472–501.

[23] E. Burman, S. Claus, A. Massing, A Stabilized Cut Finite Element Method for the Three Field Stokes Problem, SIAM J. Sci. Comput. 37 (2015) A1705–A1726.

[24] E. Burman, D. Elfverson, P. Hansbo, M.G. Larson, K. Larsson, Shape optimization using the cut finite element method, Computer Methods in Applied Mechanics and Engineering. 328 (2018) 242–261.

[25] E. Burman, P. Hansbo, Fictitious domain finite element methods using cut elements: II. A stabilized Nitsche method, Applied Numerical Mathematics. 62 (2012) 328–341.

[26] E. Burman, P. Hansbo, Fictitious domain methods using cut elements: III. A stabilized Nitsche method for Stokes' problem, ESAIM: Mathematical Modelling & Numerical Analysis. 48 (2014) 859–874.

[27] E. Burman, P. Hansbo, M.G. Larson, A stabilized cut finite element method for partial differential equations on surfaces: The Laplace–Beltrami operator, Computer Methods in Applied Mechanics and Engineering. 285 (2015) 188–207.

[28] E. Burman, P. Hansbo, M.G. Larson, A. Massing, S. Zahedi, Full Gradient Stabilized Cut Finite Element Methods for Surface Partial Differential Equations, Computer Methods in Applied Mechanics and Engineering. 310 (2016) 278–296.

[29] R. Calderer, A. Masud, A multiscale stabilized ALE formulation for incompressible flows with moving boundaries, Comput Mech. 46 (2010) 185–197.

[30] R. Calderer, A. Masud, Residual-based variational multiscale turbulence models for unstructured tetrahedral meshes, Computer Methods in Applied Mechanics and Engineering. 254 (2013) 238–253.

[31] R. Calderer, A. Masud, Residual-based variational multiscale turbulence models for unstructured tetrahedral meshes, Computer Methods in Applied Mechanics and Engineering. 254 (2013) 238–253.

[32] R. Calderer, L. Zhu, R. Gibson, A. Masud, Residual-based turbulence models and arbitrary Lagrangian–Eulerian framework for free surface flows, Math. Models Methods Appl. Sci. 25 (2015) 2287–2317.

[33] M.A. Chella, Breaking Wave Characteristics and Breaking Wave Forces on Slender Cylinders, Norwegian University of Science and Technology, 2016.

[34] D.R. Chenoweth, S. Paolucci, Natural convection in an enclosed vertical air layer with large horizontal temperature differences, Journal of Fluid Mechanics. 169 (1986) 173–210.

[35] N.J. Cherry, R. Hillier, M.E.M.P. Latour, Unsteady measurements in a separated and reattaching flow, Journal of Fluid Mechanics. 144 (1984) 13–46.

[36] S.S. Collis, Monitoring unresolved scales in multiscale turbulence modeling, Physics of Fluids. 13 (2001) 1800–1806.

[37] M.A. Cruchaga, D.J. Celentano, T.E. Tezduyar, Moving-interface computations with the edge-tracked interface locator technique (ETILT), International Journal for Numerical Methods in Fluids. 47 (2005) 451–469.

[38] S.J. Cummins, T.B. Silvester, P.W. Cleary, Three-dimensional wave impact on a rigid structure using smoothed particle hydrodynamics, International Journal for Numerical Methods in Fluids. 68 (2012) 1471–1496.

[39] I.G. Currie, Fundamental mechanics of fluids, CRC press, 2016.

[40] G.D.V. Davis, Natural convection of air in a square cavity: A bench mark numerical solution, International Journal for Numerical Methods in Fluids. 3 (1983) 249–264.

[41] O. Desjardins, V. Moureau, H. Pitsch, An accurate conservative level set/ghost fluid method for simulating turbulent atomization, Journal of Computational Physics. 227 (2008) 8395–8416.

[42] C.R. Doering, J.D. Gibbon, Applied Analysis of the Navier-Stokes Equations, Cambridge University Press, 1995.

[43] R.N. Elias, A.L.G.A. Coutinho, Stabilized edge-based finite element simulation of free-surface flows, Int. J. Numer. Meth. Fluids. 54 (2007) 965–993.

[44] R.N. Elias, M.A.D. Martins, A.L.G.A. Coutinho, Simple finite element-based computation of distance functions in unstructured grids, Int. J. Numer. Meth. Engng. 72 (2007) 1095–1110.

[45] J.A. Evans, C. Coley, R.M. Aronson, C.L. Wetterer-Nelson, Y. Bazilevs, Residual-Based Large Eddy Simulation with Isogeometric Divergence-Conforming Discretizations, in: T.E. Tezduyar (Ed.), Frontiers in Computational Fluid-Structure Interaction and Flow Simulation: Research from Lead Investigators under Forty – 2018, Springer International Publishing, Cham, 2018: pp. 91–130.

[46] C. Farhat, A. Rajasekharan, B. Koobus, A dynamic variational multiscale method for large eddy simulations on unstructured meshes, Computer Methods in Applied Mechanics and Engineering. 195 (2006) 1667–1691.

[47] Fenton John D., A Fifth-Order Stokes Theory for Steady Waves, Journal of Waterway, Port, Coastal, and Ocean Engineering. 111 (1985) 216–234.

[48] L. Franca, J.V.A. Ramalho, F. Valentin, Multiscale and Residual-Free Bubble Functions for Reaction-Advection-Diffusion Problems, JMC. 3 (2005).

[49] L.P. Franca, C. Farhat, A.P. Macedo, M. Lesoinne, Residual-free bubbles for the Helmholtz equation, International Journal for Numerical Methods in Engineering. 40 (1997) 4003–4009.

[50] P. Gamnitzer, V. Gravemeier, W.A. Wall, Time-dependent subgrid scales in residual-based large eddy simulation of turbulent channel flow, Computer Methods in Applied Mechanics and Engineering. 199 (2010) 819–827.

[51] A. Garanaik, S.K. Venayagamoorthy, Assessment of small-scale anisotropy in stably stratified turbulent flows using direct numerical simulations, Physics of Fluids. 30 (2018) 126602.

[52] C. Garnier, J. Currie, T. Muneer, Integrated collector storage solar water heater: Temperature stratification, Applied Energy. 86 (2009) 1465–1469.

[53] M. Germano, U. Piomelli, P. Moin, W.H. Cabot, A dynamic subgrid-scale eddy viscosity model, Physics of Fluids A: Fluid Dynamics. 3 (1991) 1760–1765.

[54] F. Gibou, R. Fedkiw, S. Osher, A review of level-set methods and some recent applications, Journal of Computational Physics. 353 (2018) 82–109.

[55] V. Girault, R. Glowinski, T.W. Pan, A Fictitious-Domain Method with Distributed Multiplier for the Stokes Problem, in: A. Sequeira, H.B. da Veiga, J.H. Videman (Eds.), Applied Nonlinear Analysis, Springer US, Boston, MA, 2002: pp. 159–174.

[56] S.M. Glenn, T.N. Miles, G.N. Seroka, Y. Xu, R.K. Forney, F. Yu, H. Roarty, O. Schofield, J. Kohut, Stratified coastal ocean interactions with tropical cyclones, Nat Commun. 7 (2016) 1–10.

[57] Gómez-Gesteira M., Dalrymple Robert A., Using a Three-Dimensional Smoothed Particle Hydrodynamics Method for Wave Impact on a Tall Structure, Journal of Waterway, Port, Coastal, and Ocean Engineering. 130 (2004) 63–69.

[58] Gravemeier Volker, Wall Wolfgang A., Ramm Ekkehard, Large eddy simulation of turbulent incompressible flows by a three-level finite element method, International Journal for Numerical Methods in Fluids. 48 (2005) 1067–1099.

[59] A. Hansbo, P. Hansbo, An unfitted finite element method, based on Nitsche's method, for elliptic interface problems, Computer Methods in Applied Mechanics and Engineering. 191 (2002) 5537–5552.

[60] P. Hansbo, C. Lovadina, I. Perugia, G. Sangalli, A Lagrange multiplier method for the finite element solution of elliptic interface problems using non-matching meshes, Numer. Math. 100 (2005) 91–115.

[61] M. Herrmann, A balanced force refined level set grid method for two-phase flows on unstructured flow solver grids, Journal of Computational Physics. 227 (2008) 2674–2706.

[62] C.W. Hirt, B.D. Nichols, Volume of fluid (VOF) method for the dynamics of free boundaries, Journal of Computational Physics. 39 (1981) 201–225.

[63] M. Hortmann, M. Perić, G. Scheuerer, Finite volume multigrid prediction of laminar natural convection: Bench-mark solutions, International Journal for Numerical Methods in Fluids. 11 (1990) 189–207.

[64] S. Hoyas, J. Jiménez, Reynolds number effects on the Reynolds-stress budgets in turbulent channels, Physics of Fluids. 20 (2008) 101511.

[65] A. Huerta, W.K. Liu, Viscous flow with large free surface motion, Computer Methods in Applied Mechanics and Engineering. 69 (1988) 277–324.

[66] T.J.R. Hughes, Multiscale phenomena: Green's functions, the Dirichlet-to-Neumann formulation, subgrid scale models, bubbles and the origins of stabilized methods, Computer Methods in Applied Mechanics and Engineering. 127 (1995) 387–401.

[67] T.J.R. Hughes, G.R. Feijóo, L. Mazzei, J.-B. Quincy, The variational multiscale method—a paradigm for computational mechanics, Computer Methods in Applied Mechanics and Engineering. 166 (1998) 3–24.

[68] T.J.R. Hughes, L.P. Franca, A new finite element formulation for computational fluid dynamics: VII. The stokes problem with various well-posed boundary conditions: Symmetric formulations that converge for all velocity/pressure spaces, Computer Methods in Applied Mechanics and Engineering. 65 (1987) 85–96.

[69] T.J.R. Hughes, L.P. Franca, M. Balestra, A new finite element formulation for computational fluid dynamics: V. Circumventing the babuška-brezzi condition: a stable Petrov-Galerkin formulation of the stokes problem accommodating equal-order interpolations, Computer Methods in Applied Mechanics and Engineering. 59 (1986) 85–99.

[70] T.J.R. Hughes, L.P. Franca, G.M. Hulbert, A new finite element formulation for computational fluid dynamics: VIII. The galerkin/least-squares method for advective-diffusive equations, Computer Methods in Applied Mechanics and Engineering. 73 (1989) 173–189.

[71] T.J.R. Hughes, W.K. Liu, T.K. Zimmermann, Lagrangian-Eulerian finite element formulation for incompressible viscous flows, Computer Methods in Applied Mechanics and Engineering. 29 (1981) 329–349.

[72] T.J.R. Hughes, L. Mazzei, K.E. Jansen, Large Eddy Simulation and the variational multiscale method, Comput Visual Sci. 3 (2000) 47–59.

[73] T.J.R. Hughes, L. Mazzei, A.A. Oberai, A.A. Wray, The multiscale formulation of large eddy simulation: Decay of homogeneous isotropic turbulence, Physics of Fluids. 13 (2001) 505–512.

[74] T.J.R. Hughes, A.A. Oberai, L. Mazzei, Large eddy simulation of turbulent channel flows by the variational multiscale method, Physics of Fluids. 13 (2001) 1784–1799.

[75] A. Iafrati, A. Babanin, M. Onorato, Modulational Instability, Wave Breaking, and Formation of Large-Scale Dipoles in the Atmosphere, Phys. Rev. Lett. 110 (2013) 184504.

[76] S.R. Idelsohn, E. Oñate, The challenge of mass conservation in the solution of free-surface flows with the fractional-step method: Problems and solutions, Int. J. Numer. Meth. Biomed. Engng. 26 (2010) 1313–1330.

[77] G.N. Ivey, K.B. Winters, J.R. Koseff, Density Stratification, Turbulence, but How Much Mixing?, Annual Review of Fluid Mechanics. 40 (2008) 169–184.

[78] K.E. Jansen, C.H. Whiting, G.M. Hulbert, A generalized-α method for integrating the filtered Navier–Stokes equations with a stabilized finite element method, Computer Methods in Applied Mechanics and Engineering. 190 (2000) 305–319.

[79] M.S. Jensen, Breaking of waves over a steep bottom slope, Videnbasen for Aalborg UniversitetVBN, Aalborg UniversitetAalborg University, Det Teknisk-Naturvidenskabelige FakultetThe Faculty of Engineering and Science, Institut for Vand, Jord og MiljøteknikDepartment of Civil Engineering, 2004.

[80] H. Kanchi, A. Masud, A 3D adaptive mesh moving scheme, Int. J. Numer. Meth. Fluids. 54 (2007) 923–944.

[81] C.E. Kees, I. Akkerman, M.W. Farthing, Y. Bazilevs, A conservative level set method suitable for variable-order approximations and unstructured meshes, Journal of Computational Physics. 230 (2011) 4536–4558.

[82] C.E. Kees, I. Akkerman, M.W. Farthing, Y. Bazilevs, A conservative level set method suitable for variable-order approximations and unstructured meshes, Journal of Computational Physics. 230 (2011) 4536–4558.

[83] S. Khani, M.L. Waite, Large eddy simulations of stratified turbulence: the dynamic Smagorinsky model, Journal of Fluid Mechanics. 773 (2015) 327–344.

[84] R.A. Khurram, A. Masud, A Multiscale/stabilized Formulation of the Incompressible Navier–Stokes Equations for Moving Boundary Flows and Fluid–structure Interaction, Comput Mech. 38 (2006) 403–416.

[85] S.J. Kimmel, J.A. Domaradzki, Large eddy simulations of Rayleigh–Bénard convection using subgrid scale estimation model, Physics of Fluids. 12 (1999) 169–184.

[86] M. Kiya, K. Sasaki, Structure of a turbulent separation bubble, Journal of Fluid Mechanics. 137 (1983) 83–113.

[87] K.M.T. Kleefsman, G. Fekken, A.E.P. Veldman, B. Iwanowski, B. Buchner, A Volume-of-Fluid based simulation method for wave impact problems, Journal of Computational Physics. 206 (2005) 363–393.

[88] D.A. Kopriva, J.H. Kolias, A Conservative Staggered-Grid Chebyshev Multidomain Method for Compressible Flows, Journal of Computational Physics. 125 (1996) 244–261.

[89] S. Koshizuka, Y. Oka, Moving-Particle Semi-Implicit Method for Fragmentation of Incompressible Fluid, NSE. 123 (1996) 421–434.

[90] E.V. Laitone, The second approximation to cnoidal and solitary waves, Journal of Fluid Mechanics. 9 (1960) 430–444.

[91] E. Lamballais, J. Silvestrini, S. Laizet, Direct numerical simulation of flow separation behind a rounded leading edge: Study of curvature effects, International Journal of Heat and Fluid Flow. 31 (2010) 295–306.

[92] M. Langari, Z. Yang, Numerical study of the primary instability in a separated boundary layer transition under elevated free-stream turbulence, Physics of Fluids. 25 (2013) 074106.

[93] M.G. Larson, A. Målqvist, Adaptive variational multiscale methods based on a posteriori error estimation: Energy norm estimates for elliptic problems, Computer Methods in Applied Mechanics and Engineering. 196 (2007) 2313–2324.

[94] A. Legay, J. Chessa, T. Belytschko, An Eulerian–Lagrangian method for fluid–structure interaction based on level sets, Computer Methods in Applied Mechanics and Engineering. 195 (2006) 2070–2087.

[95] C.-L. Lin, H. Lee, T. Lee, L.J. Weber, A level set characteristic Galerkin finite element method for free surface flows, Int. J. Numer. Meth. Fluids. 49 (2005) 521–547.

[96] E.F. Lins, R.N. Elias, F.A. Rochinha, A.L.G.A. Coutinho, Residual-based variational multiscale simulation of free surface flows, Comput Mech. 46 (2010) 545–557.

[97] E.F. Lins, R.N. Elias, F.A. Rochinha, A.L.G.A. Coutinho, Residual-based variational multiscale simulation of free surface flows, Comput Mech. 46 (2010) 545–557.

[98] D. Lohse, K.-Q. Xia, Small-Scale Properties of Turbulent Rayleigh-Bénard Convection, Annual Review of Fluid Mechanics. 42 (2010) 335–364.

[99] P.R.M. Lyra, K. Morgan, A review and comparative study of upwind biased schemes for compressible flow computation. Part III: Multidimensional extension on unstructured grids, Arch Computat Methods Eng. 9 (2002) 207–256.

[100] E. Marchi, On the free overfall, Journal of Hydraulic Research. 31 (1993) 777–790.

[101] J.C. Martin, W.J. Moyce, Part IV. An Experimental Study of the Collapse of Liquid Columns on a Rigid Horizontal Plane, Philosophical Transactions of the Royal Society of London A: Mathematical, Physical and Engineering Sciences. 244 (1952) 312–324.

[102] A. Masud, Effects of Mesh Motion on the Stability and Convergence of ALE Based Formulations for Moving Boundary Flows, Comput Mech. 38 (2006) 430.

[103] A. Masud, A.A. Al-Naseem, R. Kannan, H. Gajendran, B-Splines and NURBS Based Finite Element Methods for Strained Electronic Structure Calculations, J. Appl. Mech. 85 (2018).

[104] A. Masud, M. Bhanabhagvanwala, R.A. Khurram, An adaptive mesh rezoning scheme for moving boundary flows and fluid–structure interaction, Computers & Fluids. 36 (2007) 77–91.

[105] A. Masud, R. Calderer, A variational multiscale stabilized formulation for the incompressible Navier–Stokes equations, Comput Mech. 44 (2009) 145–160.

[106] A. Masud, R. Calderer, A variational multiscale stabilized formulation for the incompressible Navier–Stokes equations, Comput Mech. 44 (2009) 145–160.

[107] A. Masud, R. Calderer, A variational multiscale method for incompressible turbulent flows: Bubble functions and fine scale fields, Computer Methods in Applied Mechanics and Engineering. 200 (2011) 2577–2593.

[108] A. Masud, R. Calderer, Residual-based turbulence models for moving boundary flows: hierarchical application of variational multiscale method and three-level scale separation, Int. J. Numer. Meth. Fluids. 73 (2013) 284–305.

[109] A. Masud, L.P. Franca, A hierarchical multiscale framework for problems with multiscale source terms, Computer Methods in Applied Mechanics and Engineering. 197 (2008) 2692–2700.

[110] A. Masud, T.J.R. Hughes, A space-time Galerkin/least-squares finite element formulation of the Navier-Stokes equations for moving domain problems, Computer Methods in Applied Mechanics and Engineering. 146 (1997) 91–126.

[111] A. Masud, T.J.R. Hughes, A stabilized mixed finite element method for Darcy flow, Computer Methods in Applied Mechanics and Engineering. 191 (2002) 4341–4370.

[112] A. Masud, R. Kannan, B-splines and NURBS based finite element methods for Kohn–Sham equations, Computer Methods in Applied Mechanics and Engineering. 241–244 (2012) 112–127.

[113] A. Masud, R.A. Khurram, A multiscale/stabilized finite element method for the advection–diffusion equation, Computer Methods in Applied Mechanics and Engineering. 193 (2004) 1997–2018.

[114] A. Masud, R.A. Khurram, A multiscale/stabilized finite element method for the advection–diffusion equation, Computer Methods in Applied Mechanics and Engineering. 193 (2004) 1997–2018.

[115] A. Masud, J. Kwack, A stabilized mixed finite element method for the first-order form of advection–diffusion equation, International Journal for Numerical Methods in Fluids. 57 (2008) 1321–1348.

[116] A. Masud, G. Scovazzi, A heterogeneous multiscale modeling framework for hierarchical systems of partial differential equations, International Journal for Numerical Methods in Fluids. 65 (2011) 28–42.

[117] I. Mazzitelli, A.S. Lanotte, Active and passive scalar intermittent statistics in turbulent atmospheric convection, Physica D: Nonlinear Phenomena. 241 (2012) 251–259.

[118] W.D. McComb, Homogeneous, Isotropic Turbulence: Phenomenology, Renormalization and Statistical Closures, OUP Oxford, 2014.

[119] C. Meneveau, T.S. Lund, W.H. Cabot, A Lagrangian dynamic subgrid-scale model of turbulence, Journal of Fluid Mechanics. 319 (1996) 353.

[120] J.J. Monaghan, Smoothed Particle Hydrodynamics and Its Diverse Applications, Annual Review of Fluid Mechanics. 44 (2012) 323–346.

[121] R.D. Moser, J. Kim, N.N. Mansour, Direct numerical simulation of turbulent channel flow up to Reτ=590, Physics of Fluids. 11 (1999) 943–945.

[122] R. Nagaosa, Direct numerical simulation of vortex structures and turbulent scalar transfer across a free surface in a fully developed turbulence, Physics of Fluids. 11 (1999) 1581–1595.

[123] J.-C. Nave, R.R. Rosales, B. Seibold, A gradient-augmented level set method with an optimally local, coherent advection scheme, Journal of Computational Physics. 229 (2010) 3802–3827.

[124] A. Oberai, T. Hughes, The variational vultiscale vormulation of LES: channel flow at Reτ= 590. 40th AIAA Ann, Mtg., Reno, NV. (2002) 2002–1056.

[125] E. Oñate, S.R. Idelsohn, M.A. Celigueta, R. Rossi, Advances in the particle finite element method for the analysis of fluid–multibody interaction and bed erosion in free surface flows, Computer Methods in Applied Mechanics and Engineering. 197 (2008) 1777–1800.

[126] E. Oñate, S.R. Idelsohn, F. Del Pin, R. Aubry, The particle finite element method — an overview, Int. J. Comput. Methods. 01 (2004) 267–307.

[127] T.M. van Opstal, J. Yan, C. Coley, J.A. Evans, T. Kvamsdal, Y. Bazilevs, Isogeometric divergence-conforming variational multiscale formulation of incompressible turbulent flows, Computer Methods in Applied Mechanics and Engineering. 316 (2017) 859–879.

[128] S. Osher, J.A. Sethian, Fronts propagating with curvature-dependent speed: Algorithms based on Hamilton-Jacobi formulations, Journal of Computational Physics. 79 (1988) 12–49.

[129] Y. Pan, S. Banerjee, A numerical study of free-surface turbulence in channel flow, Physics of Fluids. 7 (1995) 1649–1664.

[130] H.K. Park, M.Y. Ha, H.S. Yoon, Y.G. Park, C. Son, A numerical study on natural convection in an inclined square enclosure with a circular cylinder, International Journal of Heat and Mass Transfer. 66 (2013) 295–314.

[131] D. Peng, B. Merriman, S. Osher, H. Zhao, M. Kang, A PDE-Based Fast Local Level Set Method, Journal of Computational Physics. 155 (1999) 410–438.

[132] F.D. Pin, S. Idelsohn, E. Oñate, R. Aubry, The ALE/Lagrangian Particle Finite Element Method: A new approach to computation of free-surface flows and fluid–object interactions, Computers & Fluids. 36 (2007) 27–38.

[133] S. Pirozzoli, M. Bernardini, R. Verzicco, P. Orlandi, Mixed convection in turbulent channels with unstable stratification, Journal of Fluid Mechanics. 821 (2017) 482–516.

[134] S.B. Pope, Turbulent flows, IOP Publishing, 2001.

[135] P.E. Raad, R. Bidoae, The three-dimensional Eulerian–Lagrangian marker and micro cell method for the simulation of free surface flows, Journal of Computational Physics. 203 (2005) 668–699.

[136] W.M. van Rees, A. Leonard, D.I. Pullin, P. Koumoutsakos, A comparison of vortex and pseudo-spectral methods for the simulation of periodic vortical flows at high Reynolds numbers, Journal of Computational Physics. 230 (2011) 2794–2805.

[137] S. Remmler, S. Hickel, Direct and large eddy simulation of stratified turbulence, International Journal of Heat and Fluid Flow. 35 (2012) 13–24.

[138] O. Reynolds, IV. On the dynamical theory of incompressible viscous fluids and the determination of the criterion, Philosophical Transactions of the Royal Society of London. (A.). 186 (1895) 123–164.

[139] W. Rodi, Turbulence models and their application in hydraulics, Routledge, 2017.

[140] P. Sagaut, Large Eddy Simulation for Incompressible Flows: An Introduction, Springer Science & Business Media, 2006.

[141] J. Salat, S. Xin, P. Joubert, A. Sergent, F. Penot, P. Le Quéré, Experimental and numerical investigation of turbulent natural convection in a large air-filled cavity, International Journal of Heat and Fluid Flow. 25 (2004) 824–832.

[142] C. Sicot, R. Perrin, T.T. Tran, J. Borée, Wall pressure and conditional flow structures downstream of a reattaching flow region, International Journal of Heat and Fluid Flow. 35 (2012) 119–129.

[143] J. Smagorinsky, General circulation experiments with the primitive equations: I. The basic experiment, Monthly Weather Review. 91 (1963) 99–164.

[144] A. Smolianski, Numerical modeling of two-fluid interfacial flows, University of Jyväskylä, 2001.

[145] W.D. Smyth, J.N. Moum, Anisotropy of turbulence in stably stratified mixing layers, Physics of Fluids. 12 (2000) 1343–1362.

[146] P.R. Spalart, Detached-Eddy Simulation, Annual Review of Fluid Mechanics. 41 (2009) 181–202.

[147] M. Sussman, E. Fatemi, An Efficient, Interface-Preserving Level Set Redistancing Algorithm and Its Application to Interfacial Incompressible Fluid Flow, SIAM J. Sci. Comput. 20 (1999) 1165–1191.

[148] M. Sussman, E.G. Puckett, A Coupled Level Set and Volume-of-Fluid Method for Computing 3D and Axisymmetric Incompressible Two-Phase Flows, Journal of Computational Physics. 162 (2000) 301–337.

[149] M. Sussman, P. Smereka, S. Osher, A Level Set Approach for Computing Solutions to Incompressible Two-Phase Flow, Journal of Computational Physics. 114 (1994) 146–159.

[150] K. Takizawa, T. Yabe, Y. Tsugawa, T.E. Tezduyar, H. Mizoe, Computation of free-surface flows and fluid–object interactions with the CIP method based on adaptive meshless soroban grids, Comput Mech. 40 (2006) 167–183.

[151] K. Takizawa, T. Yabe, Y. Tsugawa, T.E. Tezduyar, H. Mizoe, Computation of free-surface flows and fluid–object interactions with the CIP method based on adaptive meshless soroban grids, Comput Mech. 40 (2007) 167–183.

[152] Taylor Geoffrey Ingram, The instability of liquid surfaces when accelerated in a direction perpendicular to their planes. I, Proceedings of the Royal Society of London. Series A. Mathematical and Physical Sciences. 201 (1950) 192–196.

[153] C. Tenaud, B. Podvin, Y. Fraigneau, V. Daru, On wall pressure fluctuations and their coupling with vortex dynamics in a separated–reattached turbulent flow over a blunt flat plate, International Journal of Heat and Fluid Flow. 61 (2016) 730–748.

[154] T.E. Tezduyar, Finite element methods for flow problems with moving boundaries and interfaces, Arch Computat Methods Eng. 8 (2001) 83.

[155] T.E. Tezduyar, Computation of moving boundaries and interfaces and stabilization parameters, Int. J. Numer. Meth. Fluids. 43 (2003) 555–575.

[156] T.E. Tezduyar, M. Behr, J. Liou, A new strategy for finite element computations involving moving boundaries and interfaces—The deforming-spatial-domain/space-time procedure: I. The concept and the preliminary numerical tests, Computer Methods in Applied Mechanics and Engineering. 94 (1992) 339–351.

[157] T.E. Tezduyar, M. Behr, S. Mittal, J. Liou, A new strategy for finite element computations involving moving boundaries and interfaces—The deforming-spatial-domain/space-time procedure: II. Computation of free-surface flows, two-liquid flows, and flows with drifting cylinders, Computer Methods in Applied Mechanics and Engineering. 94 (1992) 353–371.

[158] W. Thomson, XLVI. *Hydrokinetic solutions and observations*, The London, Edinburgh, and Dublin Philosophical Magazine and Journal of Science. 42 (1871) 362–377.

[159] Y. Tu, Z. Cheng, M. Muskulus, A review of slamming load application to offshore wind turbines from an integrated perspective, Energy Procedia. 137 (2017) 346–357.

[160] S. Vashishtha, M.K. Verma, R. Samuel, Large-eddy simulations of turbulent thermal convection using renormalized viscosity and thermal diffusivity, Phys. Rev. E. 98 (2018) 043109.

[161] W.A. Wall, S. Genkinger, E. Ramm, A strong coupling partitioned approach for fluid–structure interaction with free surfaces, Computers & Fluids. 36 (2007) 169–183.

[162] V.C. Wong, D.K. Lilly, A comparison of two dynamic subgrid closure methods for turbulent thermal convection, Physics of Fluids. 6 (1994) 1016–1023.

[163] A.W. Woods, Turbulent Plumes in Nature, Annual Review of Fluid Mechanics. 42 (2010) 391–412.

[164] G.X. Wu, R. Eatock Taylor, D.M. Greaves, The effect of viscosity on the transient free-surface waves in a two-dimensional tank, Journal of Engineering Mathematics. 40 (2001) 77–90.

[165] S. Xu, B. Gao, M.-C. Hsu, B. Ganapathysubramanian, A residual-based variational multiscale method with weak imposition of boundary conditions for buoyancy-driven flows, Computer Methods in Applied Mechanics and Engineering. 352 (2019) 345–368.

[166] S. Xu, N. Liu, J. Yan, Residual-based variational multi-scale modeling for particle-laden gravity currents over flat and triangular wavy terrains, Computers & Fluids. 188 (2019) 114–124.

[167] V. Yakhot, S.A. Orszag, Renormalization group analysis of turbulence. I. Basic theory, J Sci Comput. 1 (1986) 3–51.

[168] J. Yan, A. Korobenko, A.E. Tejada-Martínez, R. Golshan, Y. Bazilevs, A new variational multiscale formulation for stratified incompressible turbulent flows, Computers & Fluids. 158 (2017) 150–156.

[169] Z. Yang, P.R. Voke, Large-eddy simulation of boundary-layer separation and transition at a change of surface curvature, Journal of Fluid Mechanics. 439 (2001) 305–333.

[170] W. Yue, C.-L. Lin, V.C. Patel, Large eddy simulation of turbulent open-channel flow with free surface simulated by level set method, Physics of Fluids. 17 (2005) 025108.

[171] I.B. Zeldovich, A.A. Ruzmaikin, D.D. Sokolov, Magnetic fields in astrophysics, Gordon and Breach Science Publishers, New York, 1983.

[172] P. Zhang, X. Zhang, J. Deng, L. Song, A numerical study of natural convection in an inclined square enclosure with an elliptic cylinder using variational multiscale element free Galerkin method, International Journal of Heat and Mass Transfer. 99 (2016) 721–737.

[173] L. Zhu, A. Goraya Shoaib, A. Masud, Interface-Capturing Method for Free-Surface Plunging and Breaking Waves, Journal of Engineering Mechanics. 145 (2019) 04019088.